Benedetto Villa Editor

RICERCHE DI GEOMATICA 2011

STUDI PRESENTATI ALLA SETTIMA EDIZIONE DEL PREMIO AUTeC

Associazione Universitari di Topografia e Cartografia

Associazione Universitari di Topografia e Cartografia

L' **AUTeC** (**A**ssociazione **U**niversitari di **T**opografia **e** **C**artografia) si è costituita a Bologna il 9 febbraio 1998.

Possono iscriversi a questa Associazione i docenti universitari inquadrati nel settore scientifico disciplinare ICAR/06 - Topografia e Cartografia.

L' **AUTeC** si propone i seguenti obiettivi:

- creare un luogo di incontro per discutere problemi di sviluppo della ricerca, di allocazione delle risorse e di promozione di iniziative didattiche di formazione;
- coordinare le iniziative nei riguardi di Enti ed Organismi nazionali ed internazionali, comunitari e non, con i quali intercorrono rapporti, per sviluppare e promuovere una politica di richieste e di scelte coordinata;
- promuovere quanto necessario per migliorare la qualità dell'insegnamento delle discipline del settore e il loro impatto sulla realtà produttiva del Paese;
- diffondere in maniera sistematica le informazioni che riguardano il settore.

L' **AUTeC** è retta da un Coordinatore nazionale coadiuvato dalla Giunta. Le cariche si rinnovano ogni biennio.

Hanno rivestito la carica di Coordinatore AUTeC i professori:

· Riccardo Galetto, ordinario dell'Università degli Studi di Pavia, nel biennio 1998-1999;
· Giorgio Bezoari, ordinario del Politecnico di Milano, nel biennio 2000-2001;
· Bruno Astori, ordinario del Politecnico di Torino, nel biennio 2002-2003;
· Anna Spalla, ordinario dell'Università degli Studi di Pavia, nei bienni 2004-2005 e 2006-2007.

Dal 2008 riveste la carica di Coordinatore il prof. Benedetto Villa, ordinario dell'Università degli Studi di Palermo.

Foto in copertina: Microdrone GMBH md4-1000

Renato Guttuso (1966):

Gioacchino Guttuso Agrimensore

Galleria d'Arte Moderna e Contemporanea "Renato Guttuso", Villa Cattolica, Bagheria (PA)

AUTeC **A**ssociazione **U**niversitari di **T**opografia **e** **C**artografia

RICERCHE DI GEOMATICA 2011

STUDI PRESENTATI ALLA SETTIMA EDIZIONE DEL PREMIO AUTeC

Questo volume raccoglie gli articoli che hanno partecipato al Premio AUTeC 2011. Il premio è stato istituito nel 2005. Viene conferito ogni anno ad una tesi di Dottorato giudicata particolarmente significativa sui temi di pertinenza del SSD ICAR/06 (Topografia e Cartografia) nei diversi Dottorati attivi in Italia.

Ciascun candidato riassume in un articolo i punti salienti della propria tesi. Gli articoli vengono sottoposti al giudizio di una Commissione giudicatrice costituita dai membri della Giunta AUTeC vigente nell'anno in cui si conferisce il premio. Nell'anno 2011 la Commissione è risultata composta dai professori Gabriele Bitelli dell'Università di Bologna, Alberto Cina del Politecnico di Torino, Donatella Dominici dell'Università dell'Aquila, Anna Spalla dell'Università di Pavia e Aurelio Stoppini dell'Università di Perugia.

Il premio AUTeC 2011 è stato attribuito ex-aequo al Dott. Fabrizio Girardi, afferente al Dottorato di Ricerca in "Ingegneria Geomatica e Trasporti" presso l'Università di Bologna, per la tesi dal titolo "Survey and 3d modeling for small sized objects" e alla Dott.ssa Francesca Pieralice, afferente al Dottorato di Ricerca in "Infrastrutture e Trasporti" presso l'Università di Roma "La Sapienza", per la tesi dal titolo "A radargrammetric orientation model for digital surface models generation from Synthetic Aperture Radar high resolution imagery: applications with COSMO-SkyMed and TerraSAR-X".

Il premio e la pubblicazione degli articoli in un volume vogliono essere un riconoscimento degli Universitari del SSD ICAR/06 per il lavoro di questi giovani ricercatori e una motivazione per continuare le loro ricerche.

Prof.Benedetto Villa
Coordinatore AUTeC 2008-2011

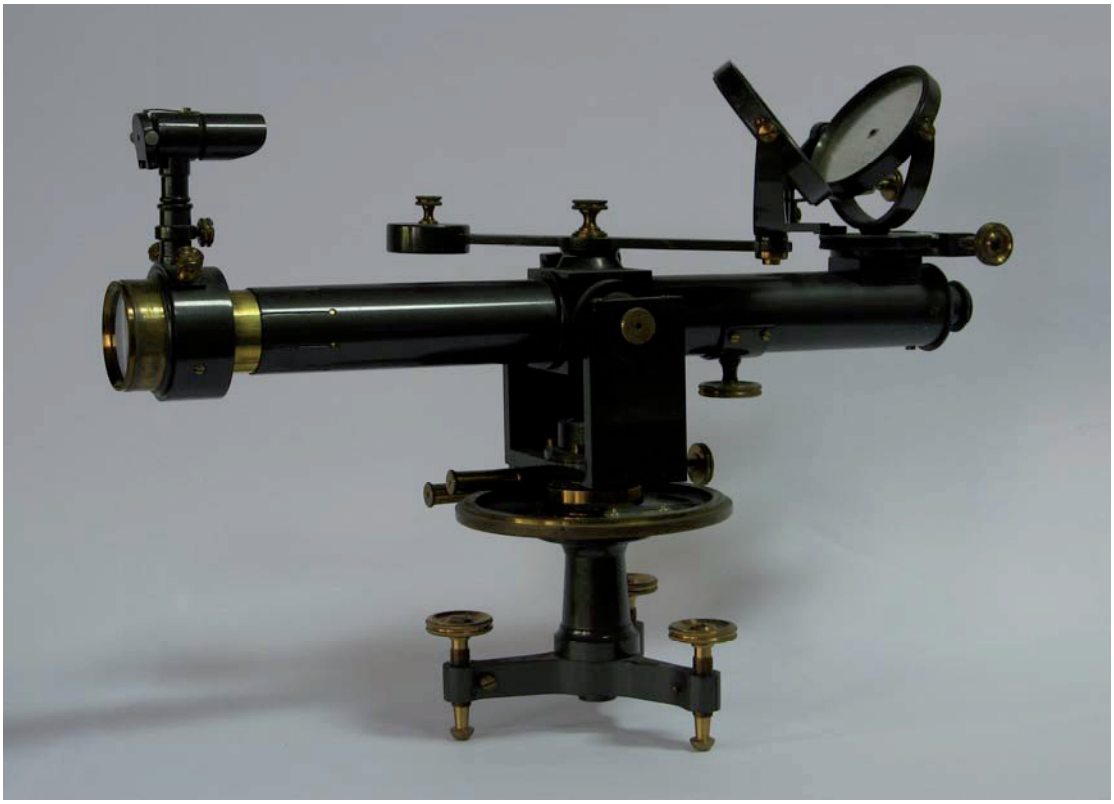

Elioscopio con cannocchiale

LA FILOTECNICA, Ing. A. Salmoiraghi & C., Milano

Collezione DICA (Dipartimento di Ingegneria Civile, Ambientale e Aeronautica), Università di Palermo

AUTeC Associazione Universitari di Topografia e Cartografia

Indice

GNSS/INS INTEGRATION METHODS

A. Angrisano

University of Naples Parthenope, Italy, antonio.angrisano@uniparthenope.it

KEY WORDS: GNSS, INS, Kalman Filter, Loosely Coupled, Tightly Coupled, aiding, GPS, GLONASS

ABSTRACT:

In critical locations as urban or mountainous areas satellite navigation is difficult, above all due to the signal blocking problem; for this reason satellite systems are often integrated with inertial sensors, owing to their complementary features. A common configuration includes a GPS receiver and an high-precision inertial sensor, able to provide navigation information during GPS gaps but with the drawback of the cost, the size and the weight. Nowadays the low cost inertial sensors with small size and weight and poor accuracy are developing and their use as part of integrated navigation system in difficult environments is under investigation. On the other hand the recent enhancement of GLONASS satellite system suggests the combined use with GPS in order to increase the satellite availability; this can be especially useful in places with lack of GPS signals. This study purpose is to assess the effectiveness of the integration of GPS/GLONASS with low cost inertial sensors in vehicular urban navigation. Different integration architectures (loosely and tightly coupled) are compared with different combinations of GNSS (GPS only or GPS/GLONASS). Generally the tight coupling is more used in urban or natural canyons because it can provide an integrated navigation solution also during partial GNSS outages; including GLONASS satellites in this context may change significantly the role of loosely coupling in urban navigation. Aiding techniques such as pseudo-observations derived from considerations about the motion of the vehicle can improve the integrated system performance during GNSS outages and are assessed in case of combined GPS/GLONASS use. In this work pseudorange and Doppler measurements are processed in single point mode; hence no differential processing is performed and no base station is necessary.

1. INTRODUCTION

Urban environments are critical locations for satellite navigation systems such as Global Navigation Satellite Systems (GNSS). In this scenario buildings block many of the signals, thus reducing satellite availability and weakening observation geometry, with the extreme case being solution unavailability. Buildings can also reflect the signals causing multipath phenomenon which introduces the greatest measurement errors in these areas. For these reasons, standalone GNSS is not adequate to guarantee a continuous and accurate navigation in urban areas. A possible approach is the integration of GNSS with other sensors such as Inertial Navigation Systems (INS).

INS are complementary with GNSS in many aspects; INS are more accurate in the short term, they can supply data with very high rate and they can also provide attitude information (Petovello 2003). On the other hand GNSS is more accurate in the long term and the error is effective time invariant (Lachapelle 1997). Consequently, the integration of GNSS/INS is very common for applications in which the GPS alone is not sufficient. In difficult environment like urban canyons, a common configuration includes a GPS receiver and an high-end INS, able to provide navigation solution during GPS gaps; the use of high-end INS is generally confined to only high accuracy navigation and geo-referencing applications, owing to their price and size (Godha 2006).

The recent advances in Micro Electro-Mechanical Systems (MEMS) technology has made possible the development of a generation of low cost inertial sensors, characterized by small size and light weight which represent an attractive option for commercial applications as pedestrian and vehicular navigation. MEMS-based INS are characterized by low performance too, so their use as part of an integrated navigation system is currently under investigation. In the last few years, several researchers have investigated the integration of GNSS systems with MEMS-based INS, characterized by low cost and low performance, for instance Nayak (2000), Shin (2005), Mezentsev (2005), Abdel-Hamid (2005), Godha (2006). These studies have focused specifically on the integration with GPS, working in differential mode; this involves the deployment of a base station not far from the area where the navigation takes place and, in case of real-time application, a data-link connecting the base and the rover must be included too.

This research investigates the performance of an integrated system GNSS/INS(MEMS), with GNSS working in single point mode. However, the use of further satellites beyond the GPS constellation can permit a performance improvement. The Russian navigation satellite system GLONASS is currently the ideal candidate to support this thesis because it is nearly fully operational and its inclusion guarantees an enhancement in satellite availability. Previous work with integrating GPS and GLONASS has shown improvements with GNSS alone (Cai and Gao 2009). However, very little work has been done to look at the integration of GPS, GLONASS and INS. With this in mind, the main contribution of this work is an assessment of such systems (an initial assessment is provided in Angrisano et al. 2010). Although GLONASS is the focus of this work, the results can be extended to the integration with the European satellite system Galileo, once it is deployed.

Different integration strategies can be used to merge satellite and inertial information for navigation purposes (El-Sheimy 2004; Godha 2006). Two common architectures considered in this work are loosely coupled (LC) and tightly coupled (TC)

strategies. In the loosely coupled strategy position and/or velocity from the GNSS receiver are used to aid the INS. Consequently, a dedicated filter is necessary to compute the GNSS navigation parameters from the observables (loosely coupled strategy is also referred to as decentralized). It is evident that an integrated solution is not available in case of partial GNSS outage and so the LC architecture is not normally adopted in urban areas. In contrast to the LC case, the tightly coupled (or centralized) strategy is based on the use of only one filter to process both INS and GNSS data. As is well known, it can be also be used when the number of visible satellites is insufficient to perform a GNSS-only fix and therefore it is often adopted in environments with bad visibility like mountainous or city areas (Godha 2006). However, including GLONASS satellites in this context may change significantly the role of loosely coupling in urban navigation.
Given the above, this work aims to assess the performance improvements obtained using additional GLONASS satellites (in addition to GPS satellites) with both loosely and tightly coupled architectures. Furthermore, the results obtained with the different integrations are compared and contrasted.
Motion constraints derived from considerations about the vehicle behavior can be used to bound the INS errors during GNSS outage (as shown in Sukkarieh 2000; Shin 2001; Godha 2006; Klein et al. 2010; Angrisano 2010). The effectiveness of these particular aiding techniques is assessed in case of the GPS/GLONASS/INS(MEMS) integrated system.

2. SYSTEMS OVERVIEW

2.1 GPS/GLONASS

GPS and GLONASS are the main GNSS systems in use today and they are similar in many aspects, but with some essential differences. Both systems are able to provide various number of air, marine, and any other type of users with all-weather three-dimensional positioning, velocity and timing, anywhere in the world or near-Earth space. Both navigation systems are based on the concept of "one-way ranging", in which the unknown user position is obtained measuring the time of flight of signals broadcasted by satellites at known positions and epochs (Parkinson and Spilker 1996).
The main difference between the two systems is that GPS and GLONASS operate with different time references and with different coordinates frames (Misra et al. 1998, Gaglione et al. 2011). Specifically, GPS time is related with UTC(USNO), Coordinated Universal Time (UTC) as maintained at the United States Naval Observatory. In contrast, GLONASS time is related to UTC(SU), UTC as maintained by Russia. The offset between the two time references can be calibrated, but this information is not included in the navigation messages broadcasted by the satellites. This causes an increase in the unknowns number from 4 to 5: three coordinates of user position and the biases of the receiver clock relative to the two system time scales (one bias can be replaced by the inter-systems time offset). The problem will be overcome with the new generation of GLONASS satellites (i.e., GLONASS-M), that are planned to broadcast the offset between the time scales. In addition, the GPS and GLONASS datum difference does not require an additional state to account, because WGS84 and PZ90 are known and fixed, and they are linked by a well-defined mathematical transformation (further details are in Mitrikas et al. 1998). Other differences are related to the signal nature, namely different signal bandwidths and multiple access schemes, or to the constellation features.
The differences between GPS and GLONASS classified in terms of constellation, signal and reference differences are summarized in Table 1.

		GPS	GLONASS
Constellation	Number of Satellites	24+surplus	24
	Orbital Planes	6	3
	Orbit Altitude	20200 Km	19100 Km
	Orbit Inclination	55°	64.8°
	Ground Track Period	1 Sidereal Day	8 Sidereal Days
	Layout	Asymmetric	Symmetric
Signal	Carrier Frequency	1575.42 MHz 1227.60 MHz	1602+K*0.5625 MHz 1246+K*0.4375 MHz
	Ranging Code Frequency	C/A: 1.023 MHz P: 10.23 MHz	C/A: 0.511 MHz P: 5.11 MHz
	Multiple Access Scheme	CDMA	FDMA
	Broadcast Ephemeris	Keplerian	ECEF
Reference	Reference System	WGS84	PZ90.02
	Reference Time	GPS Time	GLONASS Time

Table 1. Comparison between GPS and GLONASS (adapted from Cai 2009)

2.2 LOW-COST INERTIAL SENSORS

The great advances in (MEMS) has made possible the development of a generation of low cost inertial sensors. MEMS IMU are characterized by small size, light weight and low cost with respect to high-end inertial sensors. These features make the MEMS sensors an attractive option for applications such as vehicular navigation.
However, MEMS sensors are characterized by poorer performance too, so they cannot be used in autonomous mode for extended periods but they are well suited to integrated navigation systems (usually coupled with GPS systems). MEMS sensor performance are summarized in the Table 2 where also a

navigation and a tactical grade IMU performances are listed to facilitate a direct comparison.

Parameter	IMU Grade		
	Navigation	Tactical	MEMS
Accelerometers			
In Run Bias (mg)	0.025	1	2.5
Turn On Bias (mg)	-	-	30
Scale Factor (PPM)	100	300	10000
VRW (g/√Hz)	-	2.16e-06	370e-06
Gyros			
In Run Bias (°/h)	0.0022	1	<1040
Turn On Bias (°/h)	-	-	5400
Scale Factor (PPM)	5	150	10000
ARW (°/h/√Hz)	6.92	7.5	226.8
Approx. Cost	>$90000	>$20000	<$2000

Table 2. Summary of IMU Characteristics for Different Grades of Sensors (from Petovello 2003 and Godha 2006)

The turn-on bias (or bias offset) is the inertial sensor bias that occurs when the sensor is turned on. It is constant during a single mission, has a deterministic nature and can be determined during a calibration procedure (Godha 2006). The in-run bias (or bias drift) is linked to the error accumulation during the mission, it has random nature and must be modeled as a stochastic process (Godha 2006). The scale factor error is the ratio between the change in the output signal of the sensor and the change in the physical quantity to measure. In ideal conditions the scale factor should be unity (El-Sheimy 2004). This error has a deterministic nature but generally is modeled as a random process. The ARW (angular random walk) parameter describes the average deviation or error that will occur from integrating the noise on gyro output signal (El-Sheimy 2004). Similarly VRW (velocity random walk) parameter definition is based on the same concept for the accelerometers.
The performance and the cost of an IMU strongly depends on the gyro quality (El-Sheimy 2004). From Table 2 we can see that the turn on bias of MEMS gyro is about 5400 deg/h, while it is negligible in the navigation and tactical grade sensors. Also the in run bias can be 1040 deg/h in MEMS sensors, while is about 1 deg/h in a tactical grade gyro. These parameters provide a good assessment of MEMS performance with respect to higher grade sensors.

3. GNSS/INS INTEGRATION: IMPLEMENTATION

GNSS/INS integration is very common, because the systems are complementary in many aspects. INS is more accurate in the short term, it can supply data with very high rate and it can also provide attitude information. On the other hand GNSS is more accurate in the long term and the error is effective time invariant. The following sections describe the two most common integration approaches.

3.1 Loosely Coupled Approach

The LC strategy is also referred to as "decentralized" and includes a KF (Kalman Filter) to combine INS and GNSS parameters. Another KF or a LS estimator is used to compute the GNSS navigation solution. The LC scheme is showed in Figure 1.

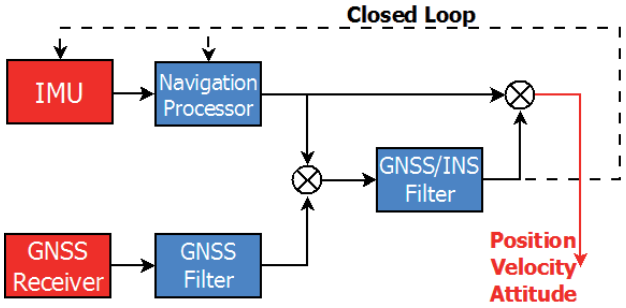

Figure 1. Loosely Coupled Scheme

In this work, the GNSS measurements are processed in single point mode, so no differential corrections are applied and the deployment of a reference station is unnecessary. Only pseudorange (PR) and Doppler observables are used. Doppler measurement is linked to the PR derivative by the formula (1):

$$PR_{dot} = D_1 * \lambda \qquad [1]$$

with λ being the carrier wavelength (meters), D1 being the Doppler measurement (Hertz) and PRdot being the pseudorange rate (meters/seconds).

To compute the GNSS fix, a LS estimator is preferred herein to simplify a direct LC/TC comparison. To account for the fact that satellite measurements at low elevation angles are generally noisier (Parkinson and Spilker 1996), the measurements are weighted by a sin(el) factor, with "el" being the satellite elevation angle (as proposed in Petovello 2003 and Angrisano 2010). To consider also the different accuracy related to the PR and Doppler observables, the weight (reciprocal of variance) associated to the generic measurement is expressed by:

$$w_{ii} = \sin(el) / \sigma_m^2 \qquad [2]$$

where σ_m^2 is the pseudorange variance σ_{PR}^2 or the pseudorange derivative variance σ_{PRdot}^2 .

The GNSS solution is obtained using the WLS (weighted LS) method, whose equation is:

$$\underline{\Delta x} = \left(H^T W H\right)^{-1} H^T W \underline{\Delta \rho} \qquad [3]$$

with $\underline{\Delta \rho}$ being the vector of measurements compensated by a priori information, H being the geometry matrix, $\underline{\Delta x}$ being the unknown vector of corrections from a priori to updated state, and W being the diagonal weighting matrix whose elements w_{ii} are from formula (2).

The inertial solution is obtain applying the mechanization equations for a strapdown configuration to the accelerations and angular rates from the IMU. For this work, the INS mechanization is implemented in the local East-North-Up (ENU) frame.
The difference between INS and GNSS solutions are used as input measurements to the KF. The WLS covariance matrix is used as measurements covariance matrix R (formula (4)):

$$R = \mathrm{cov}(\underline{\Delta x}) = \left(H^T W H\right)^{-1} \quad [4]$$

The state vector of the combined GNSS/INS KF in LC architecture is:

$$\underline{\delta x} = \left[\underline{\delta P^n} \quad \underline{\delta v^n} \quad \underline{\varepsilon^n} \quad \underline{\delta b_a} \quad \underline{\delta b_g} \quad \underline{\delta S_a} \quad \underline{\delta S_g}\right]^T \quad [5]$$

with $\underline{\delta P^n}$ position error vector, $\underline{\delta v^n}$ velocity error vector, $\underline{\varepsilon^n}$ attitude error vector, $\underline{\delta b_a}$ accelerometer bias error vector, $\underline{\delta b_g}$ gyro bias error vector, $\underline{\delta S_a}$ accelerometer scale factor vector and $\underline{\delta S_g}$ gyro scale factor. The bias error vectors $\underline{\delta b_a}$, $\underline{\delta b_g}$ are modeled as 1st order Gauss-Markov processes and include both "in-run" and "turn-on" biases; the scale factor vectors $\underline{\delta S_a}$, $\underline{\delta S_g}$ are modeled as 1st order Gauss-Markov processes too (Angrisano 2010).

3.2 Tightly Coupled Approach

The TC strategy is also referred to as "centralized", because there is only a central KF processing GNSS observations and INS data. The TC scheme is showed in Figure 2.

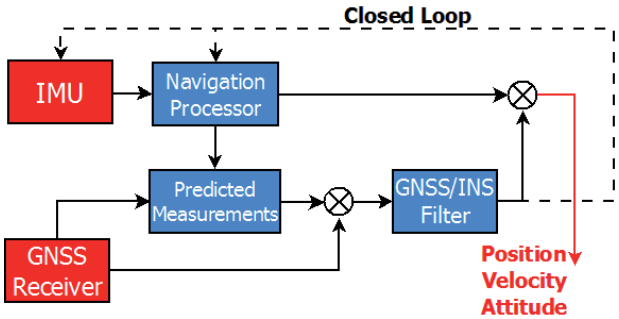

Figure 2. Tightly Coupled Scheme

The difference between PR and Doppler observables and predicted range and Doppler (computed using INS position and velocity) is used as input measurements to KF. The associated measurements covariance matrix is defined taking into account the inherent accuracies of GNSS measurements and the elevation-dependent accuracy as in the LC case.
The TC KF state vector has the same 21 states as LC (formula (5)), augmented with GPS receiver clock bias and drift. If GLONASS system is included, a further state (the GPS-GLONASS inter-systems time offset) must be considered and in this work it is modelled as a random constant stochastic process.
Both loose and tight strategies are herein implemented in closed loop configuration meaning the navigation and bias error states output from the KF are used to correct INS inputs. The closed loop configuration is necessary when low performance INS is used to reduce the inertial error growth (El-Sheimy 2004; Godha 2006), which in turn, satisfies the small angle assumptions used to derive the INS error equations.

4. AIDING METHODS

4.1 External Heading Aiding

An external aiding can be used to improve the heading estimation, adopting GNSS measurements as external source. To incorporate external heading measurements into the measurement model of the GNSS/INS filter, an equation relating the heading errors with the system error states is required (Godha 2006). Such an error equation is derived starting from the expression of the azimuth as function of the elements of the rotation matrix (from body to East-North-Up frame):

$$\psi = \arctan\left(\frac{R_b^n(1,2)}{R_b^n(2,2)}\right) \quad [6]$$

Deriving equation (6), the heading error equation is obtained as:

$$\delta\psi = \frac{\partial\psi}{\partial\varepsilon_E}\delta\varepsilon_E + \frac{\partial\psi}{\partial\varepsilon_N}\delta\varepsilon_N + \frac{\partial\psi}{\partial\varepsilon_U}\delta\varepsilon_U \quad [7]$$

with $\varepsilon_E, \varepsilon_N, \varepsilon_U$ components of vector $\underline{\varepsilon^n}$ and

$$\frac{\partial\psi}{\partial\varepsilon_E} \approx -\frac{R_b^n(1,2)R_b^n(3,2)}{\left[R_b^n(2,2)\right]^2 + \left[R_b^n(1,2)\right]^2},$$

$$\frac{\partial\psi}{\partial\varepsilon_N} \approx -\frac{R_b^n(2,2)R_b^n(3,2)}{\left[R_b^n(2,2)\right]^2 + \left[R_b^n(1,2)\right]^2}, \quad \frac{\partial\psi}{\partial\varepsilon_U} = 1$$

In the equation (7) the measurement is:

$$\delta\psi = \left[\psi_{INS} - \psi_{GNSS}\right] = \left[\psi_{INS} - \arctan\left(\frac{V_E}{V_N}\right)\right] \quad [8]$$

with ψ_{INS} azimuth estimated in the GNSS/INS filter, ψ_{GNSS} is the GNSS-derived azimuth depending on East and North velocity components and whose accuracy is expressed as

$$\sigma_\psi^2 = \frac{\sigma_{V_{HGNSS}}^2}{V_{H_{GNSS}}^2} \quad [9]$$

where $V_{H_{GPS}}$ is the horizontal speed (estimated by GNSS) and $\sigma^2_{V_{HGNSS}}$ is the associated variance.

The external heading equation can be embedded in the measurement model of the GNSS/INS KF and is used when the horizontal speed of the vehicle is high (empirically the threshold is fixed at 5 m/s).

4.2 Pseudo-measurements of Velocity and Height

In vehicular navigation a possible approach to avoid the INS error accumulation is to derive observations from the motion of the vehicle, i.e. it is possible to generate constraint equations or pseudo-measurements reflecting the behavior of the vehicle during navigation (Shin 2001; Sukkarieh 2000, Klein et al. 2010).
A set of pseudo-observations can be derived considering that during typical vehicular navigation the vehicle does not slip sideways or jump/bounce and so the motion is essentially in the forward direction. The above assumptions are described mathematically by equations:

$$\begin{aligned} v_x^b &= \eta_x \\ v_z^b &= \eta_z \end{aligned} \qquad [10]$$

where v_x^b and v_z^b are the velocity components in lateral and upward directions respectively and η_x and η_z are the (fictitious) measurement noises denoting the possible discrepancies in the above stated assumptions.

The pseudo-measurements (10) can be used during GNSS outages to aid the INS navigation by the equation

$$\underline{\delta V}^b = R_n^b \underline{\delta V}^n + R_n^b \underline{V}^n \times \underline{\varepsilon}^n \qquad [11]$$

expressing how a velocity aiding in the body frame $\underline{\delta V}^b$ can improve velocity and attitude estimation.

A second constraint equation can be generated considering the fact that the height does not change significantly in land navigation during short time periods. Hence during GNSS outages the height can be considered constant and equal to a reference value, computed just before the outage in good visibility condition (Angrisano 2010).

Both pseudo-measurements of velocity and height can be used as measurement model of a complementary Kalman filter during GNSS outages as shown in figure 3.

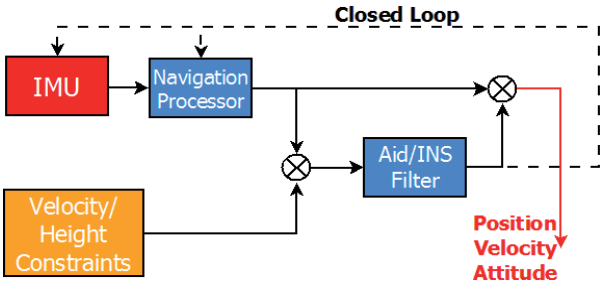

Figure 3. Velocity/Height Constraints Aiding Scheme

5. TEST: DESCRIPTION AND EQUIPMENT

The data collection was carried out in a vehicle in downtown Calgary, Canada on 22nd July 2010 in the afternoon (about 2:00 pm local time). Downtown Calgary is a typical urban scenario, characterized by skyscrapers and so it is a difficult environment for satellite navigation because of blocking and multipath problems.
The test equipment consists of a satellite receiver and a MEMS IMU to perform the experiment and more accurate devices as reference. Specifically, the NovAtel Receiver ProPak V3 ─ able to receive GPS and GLONASS satellite signals ─ and a Crista IMU from Cloud Cap Technology are used to test the different configurations.
The reference solution is obtained using the NovAtel SPAN (Synchronized Position Attitude Navigation), an integrated system consisting of the OEM4 NovAtel receiver and the HG1700 tactical grade IMU. The SPAN data are processed by NovAtel's Inertial Explorer software using phase and Doppler measurements in double difference mode. The baseline separation (relative to a base station located on the University of Calgary campus) varied between 6-7 km. The reference solution used the tight strategy. The reference solution accuracy in these conditions is summarized in Table 3.

Reference Accuracy	
Position	dm level
Velocity	cm/s level
Attitude	<1deg

Table 3. Reference Solution Accuracy

All the equipment was placed on the roof of the car as showed in Figure 4.

Figure 4. Equipment

The test started in a parking lot where the satellite visibility was good and the operational conditions can be considered semi-open sky (4-10 visible GPS satellites). The second part of the test was held in a demanding urban canyon with poor satellite coverage (0-6 available GPS satellites).
The visibility during the path in GPS-only and GPS/GLONASS cases are shown in Figure 5. In GPS-only case frequent partial and total outages are evident, particularly in the second part of the long straight stretch and around the second and third turn (located near the centre of downtown Calgary); the longest GPS outage duration is about 60 seconds between the just mentioned turns (highlighted by a dotted circle in the upper part of Figure 5). In GPS/GLONASS case the above-mentioned outage is interrupted by a combined GPS/GLONASS fix as shown in down part of Figure 5.

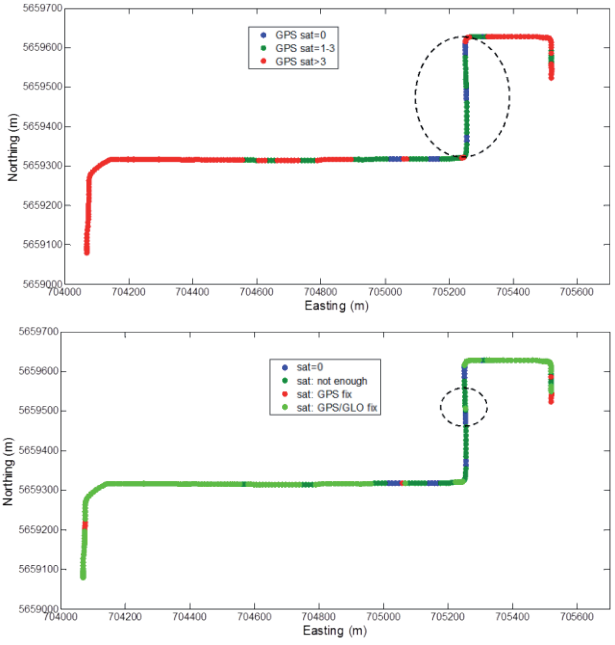

Figure 5. GNSS Visibility on the Trajectory

The main features of the GNSS coverage during the path are summarized in Table 4, in terms of solution availability and maximum outage duration, showing the benefits of including GLONASS observations in this scenario.

GPS Availability	GPS Max Outage	GG Availability	GG Max Outage
73%	60 sec	81%	30 sec

Table 4. GNSS Availability and Outage Duration

6. RESULTS AND ANALYSIS

As mentioned before, the purpose of this work is to compare the performance of GPS and GPS/GLONASS integrated with low cost INS with particular focus on assessing the benefits of including GLONASS. Both loose and tight integration strategies are tested to determine if the type of integration plays a significant role. The pseudo-measurements based on assumptions about the typical vehicular behaviour are included in both integration architectures to assess the effectiveness in this context.
To this purpose, several processing configurations are considered: the baseline configuration GPS/INS in both loose and tight integration (respectively indicated as LC GPS/INS LC and TC GPS/INS), the augmented configuration GPS/GLONASS/INS in loose and tight mode (respectively indicated as LC GG/INS and TC GG/INS) and the aided configuration including GPS/GLONASS/INS and the above-mentioned aiding techniques (respectively indicated as LC GG/INS YVH and TC GG/INS YVH).
In figure 6 the trajectories obtained with the LC approach are shown. The green line represents the horizontal solution of the baseline configuration with only GPS aiding INS navigation and shows large errors during the above-mentioned longest GPS outage. The cyan line represents the trajectory obtained with the configuration including GPS and GLONASS measurements integrated with INS and shows evident improvements relative to baseline case. In fact the isolated GPS/GLONASS fix (circled in right part of Figure 5) interrupts the largest GPS outage and allows the trajectory to stay relatively near the reference between the second and the third turns, whereas without GLONASS large errors occur.
The LC GG/INS configuration provides better performance also during the second part of the long straight stretch (between easting values of 705000 and 705200), where LC GPS/INS error tends to grow owing to short GPS only outages (15-20 seconds duration). The purple line represents the trajectory obtained with GPS/GLONASS/INS augmented with the yaw aiding and the motion constraints and shows remarkable improvements relative to the other configuration with only small disagreements with the reference trajectory.

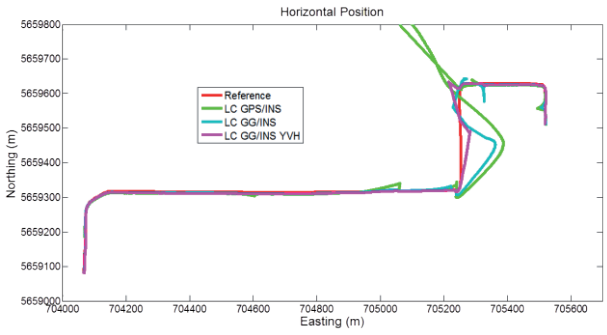

Figure 6. Trajectories obtained with LC Approach

In figure 7 the trajectories obtained with the TC approach are shown. The trajectory obtained with the baseline TC configuration (TC GPS/INS) is represented by the green line and shows better performance than the corresponding LC configuration (LC GPS/INS), without large drift in the trajectory during the long GPS outage. Including GLONASS observations yields slight enhancements in the solution (cyan line in Figure 7) relative to baseline case. The purple line represents the trajectory obtained integrating GPS/GLONASS and INS measurements in TC, augmented with the yaw aiding and the velocity/height pseudo-observations and shows remarkable improvements relative to the other TC configuration especially during the above-defined critical zone.

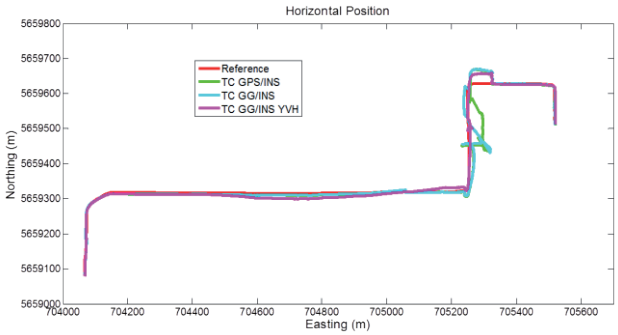

Figure 7. Trajectories obtained with TC Approach

To better perform a comparison among the analyzed configurations with LC and TC architectures, the RMS errors of position, velocity and attitude are represented with a bar chart in figure 8. The main remarks deduced from the errors overview in figure 8 are:

- in the baseline GPS/INS integration, TC architecture provides significantly better horizontal solution and similar altitude result than LC;
- including GLONASS observations in the integrated system GPS/INS provides meaningful performance improvements for both LC and TC architectures and in terms of position, velocity and azimuth estimation;
- in case of GG/INS integration, TC architecture provides only slightly better solution relative to LC;
- the configurations LC GG/INS and TC GPS/INS provide very similar performance;
- including GNSS-derided azimuth aiding and velocity/height constraints produces significant improvements of LC and TC performance in terms of position, velocity and azimuth;
- the results obtained with the configurations LC GG/INS YVH and TC GG/INS YVH are very similar.

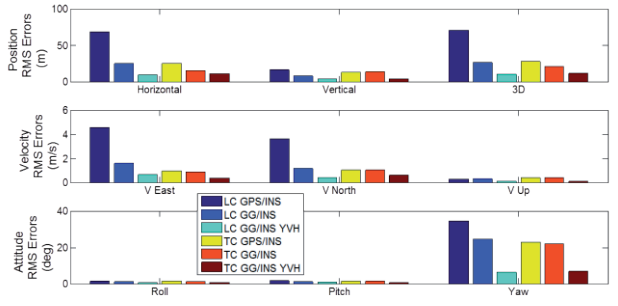

Figure 8. Comparison between LC and TC Architectures in terms of Position, Velocity and Attitude RMS Errors

CONCLUSIONS

This work looks at the integration between GNSS systems and MEMS-INS sensors to improve the navigation performance especially in difficult scenarios as urban canyons.
In this scenario the baseline GPS/INS integration in LC architecture provides unsatisfying results, showing large errors during the long GPS outages, while (as expected) in TC approach the errors are significantly smaller. Including GLONASS observations provides meaningful performance improvements for both LC and TC architectures in terms of position, velocity and azimuth estimation. The GPS/GLONASS/INS integration in LC architecture and the GPS/INS integration in TC approach provide very similar performance (in terms of RMS errors); this might change significantly the role of loosely coupling which could be preferred to tight approach in urban navigation owing to its relative implementation simplicity. Including the GNSS-derived azimuth aiding and the velocity/height pseudo-observations produces significant improvements of LC and TC performance in terms of position, velocity and azimuth and the results with the two cases are very similar.

FUTURE WORKS

The future steps of this research represent a logical extensions to the present work. The PPP technique uses precise satellite orbit and clock products to improve the accuracy of the un-differenced GNSS positioning; similarly the performance of the integrated system GNSS/INS(MEMS) can potentially be improved by using the PPP technique. The extended Kalman filter performance strongly relies on the knowledge of the system models and noise properties; the use of an adaptive Kalman filter may improve the filtering performance and can be investigated in urban scenario. Finally further satellite navigation systems, such as the rising European GNSS Galileo or the Japanese QZSS, can potentially improve the integrated performance and can be considered in the next development of this research.

REFERENCES

Abdel-Hamid, W. (2005), Accuracy Enhancement of Integrated MEMS-IMU/GPS Systems for Land Vehicular Navigation Applications. PhD Thesis. Department of Geomatics Engineering, University of Calgary, Calgary, Canada

Angrisano A., Petovello M., Pugliano G. (2010), GNSS/INS Integration in Vehicular Urban Navigation. In: Proceeding of ION GNSS 2010, Portland, Oregon, USA

Angrisano A. (2010), GNSS/INS Integration Methods. PhD Thesis. Department of Applied Sciences, Parthenope University of Naples, Italy

Cai, C. (2009), Precise Point Positioning Using Dual-Frequency GPS and GLONASS Measurements. MSc Thesis, Department of Geomatics Engineering, University of Calgary, Canada, UCGE Report No. 20291

Cai, C. S. and Gao Y. (2009), A Combined GPS/GLONASS Navigation Algorithm for use with Limited Satellite Visibility. J. Navig. 62(4): 671-685

El-Sheimy, N. (2004), Inertial Techniques and INS/DGPS Integration. ENGO 623 Course Notes. Department of Geomatics Engineering, University of Calgary, Canada

Gaglione, S. et al. (2011), A Stochastic Sigma Model for GLONASS Satellite Pseudorange. Applied Geomatics Volume 3, Number 1, 49-57, DOI: 10.1007/s12518-011-0046-0

Godha, S. (2006), Performance Evaluation of a Low Cost DGPS MEMS-based IMU Integrated with DGPS for Land Vehicle Navigation application. M.Sc. Thesis. Department of Geomatics Engineering, University of Calgary, Canada

Klein, I., Filin, S., Toledo, T. (2010), Pseudo-measurements as aiding to INS during GPS outages. Navigation 57(1), pp. 25-34, 2010

Lachapelle, G. (1997), GPS Theory and Applications. ENGO 625 Lecture Notes. Department of Geomatics Engineering, University of Calgary

Mezentsev, O. (2005), Sensor Aiding of HSGPS Pedestrian Navigation. PhD Thesis. Department of Geomatics Engineering, University of Calgary, Canada

Misra, P., Pratt, M. and Burke, B. (1998), Augmentation of GPS/LAAS with GLONASS: Performance Assessment. In: Proceeding of ION GPS-98, page 495

Mitrikas, V. V., Revnivykh, S. G. and Bykhanov, E. V. (1998), WGS84/PZ90 transformation parameters determination based on laser and ephemeris long-term GLONASS orbital data processing. In: Proceedings of ION GPS-98, Nashville, Tennessee, September 15-18, 1998

Nayak, R. A. (2000), Reliable and Continuous Urban Navigation Using Multiple GPS Antennas and a Low Cost IMU. MSc Thesis. Department of Geomatics Engineering, University of Calgary, Canada

Parkinson, B. W. and Spilker, J. J. Jr (1996), Global Positioning System: Theory and Applications. AIAA, Washington, DC

Petovello, M. (2003), Real-time Integration of a Tactical-Grade IMU and GPS for High-Accuracy Positioning and Navigation. PhD Thesis. Department of Geomatics Engineering, University of Calgary, Canada

Shin, E. (2001), Accuracy Improvement of Low Cost INS/GPS for Land Application. MSc Thesis. Department of Geomatics Engineering, University of Calgary, Canada

Shin, E. (2005), Estimation Techniques for Low-Cost Inertial Navigation. PhD Thesis. Department of Geomatics Engineering, University of Calgary, Canada

Sukkarieh, S. (2000), Low Cost, High Integrity, Aided Inertial Navigation Systems for Autonomous Land Vehicles. PhD Thesis. Australian Centre for Field Robotics, Dept. of Mechanical and Mechatronic Engineering, University of Sydney, Sydney, Australia

SISTEMI INFORMATIVI PER L'ARCHITETTURA. APPLICAZIONI SUL MODELLO DELLE "CARCERI DELL'INQUISIZIONE" A PALERMO

G. Anzalone

Università degli Studi di Palermo, Dipartimento di Rappresentazione, viale delle Scienze, Edificio 8 – Palermo, architettoanzalone@gmail.com

KEY WORDS: Sistemi informativi per l'architettura, modelli digitali, ADBC, javascript, WSN

ABSTRACT:

The final result of an architectural complex survey of cultural interest with modern techniques of Geomatics is now almost always a photorealistic 3D model multiscale and multi-resolution. To switch from the model to an information system of architectural value, it is necessary to integrate informations with some other metrical and qualitative (historical, typological and constructive, illustrations), and those concerning the state of degradation and conservation, the destination etc.. that characterize the documentation of cultural heritage. Those informations must be organized in a RDBMS. At the same time, interactive access and navigation of virtual model must be possible.
The goal of the work proposed is precisely to plan an architectural information system for easy access and manage being shared on the web. The application was carried out on the 3D model of the Carceri dell'Inquisizione in Palermo in a convention made at the Department of Representation. The model has been implemented in a multimedia platform managed with Adobe Acrobat, whose database is managed by Acrobat JavaScript language.

1. INTRODUZIONE

Il lavoro di ricerca della seguente tesi si inserisce in un'ottica di fruizione e valorizzazione del patrimonio architettonico e si propone di individuare, attraverso un "progetto pilota", un percorso applicabile non solamente al caso studio presentato ma che rappresenti un *modus operandi* per qualsiasi bene culturale. La divulgazione del patrimonio culturale, pensata nella forma di modelli digitali con annotazioni incluse (metadati) e ulteriori informazioni sul web, resta ancora una sfida importante. Partendo da questo presupposto verranno analizzati gli aspetti che connotano il processo di conoscenza, rappresentazione e fruizione, per consentire a tutti, anche ai diversamente abili, di travalicare i limiti fisici di un bene culturale.

La fase di conoscenza nel progetto di fruizione e valorizzazione del patrimonio architettonico è caratterizzata da tutte quelle operazioni finalizzate ad un'indagine multidisciplinare del bene in oggetto. Tale fase prevede un'analisi approfondita del bene in esame e si pone come obiettivo la sua conoscenza complessiva sotto diversi punti di vista: storico, fisico, geometrico etc. In questa sede si è deciso di concentrare l'attenzione su alcuni degli aspetti del progetto di conoscenza a partire da un caso applicativo. Nella scelta dell'oggetto si è tenuto conto di alcuni elementi, primo fra tutti, il carattere di bene culturale. Si è ritenuto interessante, inoltre, soffermarsi sulla documentazione di un edificio che presentasse una stratificazione di fasi costruttive e d'uso, e che fosse ricco di informazioni. Infine, era necessario avere accessibilità ad una rilevante mole di dati sulla base della quale costruire il progetto. Date le premesse, si è considerato adatto agli scopi il Tribunale del Sant'Uffizio presso il complesso dello Steri a Palermo. In questa sede ci si è posti come obiettivo la creazione di uno strumento che consentisse di gestire dati a carattere multimediale, soffermandosi principalmente su quelli di natura spaziale. Tra le sperimentazioni affrontate si è cercato di stabilire quali strumenti operativi risultassero migliori per la gestione di tali dati, con l'obiettivo ultimo di proporre un sistema di gestione che non fosse fine a se stesso, ma che garantisse la possibilità di considerare il monumento nella sua completezza, considerando aspetti differenti e diversi tipi di dati. Per raggiungere tali obiettivi sono state effettuate dapprima le opportune indagini storiche alle quali hanno fatto seguito le operazioni di rilievo metrico e fotogrammetrico del manufatto, finalizzate alla rappresentazione tridimensionale fotorealistica; per quanto attiene alle prese fotografiche queste sono state realizzate dal Centro Regionale del Catalogo di Palermo con cui è in atto una convenzione*. Il modello così realizzato è stato inserito in una "piattaforma multimediale" gestita in *Adobe Acrobat*, nella quale è stato possibile costituire un sistema informativo spaziale, e ciò grazie anche alla gestione di database relazionali con linguaggio *JavaScript* (fig. 1).

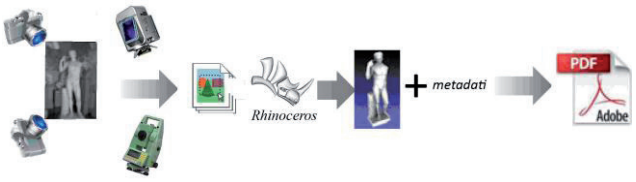

Figura 1. Schema dell'elaborazione dei dati

Oltre alle informazioni "tradizionali" che hanno arricchito il database del sistema informativo, è apparso interessante studiare la possibilità di integrare informazioni di tipo posizionale, relative ad un'unità mobile che possa muoversi all'interno e/o all'esterno del manufatto (*indoor-outdoor dinamic traking)*. Di quest'ultima applicazione sono stati condotti studi relativi alle reti wireless (*WSN)* che consentono il rilievo posizionale di sensori mobili; le tipologie di sensori sono diverse in relazione

* Convenzione tra il Centro Regionale per il Catalogo e la Documentazione dei BB. CC., la Biblioteca Centrale della Regione Siciliana, l'Università degli Studi di Palermo, il Dipartimento di Rappresentazione e il Dipartimento di Studi su Politica, Diritto e Società per la realizzazione di un progetto di documentazione digitale dei dipinti, disegni e graffiti dei prigionieri dell'Inquisizione all'interno del complesso monumentale dello Steri di Palermo.

alle applicazioni. Nello studio seguente è stata progettata una rete WSN con sensori *zigbee* operanti a 2,4 GHz e comunicanti con un server. Tale rete può fornire la posizione di sensori mobili con un'approssimazione di circa 1.5 m.
Questo approccio lascia aperte possibilità di sviluppo futuro in altri ambiti, permettendo agli esperti dei diversi settori di svolgere approfondimenti multidisciplinari ed al contempo agli utenti finali una fruizione più completa e ricca di informazioni.

2. DAL RILIEVO AL MODELLO DIGITALE

2.1 Il rilievo topografico

Il rilievo topografico delle "Carceri dell'Inquisizione" è stato realizzato a partire da una articolata rete di inquadramento, progettata in modo tale che comprendesse buona parte del complesso dello Steri nell'ipotesi di integrare, in fasi successive, il rilievo degli altri edifici che lo compongono.
La rete di inquadramento, costituita da due maglie principali e da alcuni rami di poligonale aperta, è stata progettata in modo tale da ridurre quanto più possibile il numero dei vertici che la compongono e al contempo, considerando la possibilità di osservare da questi un buon numero di punti "strategici" per rappresentare, discretizzate, le caratteristiche geometriche e morfologiche della fabbrica.
I vertici della rete sono stati materializzati negli spazi esterni con appositi chiodi topografici e negli spazi interni con target adesivi; di tutti i vertici sono state eseguite apposite monografie per poterli individuare in caso di smarrimento.
Lo schema seguente mostra la distribuzione dei vertici della prima maglia della rete di inquadramento:

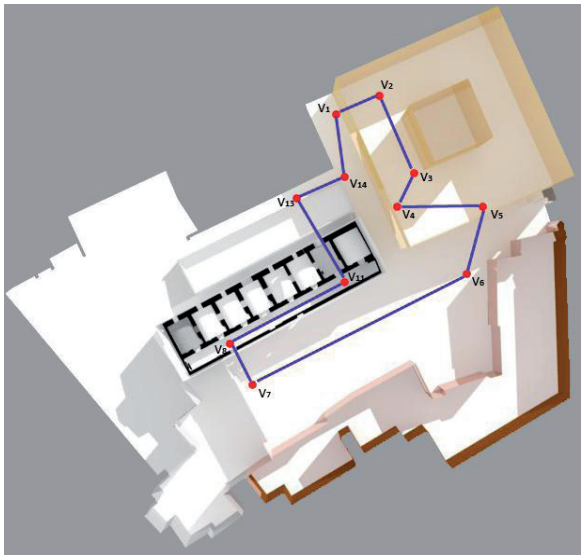

Figura 2. Schema planimetrico del primo anello della rete

Come si evince dallo schema, la rete, costituita da 11 vertici, attraversa lo Steri, esce sul piazzale e rientra, attraversando le "Carceri dei Penitenziati" alla quota del piano terra.
Le operazioni di rilievo topografico sono state condotte con l'ausilio di una *total station Leica TPS 1105* con precisione sulle misure angolari di 5" e in grado di misurare distanze con *E.D.M.* ad infrarosso fino 3000 m con prisma circolare (accuratezza pari a ± (2 mm + 2 ppm)) e fino a 170 m senza prisma, con metodologia ad impulsi laser (accuratezza pari a ± (3 mm + 2 ppm)).

Su ciascuno dei vertici materializzati è stata posta la stazione totale e sono state eseguite misure di angoli, distanze e dislivelli fra le varie coppie di vertici consecutivi.
Sono state calcolate le coordinate dei vertici imponendo un sistema di riferimento locale con l'asse delle ascisse parallelo il lato V_{04}-V_{05}, quindi con un angolo di direzione (V_{04}-V_{05}) pari a 100^g e attribuendo al vertice V_{04} coordinate X = 100,00; Y = 100,00; Z = 100,00.
Sono stati eseguiti i calcoli relativi alla chiusura angolare, lineare ed altimetrica, appurato che tali errori rientrassero nelle rispettive tolleranze, si è proceduto alla compensazione della rete con un programma di calcolo rigoroso realizzato all'interno del Dipartimento.
Di seguito (fig. 3) lo schema delle ellissi d'errore dopo la compensazione della rete e la tabella con gli elementi caratteristici.

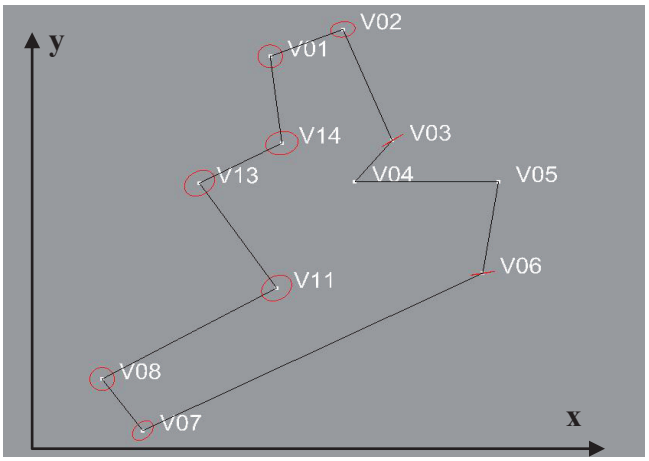

Figura 3. Schema delle ellissi d'errore

Elementi caratteristici dell'ellissi

nome	*incl.asse maggiore (gradi centes.)*	*semiasse max (metri)*	*semiasse min (metri)*
1	56.6691	0.003	0.003
2	87.4716	0.003	0.002
3	55.4034	0.003	0.000
6	89.7739	0.003	0.000
7	60.4307	0.003	0.002
8	84.3154	0.003	0.003
11	60.0472	0.004	0.003
13	65.3960	0.004	0.003
14	72.1399	0.004	0.003

La rete, inoltre, si articola in un secondo anello, comprendente anche alcuni vertici del primo, che consente di rilevare il secondo livello delle "Carceri dei Penitenziati" nonché parte dei prospetti (fig. 4).

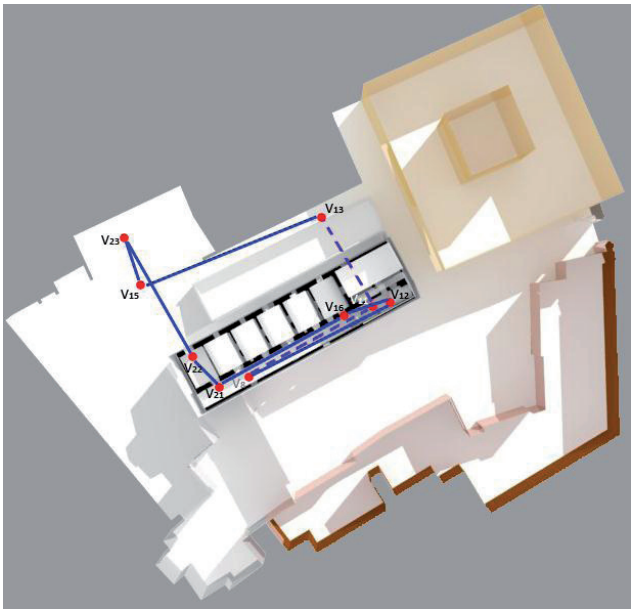

Figura 4. Schema planimetrico del secondo anello della rete

Calcolate e compensate le due maglie della rete topografica, sono state ottenute le coordinate plano-altimetriche dei vertici che le compongono e dai quali è stato possibile, in una seconda fase, eseguire il rilievo celerimetrico.
Il rilievo di dettaglio, finalizzato all'ottenimento delle coordinate di tutti quei punti "strategici" idonei alla rappresentazione del manufatto, è stato eseguito a partire dai vertici della rete precedentemente materializzata e calcolata, eseguendo misure celerimetriche tramite l'utilizzo della stazione totale con modalità ad impulsi laser.
Data la morfologia del manufatto, per il rilievo di dettaglio degli interni è stato necessario ricorrere a dei vertici supplementari, materializzati questa volta come rami di poligonale aperta; laddove si è reso necessario un vertice all'interno di uno specifico ambiente, come all'interno delle celle, per il rilievo dei punti di dettaglio, dai vertici della poligonale chiusa sono stati rilevati idonei vertici costituenti rami di poligonale aperta. Da questi vertici, si è proceduto quindi al rilievo di tutti quei punti caratterizzanti la morfologia di ogni ambiente (fig. 5) nonché al rilievo dei punti di appoggio a supporto delle successive prese fotogrammetriche per un totale di circa 800 punti.

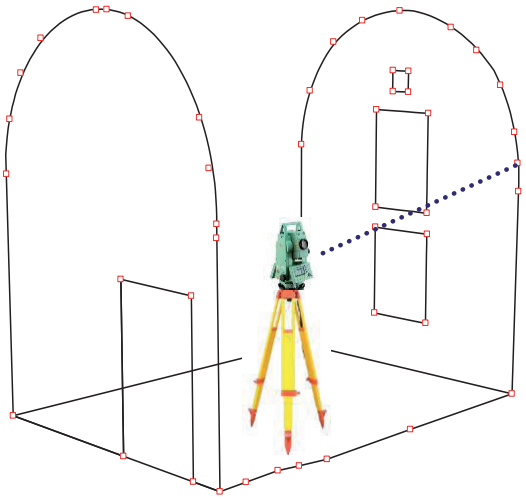

Figura 5. Rilievo di punti di dettaglio

2.2 Il rilievo fotogrammetrico

Il percorso di rilevamento, finalizzato alla modellazione tridimensionale foto realistica, è proseguito nella fase del rilievo fotogrammetrico.
Le applicazioni fotogrammetriche si sono limitate al fronte sul piazzale interno e a due celle del piano terreno, in quanto costituiscono solo un approccio metodologico alla realizzazione di un modello tridimensionale texturizzato finalizzato ad un sistema informativo.
La metodologia di rilevamento utilizzata è basata sulla realizzazione di fotopiani digitali dei fronti, visto l'andamento generalmente piano degli stessi, da realizzarsi mediante la tecnica di restituzione fotogrammetrica omografica.
Per eseguire il "raddrizzamento" di una determinata immagine è necessaria, come è noto, la conoscenza degli otto parametri che definiscono la relazione omografica fra il piano dell'immagine fotografica originaria e quello dell'immagine raddrizzata. La loro determinazione richiede la conoscenza delle due coordinate X ed Y di almeno quattro punti dell'oggetto in questione, opportunamente dislocati sull'immagine da raddrizzare, espresse nel sistema di riferimento oggetto ed individuabili nel sistema di riferimento immagine.
Le prese sono state realizzate, per quanto concerne il fronte sul piazzale, con una camera amatoriale *Lumix DMC-TZ4* con sensore CCD da 8 MegaPixel, massima risoluzione di acquisizione foto di 3264 x 2448 px e zoom ottico 10x dotata di obiettivo ultragrandangolare Leica DC da 28-280 mm. La fotocamera è stata precedentemente calibrata tramite algoritmi di self-calibration, eseguendo uno schema di prese convergenti su apposito reticolo di calibrazione fornito con il software Photomodeler. Inoltre, le prese del fronte principale, sono state eseguite mantenendo le condizioni di presa analoghe a quelle adottate per le fasi di calibrazione.
Contestualmente sono stati rilevati i punti d'appoggio idonei per una corretta restituzione omografica. I fotopiani digitali, elaborati tramite il software *PhotoMetric* della *GeoPro*, realizzati per singole immagini, sono stati ricavati applicando alle caratteristiche della macchina fotografica i parametri di calibrazione precedentemente calcolati e sono stati successivamente mosaicati fino a formare il fotopiano continuo dell'intero fronte, restituito in proiezione ortogonale secondo il piano principale di sviluppo del prospetto sul piazzale delle "Carceri dei Penitenziati" (fig. 6).

Figura 6. Fotopiano del fronte nord-ovest delle Carceri

Il fotopiano, generalmente idoneo a restituire la geometria bidimensionale dei fronti, in queste operazioni è stato elaborato, data la semplice morfologia del prospetto, per la successiva fase di mappatura del modello tridimensionale.
In questo senso il fotopiano rappresenta un supporto qualificante il modello tridimensionale, la sua rappresentazione, la produzione di tavole dei degradi e dei dissesti e dunque le analisi e la valutazione degli eventuali interventi di restauro.
Per quanto attiene invece le prese relative alla stanza n. 1 posta al piano terra delle "Carceri", queste sono state realizzate dagli operatori del Centro del Catalogo di Palermo con una fotocamera digitale Nikon D300 con obiettivo 28 mm decentrabile ed illuminazione con luce continua per un totale di circa 3000 watt.

2.3 Il modello 3D fotorealistico

Le fasi di rilievo topografico e fotogrammetrico, volte ad una più approfondita conoscenza del bene, hanno consentito l'elaborazione di rappresentazioni tridimensionali fotorealistiche; infatti, a partire dai punti di dettaglio rilevati topograficamente, sono stati disegnati in ambiente CAD, tramite il software Rhinoceros, gli spigoli e tutte le altre entità bidimensionali utili a costruire un modello *wireframe* delle "Carceri dei Penitenziati".
Il passo successivo è stato quello di modellare, a partire dallo schema a fil di ferro, tutte le superfici costituenti la "pelle" della fabbrica (pareti, solai, volte, etc.). Questa tecnica di modellazione è stata applicata, raccordando, con superfici *primitive*, *sweep* o *derivate*, dove necessario, le entità bidimensionali che costituiscono ogni singola superficie ottenendo così un modello tridimensionale per superfici.
Al modello per superfici sono state applicate successivamente le texture per renderlo fotorealistico. Infatti, i fotopiani precedentemente realizzati sono stati utilizzati per le mappature piane sulle superfici di appartenenza. Con questa tecnica, eseguita attraverso il software *Rhinoceros*, è stato ottenuto un modello tridimensionale fotorealistico (fig. 7) facilmente gestibile con qualsiasi programma CAD e inoltre esportabile in formati quali VRML o X3D per la visualizzazione e navigazione interattiva con appositi *viewer*.

Figura 7. Modello tridimensionale fotorealistico

3 INTEGRAZIONE DEL MODELLO TRIDIMENSIONALE IN UNA PIATTAFORMA MULTIMEDIALE

La realizzazione di un modello tridimensionale foto-realistico come descritto nei capitoli precedenti, consente diverse applicazioni che vanno dalla "semplice" catalogazione digitale, all'analisi finalizzata ad interventi conservativi, alla fruizione multimediale integrata ai sistemi informativi spaziali.
Il concetto fondamentale è quello di poter raccogliere, all'interno dello stesso strumento multimediale, sia il modello tridimensionale foto realistico navigabile che attributi (storici, geometrici, topologici, iconografici) relativi al manufatto e gestibili tramite un sistema informativo spaziale.
Quest'ultima applicazione risulta di notevole interesse sia per l'esplorazione tridimensionale interattiva sia per la possibilità di interrogare il modello ed ottenere informazioni supplementari sul manufatto in esame.
Tuttavia, è importante sottolineare che l'artefatto digitale non è in alcun modo sostituibile all'opera reale. L'idea è quella di affiancare ai beni culturali un modello digitale complementare che valorizzi quello reale.
Per far ciò occorre sapere:

- Quale formato 3D scegliere;
- come collegare una risorsa web ad un artefatto digitale;
- come possono essere create tutte le informazioni utili a corredo dei modelli digitali;
- come possono essere archiviate tali informazioni;
- come è possibile integrare informazioni di tipo posizionale;
- come può essere distribuito sul Web un modello di questo tipo.

Una piattaforma multimediale strutturata in questo modo offre inoltre la possibilità di creare cataloghi museali digitali interattivi incorporando metadati 3D che possono essere visualizzati dai visitatori tramite dispositivi portatili tipo *iPad* con un'interfaccia utente molto intuitiva ideale per visite guidate anche personalizzate. Infatti, oltre alle informazioni "tipiche" gestibili da un sistema informativo spaziale, integrato alla piattaforma multimediale interattiva, è possibile associare informazioni di tipo posizionale che consentono al sistema di ricevere le coordinate *x, y, z* del visitatore quindi inviare al dispositivo portatile informazioni mirate alla sua posizione e quindi alle opere d'arte vicine e/o all'ambiente in cui ci si trova.

Per ottenere informazioni relative alla posizione del visitatore, è stata progettata una rete di sensori wireless idonea al posizionamento *indoor*. Inoltre, tramite la possibilità di collegamenti di tale rete a ricevitori *GPS* esterni, è possibile integrare la maglia in un sistema *outdoor* georiferito.

3.1 Il formato 3D

La possibilità di fornire contenuti 3D su un browser web o su dispositivi multimediali portatili appare oggi di grande rilievo. Le soluzioni attualmente disponibili utilizzano plugin (Java, JavaScript o dipendenti dalla piattaforma come ActiveX, ecc) al fine di visualizzare contenuti in 3D all'interno del browser.
Altre soluzioni idonee alla fruizione di modelli 3D prevedono la strutturazione di un sistema complesso in grado di gestire oltre ai modelli tridimensionali anche altre applicazioni ad esso associate.
Gli studi della presente tesi hanno condotto all'utilizzo dei modelli 3D in ambiente *Adobe Acrobat* che consente, tramite l'utilizzo del linguaggio *JavaScript,* la possibilità di gestirli in modo semplice nonché di integrarli con appositi sistemi informativi spaziali. Nel caso di studio è stato implementato il modello tridimensionale delle "Carceri dell'Inquisizione" in un file PDF secondo opportune modalità di inserimento e gestione.
Dalla versione di *Adobe Acrobat 7.0* è possibile, creando un file PDF, inserire modelli 3D provenienti da diversi ambienti di modellazione tridimensionale. Nel caso in esame, dal software di modellazione *Rhinoceros 4.0* è stato esportato un file 3D texturizzato con estensione **.3ds* che è stato poi importato all'interno del file **pdf*
Il software *Adobe Acrobat* gestisce il file tridimensionale importato in un'area definibile all'interno dello spazio modello del formato scelto (A4, A3, etc.). Tale area può essere visualizzata anche come finestra mobile all'interno del file in modo tale che, se il file è composto da più pagine, è possibile decidere di visualizzare tramite la finestra mobile il modello 3D sempre in primo piano.
Il software gestisce inoltre diverse modalità di visualizzazione dei modelli 3D (*wireframe, solid, trasparent, textured, etc.*), diversi punti di vista predefiniti (*alto, laterale, assonometrica, etc.*), nonché viste definibili dall'utente tramite rotazioni del punto di vista o navigazione immersiva, differenti sorgenti luminose, la possibilità di eseguire delle misure sul modello nonché di effettuare sezioni verticali, orizzontali o con piani di sezione definibili dall'utente. (fig. 8).
Al tempo stesso il software consente di gestire un sistema informativo spaziale legato al modello tridimensionale, tramite l'interrogazione di un apposito database, di cui si parlerà nei prossimi capitoli, residente sullo stesso dispositivo portatile dove è presente l'applicazione *PDF* o su di un *pc* remoto.
Tale database, strutturato in *Access,* può contenere informazioni di varia natura ma appare di notevole importanza soffermarsi sulla possibilità di rilevare, gestire ed integrare, dati di tipo posizionale relativi ad un'unità mobile integrata ai dispositivi portatili a servizio dei fruitori.

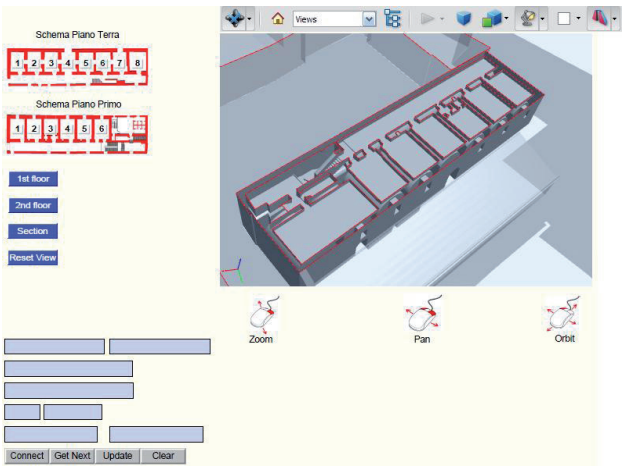

Figura 8. Interfaccia della piattaforma multimediale PDF

4 I SISTEMI INFORMATIVI PER L'ARCHITETTURA

L'elemento che contraddistingue fortemente la lettura "statica" dei modelli tridimensionali foto realistici dai sistemi informativi spaziali è appunto l'integrazione di un database interrogabile ed al contempo la navigazione del modello del nostro manufatto.
Nel caso di un bene culturale, il Sistema Informativo spaziale consente di "arricchirne" il modello digitale con informazioni supplementari utili ad un approccio multidisciplinare.
Occorre ricordare che un sistema informativo è costituito essenzialmente da quattro componenti principali:

1. Le risorse umane e materiali (hardware);
2. il software;
3. i dati;
4. le funzioni.

Ad ogni elemento tridimensionale del modello si possono associare tre tipi di attributi (dati):

a. Geometrici (posizione e forma);
b. semantici (attributi associati all'elemento od alla posizione dell'utente);
c. topologici (contiguità, inclusione, connessione con altri elementi).

Le funzioni dei Sistemi Informativi possono essere raggruppate in tre sottosistemi:

a. Funzioni di interrogazione dei dati;
b. funzioni di gestione dei dati;
c. funzioni di analisi dei dati;
d. funzioni di visualizzazione dei dati.

Il principio fondamentale di un sistema informativo è l'organizzazione di un sistema di informazioni in relazione alle scale di gestione e di intervento dove gli oggetti di interesse sono i beni architettonici, i beni ambientali, il bene territorio: in sostanza i beni culturali e i loro rapporti di continuità e contiguità. L'obbiettivo della ricerca è quello di strutturare e gestire un modello di sistema informativo per l'architettura, di semplice utilizzo e facilmente accessibile e condivisibile attraverso il Web.
In un sistema informativo la gestione delle basi di dati è uno degli aspetti fondamentali; inoltre occorre individuare un sistema o modello di catalogazione dei beni culturali (quando il sistema informativo interessa le mutue connessioni fra questi) e dei principali sistemi di classificazione delle informazioni di dettaglio (in riferimento ai sistemi rivolti ai singoli beni culturali).

Per la rappresentazione dei dati in un sistema informativo occorre formalizzare un modello rappresentativo flessibile che si adatti ai fenomeni reali. Nei Sistemi Informativi Geografici abbiamo tre tipologie di informazioni:

- **Geometriche**: relative alla rappresentazione cartografica degli oggetti rappresentati; quali la forma (punto, linea, poligono), la dimensione e la posizione geografica.
- **Topologiche**: riferite alle relazioni reciproche tra gli oggetti (connessione, adiacenza, inclusione ecc…).
- **Semantiche**: riguardanti i dati (numerici, testuali ecc…) associati ad ogni oggetto.

Il GIS prevede la gestione di queste informazioni in un database relazionale.
L'aspetto che caratterizza il GIS è quello geometrico: esso memorizza la posizione del dato impiegando un sistema di proiezione reale che definisce la posizione geografica dell'oggetto.
Nelle elaborazioni che seguono, ci si è concentrati piuttosto su un modello di sistema informativo legato alla scala architettonica. Questo comporta alcune analogie con i GIS ma anche alcuni aspetti differenti.
Infatti, i dati di riferimento non sono geografici ma architettonici e possono essere georiferiti oppure restare in un sistema locale; la morfologia dei dati è di tipo tridimensionale e le relazioni topologiche saranno certamente differenti da quelle geografiche.
Fatte queste premesse la ricerca si è rivolta verso un sistema che favorisse un utilizzo interattivo del modello con le informazioni associate in un *ambiente* omogeneo e *user friendly*.
L'ambiente Adobe Acrobat si è dimostrato versatile sia per la gestione dei modelli tridimensionali che per la diffusione del relativo software di lettura.
Inoltre il plug-in Acrobat Database Connectivity (ADBC) fornisce alcune proprietà di base JavaScript e metodi per la connessione ai database. Questi, possono essere utilizzati per ottenere informazioni su banche dati disponibili sul sistema. Inoltre, JavaScript può essere utilizzato per eseguire SQL e ricevere dati, che possono, a loro volta, essere utilizzati per arricchire un file PDF. Viceversa, attraverso JavaScript e SQL, i valori dei campi di un modulo PDF possono essere salvati in un database, per aggiornarlo, se necessario.

4.1 L'architettura del sistema informativo spaziale

Gli aspetti fondamentali sui quali ci si è concentrati nell'elaborazione di questa tesi sono stati, con riguardo ai sistemi informativi, quelli legati alla strutturazione dei dati ed al software di gestione delle informazioni.
I dati che costituiscono il sistema informativo sono essenzialmente geometrici (riferiti al modello tridimensionale realizzato) ma anche informazioni legate alle singole stanze, alla presenza o meno di graffiti, immagini delle pareti, etc.
Tuttavia, a seconda del manufatto per il quale occorre creare un sistema informativo, i dati possono essere diversi caso per caso. È possibile creare delle relazioni topologiche, discretizzare la geometria fino alle unità elementari che la compongono, etc.
In questo progetto è apparso opportuno individuare come dati elementari del sistema informativo, le celle che costituiscono il complesso delle "Carceri dei Penitenziati"; pertanto ogni record del data-base sarà costituito da informazioni legate alla cella n-esima, alla sua geometria, alla presenza o meno di graffiti, ad immagini delle pareti.
Oltre alle informazioni "tradizionali" di un Sistema Informativo, in questo studio sono state indagate le possibilità di inserimento, all'interno del data base, delle informazioni di tipo posizionale di un'unità mobile presente all'interno dello spazio di pertinenza del modello. L'ipotesi è quella di avere a disposizione dei dispositivi tipo *iPad* ai quali poter collegare un sensore wireless *zigbee* e, grazie alla presenza di un'ampia rete di sensori (WSN) dislocati all'interno dell'edificio, poter ricavare la posizione del sensore mobile e comunicare tali informazioni al database giacente sul server; grazie agli attributi posizionali, il server potrà inviare al dispositivo mobile informazioni personalizzate relative al luogo in cui ci si trova (es. la stanza di un grande museo). Tali sperimentazioni superano il limite del posizionamento *indoor* che risulterebbe impossibile con l'ausilio di sistemi di posizionamento globale come il GPS con il quale è tuttavia integrabile, consentendo un sistema di posizionamento dinamico *indoor-outdoor*.

L'altro elemento fondamentale per l'architettura del sistema informativo è il software di gestione dei dati.
Gli studi si sono rivolti verso l'ambiente *Adobe Acrobat* sia per la possibilità di implementare il modello tridimensionale fotorealistico, sia per la possibilità di poter dialogare, tramite *javascript*, con un data base *ADBC* associato.

4.2 Il posizionamento indoor

L'aspetto posizionale costituisce un valore aggiunto rispetto ad un Sistema Informativo, soprattutto quando fornisce informazioni sulla posizione "statica", ma anche dinamica (tracker) di un'unità mobile.
La tecnologia elettronica odierna mette a disposizione diverse tipologie di sensori utili a funzionare in rete a scopo posizionale e per il rilevamento dei parametri ambientali.
Una delle esigenze di rilevante importanza nelle applicazioni di posizionamento geospaziale è il poter dare continuità alla posizione di un'unità mobile sia all'esterno che all'interno degli edifici.
Mentre il primo aspetto (posizionamento all'esterno) è in buona parte risolto, esistono ad oggi notevoli difficoltà relativamente al posizionamento interno. Infatti se i ricevitori GPS, per l'esterno, risolvono il problema, pur con difficoltà di posizionamento in quelle situazioni in cui si ha una difficoltosa ricezione del segnale, all'interno tali strumenti si rivelano pressoché inutili a causa dell'elevata incertezza posizionale dovuta a vari fattori fra cui la scarsa ricezione del segnale, effetti di multipath ecc..
Sono però disponibili sistemi diversi che, opportunamente integrati, permettono di definire la posizione di un'unità mobile anche all'interno di edifici, pur con precisioni molto differenti e non sempre elevate. In realtà le soluzioni oggi proposte riguardano situazioni e campi applicativi per i quali non è richiesta una elevata accuratezza posizionale.
Infine si rileva l'esistenza di standard per la trasmissione di dati geospaziali a *server web* e la loro diffusione in tempo reale tramite interfacce web in modo grafico (applicazioni *webgis* supportate da *web services*). Mentre la tecnologia hardware è abbastanza sviluppata ed consolidata, la parte di interazione fra reti di sensori diversi e disponibilità dei dati rilevati secondo metodologie standard in grado di garantire l'operabilità fra sistemi, fa riferimento a recenti indicazioni in possibile fase di evoluzione sulle base di nuovi test e verifica emergenti dall'attività di ricerca.
L'attività di ricerca relativamente a tale ambito si è proposta pertanto di:

- indagare quali sistemi di posizionamento indoor sono disponibili sul mercato e valutarne le capacità di funzionamento e accuratezza posizionale;

- individuare un sistema adeguato alle esigenze di posizionamento relative a possibili applicazioni nel settore dei beni culturali, della protezione civile e ambientale e del supporto alle persone diversamente abili, applicazioni di contact detection;
- configurare un prototipo del sistema hardware;
- studiare i servizi web (*web services*) idonei a gestire la comunicazione dei dati al server e le relative elaborazioni (processing services);
- materializzare, con una data accuratezza, su mappe visualizzate tramite interfaccia 3D, la posizione di unità mobili.

5 LE RETI DI SENSORI WIRELESS

Le reti di sensori wireless costituiscono oggi un notevole contributo al rilevamento di differenti condizioni ambientali e, non ultimo, anche al posizionamento *indoor-outdoor.*

La struttura delle reti wireless è composta da una serie di sensori nodo e sensori controllori.

L'esigenza di utilizzare tecnologie wireless per applicazioni di tracking e posizionamento indoor è dettata dagli inconvenienti di ingombro, peso, maggiore costo offerto dalle soluzioni cablate e inoltre dall'impossibilità di altri sistemi (come il GPS) di rilevare la posizione di una unità mobile all'interno di un edificio.

Tramite la tecnologia *RTLS* (*Real Time Locating System*) basata sui sensori radio, è possibile infatti individuare, in tempo reale, la posizione di un'unità mobile che si muove in ambienti anche ostili alla ricezione del segnale GPS.

Sostanzialmente una rete WSN (Wireless Sensor Network) è costituita da una "stazione base" (gateway) eventualmente connessa ad altre reti e da un certo numero di sensori wireless (nodi).

I nodi sorgente hanno il compito di acquisire e fornire le informazioni rilevate (fenomeni fisici, potenza del segnale di nodi mobili, etc.), mentre i nodi destinazione o coordinatore (*gateway*) hanno il compito di raccogliere le informazioni rilevate dai nodi sorgente per mandarle ad un server; all'interno del server girerà un'applicazione in grado di elaborare questi dati e ricavarne informazioni spaziali (x, y, z) relative ai nodi mobili.

Esistono diverse tipologie di sensori wireless a seconda dell'utilizzo, delle caratteristiche tecniche e soprattutto della frequenza con cui dialogano.

Nell'ambito del posizionamento *indoor* l'industria dell'elettronica offre diverse soluzioni a basso costo operanti sulle frequenze dei 2,4 GHz e con accuratezze di posizionamento pari a ± 1.5 m ed alcune soluzioni, di costo più elevato, operanti nelle frequenze tra i 3 e i 10 GHz che consentono maggiore precisione nel posizionamento (± 30 cm).

5.1 Topologie delle reti wireless

La topologia di una rete è una rappresentazione schematica del modello geometrico (grafico) della rete. Le topologie più comuni per una *WSN* sono le seguenti:

1. **Rete a stella**. In questa topologia di rete c'è un nodo centrale che ha il compito di coordinare gli altri nodi. Il vantaggio principale di questa topologia è la semplicità di progettazione, ma lo svantaggio principale è rappresentato dalla robustezza di tale rete, in quanto esiste un unico punto di *failure*; se il nodo centrale si guasta compromette tutto il sistema.

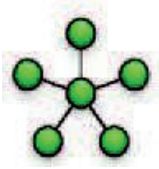

2. **Rete ad albero**. Le reti di questa topologia hanno una struttura gerarchica con più livelli di controllo; un'evoluzione delle reti a stella, in cui non c'è solo un coordinatore centrale ma una gerarchia di coordinatori.

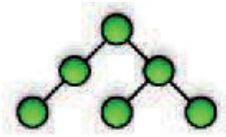

3. **Rete *Peer to Peer***. Le reti *peer to peer* (*P2P*) sono reti in cui non ci sono distinzioni tra i vari nodi. Tutti i nodi possono svolgere le stesse funzioni sia come nodo sorgente sia come nodo destinazione.
4. **Rete *mesh***. Le reti di tipo *mesh* hanno la caratteristica che tutti i nodi sono connessi a tutti gli altri nodi; il vantaggio di una tale struttura è ovviamente la robustezza della rete, (tutti i nodi sono interconnessi) lo svantaggio è rappresentato dal numero dei collegamenti e quindi dal costo dei collegamenti.

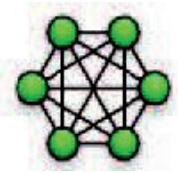

5.2 Architettura delle WSN

La rete *WSN* progettata è sostanzialmente composta da sensori – nodo che ricevono un segnale *RSSI* (received signal strength indicator cioè un valore di intensità del segnale radio ricevuto) dal/i sensore/i mobile/i lo elaborano e lo inviano al gateway; questo invia i pacchetti di dati ricevuti da tutti i sensori al server (fig. 18) sul quale è allocata un'applicazione che elabora questi pacchetti di dati *RSSI* e li trasforma in misure di distanza. Successivamente opera una serie di trilaterazioni e, minimizzando gli scarti, ottiene la posizione del sensore mobile (± 1.5 m). Queste informazioni di posizione verranno inserite in appositi record nel database del server e saranno dunque disponibili alle query eseguite da un'unità remota.

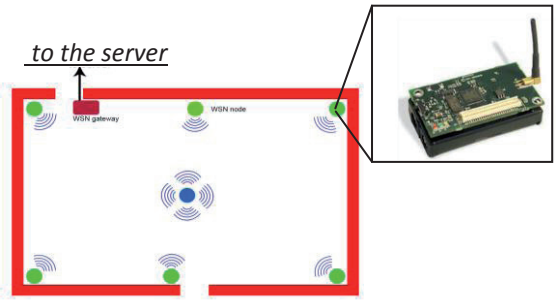

Figura 9. Schema ideale di una rete WSN

6 IMPLEMENTAZIONE DI UN DATABASE PER UN'ARCHITETTURA WSN

La rilevanza della componente spaziale nelle informazioni sui beni culturali, l'accessibilità della tecnologia GIS, l'interesse che si sta sviluppando nel mondo dei beni culturali per la partecipazione alla pianificazione e alla politica di intervento sul territorio e quindi anche sui beni culturali, la richiesta sempre più forte di divulgare i contenuti delle ricerche sono tutti aspetti che stanno spingendo l'interesse verso l'analisi e la divulgazione di informazioni sui beni culturali.
A parte la "semplice" visualizzazione tridimensionale foto realistica di un oggetto statico o dinamico, i modelli possono essere significativamente arricchiti da metadati semantici, in forma di ulteriori informazioni testuali per le parti selezionate, viste predefinite o altri oggetti 3D che possono essere introdotti e manipolati programmaticamente, anche in risposta a una interazione da parte dell'utente.
Inoltre, le informazioni posizionali dell'utente all'interno di un edificio, così come le caratteristiche geometriche di un'opera architettonica, le sue notizie storiche, le immagini e tutte quelle informazioni che possono "arricchire" la conoscenza di un bene culturale, costituiscono gli elementi essenziali per il database interrogabile del sistema informativo spaziale.
Questo archivio è strutturato in modo tale che le informazioni vengano suddivise per argomenti in ordine logico (tabelle), poi tali argomenti vengano suddivisi per categorie (campi), in modo da consentire l'accesso e la gestione dei dati stessi (l'inserimento, la ricerca, la cancellazione ed il loro aggiornamento) da parte di particolari applicazioni software *DBMS* ad essi dedicate.
Nel caso di studio è stato strutturato un database in *Access* con le informazioni ritenute idonee a descrivere il modello ed alla applicazione in esame ma integrabile nel tempo, in relazione alle esigenze che andranno maturando, con ulteriori campi. Il database contiene record relativi al codice identificativo della stanza delle carceri dell'Inquisizione che si vuole "interrogare", alla denominazione della stanza, al piano in cui si trova, alla presenza o meno di graffiti, alle immagini associate, all'identificativo del sensore mobile eventualmente presente, alla posizione X-Y del sensore relativo alla rete in fase di elaborazione ed infine un campo note.
Il linguaggio di programmazione *JavaScript* in ambiente *Adobe Acrobat*, consente di integrare, in un'unica soluzione multimediale, la visualizzazione interattiva del modello tridimensionale texturizzato con le informazioni derivanti dall'interrogazione, attraverso il modello, del database (fig. 10).

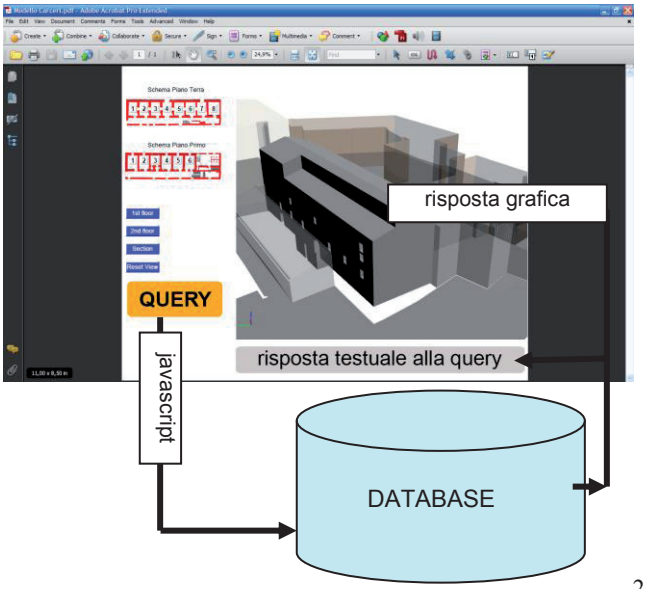

6.1 Interrogazione del database dalla piattaforma pdf3D

Definite tutte le connessioni al database a questo punto la piattaforma multimediale potrà essere fruita dagli utenti attraverso un'unità mobile come un *laptop* o un *PDA* previo caricamento del file PDF. L'interfaccia user friendly di un file *pdf* consentirà al visitatore del museo (nel caso specifico delle "Carceri dell'Inquisizione") di poter visualizzare interattivamente il modello tridimensionale fotorealistico del luogo in cui si trova, di poter eseguire delle sezioni di ogni genere, di prendere delle misure, di interrogare le parti "sensibili" del modello e di leggere gli esiti delle interrogazioni negli appositi campi creati sotto la finestra 3D (fig. 11)

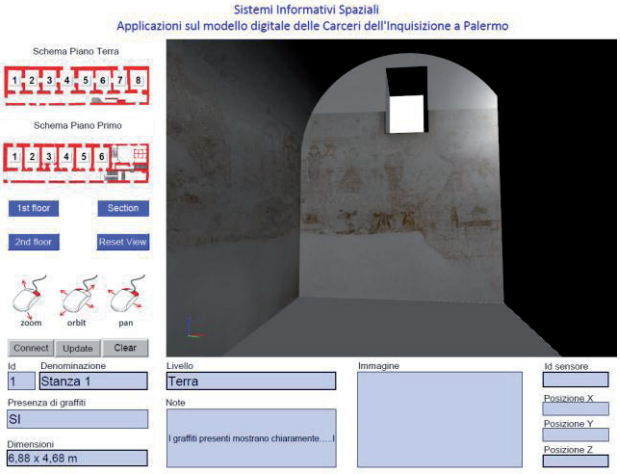

Figura 11. Interfaccia della piattaforma multimediale PDF

Nel caso in esame, si è ritenuto opportuno, per semplicità di comunicazione, rendere "sensibili" i pulsanti posti nello schema planimetrico dei due livelli delle "Carceri"; cliccando ad esempio sul pulsante "1" dello schema del piano terra, i campi di testo sottostanti restituiranno delle informazioni derivanti dall'interrogazione appena eseguita al database.
In particolare il database è stato strutturato inserendo informazioni relative alla denominazione della stanza, al piano in cui si trova, alla presenza di graffiti, ad eventuali immagini associate.

7 CONCLUSIONI E SVILUPPI FUTURI

Gli studi recenti della geomatica mirano ad una integrazione delle informazioni spaziali per poter ottenere dei modelli tridimensionali foto-realistici e metricamente accurati. Tuttavia si ritiene opportuno incrementare con altre informazioni un modello digitale.
A partire dal concetto di sistema informativo, ad oggi ampliamente studiato in ambito cartografico, si è scelto di allargare questi concetti all'ambito architettonico (spaziale). Lo studio presentato vuole infatti indagare le possibilità di integrazione dei modelli tridimensionali con i sistemi informativi.
Nella tesi vengono analizzati i metodi di comunicazione con i database come gli **Open Database Connectivity (ODBC)** che rappresentano delle API standard per la connessione ai DBMS. Queste API sono indipendenti dai linguaggi di programmazione, dai sistemi di database e dal sistema operativo. Tramite questi sistemi di comunicazione e l'implementazione del linguaggio *Javascript* in *Acrobat*

Database Connectivity, è stato possibile integrare in *Adobe Acrobat* la gestione dei modelli tridimensionali e la comunicazione con i database in un file *pdf*, facilmente distribuibile, alla portata di tutti, e idoneo soprattutto in ambito museale. Tuttavia occorre evidenziare alcuni limiti delle connessioni *ADBC* legati al fatto di poter comunicare con database "residenti" sul PC dove viene visualizzato il file pdf oppure su un PC della rete locale. Per superare tali limiti, le ricerche sono attualmente rivolte all'integrazione, in ambiente Acrobat, del linguaggio Simple Object Access Protocol (SOAP), un protocollo basato su XML utilizzato come mezzo di informazione e lo scambio di istruzione tra i servizi web.
Inoltre gli studi rivolti alla localizzazione *indoor* tramite reti WSN implementano questo sistema con la possibilità di ottenere informazioni "mirate" in funzione della posizione in cui ci si trova.
Occorre notare che gli studi sulle WSN sono ad oggi in una fase pressoché iniziale e probabilmente quando la tecnologia di maggiore precisione (UWB) raggiungerà dei costi significativamente più bassi, si potranno ampliare queste reti con risultati significativi nell'ambito della divulgazione delle informazioni spaziali.

8 BIBLIOGRAFIA

- Oreste Signore, «Verso l'interoperabilità semantica» in *Manuale per la qualità dei siti Web culturali pubblici*, Roma, Minerva europe, 2005, 195-204.
- Paolo Atzeni e altri, *Basi di dati. Modelli e linguaggi di interrogazione*, Milano, McGraw-Hill, 2002.
- Franco Vico, «Costruire il GIS: dati versus processi», in Guido Gastaldo, Matteo Panzeri (a cura di), *Sistemi Informativi Geografici e Beni Culturali*, Torino, Celid, 2000.
- ARDISSONE P., RINAUDO F., , *A GIS for the management of historical and archaeological data,* Proceedings of CIPA XX International Symposium, Torino, 2005.
- SPANO', C. FIERRO, Uso di contenuti 3D per la documentazione dei beni architettonici nei SIT, in Atti del II Convegno eArcom, , Alinea Editrice, FIRENZE 2007
- D. COPPO, P. PIUMATTI, Documentare il passato per gestire il futuro: un sistema informativo degli strumenti di gestione e rappresentazione della città, in Atti del II Convegno eArcom, Alinea Editrice, FIRENZE 2007
- P. ARDISSONE, Sistemi Informativi Spaziali per i beni culturali ambientali, Tesi di Dottorato, POLITECNICO DI TORINO, TORINO 2006
- SPANO', R. BONINO, A. MASSA, B. ASTORI, Rappresentazione e organizzazione in Sistemi Informativi dei dati di rilievo architettonico, in Il teatro di Hierapolis di Frigia, VOL I PARTE II, G. CIOTTA A CURA DI, De Ferrari (ITA), pp. 318-367, 2004
- P. ATZENI, Basi di dati. Modelli e linguaggi di interrogazione, McGraw-Hill, MILANO 2002

8.1 Sitografia

- http://www.opengeospatial.org - Ultimo accesso: 20/11/2009
- CISIS, Intesa Stato Regioni Enti Locali - Sistemi Informativi territoriali - Specifiche per la realizzazione dei data base topografici di interesse generale - Specifiche di contenuto: gli strati, i temi, le classi, aprile 2004, http://www.centrointerregionale-gis.it - Ultimo accesso: 30/11/2009
- REGIONE PIEMONTE, Piano di e-governmenti piemontese - Linee guida, TORINO, aprile 2001, http://www.ruparpiemonte.it - Ultimo accesso: 5/11/2009

AUTOMATIC TIE POINT EXTRACTION FROM MARKERLESS IMAGE BLOCKS IN CLOSE-RANGE PHOTOGRAMMETRY

L. Barazzetti

Politecnico di Milano, Piazza Leonardo da Vinci 32, Milan, Italy
luigi.barazzetti@polimi.it, web: http://www.icet-rilevamento.lecco.polimi.it/

KEY WORDS: Automation, Accuracy, Computer Vision, Matching, Orientation, Photogrammetry

ABSTRACT:

The complexity and diversity of image network geometry in close-range applications, with wide baselines, convergent images, illumination changes, occlusions and varying overlap, makes the automatic identification of tie points a very complicated task. This work introduces a new photogrammetric procedure that recovers such information using the original texture of the analyzed scene or object. The method can be properly tuned to deal more effectively with different image sets thanks to the optional choice between techniques and input parameters. This allows a wider range of images, acquired with different sensors under different image networks, to be handled. The whole processing can be considered as a multi-step process in which several parameters are estimated and refined. This methodology combines feature-based and area-based matching algorithms, robust estimation techniques, and methods for tie point decimation and regularization. Once the correspondences between opportune image combinations are extracted the method seeks to link all the data together. To demonstrate the reliability, precision and robustness of the procedure, several tests on different kinds of datasets are illustrated and discussed.

1. INTRODUCTION

Today, the scientific interest in close-range photogrammetry and Computer Vision (CV) is growing rapidly. Generally speaking, these disciplines have similar aims but different motivations. In the field of CV several innovative ideas (often presented with an elegant and concise mathematical approach) were developed to automate the entire procedure and to extract a 3D model from different kinds of images. It could be said that a major goal within CV is to achieve fully automated 3D scene reconstruction from an arbitrary set of overlapping images, without reference to external data such as sensor calibration or prior knowledge of the scene or object. However, there's a long way to go if something more than crude virtual reconstructions of uncertain integrity and reliability are to be produced.

In the discipline of Photogrammetry, the 'holy grail' is somewhat the same as that hinted at above for CV. Indeed, Photogrammetry is used in several applications (topographic mapping, engineering metrology, cultural heritage documentation, …). Its main goal is the creation of accurate and detailed 3D models. Progress has been made towards realising the aim of automated 2D image to 3D object reconstruction, but only in the presence of constraints. A major constraint centres upon the current need for targets or markers (Ganci and Handley, 1998; Cronk et al., 2006) such that the image point correspondence problem can be solved at the initial network orientation stage.

An immediate goal within research into close-range photogrammetry is to be able to dispense with markers such that automated 3D reconstruction envisaged by the CV community can be realised with the metric quality needed in Photogrammetry, which has a focus on engineering measurement/metrology. In this sense, a functional automated commercial solution for the case of markerless images is still to be developed (although the new version of PhotoModeler, released towards the end of October 2010, could become the first one). Some research solutions capable of automatically orienting a set of calibrated images were presented by Roncella et al. (2005), Läbe and Förstner (2006), Remondino and Ressl (2006), and Barazzetti et al. (2010).

Recently the *Computer Vision* (CV) community has proposed several methods for automatic and markerless image orientation or 3D modelling. Some solutions were also implemented and are now available on the Internet (e.g. ARC 3D Webservice, Photosynth, Photofly). However, in the best of cases a low accuracy has been reached, limiting the use of such software to applications requiring only 3D models for pleasant visualization or image browsing purposes. An interesting application of CV methods is the use of unstructured photo collections downloaded from the Internet. In fact, as Internet provides billions of photographs, several CV research workers have tried to reconstruct 3D objects from their projections into 2D images. This is a convenient choice: the data acquisition phase has already been completed by someone else, who has decided to freely distribute his material.

The state of the art for such applications is Clustering Views for Multi-view Stereo Software (CMVS - Furukawa et al., 2010), which combines software for Structure from Motion (Bundler - Snavely et. al, 2008) with software for surface reconstruction coined Patch-Based Multi-view Stereo Software (PMVS2 - Furukawa and Ponce, 2010). The final result obtainable with CMVS is a dense point cloud automatically derived from an impressive number of images downloaded from the Internet. The method was tested on several archaeological sites and then extended for the reconstruction of whole cities. However, this software was developed for visualization purposes and the accuracy and the completeness of the reconstruction are rarely checked. The use of uncalibrated methods, coupled with orientation strategies based on projective geometry, do not always provide a guarantee on metric accuracy.

To understand better the differences and a possible interaction between photogrammetry and CV the reader is referred to Förstner (2002).

There is a question which summarizes this paper: how can we combine accuracy with automation? In this work a possible answer is given, with also a description to the implemented

procedure (coined ATiPE - Automatic Tie Point Extraction), that is the practical solution obtained. The main idea is the development of appropriate computational models and processes that really demonstrate the feasibility of the concept of automated 3D measurement of complex objects from multi-station convergent configurations of imagery, without the need for markers such as coded targets or interactive measurements.

2. THE METHOD FOR TIE POINT MATCHING

2.1 Overview

The automated image matching procedure can be considered as a multi-step process in which several parameters are estimated and refined. The procedure can be properly tuned to deal more effectively with different image sets, thanks to the optional choice between techniques and input parameters. Therefore, the methodology is not limited to pinhole images (figure 1a) but it can deal with spherical image blocks created with the equi-rectangular projection (figure 1b), panoramic intensity images generated with laser data (figure 1c) and particular sequences of multispectral images (figure 1d). Basically, corresponding image points can be matched with the combination of operators for feature detection and robust estimators.

The input elements for the automated tie point extraction and transfer are the images and the calibration parameters of the camera used. A generic block of n images can be considered composed of $(n^2-n)/2$ combinations of stereo-pairs, which are firstly analysed independently for the identification of the correspondences, and then progressively combined. However, if images form an ordered sequence, the number of image combinations to be worked upon becomes n-2, with a significant reduction of computational time. Thus, two procedures for image matching were implemented in the case of *ordered sequences* or *sparse blocks*, respectively.
The innovative aspects of the developed method are:

- effectiveness on a large variety of unorganised image datasets;
- capability of working with high-resolution images;
- accurate image measurements based on Least Squares Matching;
- combination of feature-based (FB) and area-based (AB) matching algorithms;
- procedures for image point reduction and regularization;
- extension to spherical images, laser scans, and multispectral images (for more details, the reader is referred to Barazzetti, 2011).

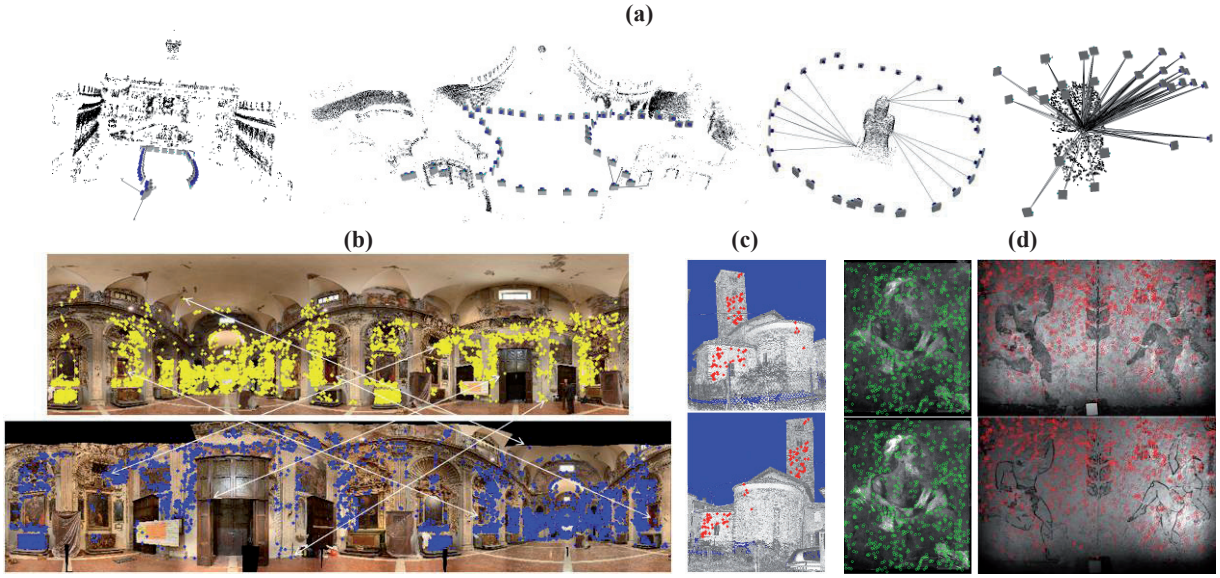

Figure 1. Different kinds of images that the procedure can process: (a) pinhole images, (b) spherical images, (c) laser intensity images, and (d) multispectral images.

As previously mentioned, the implementation of the proposed technique led to a new software for photogrammetric applications coined ATiPE. This was designed for photogrammetric and detailed applications, therefore a real-time processing is not an issue of primary importance, but there is a particular attention to the final accuracy and uniform distribution of the extracted tie points. The implemented FBM strategies, coupled with an initial network geometry analysis (called visibility map), allow a computational time of few hours for image blocks composed of several tenth of high resolution images (>20 Mpix) used at their original size. The robust detection of correspondences with the proposed procedure is achieved by combining the accuracy of traditional photogrammetric methods with the automation of CV approaches.

In the case of pinhole imagery, the input elements of ATiPE are the images, the full set of interior orientation parameters (optional) and a visibility map between the images (optional). All images are normally used with their calibration parameters in order to avoid self-calibration which is generally not appropriate and reliable in practical 3D modelling projects. The visibility map might contain information about the overlap between all images and can be derived (i) from GNSS/INS data with an approximate DTM/DSM or (ii) with a preliminary and quick orientation procedure performed on low resolution images (e.g. 2 Mpix). The visibility map can significantly reduce the running time by limiting the combination of images that must be analyzed and matched.
Although the main goal of ATiPE is the analysis of large and complex datasets, the pairwise registration concept always remains the core method used for global processing. This

formulation of the general problem, combined with a successive combination that includes all the original data, makes the whole processing possible with a high degree of automation.

2.2 Processing of pinhole images

The complexity of image network geometry in terrestrial surveys makes the extraction of corresponding points more complex than in aerial photogrammetry. Automatic aerial triangulation (AAT) has reached a significant level of maturity and reliability demonstrated by the numerous commercial software packages available on the market. On the other hand, in close-range photogrammetry, up until now there doesn't seem to be a software adapted for the automated orientation of markerless sets of images.

For many years, commercial solutions used coded targets for the calibration and orientation phase. Targets are automatically recognized, measured and labelled to solve the identification of the image correspondences. This solution becomes very useful and practical for camera calibration, but in many surveys targets cannot be used or applied to the object and the detection of image correspondence is carried out with interactive measurements performed by an operator. In this sense, the state of the art for image orientation in close-range photogrammetric surveys still needs manual measurements. The aim of this work was a reliable and precise procedure for automated tie point extraction from terrestrial image blocks. The flowchart of the orientation procedure is shown in figure 2.

The core of global processing is always a preliminary subdivision of the original block into image pairs (or triplets). An *ordered sequence* is composed of n consecutive images. As the overlap between consecutives images is guaranteed, the whole sequence is split into n-2 triplets. If I is a generic image, each triplet T_i is made up of the images $\{I_i, I_{i+1}, I_{i+2}\}$. For each triplet T_i the pairs of images $C_i = \{I_i, I_{i+1}\}$ and $C_i'' = \{I_{i+1}, I_{i+2}\}$ can be independently matched in order to determine a set of corresponding features. After the single image triplet matching, the coordinates of points of consecutive triplets are compared in order to determine correspondences in the whole sequence. The triplet T_i and the next one $T_{i+1} = \{I_{i+1}, I_{i+2}, I_{i+3}\}$ share two images and tie points can be transferred with a simple comparison based on the value of the image coordinates. For a closed sequence, it is sufficient to create a triplet $T_{n-1} = \{I_{n-1}, I_n, I_1\}$ to match first and last images. This method has a linear computational cost O(n) with respect to the global number of images.

When the images form a sparse (regular or irregular) image block, it is necessary to check all possible image pair combinations to determine the image correspondences. Therefore each image must be compared with all the others, leading to a computational cost O(n^2).

2.2.1 Tie point extraction from a single image pair

Several interest operators for feature detection and description have been developed over recent years. Generally, the most valuable property for an operator is its *repeatability*, which means the capability of finding the same point or feature under different viewing and illumination conditions. The developed methodology starts extracting features (interest points and regions) with the SIFT (Lowe, 2004) and SURF (Bay et al., 2008) operators. Both have a detector capable of finding interest points in the images and a descriptor to associate a vector of information to each single detected point for further matching purposes.

A descriptor is a vector with a variable number of elements that describes the feature. Corresponding points can be found by simply comparing the descriptors, without any preliminary information about the image network or epipolar geometry. For the SURF operator a vector length of 128 is used, although the regular SURF and U-SURF (rotation invariance is not considered) have a descriptor length of 64.

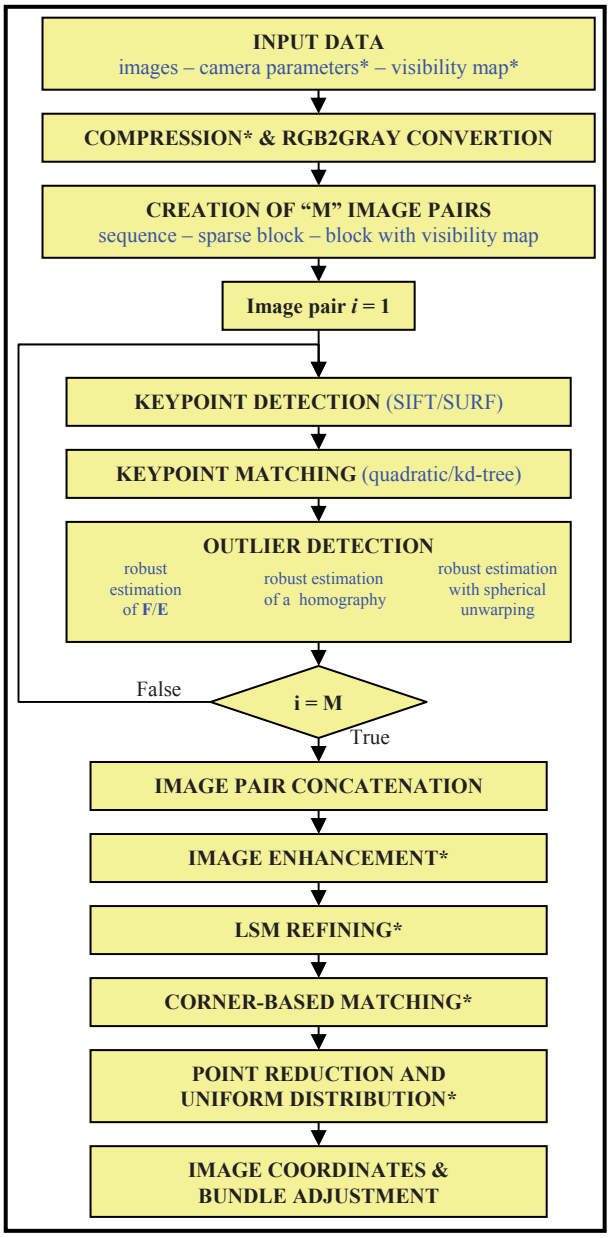

Figure 2. The flowchart of the implemented method. The "*" symbol indicates optional functions or data.

Two strategies for comparing the descriptors are available: a *quadratic matching* procedure (slow but rigorous) and a *kd-tree* procedure (fast but approximate). The user has to select the detector-descriptor operator and the procedure to compare the vectors and to extract the correspondences. This choice depends on the number of images and extracted features, with results that can be really different in terms of time.

Given two images I and J, in which m and n features were detected with descriptors $\mathbf{D}_m$ and $\mathbf{D}_n$, the quadratic matching procedure compares all descriptors of the image I with all those

of the image *J*. Then the Euclidean distance between both descriptors is estimated as a measure of the difference. Moreover, a constraint between the first- and the second-best candidate is added to be more distinctive. The method can be summarised as follows:

- each descriptor $\mathbf{D}_m$ is compared with all the descriptors $\mathbf{D}_n$ by estimating the Euclidean distance $\mathbf{d}_{mn} = \|\mathbf{D}_m - \mathbf{D}_n\|$;
- all distances $\mathbf{d}_{mn}$ are sorted from the shortest $(\mathbf{d}_{mn})^1$ to the longest $(\mathbf{d}_{mn})^n$;
- an image correspondence is accepted if $(\mathbf{d}_{mn})^1 < t \cdot (\mathbf{d}_{mn})^2$.

The value of the threshold *t* generally varies from 0.5 to 0.8. This method ensures a good robustness but is computationally expensive. The second strategy to compare the descriptors is based on a *kd-tree* approach, a widely-used strategy in applications requiring automatic image matching, for example for panorama generation from unoriented images (Brown and Lowe, 2003). The kd-tree can be defined as a binary search tree in which every node is *k*-dimensional point. For two generic images *I* and *J*, the procedure creates a kd-tree with the descriptors ($\mathbf{D}_m$) of the image *J* and the descriptors ($\mathbf{D}_n$) of *I* are compared by using the kd-tree. Then the control based on the Euclidean distance between the first two candidates is applied. Two fast libraries are the approximate nearest neighbour (ANN) library (Arya et al., 1998) and the fast library for approximate nearest neighbours (FLANN) (Muja and Lowe, 2009).
SIFT and SURF usually retrieve a sufficient number of image correspondences, although some mismatches are often still present. To remove these outliers the procedure uses the robust estimation of the *fundamental matrix* **F** (Hartley and Zisserman, 2004), or the *essential matrix* **E** (Longuet-Higgins, 1981). Both 3×3 matrices feature rank 2 and they encapsulate the epipolar geometry of a stereo pair with known (**E** matrix) or unknown (**F** matrix) camera calibration parameters, respectively.
Given a set of image points $\mathbf{x}_i = (x_i, y_i, 1)^\mathbf{T} \leftrightarrow \mathbf{x}_i' = (x_i', y_i', 1)^\mathbf{T}$ between two views (written in homogeneous coordinates), the condition:

$$\mathbf{x'}_i^{\mathbf{T}} \mathbf{F} \mathbf{x}_i = 0 \tag{1}$$

must be satisfied. This condition can be easily demonstrated by considering that the **F** matrix represents a connection between a point in the first image and the epipolar line in the second one $\mathbf{l}_i' = \mathbf{F}\mathbf{x}_i$ (and vice versa $\mathbf{l}_i = \mathbf{F}^\mathbf{T}\mathbf{x}_i'$), in which also lines are expressed by homogeneous vectors. Thus, the dot product between a point in the second image and the epipolar lines of the corresponding point in the first one must be zero because the point lies on the line ($\mathbf{x}_i^\mathbf{T} \mathbf{l}_i = 0$).
A very popular method to estimate **F** is based on 7 image correspondences, which represent the minimum number of observations to solve for the unknown matrix elements. Indeed the **F** matrix has a scale ambiguity that coupled with the singular constraint det(**F**) = 0 reduces the number of independent elements to 7.
Eq. 1 leads to a system of equations of the form

$$\mathbf{z}_i^{\mathbf{T}} \mathbf{f} = 0 \tag{2}$$

where **f** contains the elements of **F** ordered into a vector. If 7 points are selected to form the data matrix $\mathbf{Z} = [\mathbf{z}_1, \ldots, \mathbf{z}_7]^\mathbf{T}$, the null space of $\mathbf{Z}^\mathbf{T}\mathbf{Z}$ is dimension 2, barring degeneracy. Therefore, the solution is a 2D space $\alpha\mathbf{F}_1 + (1\text{-}\alpha)\mathbf{F}_2 = 0$, which coupled with the determinant constraint gives the relationship $\det|\alpha\mathbf{F}_1 + (1\text{-}\alpha)\mathbf{F}_2| = 0$. This last is a cubic polynomial equation in α that can be easily solved.
The solution of **F** (or **E**) needs to be sought with robust techniques as they allow the detection of possible outliers in the observations. All the proposed methods are based on the analysis of several sets of image coordinates randomly extracted from the whole dataset. In this procedure three popular high breakdown point estimators are included: RANSAC, *least median of squares*, and MAPSAC. Robust methods are really necessary when the correspondences are extracted automatically, as a number of outliers can be present in the data, especially in case of wide baselines. The idea of having robustness in the estimation is to have safeguards against deviations from the assumptions. Their efficiency depends on different factors but primarily on the number (percentage) of outliers. Generally there is a lack of repeatability because of their random way of selecting the points (random sampling).
Outliers can be identified and removed with an iterative process where several **F** matrices are estimated. Rousseuw and Leroy (1987) proposed a minimum number of trials m_s to obtain a good subsample with a given probability *P* and a percentage of outliers ε:

$$m_s > \frac{\log(1-P)}{\log(1-(1-\varepsilon)^p)} \tag{3}$$

where *p* is the number of correspondences, that is the parameters to be estimated, 7 in this case. After several tests with different implementations, the MAPSAC (Torr, 2002) method provided better results. It is based on the Bayesian estimation of the **F** matrix and provides new criteria to check the quality of the solution. MAPSAC solves the problem related to the manual selection of the threshold *T* of standard RANSAC approaches. In fact, a high *T* leads to weak solutions. A difference between these two methods is given by the introduction of the "score function". RANSAC finds a minimum of the function $C = \Sigma\, \rho(e_i^2)$, where e_i is the error of each datum and:

$$\rho(e_i^2) = \begin{cases} 0 & e^2 < T^2 \\ const & e^2 \geq T^2 \end{cases} \tag{4}$$

It is possible to demonstrate that without any extra cost a new function $C_2 = \Sigma\, \rho_2(e_i^2)$ can be minimised, where:

$$\rho_2(e_i^2) = \begin{cases} e^2 & e^2 < T^2 \\ T^2 & e^2 \geq T^2 \end{cases} \tag{5}$$

Thus inliers have a score that depends on how well they fit the data, while with standard RANSAC formulation they score constantly. It leads to a significant solution improvement.
In this methodology, the computed epipolar geometry is used as a constraint to check the extracted image correspondences and to remove mismatches (Scaioni, 2000).

2.2.2 Image coordinates refinement and block adjustment

As shown in Remondino (2006), the image coordinates of the homologous points extracted using FBM can be improved with ABM. Therefore to improve the location accuracy of SIFT and SURF image coordinates, a Least Squares Matching (LSM) algorithm (Grün, 1985) is applied. This is also useful to speed up the entire tie point transfer process. Indeed the

computational time is strictly dependent on the image size. Generally, large images have more features and the time necessary to extract the points and to compare their descriptors can rapidly increase. The same analysis can be carried out with compressed images, following a coarse-to-fine approach, in which LSM allows one to include original resolution images. In Barazzetti (2011) some results on the orientation of several image pairs are illustrated, in which SIFT or SURF were directly used with or without an LSM refinement of the extracted image coordinates. It is clearly visible how the LSM step always improves the orientation results. However, the LSM refinement is an optional choice for the user. In fact, LSM can cope with a variation in scale up to 30% and rotation up to 25°, if good approximate values are not available. But some terrestrial projects feature larger scale variations or image rotations, and therefore only SIFT and SURF operators should be employed.

These operations are repeated for all image pair combinations in order to complete the pairwise matching phase. The data are then organized into tracks and the comparison of the numerical values of all image points gives the set of image correspondences for the entire block. This completes the basic processing and allows the user to obtain the exterior orientation parameters with a bundle adjustment. The mathematical model used is a photogrammetric bundle adjustment based on collinearity equations, where the linearized model can be solved via Least Squares, and its solution is rigorous in a functional and stochastic sense. Good initial values are needed for the linearization using a Taylor series expansion. External constraints, such as GNSS/INS data and GCPs, that are usually available in real close-range surveys, can be efficiently incorporated into the general model. The final system is made up of condition equations (those written as functions of both observations and parameters) and constraint equations (those written in terms of the parameters), where all the variables in the adjustment become weighted observations.

As previously mentioned, a photogrammetric bundle approach based on collinearity equations needs approximate values to write a linear system of correction equations. Rather than trying to obtain initial values for all unknown parameters, an incremental approach is used: starting from the relative orientation of an initial image pair, a combination of resections, intersections, and bundles provide these approximations. This procedure may be indented as a progressive stabilization of the image block since the number of 3D rays per point increases.

Finally, after the automatic tie point transfer and the successive bundle adjustment, a question arises about the quality of the results achieved. For this reason the results were compared with those obtainable with interactive manual measurements that are the best available ground truth.

This analysis can be carried out by estimating the covariance matrix of the bundle solution. Several projects were oriented with interactive measurements and with the proposed methodology using a free-network adjustment, then they were scaled with a known distance. All tests demonstrated how the average precision of the object coordinates (from the covariance matrix) is slightly better in case of manual measurement than the precision given by a two-step matching approach performed with FBM followed by LSM.

This is due to the tie point redundancy. In fact, with manual measurements the same point can be identified in more images while a feature operator has less repeatability. Thus the repeatability of a human operator is better than that of either SIFT and SURF. According to Fraser (1996), the theoretical precision depends on the standard deviation of image measurements σ_{im}, the image scale S, an empirical design factor q (0.4-2 according to the number of images and their distribution) and the number of images k:

$$\sigma_{x,y,z} = qS\sigma_{im} / k^{1/2} \quad (6)$$

Therefore, a larger number of images in which the same point is visible improves the precision of the global project. According to this consideration, the FAST interest operator (Rosten and Drummond, 2006) was included in the pipeline. FAST proved to extract a large number of corners under a higher repeatability quicker than SIFT and SURF, and also with a better distribution in the images. Jazayeri and Fraser (2010) proved that FAST is excellent for high accuracy point cloud generation in multi-image networks.

The FAST algorithm operates by considering a circle of sixteen pixels around the corner candidate. A corner is found when n continuous pixels in the circle are all brighter than the intensity of the considered pixel plus a threshold t. In this procedure, the corners are automatically extracted in the images once the user has fixed a threshold t by visually checking at least one image to verify the point distribution. Rays are compared in order to find corresponding points in the object space; the EO parameters computed with FBM are used at this stage. It is also possible to specify the minimum number of images in which a point to be used during the orientation step must appear (a good choice is 4). Then, point locations are improved via LSM by fixing the position of a feature (template) and searching for the remaining points (slaves).

In some cases images might present a bad texture and a limited number of corners can be extracted. In addition, the distribution of points could be inhomogeneous. To overcome this drawback a procedure based on a preliminary image enhancement can be used. Many methods are today available and generally work by considering global parameters: most software for image enhancement have automatic functions capable of modifying the contrast of the image, but the same level is used for the whole image. If a homogenous distribution of all points is needed this can lead to a poor solution. This is the reason why the image enhancement with ATiPE is carried out with a local optimization based on the Wallis filter.

2.2.3 Decimation of image pairs and image points

The use of FBM techniques like SIFT and SURF for the detection of image points allows the processing of complex close-range blocks. A large variety of deformities, for instance scale variations, radiometric changes, convergent angle views, and wide baselines, can be taken into consideration in order to obtain a good set of image points.

Usually, the image points detected in a fully automated way are more than sufficient for an estimation of the EO parameters. However, two opposite situations could occur:

- a great number of image points is the final results of the feature-based matching;
- the image block is composed of tens of images, which must be progressively analyzed.

The former, which seems a good result, has a significant drawback: if too many points are used in the bundle adjustment, it is impossible to obtain a solution due to the high computational cost. This is the usual case of well-textured bodies with images having the typical aerial configuration (e.g. UAV blocks). Here, the camera is translated and rotated around its optical axis during the acquisition of the images. SIFT and SURF are completely invariant to these effects and often

provide too many points, much more than those strictly necessary for a more traditional manual orientation. These problems are also increased by the use of high resolution images, processed without any preliminary geometric image compression.
To overcome this drawback an ad-hoc procedure for tie point decimation was implemented. After the matching of all image pair combinations, points can be reduced according to their multiplicity (i.e. the number of images in which the same point can be matched). A regular grid is projected onto each image, and for each cell only the point with the highest multiplicity is stored. Obviously, the same point must be kept for the other images.
The size of the cell depends on the geometric resolution of the images (e.g., for a 12 Mpix image, a good choice is 200×150 pix).
As SIFT (or SURF) feature points are randomly distributed in the images, the extraction and matching of FAST corners improves their geometric distribution. The combination of this technique with the following decimation not only improves the quality of the result in terms of geometric distribution, but also in terms of CPU time. It is important to apply this method after the concatenation of all image pair combinations. Indeed, this procedure cannot be used during the matching of the single image pairs. The method is also quite simple to implement and does not require long processing time.
In the next section some numerical results will be presented for UAV image blocks, which are a normal case for making this method indispensable. In particular, a reduction of more than 100 times of the global number of tie points was achieved.
The second limit here listed is due to the number of images. For blocks made up of several photos the processing time can significantly increase. In fact, for a block of n images $(n^2-n)/2$ image pair combinations must be analyzed, with a consequent processing time proportional to the global number of combinations.
However, only a limited number of pairs share tie points, therefore the remaining ones should be removed from the series of stereo pairs. The method used to discard these useless couple of images is a *visibility map*, which must be estimated at the beginning of the processing.
The visibility map contains the connections between all image pairs sharing tie points, and can be estimated as follows:

- *visibility from images*: if high-resolution images are employed, a preliminary processing with compressed images (e.g., less than 2 Mpx) is rapidly performed. This provides the image combinations of the whole block. Then, the same matching procedure is repeated with the original images but taking into account the produced map;
- *visibility from GPS/INS data*: these values combined with an approximate DSM of the area allow the estimation of the overlap between the images. This method is faster than the previous one. However, it can only be applied for images with a configuration similar to that of an aerial block. In some cases, the DSM can be approximated with a plane.

A graphical visualization of the visibility map is shown in figure 3. The block is made up of 87 images (4000×3000 pix), providing 3,741 image combinations. After the estimation of the visibility map, only 897 pairs were found. This speeded up global processing of a factor 4. The visibility map can be represented with a connection graph, where images (red dots) are connected with blue lines to indicate the presence of corresponding points.
In this case ATiPE found more than 331,000 image points (visible in at least three images), with a consequent problem (in terms of CPU cost) during the estimation of the bundle adjustment. The reduction and regularization procedure provided a final number of 18,320 2D points and gave the possibility to estimate the exterior parameters, obtaining a final RMS of 1.06 pix.

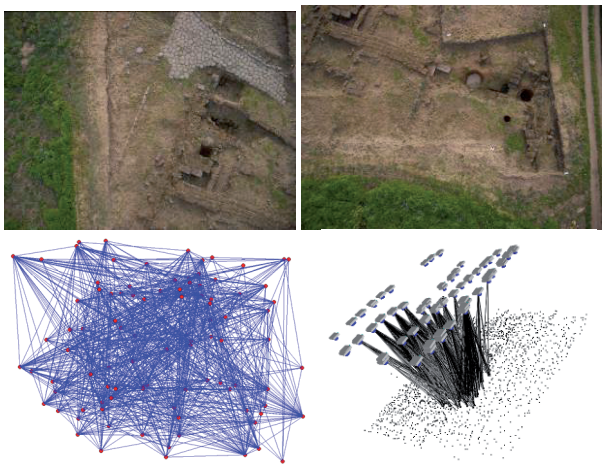

Figure 3. Results for a sparse block: images (top), visibility map and 3D view (bottom).

3. ORIENTATION OF BLOCKS AND SEQUENCES

ATiPE was tested on several blocks and sequences. In particular, some images were taken by rotary wing UAVs, with and without autonomous flight systems. Indeed, in recent years, UAV platforms have demonstrated their great potential for photogrammetric measurements in several applications. UAV photogrammetry opens numerous new scenarios in the close-range domain. It may be intended as a low-cost alternative to classical aerial photogrammetry. In particular, rotary or fixed wing UAVs, which are capable of performing photogrammetric data acquisition with amateur or SLR digital cameras, can fly in manual, semi-automated, and automated flight modes. For the orientation of large image blocks, an interactive tie point extraction approach may require a long processing time, which makes automation necessary.
Shown in figures 4.1 and 4.2 are different case studies and their main characteristics. Block 1 is a photogrammetric block acquired by flying a radio-controlled (RC) helicopter around the roof of the Cathedral of Milan. The complexity of the block structure, composed of several tens of unordered convergent images around architectural structures (without approximations for the EO parameters), represents a difficult test for the capabilities of the developed automated orientation procedure. Block 2 was acquired with a mini UAV-system (Copter from Surveycopter) over the archaeological Mayan area of Copan, Honduras. The block features a structure similar to an aerial survey, but with much larger scales and strong perspective differences among the images. Several problems were found, from the bad texture of the ground to the occlusions created by dense vegetation.
The automated matching phase of each block with ATiPE took some hours (the smaller block has 70 images). In all these experiments, the visibility map was estimated to reduce the

number of image pair combinations. The advantage of this procedure was remarkable: for each block, it led to a significant reduction of the computational time (the time is directly proportional to the number of combinations), obtaining a total reduction of a factor 3.
The matching phase of the image pairs was relatively simple for the second block. The geometry of the network is quite similar to that of standard aerial photogrammetric applications, in which there is only a translation and a rotation around the optical axis of the camera. On the other hand, Block 1 is made up of convergent images with strong perspective deformations. However, the SIFT operator could extract an impressive number of tie points even under these extreme viewing conditions (relative rotations up to 30°).

Block 1 – Milan
Nikon D200
20 mm lens – 80 images
3872×2592 pixels
pixel size 6.1 µm
Manual flight

Block 2 – Copan
Nikon D2Xs
35 mm lens – 70 images
4288×2848 pixels
pixel size 5.5 µm
Autonomous flight

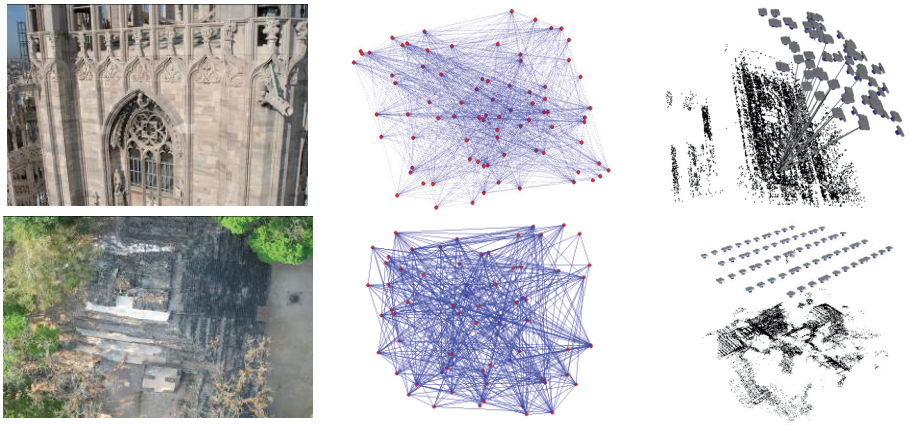

Figure 4. Two UAV blocks oriented with ATiPE: image and flight characteristics, visibility maps and 3D views.

It is also important to say that the global number of matched points for all projects was remarkable (120,765 and 74,477, respectively). This was a limit for the computation of the LS bundle adjustment. Furthermore, the distribution of the extracted correspondences was not optimal, with some areas presenting too many points while in other parts, data are completely missing. Therefore, a reduction and regularization of the extracted tie points becomes necessary to operate with standard PCs and achieve better adjustment results. As described in the previous section, ATiPE uses a reduction based on rectangular cells to remove several useless points, keeping those with a better multiplicity. The computed RMS values of the bundle adjustment show that this method does not degrade the precision of the final solution, but, from a computational point of view, the system with reduced image points was solved in a few seconds, while the processing took several minutes with the original dataset.

3.1 Results with long sequences

Another interesting result discovered with ATiPE was the behaviour of both matching algorithms and bundle techniques with long image sequences. A very complex situation is the analysis of objects with bad textures and several repetitive elements (e.g. architectural objects or building facades). In this case a restrictive threshold during the comparison of the descriptors with the ratio test removes many good image correspondences. This means that the threshold should be modified according to the texture of the images, obtaining values of about 0.75-0.8. Obviously, several incorrect data remain in the dataset and they should be removed with the analysis of the epipolar geometry. However, the robust estimation of the **F** matrix does not allow the removal of mismatches which lie on the epipolar line. This situation often occurs with image sequences of building facades, where all photos are taken under a "quasi linear motion". All epipolar lines become parallel and almost horizontal, thus aligned with architectural objects like doors and windows.
As the **F** matrix cannot detects these outliers, all remaining wrong points must be removed during the estimation of the bundle adjustment. A robust photogrammetric bundle formulation plays an essential role, because multiple data for the same 3D points can be combined. The redundancy of the LS system can be the solution to overcome the drawbacks of the **F** matrix.
Figure 5 shows a sequence of images of Piazza Navona (Rome). 92 photos were taken from inside the square with a low-cost Samsung ST45 (12 Megapixels). They form a closed sequence and represent a very complex case with several repetitive elements (windows, …) and moving objects (people, …).

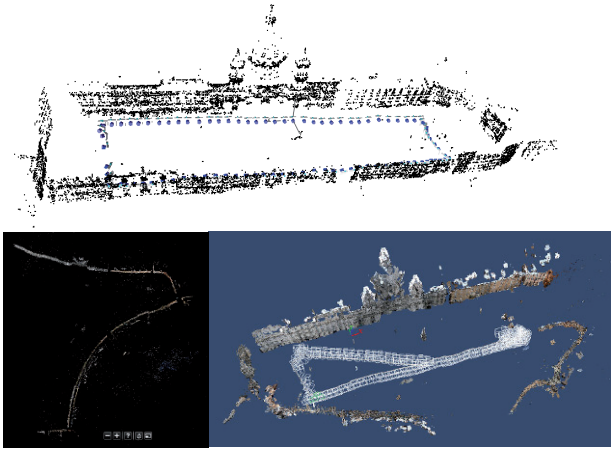

Figure 5. Results with ATiPE (top) and wrong orientation parameters obtained with Photosynth and Photofly (bottom) for the sequence "Piazza Navona".

Images were matched with the SIFT operator and then the orientation was completed with Australis. The choice of this software is motivated by the impressive number of image points matched: other software packages were not able to work with all these tie points. The software removed several wrong data during the computation of the bundle adjustment. The final RMS was 1.05 µm (pixel size is 1.5 µm), with approximately

18,300 3D points and an estimated overall theoretical accuracy superior to 1:6,900.
Beyond the statistical results, it is important to verify the correct closure of the sequence. Figure 5 (top) shows a 3D view with the camera poses and 3D points, and demonstrates the quality of the orientation results obtained with ATiPE.
The images were also processed with two well-known software for camera pose estimation: Microsoft Photosynth and Autodesk Photofly. Both software can determine the orientation parameters in an automated way and can be used for 3D reconstruction purposes. The processing was quite fast, and the obtained results are shown in figure 5 (bottom). As can be seen both software failed to close the sequence. Probably, these results are due to the bundle adjustment algorithm implemented in these packages, which is based on projective geometry and minimization errors that do not provide any guarantee on metric accuracy.

3.2 Accuracy analysis

The expected accuracy of the orientation phase (in terms of theoretical precision, RMS errors of image coordinates and σ_0) should be similar to that of traditional manual orientations, achievable with any photogrammetric software. For this reason, the orientation results obtained with the automated tie point extraction technique presented here were compared with those obtainable with interactive manual measurements. The accuracy analysis was carried out by estimating the covariance matrix of the bundle solution, with a particular attention to the average theoretical precision ($\sigma_{x,y,x}$) of the computed object coordinates. The projects were scaled with a known distance, after a free-network adjustment. They were also rotated in order to obtain a common reference system.
Numerical results are reported in table 1, showing the adjustment results derived with manual measurement, FB tie points refined with LSM ("FBM+LSM"), and corner-based tie points refined with LSM ("FAST+LSM"). Other than the larger number of tie points for both automated approaches, the precision of the corner-based method is very similar to the manual measurement approach. Other examples can be found in Barazzetti (2011).

	5 images – 3,872×2,592 (pix) *Object size: 1.2×0.6×0.2 (m)*		
	manual	FBM+LSM	FAST+LSM
3D points	17	337	649
σ_0 (pix)	0.68	0.59	0.62
RMS (pix)	0.59	0.59	0.7
σ_x (mm)	0.19	0.17	0.14
σ_y (mm)	0.2	0.19	0.15
σ_z (mm)	0.32	0.54	0.33

Table 1. Comparison between manual results and those provided by feature- and corner-based orientation procedures.

A second type of analysis was performed by comparing the photogrammetric results with theodolite measurements. Several targets distributed onto an object were used and their 3D coordinates were computed in the photogrammetric project only as intersections of homologous rays, after the bundle adjustment performed with the automatic method (exception made for 3 targets used as GCPs). 16 targets on the façade were assumed as check points and their 3D coordinates were measured with a theodolite. The results are shown in figure 6, where it can be seen how the standard deviation of the differences is lower than 5 mm. In addition, the absolute values of maximum and minimum discrepancies are less than 1 cm, and demonstrate a relative accuracy of about 1:3,000, which is more than sufficient for this kind of survey (the object is 15 m wide, with an average image scale of about 1:800).

	X	*Y*	*Z*
Mean	1	0	1
Std. dev.	2	4	2
Max	2	10	3
Min	-4	-5	-2

Figure 6. Differences (mm) between theodolite and photogrammetric data.

Another comparison with theodolite data was carried out for a block of images taken around a small church (20 m wide). Also in this case, some targets (24) were applied to the building façade and were measured with a Leica TS30 using a network composed of 6 stations. All targets were made up retro-reflective materials, with a central cross to identify their centres also in the images.
136 images (acquired with a Nikon D700 equipped with a 20 mm lens) were automatically oriented (figure 7), including some GCPs to obtain a georeferenced result. The overall RMSE value estimated using a set of check points was ca 1.1 cm, that is equivalent to the theoretical accuracy extracted from the covariance matrix (1.03 cm). The RMSE values computed using all GCPs was instead slightly better (0.7 cm). In all, more than 15,000 3D points were found and sigma-naught was 1.07 pix.

Figure 7. A sparse and unorganized block (136 images) automatically oriented with ATiPE.

4. EXTENSION TO OTHER DATA SOURCES

ATiPE is not only limited to pinhole images. Matching with feature-based algorithms and coupled with the analysis of the intrinsic geometry of the data, allows the processing of different kinds of data acquired with different sensors. Although the main goal is the analysis of large and complex datasets, the pairwise registration concept always remains the core method used for global processing. This formulation of the general problem, combined with a successive combination that includes

all the original data, makes the whole pipeline possible with a high degree of automation.

In addition, each specific geometric model used (e.g., the fundamental matrix, homography, etc.) during the pairwise matching phase strictly depends on the intrinsic characteristics of the sensor employed. However, it is remarkable that, even with different data, a relationship between corresponding features can often be mathematically defined as a linear transformation. Then, this model can be applied for outlier rejection in order to work with datasets that contain partially incorrect matches. Therefore, due to this common formalisation of the matching problem, the proposed solution can be adapted to work with many different categories of images, and it will be used in future works requiring the processing of data acquired with other instruments.

For instance, spherical images (Fangi, 2007), which can be assumed as belonging to a new branch of photogrammetry, can be matched and orientated with a strategy based on a spherical unwarping. The partitioning of the sphere into zones, which are independently matched and then combined, transforms the data into local pinhole images. Finally, the estimation of the camera poses can be carried out with a mathematical formulation between (i) the centre of the sphere, (ii) image point (on the sphere) and (iii) object point. Therefore, there exists an analogous form of collinearity equations for this category of images.

Laser scans can be registered by using the panoramic images generated from 3D points and their intensity values. Although this procedure aligns a set of scans without using any initial approximation, some limits were found in the case of highly convergent scans. As things stand now, it is difficult to forecast a massive use of such a method in complex practical projects. Further developments are necessary to improve the repeatability of feature-based operators.

Finally, the procedure was adapted to analyse particular sequences of multispectral data. Images taken from the same point with a special camera mounting different filters are related by a homography and can therefore be automatically matched and registered. More details and examples can be found in Barazzetti (2011).

Lastly, it is important to say that the general FB matching problem can be properly generalised using a common formulation.

	$\mathbf{M}_{ij}$	Type	Size	Formula	DoF
Essential matrix	**E**	2D↔2D	3×3	$\mathbf{x}_2^T\mathbf{E}\mathbf{x}_1$	5
Fundamental matrix	**F**	2D↔2D	3×3	$\mathbf{x}_2^T\mathbf{F}\mathbf{x}_1$	7
Projection matrix	**P**	3D→2D	3×4	$\mathbf{x}=\mathbf{P}\mathbf{X}$	11
2D Homography	**H**	2D↔2D	3×3	$\mathbf{x}_2=\mathbf{H}\mathbf{x}_1$	8
3D Rigid-body	$\mathbf{H}_e$	3D↔3D	4×4	$\mathbf{X}_2=\mathbf{H}_e\,\mathbf{X}_1$	6
3D Affine	$\mathbf{H}_a$	3D↔3D	4×4	$\mathbf{X}_2=\mathbf{H}_a\,\mathbf{X}_1$	12
3D Homography	**H**	3D↔3D	4×4	$\mathbf{X}_2=\mathbf{H}\,\mathbf{X}_1$	15

Table 2. Geometric models that can be included in the *generalized model for outlier rejection*.

Although different source data are connected by different mathematical relationships, a general criteria can be easily formulated by assuming corresponding datasets of 2D or 3D points $x_i \leftrightarrow x_j$ in homogenous coordinates. They can be considered related by a linear formulation involving a *registration matrix* $\mathbf{M}_{ij}$. Several geometric relationships can be written by considering the size and the elements of $\mathbf{M}_{ij}$, as shown in table 2.

The resulting equations in the parameters m_{ij} are linear, property which simplifies their estimation as initial approximations are not required. The analysis of outliers per each solution is computed on the basis of the residuals or by using a distance between projected and measured points. Finally, a rigorous Least Squares solution can be estimated by employing only the data classified as inliers. The solution of the final adjustment is always rigorous in a functional and stochastic sense. External constraints can be efficiently incorporated into the general model. The final system is made up of condition equations (those written as functions of both observations and parameters) and constraint equations (those written in terms of the parameters).

5. CONCLUSION

This paper presented an automated methodology with an aim to match tie points in different categories of data. The algorithmic implementation of the proposed technique is encapsulated into a software called ATiPE, that being the practical solution obtained.

This work was started few years ago with a simple consideration in mind: there does not seem to be a software adapted for the automated orientation of markerless sets of images. Indeed, the complexity and diversity of image network geometry in close-range applications makes the identification of tie points more complex than in aerial photogrammetry. Therefore, functional commercial solutions (say proven techniques) for automated image orientation and sparse 3D geometry reconstruction from markerless sets of images are still pending.

It is also worth noting that at the end of October 2010 Eos Systems Inc. released a new version of PhotoModeler, which has a new promising SmartMatch module for target-less image orientation. This confirms the growing interest in automation in close-range photogrammetry. However, this software was not taken into consideration during the preparation of this work due to the forthcoming discussion of the PhD thesis behind this paper, but it will be surely interesting to compare the results obtainable with PhotoModeler 2010 (now 2011) and ATiPE.

The entire procedure combines several algorithms of both CV and Photogrammetry in order to obtain an accurate reconstruction in an automated way. FB operators are used for a preliminary feature-based orientation, which is then improved by using the FAST interest operator. Indeed, the normal results obtainable with matching methodologies based on scale invariant features are usually worse than those achievable with manual (interactive) measurements. It becomes necessary to improve (i) the measurement precision of the image points, (ii) their multiplicity, and (iii) their final distribution in the images.

Images must be used at their original size. An initial image compression is followed by a coarse-to-fine approach to make full use of the acquired data.

The proposed methodology for orienting calibrated images estimates the unknown parameters with the same accuracy as the traditional and manual measurements. Furthermore the perspective functional model based on collinearity equations allows one to control the results with a rigorous statistical evaluation.

Lastly, a final consideration deserves to be mentioned. The results presented in this work, and the growing attention that these automatic procedures are bringing into the sector of close-range photogrammetry (e.g., with the introduction of new

commercial packages), show how image-based 3D modelling techniques can become more popular, even for non-expert operators.

From this point of view, a moderate balance between Photogrammetry and Laser Scanning can be expected. However, it is quite difficult to forecast that non-expert operators will be immediately able to orient complex photogrammetric blocks, generate detailed digital surface models, and produce 3D models or orthophotos, especially when the completeness and the accuracy of the final product are the main goals.

For instance, the 3D accuracy obtainable from the images strongly depends on the network geometry. Due to the unlimited number of possible situations that can occur during the survey of terrestrial objects, it is quite difficult to arrange general rules on the procedure for image acquisition. In a few words, if in aerial photogrammetry this phase is well defined by simple geometric relationships that allow for the preparation of an efficient flight plan, in close-range applications, a global standardization remains missing. This lack is even more significant when the survey comprehends additional information acquired with external sensors, such as theodolites and GNSS/INS systems.

Future work can therefore be related to this topic, e.g., beginning with the most typical practical cases. On the other hand, an operator with a good background in surveying techniques will be able to take advantage rapidly of all these new matching strategies because the transition from manual- or target-based procedures to feature-based ones will be surely quite simple.

REFERENCES

Arya, S., Mount, D.M., Netenyahu, N.S., Silverman, R. and Wu, A.Y., 1998. An optimal algorithm for approximate nearest neighbor searching fixed dimensions. *Journal of the ACM*, 45(6): 891-923.

Bay, H., Ess, A., Tuytelaars, T. and van Gool, L., 2008. Speeded-up robust features (SURF). *Computer Vision and Image Understanding*, 110(3): 346-359.

Barazzetti, L., 2011. Automatic Tie Point Extraction from Markerless Image Blocks in Close-range Photogrammetry. *PhD Thesis*, Politecnico di Milano, Milan, Italy.

Barazzetti, L., Remondino, F., and Scaioni, M. (2010). Orientation and 3D modelling from markerless terrestrial images: combining accuracy with automation. *The Photogrammetric Record*, 25(132): 356-381.

Brown, M. and Lowe, D.G., 2003. Recognizing Panoramas. *International Conference on Computer Vision*, 2: 1218-1225.

Cronk, S., Fraser, C. and Hanley, H., 2006. Automated metric calibration of colour digital cameras. *Photogrammetric Record*, 21(116): 355-372.

Fangi, G., 2007. The multi-image spherical panoramas as a tool for architectural survey. *Proceeding of the XXI International CIPA Symposium*, XXXVI-5/C53: 311-316.

Förstner, W., 2002. Computer Vision and Photogrammetry -- Mutual Questions: Geometry, Statistics and Cognition. *Bildteknik/Image Science, Swedish Society for Photogrammetry and Remote Sensing*: 151-164.

Fraser, C.S., 1992. Photogrammetric measurement to one part in a million. *Photogrammetric Engineering & Remote Sensing*, 58: 305-310.

Furukawa, Y. and Ponce, J., 2010. Accurate, dense, and robust multi-view stereopsis. *IEEE Transactions on Pattern Analysis and Machine Intelligence*, 32(8): 1362-1376.

Furukawa, Y., Curless, B., Seitz, S.M. and Szeliski, R., 2010. Towards Internet-scale Multi-view Stereo. *Proceedings of IEEE Conference on Computer Vision and Pattern Recognition*. 8 pages.

Ganci, G. and Handley, H.B., 1998. Automation in videogrammetry. *IAPRS*, 32(5): 53-58.

Grün, A., 1985. Adaptative least squares correlation: a powerful image matching technique. *South African Journal of Photogrammetry, Remote Sensing and Cartography*, 14(3): 175-187.

Hartley, R.I. and Zisserman A., 2004. *Multiple View Geometry in Computer Vision*. Second edition. Cambridge University Press, Cambridge, 672 pages.

Jazayeri, I. and Fraser, C.S., 2010. Interest operators for feature-based matching in close range photogrammetry. *Photogrammetric Record*, 25(129): 24-41.

Lounguet-Higgins, H.C., 1981. A computer algorithm for reconstructing a scene from two projections. *Nature*, 292: 133-135.

Läbe, T. and Förstner, W., 2006. Automatic relative orientation of images. *Proceedings of the 5th Turkish-German Joint Geodetic Days*, Berlin. 6 pages.

Lowe, D.G., 2004. Distinctive image features from scale-invariant keypoints. *International Journal of Computer Vision*, 60(2): 91-110.

Muja, M. and Lowe, D., 2009. Fast approximate nearest neighbours with automatic algorithm configuration. *Proceedings of the International Conference on Computer Vision Theory and Applications*. 10 pages.

Remondino, F., 2006. Detectors and descriptors for photogrammetric applications. *IAPRSSIS*, 36(3): 49-54.

Remondino, F. and Ressl, C., 2006. Overview and experiences in automated markerless image orientation. *International Archives of Photogrammetry, Remote Sensing and Spatial Information Sciences*, 36(3): 248-254.

Roncella, R., Forlani, G. and Remondino, F., 2005. Photogrammetry for geological applications: automatic retrieval of discontinuity in rock slopes. *SPIE 5665*: 17-27.

Rosten, E. and Drummond, T., 2006. Machine learning for high-speed corner detection, *Proceedings of the European Conference on Computer Vision*, Graz, Austria. Pages 430-443.

Rousseeuw, P.J. and Leroy, A.M. ,1987. *Robust Regression and Outlier Detection*. John Wiley, New York. 329 pages.

Scaioni, M., 2000. Robust estimation of relative orientation through the fundamental matrix. *IAPRSSIS*, 32(6W8/2): 253-259.

Snavely, N., Seitz, S.M. and Szeliski, R., 2008. Modeling the world from internet photo collections. *International Journal of Computer Vision*, 80(2): 189-210.

Torr, P.H.S., 2002. Bayesian model estimation and selection for epipolar geometry and generic manifold fitting. *International Journal of Computer Vision*, 50(1): 35-61.

NEW ADVANCES IN SPACEBORNE RADAR INTERFEROMETRY: SEISMIC AREA ANALYSIS AND COHERENCE ENHANCEMENT METHODS

Laura Calcagni

Area di Geodesia e Geomatica, Dipartimento di Ingegneria Civile, Edile e Ambientale, Università di Roma ``La Sapienza´´
via Eudossiana, 18 - 00184 Roma

Istituto per il Rilevamento Elettromagnetico dell'Ambiente - Consiglio Nazionale delle Ricerche
via Diocleziano, 328 - 80127 Napoli

KEY WORDS: SAR, interferometry, coherence, variogram, kriging

ABSTRACT:

Differential Synthetic Aperture Radar Interferometry (DInSAR) is an Earth observation technique based on the elaboration of the radar signal able to estimate the (vertical) displacements of an observed area. This technique has been applied for several years with good results but, also if its potentiality is known, some of its critical aspects remain open problems.
This PhD thesis investigated the crucial issue of enhancing the correlation (coherence) within a stack of radar images used to form interferograms and proposes an original geostatistical approach.
The DInSAR is based on the use of sequential images obtained on the area of interest in different times; due to the different position of the satellite in the different acquisitions and to the changes of the imaged scene during the observation period, one of the main problem of the technique is the lack of coherence between the images. The low coherence can strongly reduce the possibility to obtain information about the deformations, especially in non-urban areas, whose characteristics are not optimal to reflect the radar signal always in the same manner.
In this work is analyzed the application of the DInSAR to the characterization of the displacement fields caused by active seismic faults. Observing that generally the most significant seismogenetic faults are located in correspondence of mountain dorsals where non-urban areas are predominant, it is clear that the problem of the low coherence can have an huge impact on the application of DInSAR in these contexts.
A solution to mitigate this problem can be found in the application of kriging interpolation to ``fill-in´´the incoherent areas of interferograms formed by image pairs within the considered stack. In particular an innovative kriging algorithm is developed, in order to build up a method suitable for the particular characteristics of interferograms.
After the definition of the algorithm, an IDL code has been implemented, taking into account specific computing solutions in order to have a routine able to deal with a large amount of data.

1 INTRODUCTION

Differential Synthetic Aperture Radar Interferometry (DInSAR) is a remote sensing technique based on the use of radar systems to investigate surface deformations phenomena. The technique exploits the phase difference, known as interferogram, between two SAR images relative to the same investigated area and obtained in different times, and provides an estimation of the ground deformation projection along the radar line of sight (LOS). The capability of DInSAR to estimate ground deformations is limited by decorrelation phenomena, due to differences in the two radar images that form an interferogram. The correlation of an interferogram, that is the correlation between the two SAR images which form it, is represented in probabilistic terms, the most commonly used parameter being the coherence. The DInSAR algorithms to estimate surface deformations can be applied only on points of interferograms that exhibit high coherence values. In this work the use of DInSAR for the analysis of deformations of seismic structures is exploited, in particular a procedure to overcome the problems due to the low coherence is investigated. A set of 108 interferograms relative to the L'Aquila area is analyzed, including a subset displaying coseismic deformations related to the earthquake occurred on April 6, 2009 (M=6.3, UTC 1:32:39). The dataset underlines how the density of coherent pixels can be strongly not homogeneous in non-urban areas, due to the decorrelation phenomena. Here we show that it is possible to ``fill-in´´the incoherent areas with kriging interpolation, with a significant enhancement. A suited IDL code was implemented to perform the new proposed methodology.

2 THE DIFFERENTIAL SAR INTERFEROMETRY

The spaceborne Differential SAR Interferometry is based on the concept of the combination of two SAR images acquired, as possible at the same angular view, in the repeated passes of the satellite on the same area. If R (range) represents the distance between the satellite and the target and x the position of the satellite respect to its path (azimuth), the two SAR images can be expressed as:

$$u_1(R,x) = |u_1(R,x)| \exp j\varphi_1(R,x),$$
$$u_2(R,x) = |u_2(R,x)| \exp j\varphi_2(R,x), \quad (1)$$

The SAR interferogram is generated by cross-multiplying, pixel by pixel, the first SAR image with the complex conjugate of the second one (Bamler and Hartl, 1998):

$$v(\cdot) = u_1(\cdot)u_2^*(\cdot) = |u_1(\cdot)||u_2(\cdot)| \exp j\varphi(\cdot) \quad (2)$$

where

$$\varphi(\cdot) = \varphi_1(\cdot) - \varphi_2(\cdot) \quad (3)$$

is the *interferometric phase*. The phase of a SAR image is proportional to the range, plus a possible shift due to the scatterer itself:

$$\varphi_1 = \tfrac{4\pi}{\lambda} R_1 + \varphi_{scat,1},$$
$$\varphi_2 = \tfrac{4\pi}{\lambda} R_2 + \varphi_{scat,2}. \quad (4)$$

Assuming that the scattering phase is the same in both images, the interferometric phase is a very sensitive measure of the range difference:

$$\Delta\varphi = \frac{4\pi}{\lambda}\Delta R. \quad (5)$$

It is important to underline that $\Delta\varphi$ is ambiguous to within integer multiples of 2π; therefore, in order to use the interferometric phase to estimate ΔR it is necessary to perform the reconstruction of the real interferometric phase (unwrapped) given its value modulo 2π (wrapped); this process is called phase unwrapping. This is one of the most crucial aspect of SAR interferometry; different algorithms were developed to solve it (Costantini, 1998), (Pepe and Lanari, 2006) according with different methods, but all of them present problems in finding of solution in low coherent areas, where interferometry does not furnish an accurate phase information. The equation 5 shows the dependency of the interferometric phase on the range; if in the observed scene changes occurred, such as height ground variation, this can be detected as range difference in the interferometric phase and this explains how it is possible to estimate ground deformations with the differential SAR interferometry. Because the scene is imaged from two different points of view, in order to distinguish the surface changes from the parallax caused by topography, a DEM must be used to remove the topography (Gabriel et al., 1989).Despite its correlation with the ground deformations, the interferometric phase cannot be directly used to estimate the surface changes, because it also depend on other contributes. A more general formulation of the interferometric phase is:

$$\Delta\varphi = \Delta\varphi_d + \Delta\varphi_t + \Delta\varphi_a + \Delta\varphi_n \quad (6)$$

where $\Delta\varphi_d$ represents the term linked with the deformation in the direction of view (LOS), $\Delta\varphi_t$ represents the possible topographic artifacts present in the DEM used for topographical correction, $\Delta\varphi_a$ represents the refraction of the radar signal during its passage in the atmosphere and $\Delta\varphi_n$ is the contribute relative to the noise. There are different algorithms to obtain the information of deformation from the interferometric phase, based on the decoupling of the deformation component from the undesired patterns. The basic idea is using a large number of SAR images to obtain multiple interferograms, in order to have the necessary redundancy to filter out the other effects from the sought deformation. In literature it is possible to find two different types of strategies, the coherence-based methods (Berardino et al., 2002a) and the so-called permanent scatterers (Ferretti et al., 2001). Images obtained in different times mean redundancy but also uncorrelation, due to the changes in the observed scene, that can be described only in a probabilistic terms. One of the most representative statistical index is the *coherence* between the two SAR images u_1 and u_2. The coherence can be theoretically defined on a pixel basis as the correlation coefficient between two zero-mean, complex gaussian random variables: $u_1 = u_{1r} + ju_{1i}$ and $u_2 = u_{2r} + ju_{2i}$ (Monti Guarnieri and Prati, 1997):

$$\gamma = \frac{|E[u_1 \cdot u_2^*]|}{\sqrt{E[|u_1|^2]E[|u_2|^2}} \quad (7)$$

Actually the coherence cannot be estimated on a pixel basis, thus it is obtained from (7) by substituting the ensemble average with spatial sampled averages, by assuming process ergodicity in a small estimation area.

3 KRIGING INTERPOLATION AS A COHERENCE ENHANCEMENT METHOD

As we discussed, the coherence can significantly limit the use of DInSAR for the study of deformations, especially in areas with characteristics not suite fro a persisten reflection of the radar signal, such as not-urban areas with vegetation. This can have a strong impact on the application of this technique for estimating deformations over seismic areas. In Italy, for example, the major seismogenetic structures are located in the Alps and in the Apennines. A solution to overcome the problem of the low coherence is found in the interferograms kriging interpolation, used to ¨fill-in¨the incoherent areas. Kriging is a well known geostatistical interpolation method based on regression against observed values of surrounding data point, weighted according to spatial covariance values. Respect to other interpolation methods, it presents some advantages: it is an exact interpolator, supplies an estimation error and it is able to compensate the effects of data clustering, assigning to individual points within a cluster a weight lower than the one of isolated points. The kriging interpolation is based on the study of the spatial variability of data, through the computation of the *experimental variogram*, that represents the dissimilarity between data pairs respect to a vector class H_k (n_c is the total number of pairs):

$$\gamma^*(H_k) = \frac{1}{2n_c}\sum_{\alpha=1}^{n_c}(z(x_\alpha + h) - z(x_\alpha))^2, h \in H_k \quad (8)$$

Usually the average dissimilarity increases when the spacing between pairs of samples grows up. The behaviour at very small scales, near the origin of the variogram, indicates the type of continuity in the data: if it appears discontinuous, it means that the value of the variable changes significantly at a very small scale, this is known as *nugget effect*. For large spacing, the experimental variogram can become constant, meaning that there is no more spatial structure in the data: the corresponding distance is called *range* and the variogram value *sill*. If the variogram changes not only in dependence of distance, but also with direction, this means that the data present an anisotropic spatial structure. An experimental variogram has to be replaced by a theoretical variogram function, in order to guarantee that the variance of any linear combination of sample values is positive, a necessary condition to use the variogram in a kriging estimation. The experimental variogram is thus fitted with a theoretical model of variogram, which is defined under the hypothesis of intrinsic stationarity of order two (Wackernagel, 1995). In literature different theoretical models of variogram are defined: the most commonly used are the nugget effect model (9), accounting for a discontinuity in the origin, the power law model, that grows without bounds (10), the exponential model (11), that falls off exponentially with increasing distance and the spherical model (12); hereafter the analytical formulations of these isotropic models are reported:

$$C_{nug}(h) = \begin{cases} b & \text{for } |h| = 0 \\ 0 & \text{for } |h| > 0 \end{cases} \quad (9)$$

$$C_{pow}(h) = b|h|^a \quad (10)$$

$$C_{exp}(h) = b\exp -\frac{|h|}{a} \text{ with } a, b > 0 \quad (11)$$

$$C_{sph}(h) = \begin{cases} b(1 - \frac{3}{2}\frac{|h|}{a} + \frac{1}{2}\frac{|h|^3}{a^3}) & \text{for } 0 \le |h| \le a \\ 0 & \text{for } |h| > a \end{cases} \quad (12)$$

As mentioned sometimes the spatial variability of data can change also with directions: this is the case of the presence of an anisotropic spatial structure within the data, that have to be suitably modeled. The standard method described in the literature to model the anisotropies is based on the idea to combine directional variograms into a single model that is consistent in all directions (Eriksson and Siska, 2000). Two different types of anisotropy can occur: it is possible to have variograms that exhibit different values of range in different directions (*geometrical anisotropy*) and variograms whose sill changes with direction (*zonal anisotropy*). A widely applied approach to solve the geometrical anisotropy is based on the detection of the so called ``separation angle´´ θ which identifies the direction of the maximum range (a_{max}), being supposed that the range is minimum (a_{min}) along the orthogonal one ($\theta \pm \frac{\pi}{2}$). The minimum and maximum ranges can be viewed as the semi-minor and semi-major axes of an ellipse, whose equation in a Cartesian coordinate system (u, v) oriented along its major and minor axes reads:

$$(\frac{u}{a_{max}})^2 + (\frac{v}{a_{min}})^2 = 1. \quad (13)$$

The separation angle can be expressed as:

$$\xi = \tan^{-1} \frac{u}{v} = \phi_{ij} - \theta \quad (14)$$

and the range in a whatever direction from point i to point j results:

$$a_{ij} = \frac{a_{max} a_{min}}{\sqrt{a_{min}^2 \cos^2(\phi_{ij} - \theta) + a_{max}^2 \sin^2(\phi_{ij} - \theta)}}, \quad (15)$$

The range a_{ij} is used to obtain the anisotropic model, instead of range a used in the isotropic case. The zonal anisotropy can be

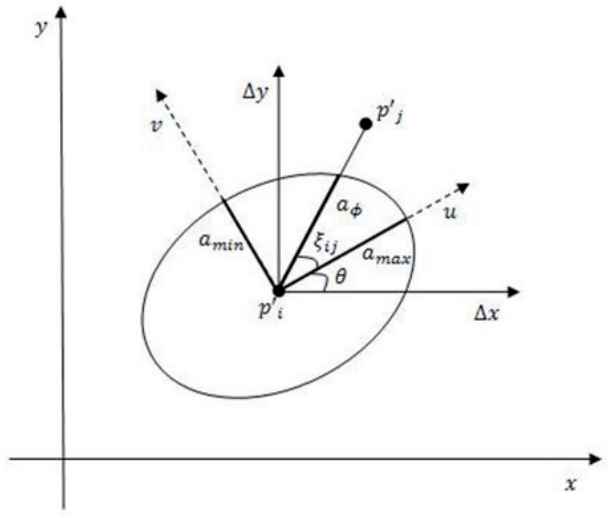

Figure 1: Modeling of geometrical anisotropy.

accommodated using two range-anisotropic structures, one with a very large anisotropy ratio. The method is based on several steps. At first, the experimental variogram in the direction of minimum sill is fitted with an isotropic model. After this, a second anisotropic variogram is added, whose sill is the difference between the maximum and minimum sill observed in the directional variograms. The minimum range of the structure corresponds to the range of direction of maximum sill, whereas the maximum is set to a very large value. The zonal anisotropy is thus solved by elongating the range ellipse (Eriksson and Siska, 2000).

4 CHARACTERIZATION OF THE SPATIAL STRUCTURE OF A DINSAR INTERFEROGRAM

A satisfactory interpretation of the spatial structure of a DInSAR interferogram begins from a detailed knowledge of its characteristics. As already introduced, the interferometric phase (6) is given by different contributes, where the two principal are due to the atmospheric artifacts and to the displacements. The atmospheric signal presents a spatial correlation, whereas the deformation can be correlated or not. In the case of significant deformations (e. g. seismic events) the radar signal due to atmosphere and deformation can be very different. If the deformations are moderate, instead, the two signals present a similar amplitude, what means a comparable structure of variability in the spatial domain and the high difficulty to distinguish between them. An additional complication comes also from the significant dimensions of the area covered by an interferogram (about 100 km^2 in the case of ENVISAT sensor): in fact, for this reason, it is possible to have different deformation phenomena in the same interferogram. Summarizing, the study of the spatial structure of an interferogram, thus, meets two problems, the presence of two signals, the deformation and the atmosphere, that can be comparable and the variability of these two signals in the different areas of the interferogram. Hereafter we will see that the proposed kriging interpolation is an effective methodology, flexible to be adapted to the different signals present in an interferogram. A dataset constituted by 4 ENVISAT interferograms relative to the L'Aquila area has been analyzed at first, in order to define an efficient strategy to model the spatial variability of an interferogram. Since the analyzed interferogram have not any significant deformations, the contribute of the interferometric phase due to the deformation can be supposed with a magnitude comparable with the atmospheric delay. The first step was the computation of the experimental variogram, according to (8), considering 15 km as maximum computing distance, 40 lags in distance and 40 lags in direction (for checking possible anisotropies). In Fig.2 are represented the isotropic experimental variograms, presenting comparable trends. In Fig.3 the variation of the variograms

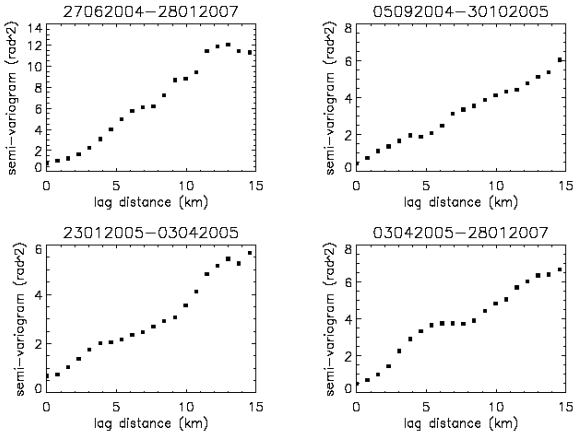

Figure 2: Experimental isotropic variograms.

according to the direction is represented (the so-called variogram map), that reveals an anisotropic pattern of the phase variability: the sills and the ranges change with direction. Since there is a directional variability both of range and sill, we have to deal with the most complex case of zonal anisotropy. Since the experimental variograms exhibit an anisotropic pattern, both anisotropic and isotropic models of variograms are considered for fitting the experimental variograms. In details, three different teoretical vari-

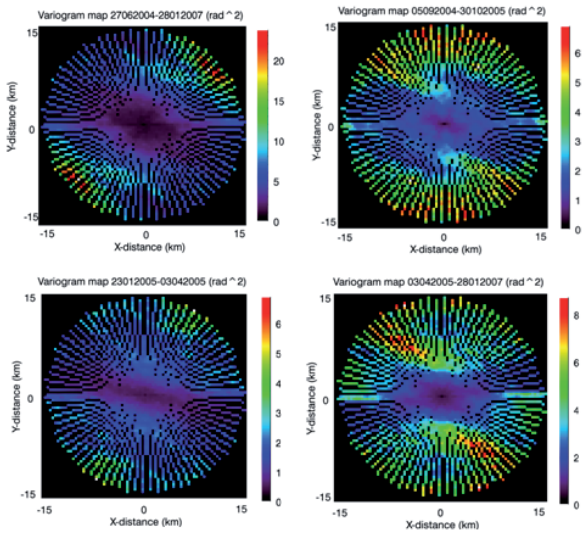

Figure 3: Experimental variogram maps.

ograms were considered, the exponential (11), the spherical (12) and the power law (10) models. For the power model the exponent was fixed because, under the hypothesys that the deformation contribute is comparable with the atmospheric delay, it is supposed it follows the Kolmogorov theory, where the atmospheric turbulence is described by a "$\frac{2}{3}$ law"(Williams et al., 1998). The approximate parameters for the variogram models were obtained by a visual inspection of the experimental variograms, the they were refined through a least squares adjustment by: The anisotropic models of variograms are obtained, under the hypothesis of zonal anisotropy, combining the mentioned isotropic models and considering a variation of the range with direction according to (15). It was, thus, necessary to individuate, on the experimental maps of variogram, the anisotropy direction, that is the direction where the variogram reaches the higher value of sill, corresponding to the direction of minimum range; then, it is possible to define some parameters which are necessary to estimate the model:

- maximum sill ($sill\_max$), the sill in the anisotropy direction;
- minimum range ($range\_min$), the range in the anisotropy direction;
- minimum sill ($sill\_min$), the sill in direction perpendicular to the anisotropy one;
- maximum range ($range\_max$), the range in direction perpendicular to the anisotropy one.

Also these parameters are obtained by an eye inspection of the experimental variograms. In the Tab. 1 are summarized the parameters to build up the anisotropic models of variogram. The reliability of the hypothized anisotropic models is evaluated comparing the model maps of variogram with the experimental ones. The obtained results are not satisfactory: in particular observing the Fig. 4 it is possible to understand the origin of the problem. The anisotropic model is built up on the assumption that the variation of the range of the variogram in the different directions describes an ellipse, whose minor axis is in the anisotropy direction, where the sill is maximum. Since the very high values of the sill in the

interf	I1	I2	I3	I4
ani_dir (degree)	40.5	90	49	108
range_min (pixel)	170	130	170	180
sill_max (rad^2)	25	10	12	9.5
range_max (pixel)	230	230	210	250
sill_min (rad^2)	7.5	4.5	2.5	7.5
nugget (rad^2)	0.5	0.5	0.5	0.5
model_iso	expo	expo	expo	expo
model_aniso	expo	expo	expo	spher

Table 1: Parameters for the anisotropic model of variogram.

anisotropy direction in the experimental variogram, it is necessary to suppose a very small range to model them, but this not correspond to the behaviour of the experimental variogram, which presents the maximum values of sill for ranges relatively large. The standard theory for the modeling of the anisotropic models of variogram, thus, does not appear appropriate to model the spatial structure of the analyzed interferograms. Then we went back

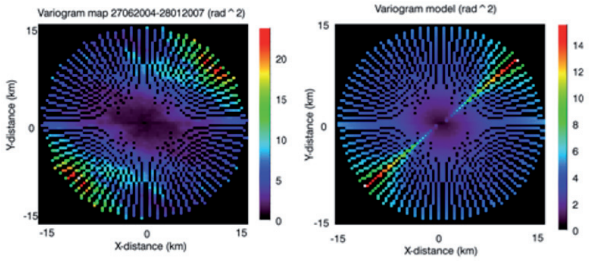

Figure 4: The anisotropic model of variogram for interferogram I1: the experimental variogram (a) and the theoretical model (b).

to the isotropic model; in the Tab. 2 are summarized the parameters chosen for the isotropic models of variogram. In this case the goodness of the different supposed models is evaluated applying a cross-validation method. This consists in the removal of the observations at specific locations and in the kriging estimation of the interferometric phase itself on these points using the other samples. The residuals between the observed values and the estimated one was chosen as an index of the goodness of the kriging interpolation. Some statistics on the residuals are computed, in particular the average of the residuals (*ME*), the mean square error (*MSE*) and the mean square error standardized respect to the prediction variance (*MSSE*). The cross-validation was carried out on a set of 1000 points, randomly selected between the coherent points of the interferograms. The results of cross-validation (Tab. 3), in particular the parameter MSSE, show that the power law model presents the best fitting with the experimental values.

In order to check if the chosen isotropic variogram model can account for local anisotropies, a deeper analysis was carried out. The interferograms were divided in 16 sub-areas, for which the experimental variogram maps were computed (Fig. 5): they do not show significant anisotropy. The vanishing of the anisotropy at a local level explains the good results obtained by the application of an isotropic model of variogram. Moreover, it has to be considered that it was decided to base the kriging prediction on the 20 observations closest to the estimation point, in order to reduce the computation time, thus the effect of the anisotropy becomes irrelevant. An isotropic power law model of variogram, thus, could be adopted to model the spatial variability of the differential interferometric phase.

		POWER	EXPO	SPHER
I1	NUGGET (rad^2)	0.2	0.5	0.5
	SILL (rad^2)	-	16	9.5
	RANGE (pixel)	-	220	220
I2	NUGGET (rad^2)	0.2	0.5	0.5
	SILL (rad^2)	-	7	4.5
	RANGE (pixel)	-	220	250
I3	NUGGET (rad^2)	0.4	0.6	0.6
	SILL (rad^2)	-	6.5	3.8
	RANGE (m)	-	230	250
I4	NUGGET (rad^2)	0.2	0.4	0.6
	SILL (rad^2)	-	9	5.5
	RANGE (pixel)	-	230	280

Table 2: Parameters of the isotropic variogram model.

		POWER	EXPO	SPHER
I1	ME (rad)	0.00	0.00	0.00
	MSE (rad^2)	0.43	0.44	0.44
	MSSE	1.15	4.53	5.08
I2	ME (rad)	0.01	0.01	0.01
	MSE (rad^2)	0.297	0.30	0.30
	MSSE	1.60	7.29	8.59
I3	ME (rad)	0.01	0.01	0.01
	MSE (rad^2)	0.29	0.30	0.30
	MSSE	1.73	8.99	9.21
I4	ME (rad)	0.02	0.02	0.02
	MSE(rad^2)	0.80	0.81	0.81
	MSSE	1.51	6.97	9.25

Table 3: Results of cross-validation.

5 KRIGING INTERPOLATION TO ENHANCE THE DINSAR INTERFEROGRAMS COHERENCE

The individuation of an effective approach to model the spatial variability of DInSAR interferograms represents the starting point to define a method to enhance the coherence of a stack of interferograms. As explained, the DInSAR interferometry is based on the use of a large number of interferograms, thus the goal is to define a method to elaborate simultaneously a whole stack of differential interferograms. This means to deal with significant computational times but also with interferograms characterized by deformation signals of different magnitude, whose behaviour can be significantly different respect to the atmospheric delay. To explain the developed kriging interpolator, we present its application on the mentioned stack of 108 ENVISAT interferograms, relative to Abruzzo (Central Italy) for the period (yyyymmdd) 20021215-20100815, that includes the epoch (6 April 2009) when an earthquake occurred in L'Aquila, causing hundreds of victims. A significant portion of the analyzed area is relative to the Apennines, where there is a diffuse problem of low coherence of the interferometric phase. This stack contains pre-seismic and post-seismic interferograms, where the main contribute of interferometric phase is due to the atmospheric delay and to the co-seismic interferograms, characterized by a significant deformation. This dataset represents an interesting example to show the characteristics of the implemented interpolation method. The first step of the procedure consists into the computing of the isotropic experimental variograms, obtained considering a maximum computing distance of 15 km, discretized in 40 lags. In Fig. 6 there are the variograms relative to four interferograms referred to the period summarized in Tab. 4, two pre/post-seismic and two co-seismic. It is possible to note that the variograms relative to the last ones present a peculiar shape and, above all, reach very high values of sill. This is reasonable because the seismic deformation, localized in a limited area represents a remarkable local anomaly and introduces a strong decorrelation between point pairs. Because the different characteristics of the variograms, it is not possible to use the same model to interpolate all the interferograms of the stack. The strong localized deformation, moreover, makes not applicable the kriging interpolation, because the hypothesis of stationarity of order two. A different strategy, thus, is proposed to interpolate with kriging the whole stack of interferograms. This is based on the observation that the spatial variability of a localized strong deformation, differently by the atmosphere or spatially correlated deformation signal, presents a deterministic trend, that has not to be described in stochastic terms, so it is not considered in the modeling of the spatial structure of the data. This means that the deterministic component of the deformation signal, peculiar of strong motions, has not be involved in the computing of the experimental variogram. Therefore, the experimental variogram is computed in an innovative way, consisting in the partition of the interferograms in a fixed number of sub-areas, in the computing of the experimental variogram for each of them and then in the computing of the median interferogram, assumed as representative of the whole interferogram. Because the seismic deformation is localized on a small area, its variogram behave as an outlier with respect to the others and it is filter out by the median operator. The variograms obtained with the method of "median variogram" appear comparable in values and in shape both for pre/post-seismic and co-seismic interfero-

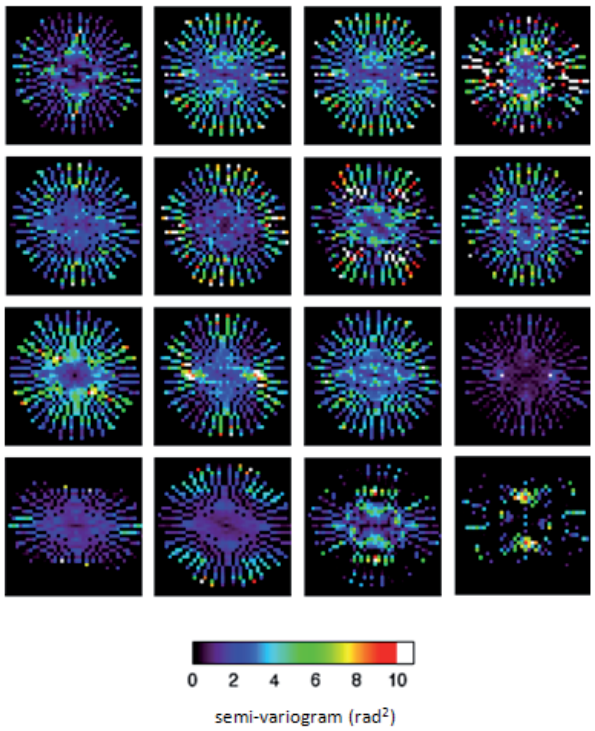

Figure 5: Variogram maps for sub-areas of an interferogram.

INTERFEROGRAM	PERIOD
33	20041219-20090726
51	20051030-20060319
75	20080427-20090412
105	20100117-20100815

Table 4: The examined interferograms, in grey the co-seismic ones are underlined.

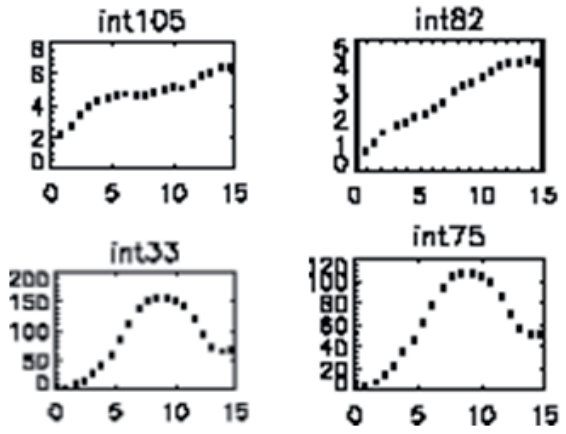

Figure 6: Experimental isotropic variograms: pre- and post-seismic interferograms (above), co-seismic interferograms (below).

grams, as shown in Fig. 7, where the median variograms of the interferograms summarized in Tab. 4 are represented. The consistency of the median variograms is also evaluated comparing them with the traditional ones. Chosen two reference interferograms, a pre-seimsic one (30102005-19032007) and a co-seismic (19122004-2607009), they are divided in 16 sub-areas and for each both the traditional and the median variograms are computed. It is observed a good agreement between the two different variograms, except in the sub-areas interested by the seismic deformation, this is the demonstration that the method of the median variogram allows to obtain a modeling of spatial structure of data that is not influenced by strong and localized deformations. The experimental median variograms was fitted with a power law model. The adopted model is improved considering a variable exponent, following the equation:

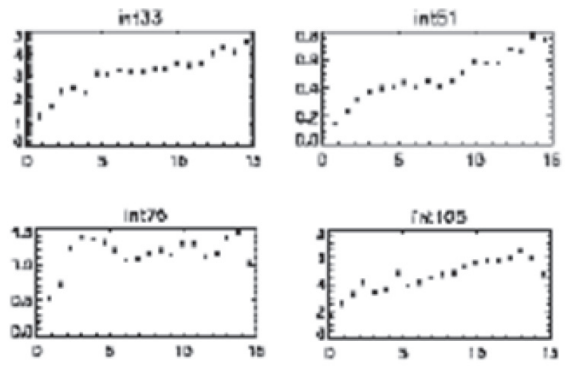

Figure 7: The median variograms.

$$\gamma = n + c \cdot d^e \tag{16}$$

The parameters of model, n, c, e are estimated by applying a weighted least squares method proposed by Cressie (Cressie, 1985). The fitting between the experimental and the theoretical model is obtained by minimizing the relation:

$$P(\theta) = \sum_{j=1}^{K} |N(h_j)|(\frac{\gamma(h_j)}{\gamma(h_j;\theta)} - 1)^2 \tag{17}$$

where:

- $h_1, ..., h_k$ are equally spaced lags at which the variogram is estimated;
- $\gamma(h)$ is the experimental median variogram;
- $\gamma(h, \theta)$ is the theoretical model of variogram;
- N(h) is the number of samples for each distance lag.

The minimization of (17) is performed numerically, considering different values for the parameters θ. In particular, for each parameter n, c, e, a minimum and a maximum values are supposed, defining an interval where the solution is searched. Dividing the interval in a fixed number of lags an increment is found, adding it to the minimum value supposed, until the maximum one, different combinations of parameters are tried and it is possible to determine those values which minimize (17). The supposed model presents a good fitting with the experimental one, for each interferogram of the stack, as it is shown in Fig. 8. In order to evaluate the reliability of the defined model of variogram, a cross-validation was carried out on a set of 1000 points as before. In Tab. 5 the results of cross-validation for the interferograms of Tab. 4 are summarized. The mean of the residuals is small and the mean of squared residuals standardized respect to the variance prediction is quite close to 1 (except for the interferogram 105), what indicates a good adequacy of the model and of its parameters. An aspect to underline is that satisfactory results are obtained for all interferograms, both for pre/seismic and co-seismic interferograms, this confirms that the proposed method of the kriging interpolation is an efficient tool to elaborate interferograms even with different characteristics. The visualization allows to evaluate the interpolated interferograms against the original ones, where the phase differences are present only in the coherent points. The Fig. 9 illustrate the situation for a pre-seismic interferogram (15122002-21082005), on the left there are the coherent point before the kriging interpolation and on the right there is the interpolated interferogram. The Fig. 10 is relative to a co-seismic interferogram (27042008-12042009) where in the right part of the figure it is possible to observe the area interested by the earthquake. It is possible to observe that the interferometric

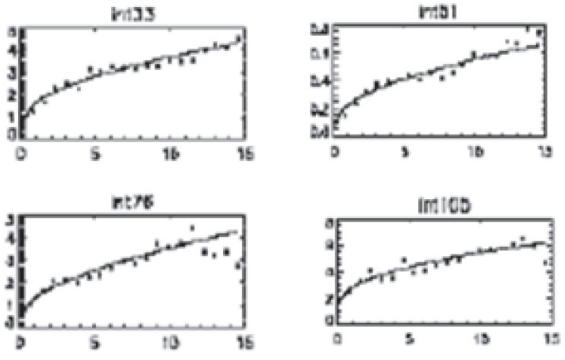

Figure 8: Theoretical model fitted to the median variograms.

INTERFEROGRAM	ME	MSE	MSSE
33	0.006	1.358	1.143
51	0.014	0.137	0.846
75	0.023	0.403	0.797
105	0.046	1.756	2.126

Table 5: The considered interferograms (33 and 105 are the coseismic ones).

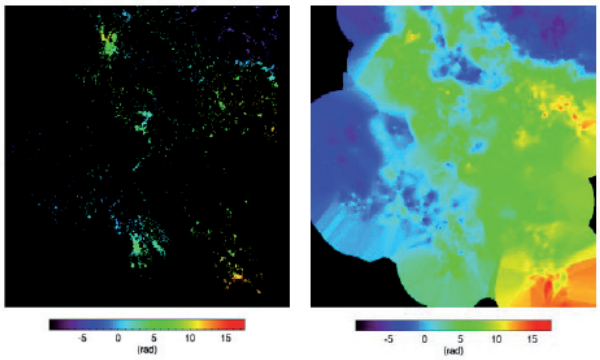

Figure 9: Interferogram 15122002-21082005, on the left before (left) and after (right) the kriging interpolation.

phase is re-constructed in a very efficient way, in fact the shape of the deformation is clearly visible. An additional check of the effectiveness of the kriging interpolation, besides the cross-validation procedure, was performed, by a comparison between the wrapped and the unwrapped interferograms, that are opportunely re-wrapped. This allows to compare on the interpolated phase respect to the beginning one. The check is executed on the whole stack of interferograms, analyzing the temporal coherence between the wrapped and the unwrapped interferograms. Considering a point of coordinates (x, y), being $\varphi_w(x, y)$ its wrapped interferometric phase and $\varphi_{uw}(x, y)$ its unwrapped interferometric phase, the temporal coherence is expressed by:

$$\gamma(x,y) = \frac{1}{N}\sum_{k=1}^{N} \exp j \cdot (\varphi_w(x,y) - \varphi_{uw}(x,y) \qquad (18)$$

where N represents the number of interferograms. Points which exhibit high values of function (18) are characterized by a good coherence between the wrapped and unwrapped interferograms. This means that the kriging allows to obtain interpolated values of interferometric phase congruent with the beginning ones, the

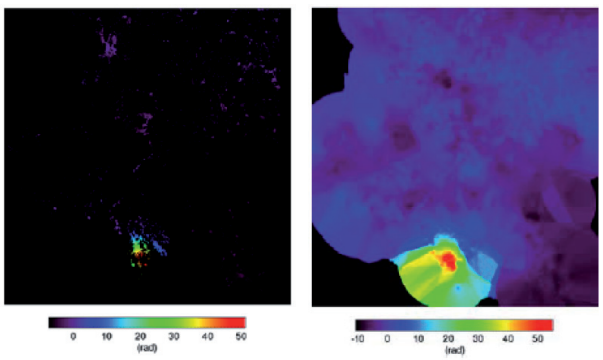

Figure 10: Interferogram 27042008-12042009, on the left before (left) and after (right) the kriging interpolation.

wrapped phases. Finally, in order to evaluate the coherence gain due to a new selection of the coherent points is performed fixing a threshold on the temporal coherence. In particular, if a threshold of 0.7 is chosen the original number of coherent points (28553) increases up to 39955, with a gain of 38%. In Fig. 11 there is a representation of coherent points for a portion of the area of the interferograms: on the right part of the figure it is possible to note that areas with coherent points remarkably enlarge after the kriging interpolation.

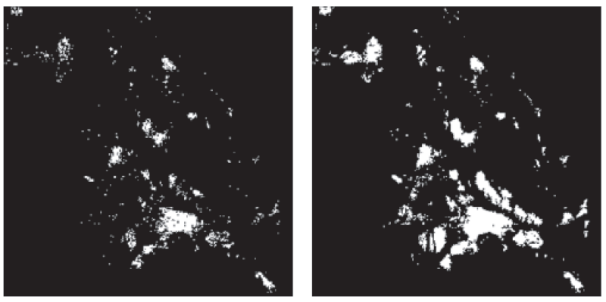

Figure 11: Coherent points in an area of the interferograms, before (left) and after (right) the kriging interpolation.

6 THE IMPLEMETED ALGORITHM FOR THE KRIGING INTERPOLATION

To execute the kriging interpolation of a stack of DInSAR interferograms an IDL code has been implemented. The IDL language offers some kriging routines; nevertheless, in this work, new routines were implemented to include the particular solutions for the interpolation of DInSAR interferograms. In particular, the computing of experimental variogram is realized using an unusual method which involve the computing of a median variogram and for the theoretical model of variogram is considered a power law model, whose parameters are estimated by a least squares procedures, whereas in IDL routines only exponential and spherical model are implemented. In addition, since the significant dimensions of DInSAR interferograms, the developed code was optimized to lower the computational time. The implemented code consists in several routines, performing the different steps of the kriging interpolation (12)

- estimation of experimental variogram;
- estimation of theoretical model of variogram;
- cross-validation to validate the model of variogram;
- prediction.

The routine kriging.pro allows to set the processing variables and the parameters necessary to all the routines of the process. The routine vrgEST.pro performs the computing of the experimental variogram. The computing is carried out by averaging one-half the difference squared of variable values over all pairs of observations with the specified separation distance and direction, within a maximum computing distance. If there are n observed data, there are $\frac{n(n-1)}{2}$ unique pairs of observations. Even a data set of moderate size generates a large number of pairs and this extremely time consuming. In order to contain the computing time, the developed algorithm is based on a pre-computing of the pairs, which are stored in a variogram grid where the columns represent

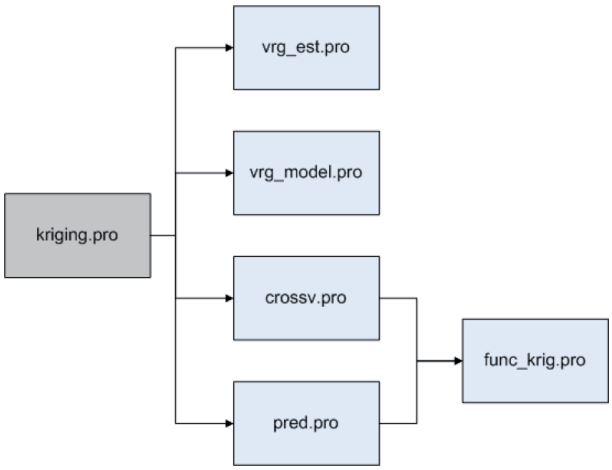

Figure 12: Flowchart of the code for the kriging interpolation of DInSAR interferograms.

the direction lags and the rows represent the distance lags. For each cell of the grid is progressively executed the sum of the difference pairs, and finally the variogram is obtained by an average respect of the directional lags, for each distance lag. Obviously, to assign a pair to a cell of the grid, opportune angular and distance tolerance are considered respect to the fixed lags. The described algorithm represents the implementation of the standard method to compute the experimental variogram; however, here the computation is applied to sub-areas of each interferogram, in order to compute the median interferogram accounting for possible local anomalies which are filtered out. The routine vrgMODEL.pro performs the computing of the parameters of the theoretical variogram model. The model of variogram implemented in the code is a power law model with a nugget effect, expressed by the relation:

$$\gamma = n + c \cdot d^e \tag{19}$$

where n represents the nugget effect. The parameters are computed by applying a weighted leasted squares method proposed by Cressie ((Cressie, 1985)), where the solution is searched numerically. The routine pred.pro computes the kriging weights and by selecting a fixed number of obervations performs the interpolation. The routine crossv.pro performs the cross-validation on a set of points. At first the number of the points used for the cross-validation is chosen; then the routine select them randomly between the coherent points of the interferogram. After the selection, the routine removes the points from the observations and executes the kriging interpolation, considering the remaining observations. The estimated values of interferometric phase on the points selected for the cross-validation are compared with the original ones, and some statistic parameters are computed on the residuals (mean of squared residuals, mean of squared residuals standardized respect to the prediction variance and mean of prediction variance).

7 CONCLUSIONS

The DInSAR technique is widely applied to monitor deformations, also on seismic structures, but its effectiveness can be seriously limited by problems of low coherence, present in areas with characteristics not suited for a permanent reflection of the radar signal, for example areas with vegetation. In this case it is necessary to individuate opportune strategies to overcome the problem and maximize the application of DInSAR to the deformations monitoring. The kriging interpolation represents a solution to ``fill-in´´incoherent areas, using the information carried by the coherent points. Kriging interpolation requires the study of the spatial structure of the data, that is executed in two next steps. The first one is the analysis of the spatial variance of the data, with the variogram estimation and its fitting with a theoretical model and the second one is the prediction using the observations surrounding to the point to estimate. The estimation of variogram and the choosing of a proper theoretical model is a crucial step, because a model representative of the spatial nature of the data is a basis to obtain a satisfactory interpolation. For this reason an interpolation process has to be preceded by an accurate study of the spatial structure of the data, executed in relation to the characteristics of the dataset. Here we evidenced that, even if at a large scale the variogram may appears anisotropic, at a local scale it is isotropic. So, it is convenient to compute the kriging interpolation just on the basis of a reasonable number of observations (here we use 20) close to the interpolation point, also for obvious computational reasons. The variogram model which exhibits the best fit with the experimental data was the power law model with a nugget effect. The parameters of the model were least squares estimated following a procedure proposed by Cressie. When long time series of interferograms are examined, it is possible to have data with strong localized deformations, for example if an earthquake is occurred. A deformation of this type presents a spatial variability strongly different from the atmospheric delay and the slow deformations. In this situation the kriging interpolation is not directly applicable because the hypothesis (second-order stationarity)on which it is founded falls down. An alternative strategy is individuated to apply the kriging, to make this type of interpolation proper for DInSAR data. Observing that the strong deformations, differently from the atmospheric delay and the spatial correlated deformations, present a deterministic trend, it is not necessary to describe them in a stochastic way, thus they have not be considered in the definition of the spatial structure of the data. To obtain this task an innovative way to obtain the experimental variogram was proposed, based on the computation of the so called median variogram, computed respect to the variograms obtained for subareas of an entire interferogram. The localized strong deformation is treated as an outlier with respect to the spatial correlated phenomena (atmosphere and deformations) and the median variogram allows to filter it out from the stochastic representation. The median variogram represents the spatial structure only of the stochastic part of the interferometric phase, due to the atmosphere and to not localized deformations. The information relative to the localized deformation is not loosen, but it is accounted for in the prediction in a deterministic way directly by the observations. The proposed method of the median variogram is good solution to execute an interpolation of a whole stack of interferograms, with interferograms characterized by different features. The procedure was applied to a test data set constituted by 108 interferograms relative to L'Aquila area, where 15 are co-seismic. The effectiveness of the kriging interpolation allowed to obtain an increment of the coherent points of the stack approximately equal to 38%. Therefore, the kriging interpolation, realized with the innovative strategy of the median variogram, is an effective tool to interpolate a whole stack of interferograms, constituted by a large number of interferograms with different features, which represents the normal situation in a DInSAR analysis, without caring about the possible intervention of strong and localized deformations. The interpolation procedure achieves a significant increment of the coherent points, and this represents an important improving of the technique, especially for areas where there are not conditions favorable for radar analysis. The possibility to have a bigger number of coherent points improve the possibility to apply particular DInSAR algorithms, for example unwrapping algorithms, but also the possibility to obtain a better estimation

of the velocity field that can be interpreted in a more useful way. The proposed procedure presents also important future developments. The technique, in fact, can be applied also to temporal series of deformation. The possibility to estimate through the interpolation the components of the interferometric phase due to the atmospheric delay and to the spatially correlated deformation, could permit to remove them from the phase. This opens the opportunity or further improvements of the resolution for deformation analysis and to obtain the displacements relative to quite localized areas (for example single buildings).

References

Bamler, R. and Hartl, P., 1998. Synthetic aperture radar interferometry. Inverse problem 14, pp. R1–R54.

Berardino, P., Fornaro, G., Lanari, R. and Sansosti, E., 2002a. A new algorithm for surface deformation monitoring based on small baseline differential sar interferograms. IEEE Transactions on Geoscience and Remote Sensing 40, pp. 2375–2383.

Berardino, P., Fornaro, G., Lanari, R. and Sansosti, E., 2002b. A new algorithm for surface deformation monitoring based on small baseline differential sar interferograms. IEEE Transactions on Geosciences and Remote Sensing 40, pp. 2375–2383.

Biescas, E., Crosetto, M. and Monserrat, O., 2007. Two radar interferometric approaches to monitor slow and fast land deformation. Journal of Surveying Engineering 133, pp. 67–71.

Costantini, M., 1998. A novel phase unwrapping metods based on network programming. IEEE Transaction on Geoscience and Remote Sensing 36, pp. 813–821.

Cressie, N., 1985. Fitting variogram models by weighted least squares. Mathematical geology 17, pp. 563–586.

Eriksson, M. and Siska, P. P., 2000. Understanding anisotropy computation. Mathematical geology 93, pp. 683–700.

Ferretti, A., Prati, C. and Rocca, F., 2001. Permanent scatterers in sar interferometry. IEEE Transactions on Geoscience and Remote Sensing 39, pp. 8–20.

Gabriel, A. K., Goldstein, R. M. and Zebker, H. A., 1989. Mapping small elevation changes over large areas: Differential interferometry. Journal of Geophysical Research 94, pp. 9183–9191.

Gudmundsson, S., Sigmundson, F. and Carstensen, J. M., 2002. Three-dimensional surface motion maps estimated from combined interferometric synthetic aperture radar and gps data. Journal of Geophysical Research 107, pp. 2250–2264.

Monti Guarnieri, A. and Prati, C., 1997. Sar interferometry: a ”quick and dirty” coherence estimator for data browsing. IEEE Transactions on Geoscience and Remote Sensing 35, pp. 660–669.

Pepe, A. and Lanari, R., 2006. On the extension of the minimum cost flow algorithm for phase unwrapping of multitemporal sar interferograms. IEEE Transaction on Geoscience and Remote Sensing 44, pp. 2374–2383.

Wackernagel, H., 1995. Multivariate geostatistic. Springer-Verlag, Berlin.

Williams, S., Bock, Y. and Fang, P., 1998. Integrated satellite interferometry: tropospheric noise, gps estimates and implications for interferometric synthetic aperture radar products. Journal of Geophysical Research 103, pp. 27051–27067.

Zebker, H. H. and Villasenor, J., 1992. Decorrelation in interferometric radar echoes. IEEE Transactions on Geosciences and Remote Sensing 30, pp. 950–959.

KRIGING ITERATIVO PER L'INTERPOLAZIONE DEI DATI: APPLICAZIONI PER LA COSTRUZIONE DEL DTM

A. Errico

Università degli Studi di Napoli Parthenope, Centro Direzionali, Isola C4, Napoli, Italia
angela.errico@uniparthenope.it

KEY WORDS: Interpolazione, Geostatistica, Kriging Iterativo

ABSTRACT:

In questo studio si vuole realizzare un metodo iterativo (Kriging Iterativo) per le superfici di interpolazione per la costruzione dei modelli digitali del terreno (DTM). In particolare, nella prima parte di questo studio, sono create le mappe raster di altitudine mediante interpolatori deterministici e stocastici (come IDW, Kriging) utilizzando software GIS; una cartografia vettoriale in scala 1:5000 della Regione Campania è utilizzata per ottenere un dataset dei punti di campionamento. Il confronto della metodologia di interpolazione Kriging conferma il migliore interpolatore per il set di dati forniti. Nella seconda parte della tesi, lo scopo della ricerca è stato quello di dimostrare la possibilità di implementare un metodo iterativo per la redistribuzione dei residui ottenuti sulla quota lungo Z. I risultati mostrano che i residui migliorano più dell' 88% fino a 11 iterazioni, e il 95% per 100 iterazioni.

1. INTRODUZIONE

L'interpolazione viene impiegata quando si vuole ottenere una rappresentazione continua di un fenomeno, il cui andamento globale, su tutta l'area di studio, viene analizzato a partire da un insieme finito di punti.
La prima parte di questo lavoro affronta le problematiche della Geostatistica: tale disciplina nacque grazie al contributo di molte scienze (Matematica, Statistica, Ingegneria mineraria, Geologia,...), per far fronte ad esigenze di forte impatto come le stime degli standard di produzione nelle miniere di diamanti in Sudafrica e la valutazione dell'impatto di alcuni inquinanti sull'equilibrio ambientale.
Oggetto dello studio è stata la morfologia del territorio relativo alla zona del Comune di Rocca d'Evandro, in provincia di Caserta, partendo dall'elemento 403152 della cartografia vettoriale della Regione Campania in scala 1:5000. Da questo, con il software ArcGis 9.3, sono stati selezionati i layers relativi alle curve di livello e ai punti quotati; da essi è stato estratto un numero finito di punti quotati, e importati nel software Surfer 8.
La ricerca si propone, come primo step, alcune applicazioni per la ricostruzione della superficie tridimensionale del terreno attraverso l'uso di interpolatori differenti: in particolare si analizzano i dodici metodi di interpolazioni del software Surfer 8, i quali hanno consentito la costruzione di mappe numeriche (raster) della quota.
In seguito si approfondiscono le caratteristiche del metodo di interpolazione impiegato in Geostatistica: il Kriging. Il vantaggio della modellizzazione geostatistica mediante Kriging è costituito dal fatto che esso tiene in considerazione alcune componenti solitamente non considerate nella statistica classica, come il trend spaziale e la correlazione nello spazio.
La seconda parte della tesi ha lo scopo di costruire i Modelli Digitali del Terreno mediante l'implementazione sperimentale di un metodo iterativo capace di ridistribuire i residui sulla Z, derivanti dalle interpolazioni, al fine di ottenere un DTM, inteso come la somma tra le distribuzioni dei residui sulle corrispondenti superfici interpolanti e il DTM ricavato mediante la prima interpolazione. Il fine è quello di migliorare la rappresentazione 3D del terreno (sia in termini grafici che di accuratezza), integrando l'uso di software per la gestione dei dati territoriali (GIS) con quello per l'elaborazione di algoritmi matematici (MATLAB). In particolare, in ambiente MATLAB, richiamando le applicazioni del Surfer 8, sono stati costituiti i modelli col Kriging iterativamente implementato per raffinare i precedenti modelli stocastici. Questo processo è continuato fino a quando i criteri di convergenza sono stati soddisfatti.
Dal dataset iniziale è stato estratto un numero di punti quotati (distribuiti quanto più uniformemente possibile, e mediante un tool di ArcGis) pari al 5% dell'insieme campione, e non utilizzato per la creazione dei DTM; successivamente sono stati analizzati i valori statistici (massimo, minimo, media, media assoluta, deviazione standard) anche per tali punti, verificando il riscontro e la validità sull'implementazione del metodo.

2. L'INTERPOLAZIONE

2.1 Overview: Geostatistica

La Geostatistica può intendersi come una branca della Statistica, cioè si basa su un approccio statistico e probabilistico per quantificare l'interdipendenza spaziale fra i campioni e quindi utilizzare tale informazione per le fasi successive di interpolazione, e di analisi della accuratezza della stima.
Ma in che senso approccio statistico e probabilistico insieme?
La Geostatistica si avvale della Teoria delle variabili regionalizzate che si riassume come segue:
un fenomeno si dice "regionalizzato" quando questo è un fenomeno naturale, che si concretizza nello spazio e nel tempo, manifestando un determinato comportamento. Le variabili che determinano questo fenomeno vengono individuate come delle variabili a scala regionale. Tali variabili si intendono come una funzione spaziale, il cui valore varia da un sito all'altro con un certo andamento continuo nello spazio, senza che sia possibile rappresentarne completamente i cambiamenti mediante una relazione analitica.
Infatti se da un lato, una variabile regionalizzata sembrerebbe una variabile puramente deterministica, poiché, secondo definizione è una funzione matematica che assume in ogni punto dello spazio un determinato valore numerico, dall'altro, se si osserva l'andamento di un tale fenomeno lungo una determinata direzione, si può notare irregolarità alla piccola scala, ma tuttavia una variabilità "strutturata" che ubbidisce a delle regole. In altri termini, quando un attributo non è distribuito omogeneamente sull'area o il volume in esame, ma varia in maniera continua, si dice che è "dipendente spazialmente " (o "correlato spazialmente" o "strutturato

spazialmente") cioè che mostra una variazione spaziale di componenti sia deterministiche che casuali.
Se i punti campione sono distribuiti uniformemente e indipendentemente tra loro su un'area d'interesse, allora l'approccio più semplice per il fitting dei dati, è quello di trattare la variabile regionalizzata come deterministica e le posizioni dei campioni come causali. Ma quando queste sono disposti secondo un reticolato sistematico, e quindi tra i punti vi è dipendenza, allora la Geostatistica associa la casualità con la variabile regionalizzata stessa, usando un modello stocastico, in cui la variabile regionalizzata è considerata come una realizzazione di una funzione random.
È chiaro che il modello non corrisponde alla realtà, in quanto la probabilità non esiste in Natura, ma solo nei modelli, e questo non significa che si scelgono i modelli stocastici perché si assume che la Natura sia casuale, ma semplicemente perché i modelli, limitati a rappresentare la realtà solo in determinati punti campioni, sono analiticamente utili.

2.2 Dati utilizzati: Campionamento

Considerando come variabile, la quota z dei punti, la tesi si propone la costruzione di carte georeferenziate, dove si mostra l'andamento della quota, a partire dai valori della variabile misurati all'interno dell'area di interesse, e osservare i valori relativi ai punti circostanti per capire se esiste continuità, o variazione simile in tutte le direzioni.
Come prima fase per la mappatura geostatistica, designiamo il campionamento per l'elaborazione dei dati:
oggetto dello studio è stata la morfologia del territorio relativo alla zona del Comune di Rocca d'Evandro, in provincia di Caserta, partendo dall'elemento 403152 della cartografia vettoriale della Regione Campania in scala 1:5000. Da questo, con il software ArcGis 9.3, sono stati selezionati i layers relativi alle curve di livello e ai punti quotati; da essi è stato estratto un numero finito di punti quotati, e importati nel software Surfer 8.

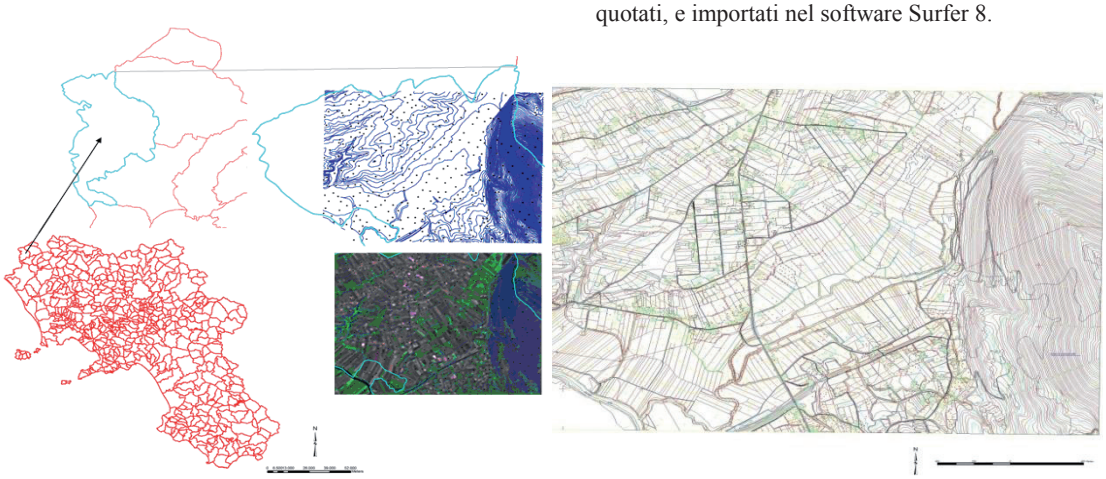

Figura 1: Inquadramento territoriale e elemento 403152 della cartografia vettoriale della Regione Campania in scala 1:5000

Dopodiché si passa ad analizzare i dati in laboratorio, stimare il modello, implementare questo e valutarne le prestazioni, produrre e distribuire la geo-informazione dell'output.
Tuttavia, queste analisi si sviluppano su domande del tipo: come fa una variabile a variare nello spazio?; cosa controlla la sua variazione nello spazio?; qual è un valore di una variabile a una certa nuova posizione?; qual è l'incertezza della stima?.
L'indagine che abbiamo condotto è basata sull'Analisi Esplorativa dei Dati (EDA), in cui, a differenza dell'approccio classico che adotta un modello (deterministico o probabilistico) a priori, la raccolta dei dati viene seguita immediatamente dall'analisi dei dati stessi, e non viene adottato alcun modello a priori: anzi l'obiettivo è proprio quello di determinate quale modello sia migliore per descrivere i caratteri strutturali dei dati.
Le tecniche caratteristiche dell'EDA sono principalmente di tipo grafico, e rappresentano i dati nella loro forma grezza, come mostrato nell'Istogramma e nel Box Plot per i dati qui utilizzati.
Istogramma: lo strumento Istogramma diagramma la distribuzione dell'attributo z, con l'intervallo di valori separato in 10 classi. La proporzione relativa dei dati, cioè la densità dei dati in ogni classe è rappresentata dall'altezza di ogni barra. Si nota che i dati non sono simmetrici, e la distribuzione non normale. La coda destra (quote elevate) della distribuzione indica la presenza di un numero relativamente piccolo di punti campione, rispetto alla coda sinistra.

Box Plot: il Box Plot, oltre a confermare la distribuzione dei dati più frequenti in corrispondenza delle basse quote, permette di verificare se esistono valori di outlier cioè quei valori molto lontano dalla media che ricadono prima del 5° percentile o dopo 95° percentile. Nel boxplot si nota che nessun punto è graficato oltre il 95° (linea orizzontale più in alto) percentile né oltre il 5° (linea orizzontale più in basso), quindi non ci sono evidenze di outliers.
La tecnologia GIS è utilizzata da circa 30 anni, ma solo negli ultimi 5 anni, in Italia si è assistito ad un vero e proprio boom dei Sistemi Informativi Geografici, approfondendo così la conoscenza delle tecniche e dei processi di analisi spaziale volta non solo alla generazione di mappe, ma anche a produrre soluzioni nei più svariati campi di applicazione e a fornire supporto alle decisioni con un livello di sicurezza il più elevato possibile.
ArcGIS 9.3, rende disponibile le operazioni di analisi spaziale nei vari ambienti di accesso alle funzionalità di Geoprocessing. Con Geostatistical Analyst, è possibile creare una superficie continua, o una mappa, da punti campione misurati memorizzati in un layer di features puntiformi, in un layer raster oppure usando centroidi di poligoni. I punti campione possono essere delle misure, come l'elevazione, la profondità, la temperatura, ecc. Con le funzioni di MapAlgebra, ArcMap, il Geostatistical Analyst (e da questo la funzione Geostastistical Wizard) fornisce gli strumenti per creare superfici che possono essere usate per visualizzare, analizzare e comprendere i fenomeni spaziali. In questo studio il software è stato ampiamente utilizzato.

Il Software ArcGIS 9.3 è stato utilissimo nell'analisi spaziale esplorativa dei dati, come dimostrano le valutazioni di ESDA esposte in seguito.
L'analisi spaziale esplorativa dei dati è stata effettuata anche mediante altri strumenti in ambiente GIS, come il QQplot e il Trend analysis.
QQplot: il QQPlot permette di paragonare la distribuzione dei dati ad una distribuzione normale standard, ottenendo un'altra misura della normalità dei dati: più i punti si dispongono in linea retta, più la distribuzione è prossima ad una normale.
Trend Analysis: lo strumento Trend Analysis, mostrato in figura, permette di identificare la presenza o l'assenza di tendenze nel dataset di input. La tendenza rappresenta la componente non casuale (deterministica) della superficie che può essere rappresentata da alcune formule matematiche.

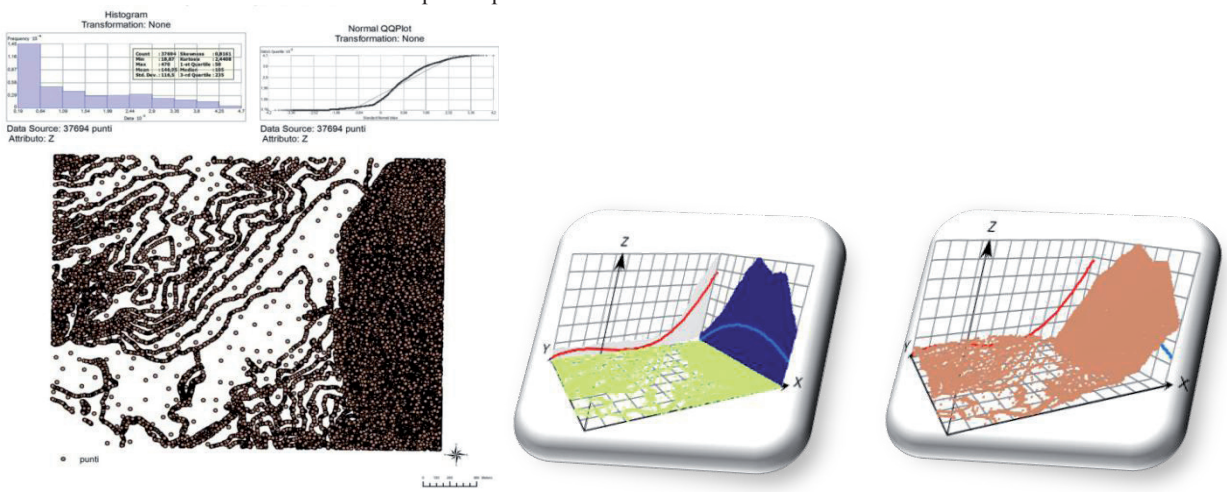

Figura 2: Mappa dei punti campione e Analisi Spaziale Esplorativa dei Dati: Istogramma, Normal QQPlot, Analisi del trend (ArcGis 9.3 ESRI)

Nella tesi si indaga sulle relazioni esistenti nei dati per identificare il migliore strumento di interpolazione spaziale da utilizzare. Una prima indagine viene compiuta per accertare l'esistenza di "drift" e di "trend".
Ricordiamo che non abbiamo covariate (disponiamo solamente della quota e delle coordinate senza alcuna ulteriore variabile esplicativa come nel caso delle variabili ambientali - temperatura, pioggia, ecc.). Si studia qui solo la presenza del trend intesa nel caso studio come la dipendenza della quota con le coordinate (ammettendo che non si cerca nessuna giustificazione fisica per tale dipendenza, ma si vuole solo quantificare eventualmente il legame che di fatto può esistere tra quota e coordinate del nostro dataset).

2.3 Modelli di predizione spaziale

Oggetto di studio sono stati i dodici algoritmi di interpolazione usati dal Software Surfer 8, risultando che le metodologie deterministiche non rappresentano in modo completo il reale meccanismo responsabile della distribuzione spaziale di una variabile, limitandosi a modellizzare soltanto la variabilità intrinseca del sistema, con vincoli matematici. In tutta l'attività di ricerca sono stati considerati dodici metodi di interpolazione: Media pesata (Inverse Distance Weighed), Kriging, Minima curvatura, Metodo Modified Shepard, Prossimo naturale (Natural Neighbor), Prossimo più vicino (Nearest Neighbor), Regressione Polinomiale, Radial Basis Function, Triangolazione con interpolazione lineare, Polinomio locale, Data metrics methods, Media Mobile. Per ragioni si sintesi si approfondiscono solo i due metodi, deterministico e stocastico.

2.3.1 Media pesata (Inverse Distance Weighted or Inverse Distance to a Power)

Il metodo della Media pesata si avvale di un interpolatore della media pesata, che può essere sia esatto che smoothing. Con l'IDW, i dati sono pesati durante l'interpolazione, cosicché l'influenza di un punto, relativo a un altro, diminuisce al crescere della distanza dal nodo del grid, per cui è rispettato il principio di Tobler secondo cui i punti più prossimi influenzano in misura maggiore il risultato rispetto a quelli più lontani. Il peso è assegnato attraverso l'uso di una potenza, che controlla come il fattore peso decresce al crescere della distanza dal nodo del grid. Quando la potenza aumenta, il valore del nodo del grid si avvicina al valore del punto più vicino. Per una potenza più piccola, i pesi sono più uniformemente distribuiti tra i punti vicini.
Normalmente, la Distanza Inversa a una Potenza si comporta come un interpolatore esatto. Quando si calcola un nodo del grid, i pesi assegnati ai punti sono frazioni, la somma di tutti i pesi è uguale a 1,0. Quando un'osservazione particolare è coincidente con un nodo del grid, la distanza tra quella osservazione e il nodo del grid è 0,0 per cui, a quella osservazione è dato un peso di 1,0; a tutte le altre osservazioni si danno pesi di 0,0. Quindi, al nodo del grid è assegnato il valore della coincidente osservazione. Il parametro di smoothing (lisciatura) è un meccanismo per "raggirare" questo comportamento. Quando si assegna un parametro non-zero di smoothing, a nessun punto è dato un peso schiacciante, il che significa che a nessun punto è dato un fattore peso uguale a 1,0. Una delle caratteristiche dell' IDW è la generazione di "occhi di bue" (bull's-eyes) nei dintorni della posizione dell'osservazione entro l'area del grid. Un parametro di smoothing può essere assegnato durante il metodo IDW per ridurre l'effetto "bull's-eye" mediante smoothing del grid interpolato.
Mediante l'interpolazione IDW la quota in corrispondenza di ciascun nodo del grid è calcolata mediante la seguente formula:

$$Q_{i,j} = \frac{\sum_k \left(\frac{q_k}{d_{i,j}} \right)}{\sum_k \left(\frac{1}{d_{i,j}} \right)} \qquad [1]$$

dove:

$i = 1,...,m; \quad j = 1,...,n; \quad k = 1,...,p;$

$Q_{i,j} = quota \ \ calcolata \ \ per \ \ l'elemento \ \ del \ \ grid \ \ alla \ \ posizione \ \ (i,j);$

$\sum = sommatoria \ \ estesa \ \ ai \ \ punti \ \ quotati \ \ prossimi \ \ alla \ \ posizione \ \ (i,j);$

$q_k = quota \ \ punto \ \ k-esimo, \ \ appartenente \ \ ai \ \ prossimi \ \ considerati;$

$d_{i,j} = dist. \ \ del \ \ punto \ \ i,j \ \ dal \ \ punto \ \ k-esimo.$

L'elemento k-esimo è il punto in cui è nota l'altezza; il peso attribuito a ciascun valore q è dall'inverso della distanza dello stesso punto k-esimo dal nodo del grigliato in cui si vuole stabilire quanto vale Q.

2.3.2 Kriging

Il Kriging è un metodo geostatistico che produce mappe visivamente soddisfacenti da dati spaziati irregolarmente. Il Kriging cerca di esprimere i trend indicati nei dati dell'utente, cosicché, per esempio, i punti alti possono essere connessi lungo una cima piuttosto che contorni isolati tipici dell'effetto "occhio di bue" dell'IDW. Il Kriging è un metodo molto flessibile; è stimato per produrre un accurato grid dei dati; può essere adattato al dataset, specificando l'appropriato modello di variogramma. In Surfer, il Kriging può essere sia un interpolatore esatto che smoothing, secondo i parametri

Ordirary Kriging:
Qui le previsioni si basano sul modello:

$$Z(s) = \mu + \varepsilon'(s) \qquad [2]$$

dove μ è la funzione costante stazionaria (media globale) e $\varepsilon'(s)$ è la parte stocastica di variazione correlata spazialmente.
È intuitivo pensare che ci dovrebbe essere un modo per stimare i pesi in modo obiettivo, cioè in modo che i pesi riflettono la vera struttura di autocorrelazione spaziale. L'analisi esplorativa si occupa di questa analisi, in modo da descrivere quanto una misura influenzi le misure vicine mediante lo studio del variogramma, utilizzando le semivarianze:

$$\gamma(h) = \frac{1}{(2m(h))} \sum_{i=1}^{m(h)} \left(Z(s_i + h) - Z(s_i) \right)^2 \qquad [3]$$

dove $z(s_i)$ è il valore della variabile target ad una posizione campione e $z(s_i + h)$ è il valore della vicina alla distanza $(s_i + h)$. Si veda il grafico coi parametri fondamentali.
In linea di principio, le ipotesi di kriging sono che la variabile è stazionaria e che ha una distribuzione normale, cosa difficile da verificarsi nella pratica. Il Regression-Kriging non prevede questa ipotesi!
Regression-Kriging:
Generalizziamo il concetto di Kriging mediante una assunzione di Matheron (1969) secondo cui il valore di una variabile a una certa posizione può essere modellata come una somma degli elementi deterministici e stocastici, e che tali componenti possono essere modellate separatamente. specificati dall'utente. Esso incorpora medie (trend) anisotrope e sottostanti in modo naturale ed efficiente.
L'elemento cardine è il semivariogramma, che esprime le differenze spaziali e quantitative di tutte le possibili coppie di punti misurati come una funzione della distanza tra i punti stessi.
Poiché nella fase di interpolazione il metodo prevede che i valori di semivarianza siano calcolati per qualunque distanza h, al variogramma sperimentale viene adattato un modello teorico matematico, caratterizzato da due parametri: range e sill. Il primo è la distanza entro la quale le coppie di valori della grandezza in esame sono spazialmente correlate; il secondo è il valore di semivarianza corrispondente al range.
Per la scelta dell'adattamento ottimale si utilizza la cross-validation: si rimuove temporaneamente uno dei valori misurati alla volta e se ne effettua una stima basandosi sui rimanenti valori misurati. La differenza tra valore stimato e valore misurato, detta errore sperimentale di stima, deve essere il più possibile prossima a zero. Per determinare i valori nei punti non campionati vengono proposte differenti soluzioni, così da caratterizzare differenti metodi di Kriging (Govaerts, 1997).
A seconda dell'ipotesi che si sceglie per il trend, si possono distinguere tre metodi di Kriging:
Simple Kriging, se si suppone che la media sia nota;
Ordinary Kriging, se come ipotesi la media è ignota e costante;
Universal Kriging, se si suppone che la media sia ignota e non costante, ma intesa come combinazione lineare di funzioni note (generalmente si scelgono funzioni polinomiali), per cui i parametri ignoti sono da stimare con qualche metodo parametrico.
Combinando i due approcci si ottiene un modello universale della variazione spaziale:

$$\hat{z}(s_0) = \hat{m}(s_0) + \hat{e}(s_0) = \sum_{k=0}^{p} \hat{\beta}_k \cdot q_k(s_0) + \sum_{i=1}^{n} \lambda_i \cdot e(s_i) \qquad [4]$$

dove

$\hat{m}(s_0)$ è la parte deterministica,

$\hat{e}(s_0)$ è il residuo interpolato,

$\hat{\beta}_k$ sono i coefficienti stimati del modello deterministico,

λ_i sono pesi del Kriging determinati dalla struttura di dipendenza spaziale del residuo,

$e(s_i)$ è il residuo alla posizione s_i.

I coefficienti di regressione $\hat{\beta}_k$ possono essere stimati dal campionamento con un metodo di fitting, utilizzando Generalized Least Squares. Una volta che la parte deterministica di variazione è stata stimata, il residuo può essere interpolato con il Kriging e aggiunta al trend stimato.
Di seguito la tabella ottenuta per il Regression-Kriging.
L'RK ha il vantaggio che separa in modo esplicito la stima della tendenza dalla previsione spaziale dei residui, permettendo l'uso di forme arbitrariamente complesse di regressione.

3. LA METODOLOGIA: KRIGING ITERATIVO

L'idea di attuare un processo iterativo (prima manuale, in seguito automatizzato mediante il supporto fornitomi dal settore informatico-geomatico) nasce dall'analisi sui residui della prima interpolazione e dalla considerazione di come questi si possano distribuire secondo un numero di iterazioni sufficientemente accettabili.

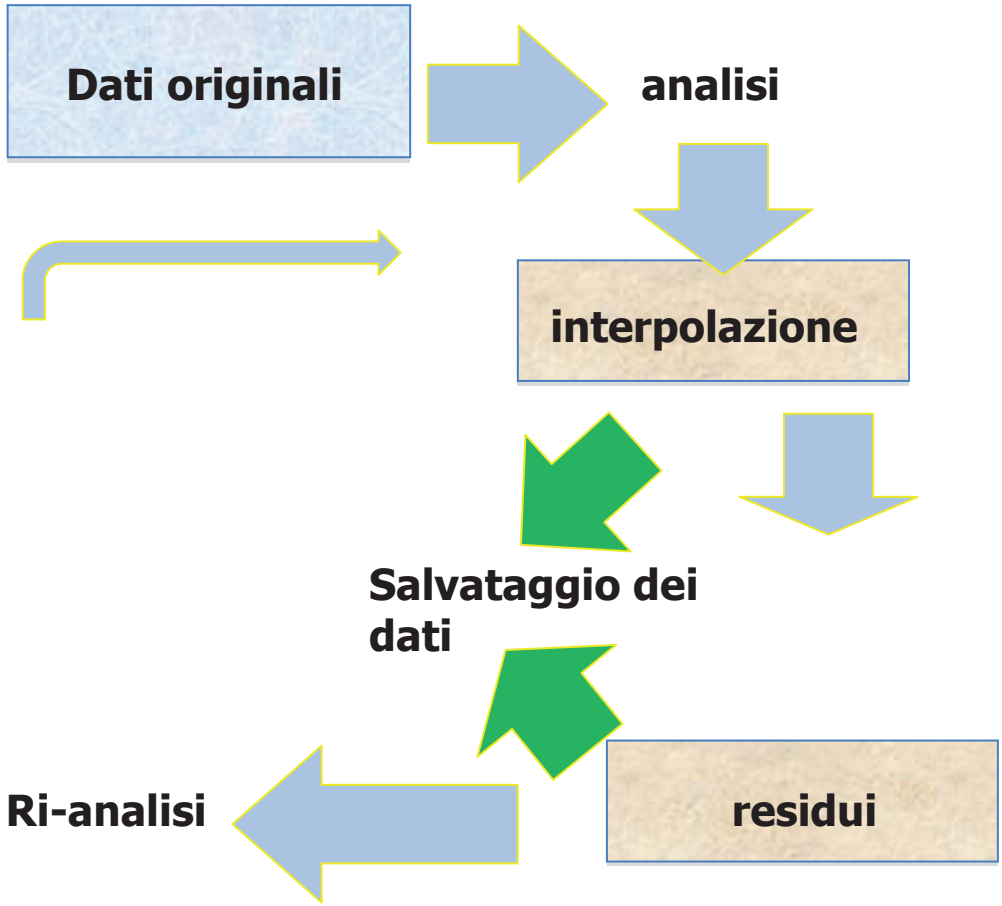

Figura 3: Iterazione e Ridistribuzione dei residui

Il processo prevede la fase iniziale di raccolta dei dati, poi l'analisi esplorativa spaziale dei dati; l'implementazione del metodo di interpolazione, il salvataggio del Grid; vengono calcolati i residui e salvati nel database; si ripete l'analisi spaziale al fine di individuare ancora il metodo di interpolazione da usare, iterando in fine la metodologia.

3.1 Software utilizzati e implementazione del metodo sperimentale

Di seguito si riportano i vantaggi/svantaggi riscontrati nell'impiego dell'ArcGis 9.3, Surfer 8, Matlab 7.9.0.
In ArcGIS si sono riscontrati alcuni inconvenienti nell'applicazione delle metodologie di interpolazione, come il Kriging, che insieme a ulteriori considerazioni hanno portato alle seguenti conclusioni:

1. difficoltà nel convertire vector in raster: nel processo iterativo sperimentale la combinazione dei file vettoriali, puntuali e raster ha aumentato la complessità dell'elaborazioni, e di conseguenza, per l'enorme dataset (piuttosto irregolare), ha reso a volte indisponibile la capacità di trasformare i punti in raster (o meglio, nei centroidi corrispondenti);
2. molti parametri e le scelte degli utenti: il Kriging dell'ArcGIS fa leva su metodi di interpolazione ad hoc che implicano una serie di parametri e le scelte degli utenti per fare il fitting dei dati. Il grado di smoothness o levigatezza della superficie stimata nell'approccio Kriging introduce ulteriore complessità con un piccolo cambiamento nella capacità di adattare la superficie;
3. Mancanza di trasparenza: il codice di base di cui è fatto il Kriging in ArcGIS non è accessibile (o almeno non ancora è stato trovato un modo per intervenire sui codici), e può richiedere un certo sforzo per capire esattamente cosa è stato fatto sulla base della documentazione. A volte tale documentazione online è limitata nei dettagli tecnici.

Il Software Surfer è utilizzato per effettuare: modellazione del terreno, visualizzazione del paesaggio, analisi della superficie, reticolato, volumetrico, generazione di mappe 2D e molto altro. Le dodici possibili metodologie di interpolazione estremamente sofisticate rivestono Surfer di un ruolo fondamentale per questa tesi: cioè è stato possibile trasformare i dati X, Y, Z in mappe di alta qualità. Il potente foglio di lavoro ed la capacità d'importazione hanno reso relativamente più facile l'acquisizione dei dati, e la loro visualizzazione.
Si mostrano le tabelle delle interpolazioni e della cross-validation per la costruzione del DTM a 35m.

Metodo di interpolazione	Tempo impiegato da Surfer (sec)	DZ Medio (m)	DZ Minino (m)	DZ Massimo (m)	Dev. St. (m)
IDW	1,54	0,922929644584	-8,216626830131	8,486570117958	1,070995899969
Kriging	12,1	0,795176151428	-9,034272428336	7,261731371772	0,971580351281
	187,7	0,618510334268	-8,656061618326	6,306154455654	0,851299280064
	494,4	0,618512329282	-8,656061134548	6,306154356452	0,851297639496
Minima curvatura	0,12	0,988552717400	-16,452887592647	24,434978353781	1,062825791491
Modified Shepard	1,57	0,703498093052	-10,558071905654	46,072939943855	1,193155788421
Natural Neighbor	1,26	0,616749548469	-7,924678591357	6,452208126097	0,855324279685
Nearest Neighbor	0,10	0,951694020647	-9,340924189486	7,575723572876	1,025700183832
Regressione Polinomiale	0,04	73,33694193331	-164,720486029129	244,774434954382	45,688580652389
	0,04	50,52517317871	-220,274735115787	159,053439213085	36,786984995655
	0,04	73,26290533710	-174,807055556878	243,447442587790	46,074123814217
RBF	127,8	0,626778982102	-10,515475927110	10,204591598269	0,892157272771
Triang. interp. lin.	0,42	0,632840314998	-8,531271956378	6,432289482653	0,871160119708
Polinomio locale	2,21	0,688262300795	-8,705683809671	8,098681455276	0,850141584518
Data metrics	1,60	1,497901129392	-10,706131306296	10,570977747992	1,591389347955
Media Mobile	1,99	82,05462624437	-144,287583916717	297,083548291804	60,526390739889

Tabella 1: Analisi statistica (media, minimo, massimo, deviazione standard) relativa alle differenze tra quote calcolate e quote iniziali nei punti del data set iniziale con un Processore Intel(R) Core(TM)2 duo CPU T9400, 2,53 GHz, e memoria 4,00 GB.

Metodo di interpolazione	ΔZ Medio (m)	ΔZ Minino (m)	ΔZ Massimo (m)	Dev. St. (m)
IDW	0,664224402390	-9,423255332895	9,146831358920	0,845617663790
Kriging	0,166141489567	-9,343325777440	4,686525351046	0,337354874436
	0,166108353832	-9,343325613865	4,686525270102	0,337342858224
	0,166104406687	-9,343325427143	4,686525190444	0,337341813065
Minima curvatura	-	-	-	-
Modified Shepard	-	-	-	-
Natural Neighbor	-	-	-	-
Nearest Neighbor	0,892824194529	-9,569972992000	5,000000000000	1,901670975132
Regressione Polinomiale	73,336941933311	-244,774434954380	164,720486029130	45,688580652389
	50,524503330569	-159,063258147260	220,268441896860	36,787861828826
	73,262905327156	-243,447442556400	174,807055785860	46,074123829637
RBF	0,140629203557	-26,351859880495	40,195420719444	0,535947500783
Triang. interp. lin.	0,173016218147	-54,690395616904	17,861029187982	0,543922996017
Polinomio locale	0,487380054729	-11,630285016813	7,781411681344	0,618040740947
Data metrics	-	-	-	-
Media Mobile	82,060675696963	-297,042101409380	144,390907933450	60,530133020119

Tabella 2: Analisi statistica (media, minimo, massimo, deviazione standard) relativa ai residui ottenuti con la cross-validation.

Gli inconvenienti riscontrati sono:

1. L'iterazione della metodologia di interpolazione dei residui è manuale;
2. Sussiste una notevole difficoltà nel gestire l'elevato numero di colonne del foglio di lavoro

Il software MATLAB, creato alla fine degli anni '70 alla New Mexico University da Chris Molen ed altri, ebbe lo scopo iniziale di fornire un ausilio ai corsi di algebra lineare e di calcolo numerico per studenti senza conoscenze di programmazione, integrando gradatamente librerie già disponibili allora. Nel 1984 iniziò la commercializzazione da parte di Mathworks, evolvendosi successivamente come strumento completo di supporto alla ricerca scientifica ed allo sviluppo di applicazioni ad elevato contenuto scientifico.
Relativamente all'interpolazione, il Software MATLAB, in generale, analizza il fitting dei dati, ponendosi l'obiettivo di adattare un generico modello matematico a dei dati sperimentali. Tramite il modello è possibile ricostruire dati mancanti (interpolazione), stabilire delle tendenze (trend analysis), fare previsioni (estrapolazione), fornendo grande ausilio per affrontare l'analisi statistica dei dati attraverso diverse funzioni specifiche. Molte considerazioni durante lo svolgimento e l'applicazione delle tematiche sperimentali in questa tesi hanno condotto a numerosi vantaggi nell'uso di questo programma:

1. si possono importare in MATLAB dati in qualunque formato e da qualunque piattaforma, ed esistono librerie per compiere qualunque tipo di analisi sui dati;
2. è possibile controllare in maniera totale la formattazione e qualunque elemento visivo, seguendo una modellizzazione dinamica, e costruendo modelli dell'interazione di sistemi dinamici complessi e verificarli su dati sperimentali;
3. il MATLAB contiene un numero enorme di funzioni pronte per l'uso, organizzate in toolbox tematici e perfettamente commentate, il sito di Mathworks è ricchissimo di esempi ed applicazioni pronte per l'uso e sono disponibili in rete risorse di pubblico dominio che estendono ulteriormente questo insieme a specifici problemi applicativi.

La possibilità di creare script .m apportando possibili modifiche a valle dell'esecuzione, la disponibilità on line di documentarsi ampiamente sulle tematiche oggetto di studio, e la capacità del programma di richiamare le funzionalità, nonché l'operatività del Software Surfer, hanno permesso l'implementazione di codici intenti all'iterazione delle metodologie d'interpolazione mediante la ridistribuzione dei residui, cioè la tesi ha lo scopo di costruire i Modelli Digitali del Terreno mediante l'implementazione sperimentale di un metodo iterativo capace di ridistribuire i residui sulla Z, ottenuti dalle interpolazioni, al fine di ottenere un DTM, inteso come la somma tra le distribuzioni dei residui sulle corrispondenti superfici interpolanti e il DTM ottenuto mediante la prima interpolazione.

Il fine è quello di migliorare la rappresentazione 3D del terreno (sia in termini grafici che di accuratezza), integrando l'uso di software per la gestione dei dati territoriali (GIS) con quello per l'elaborazione di algoritmi matematici (MATLAB). In particolare, in ambiente MATLAB, richiamando le applicazioni del Surfer 8, sono stati costituiti i modelli col Kriging iterativamente implementato per raffinare i precedenti modelli stocastici. Questo processo è continuato fino a quando i criteri di convergenza sono stati soddisfatti.
Si tabellano i risultati per il Kriging iterativo.
Nelle nuove elaborazioni ci si è spinti a creare DTM con una cella ridotta a 5m, a discapito dei tempi computazionali, ma sicuramente più adatta per il dataset a disposizione.

	Massimo (m)	Minimo (m)	Media (m)	Media sui valori assoluti dei residui (m)	Dev_Standard (m)
prima interpolazione	3,7299	-3,3814	-0,0017	0,0896	0,1980
1° iterazione	3,7840	-3,2660	-0,0007	0,0403	0,1286
2° iterazione	3,6484	-3,0193	-0,0005	0,0269	0,1076
3° iterazione	3,5329	-2,8624	-0,0004	0,0207	0,0972
4° iterazione	3,5289	-2,8263	-0,0003	0,0173	0,0911
5° iterazione	3,5251	-2,7997	-0,0003	0,0151	0,0870
6° iterazione	3,5215	-2,8930	-0,0003	0,0136	0,0840
7° iterazione	3,5181	-3,0164	-0,0002	0,0126	0,0817
8° iterazione	3,5148	-3,1213	-0,0002	0,0117	0,0798
9° iterazione	3,5116	-3,2104	-0,0002	0,0111	0,0783
10° iterazione	3,5083	-3,2860	-0,0002	0,0106	0,0769
11° iterazione	3,5051	-3,3502	-0,0002	0,0101	0,0757
…					
95° iterazione	3,2072	-3,6347	-0,0003	0,0052	0,0571
96° iterazione	3,2039	-3,6329	-0,0003	0,0051	0,0570
97° iterazione	3,2005	-3,6312	-0,0003	0,0051	0,0570
98° iterazione	3,1971	-3,6294	-0,0003	0,0051	0,0570
99° iterazione	3,1937	-3,6276	-0,0003	0,0051	0,0570

Tabella 3: Tabella dei valori di massimo, minimo, media, e deviazione standard ottenuti applicando il Regrssion-Kriging Iterativo per la creazione del DTM a 5 m, utilizzando il completo dataset a disposizione.

In linea di principio, le ipotesi di kriging sono che la variabile è stazionaria e che ha una distribuzione normale, cosa difficile da verificarsi nella pratica. Il Regression-Kriging non prevede questa ipotesi.
Regression-Kriging:
Generalizziamo il concetto di Kriging mediante una assunzione di Matheron (1969) secondo cui il valore di una variabile a una certa posizione può essere modellata come una somma degli elementi deterministici e stocastici, e che tali componenti possono essere modellate separatamente. Di seguito si mostrano i risultati ottenuti applicando il Regression-Kriging Iterativo.

	Massimo (m)	Minimo (m)	Media (m)	Media sui valori assoluti dei residui (m)	Dev_Standard (m)
prima interpolazione	3,7299	-3,3805	-0,0020	0,0890	0,1932
prima interpolazione dei residui Kriging	3,7853	-3,2574	-0,0008	0,0393	0,1230
1° iterazione	3,6499	-3,0072	-0,0005	0,0260	0,1018
2° iterazione	3,4878	-2,8622	-0,0004	0,0199	0,0913
3° iterazione	3,4435	-2,8261	-0,0003	0,0165	0,0851
4° iterazione	3,3893	-2,7995	-0,0003	0,0144	0,0809
5° iterazione	3,3281	-2,8972	-0,0002	0,0129	0,0779
6° iterazione	3,2620	-3,0208	-0,0002	0,0119	0,0756
7° iterazione	3,2096	-3,1255	-0,0002	0,0111	0,0737
8° iterazione	3,1976	-3,2143	-0,0002	0,0104	0,0721
9° iterazione	3,1799	-3,2895	-0,0001	0,0099	0,0707
10° iterazione	3,1586	-3,3532	-0,0001	0,0095	0,0695
11° iterazione	3,1351	-3,4071	-0,0001	0,0091	0,0684
…					
95° iterazione	2,0576	-3,6053	-0,0002	0,0046	0,0495
96° iterazione	2,0530	-3,6032	-0,0002	0,0046	0,0495
97° iterazione	2,0484	-3,6011	-0,0002	0,0045	0,0495
98° iterazione	2,0439	-3,5990	-0,0002	0,0045	0,0494
99° iterazione	2,0395	-3,5970	-0,0002	0,0045	0,0494

Tabella 4: Tabella dei valori di massimo, minimo, media, e deviazione standard ottenuti applicando il Regrssion-Kriging Iterativo per la creazione del DTM a 5 m, utilizzando il completo dataset a disposizione.

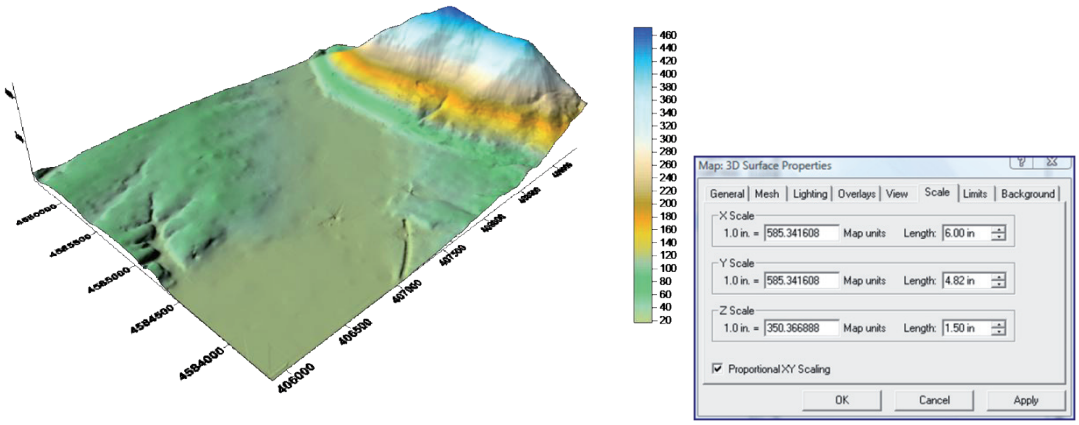

Figura 4: Grid somma di tutte le superfici interpolanti dei residui col DTM iniziale.

Anche dall'analisi dei residui risultano ancora dei trend. Ricordando che il Kriging parte da un modello stocastico della Natura, è possibile fare un'analogia (convenzionale), con la previsione del problema in serie temporale: dati dei valori,di solito disposti in regolari intervalli di tempo, predire il valore del segnale in un certo istante futuro.
Il Kriging segue un approccio simile ma in uno scenario spaziale dove non c'è nessun concetto generale di passato e di futuro.

Per questo lavoro si è preso in esame il comportamento dei due punti per i quali si è riscontrato il peggior residuo (uno nel valore massimo e l'altro nel valore minino) sin dalla prima interpolazione e si è studiato il loro comportamento durante le 100 iterazioni, di cui si riporta il grafico.
Come si comportano i residui applicando la detrendizzazione ad ogni iterazione dell'interpolazione del residuo?
Si tabellano i valori per il Kriging iterativo, ove si nota un miglioramento per i valori di deviazione standard.

Kriging iterativo sui residui preliminarmente detrendizzati	Massimo (m)	Minimo (m)	Media (m)	Media sui valori assoluti dei residui (m)	Dev_Standard (m)
prima interpolazione	3,7299	-3,3805	-0,0020	0,0890	0,1715
1° iterazione	3,7854	-3,2573	-0,0008	0,0393	0,1165
2° iterazione	3,6499	-3,0071	-0,0005	0,0260	0,0984
3° iterazione	3,4876	-2,8623	-0,0004	0,0199	0,0891
4° iterazione	3,4434	-2,8262	-0,0003	0,0165	0,0835
5° iterazione	3,3892	-2,7996	-0,0003	0,0144	0,0796

Tabella 5: Tabella dei valori di massimo, minimo, media, e deviazione standard ottenuti applicando il Kriging Iterativo sui residui preliminarmente detrendizzati per la creazione del DTM a 5 m, utilizzando il completo dataset a disposizione.

3.2 Metodo di verifica

La necessità di testare il metodo su un numero di punti uniformemente distribuiti (per quanto possibile) sull'area di interesse, ha condotto alla scelta di estrarre il 5% di punti dal dataset originale (mediante tools aggiuntivi del Software AcgGis 9.3), costruendo il modello col restante 95% e di effettuare le analisi sui punti di verifica.

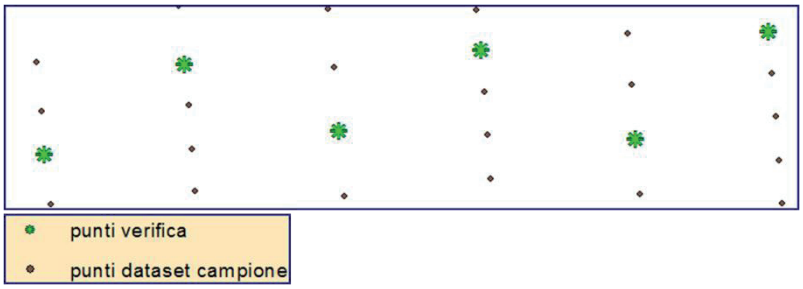

Figura 4: esempio di punti di verifica

Kriging iterativo sui residui	Massimo (m)	Minimo (m)	Media (m)	Media sui valori assoluti dei residui (m)	Dev_Standard (m)
prima interpolazione	3,7299	-3,3805	-0,0020	0,0890	0,1932
1° iterazione	3,7854	-3,2573	-0,0008	0,0393	0,1230
2° iterazione	3,6499	-3,0072	-0,0005	0,0260	0,1018
3° iterazione	3,4876	-2,8623	-0,0004	0,0199	0,0913
4° iterazione	3,4434	-2,8262	-0,0003	0,0165	0,0851
5° iterazione	3,3892	-2,7996	-0,0003	0,0144	0,0809

Tabella 6: Elaborazioni sul 95% del dataset originale

	Massimo (m)	Minimo (m)	Media (m)	Media sui valori assoluti dei residui (m)	Dev_Standard (m)
prima interpolazione	5,4246	-4,9883	-0,0155	0,3815	0,6238
1° iterazione	6,3451	-4,9132	-0,0132	0,3711	0,6125
2° iterazione	7,1488	-4,9374	-0,0117	0,3655	0,6077
3° iterazione	7,8640	-4,9653	-0,0110	0,3625	0,6059
4° iterazione	8,5080	-4,9988	-0,0107	0,3608	0,6060

Tabella 7: Elaborazioni sul 5% del dataset: punti di verifica

4 CONCLUSIONI

È emerso chiaramente, dal lavoro svolto nella prima parte della tesi, relativa alla ricostruzione di superfici tridimensionali del terreno attraverso l'uso di interpolatori deterministici e stocastici, che il metodo del Kriging ha fornito i risultati più realistici in quanto, essendo un interpolatore stocastico, ha tenuto in considerazione le variazioni casuali della variabile di input, fornendo quindi risultati in termini di probabilità, cioè risultati migliori dal punto di vista dell'errore statistico sui residui.

I nuovi modelli costituiti dai Kriging iterativamente implementati in ambiente MATLAB, nella seconda parte della ricerca, hanno dato migliori risultati. Dunque, lo studio

svolto ha raggiunto lo scopo di raffinare i precedenti modelli stocastici. Questo processo è continuato fino a quando i criteri di convergenza sono stati soddisfatti: ad un numero di iterazioni pari ad undici si può ritenere che il metodo ha prodotto un assestamento dei valori dei residui.
Il Regression-Kriging Iterativo ha ottenuto risultati non di molto variabili rispetto al Kriging Iterativo, pur ottenendo un valore di deviazione standard migliore.
Il Kriging Iterativo permette di ridistribuire i residui in maniera ottimale mantenendo il totale controllo sull'implementazione del metodo.
Inoltre il procedimento di verifica utilizzato per questa tesi, secondo cui è stato prelevato, dal dataset originale, il 5% dei punti (quanto più uniformemente possibile) costruendo il DTM senza che questi contribuissero all'interpolazione, e analizzandoli successivamente, ha prodotto risultati accettabili e in miglioramento all'aumentare del numero di iterazioni.

4.1 Sviluppi futuri

L'accuratezza riscontrata nel metodo sperimentale permette di pensare a future applicazioni come l'automatizzazione del ciclo di verifica e dell'accuratezza del risultato che si vuole raggiungere, l'applicazione del Kriging Iterativo a partire da dati più accurati, e nei processi di fitting dei dati nelle reti topografiche GPS e per la ridistribuzione dei residui dell'errore nella griglia ionosferica (GIVE in SBAS).

5 RINGRAZIAMENTI

Questo studio è stato permesso grazie all'impegno del mio Tutor, Prof. R. Santamaria, che mi ha trasmesso la passione per le Sue materie, preparandomi al mondo della Ricerca.

BIBLIOGRAFIA

A., TONINI. 2006. *Metodologie per la creazione di modelli geologici 3D sulla base di dati di superficie. Tesi di dottorato. Università degli Studi di Siena. Dipartimento di Scienze della Terra, GCT.* 2006.
A.J., DESBARATS. 1996. *"Modeling spatial variability using geostatistical simulation.".* 1996.
ADAMI A., GUERRA F. 2006. *Modelli 3d della città e del territorio: uno strumento per analisi urbane e territoriali. SIFET.* 2006.
ADLER R., TAYLOR J. 2004. *Random Fields and Stochastic Geometry.* 2004.
B., DAVIS. 1983. *Indicator Kriging as applied to an alluvial gold deposit. In M.David, A. Journel, A.Marechal, & G.Verly (Eds.), Geostatistics for natural resources characterization (Vol. 1, p. 337-348). D.Reidel Publishing Company.* 1983.
BASILE GIANNINI M., CARNEVALE L., PARENTE C. 2006. *Confronto tra metodi di interpolazione utilizzabili nella realizzazione di DTM, ASITA.* 2006.
D.G., KRIGE. 1951. *A statistical approach to some basic mine valuation problems on the Witwatersrand. - Chemical Metallurgical and Mining Society of South Arfica Journal, no.52.* 1951.
D.R., HACK. 2005. *Issues and challenges in the application of Geostatistics and Spatial-Data Analysis to the characterization of sand-and-gravel resources.- U.S. Geological survey.* 2005.
DEUTSCH C., JOURNEL A. 1992. *Geostatistical software library and user's guide. Oxford Univ. Press, New York.* 1992.
FABRIS M., ACHILLI V., SALEMI G. 2004. *"Efficienza computazionale di algoritmi di interpolazione per l'analisi di modelli digitali del terreno", VIII Conferenza ASITA, Roma 14-17 Dicembre 2004, Atti della Conferenza, Vol. II: 1029-1034.* 2004.
G., RASPA. 2004. *Dispense di geostatistica applicata.* 2004.
GORSICH D.J., GENTON M.G. 2000. *Variogram model selection via nonparametric derivative estimation. Mathematical Geology, 32:249–270.* 2000.
GRIBKO L. S., LIEBHOLD A. M., HOHN M.E. 1995. *Model to predict gypsy moth (Lepidoptera: Lymatriidae) defolation uning Kriging and logistic regression. - Envioronmental Entomology.* 1995.
H., WACKERNAGEL. 1995. *Multivariate Geostatistics. Springer Verlag, Berlin.* 1995.
HAMARAH M., SHOJAEE D., MOSAVI A. 2006. *Evaluation of DTM Generation in Surfer 8.0. http://www.gisdevelopment.net/proceedings/mapindia/2006/student%20oral/mi06stu_128.htm.* 2006.
HENGL T., HEUVELINK G., STAIN A. 2003. *Comparison of Kriging with external drift and regression-Kriging (Tech. Rep.). Avaiable on-line at http://www.itc.nl/library/Academic_output/.* 2003.
HEUVELINK G.B.M., BORROUGH P.A., STAIN A. 1989. *"Propagation of errors in spatial modeeling with GIS". International Journal of geographical Information Systems, 303-322.* 1989.
ISAAKS E. H., R. M. SRIVASTAVA. 1989. *an Introduction to Applied Geostatistics, Oxford University Press.* 1989.
M., BEVILACQUA. 2008. *Composite likelihood inference for space-time covariance models.* 2008.
M.G., GENTON. 1998. *robust variogram estimation. Mathematical Geology, 30:213–221.* 1998.
MARCHIONE A., SANTAMARIA R. (Relatore) 2004. *Tesi Metodi e tecniche di interpolazione ed applicazioni GIS: dal dato puntuale alla rappresentazione continua.* 2004.
MARTUSCIELLO E., PARENTE C. 2006. *Metodi di interpolazione per la modellazione batimetrica nei GIS marini. Annali della Facoltà di Scienze e Tecnologie. Università degli Studi di Napoli "Parthenope", Napoli.* 2006.
N.A.C., CRESSIE. 1990. *"The origins of Kriging", Mathematical Geology, 22: 239 – 252 ESRI (2002), ArcGIS 8.3 – Help, Redlands (CA), USA.* 1990.
P., GOOVAERTS. 1997. *Geostatistical for natural resources evaluation. Oxford University Press, New York, 483 pp.* 1997.
PARENTE C., PREZIOSO G., SANTAMARIA R. 2009. *Confronto tra metodi di interpolazione per la costruzione di DTM, Atti del Convegno Nazionale SIFET.*
ROSSI R.E., MULLA D.J., JOURNEL A.G., FRANZ E.H. 1992. *Geostatistical tools for modelling and interpreting ecological spatial dependence. - Ecological Monographs.* 1992.
VOLTZ M., WEBSTER R. 1990. *"A comparison of Kriging, cubic splines and classification for predicting soil properties from sample information." Journal of Soil Science, 41 : 473-490.* 1990.
W.R., TOBLER. 1979. *Cellular Geography, Philosophy in Geography, Dordrecht, Holland, pp. 379-386.* 1979.
YANG C.S., KAO S.P.,LEE F.B., HUNH P.S. *Twelve different interpolation methods: A case study of Surfer 8.0.*
YANG S., KAO S.P., LEE F.B., HUNG P.S. 2004. *Twelve different interpolation methods: a case study of Surfer 8.0. http://www.isprs.org/congresses/istanbul2004/comm2/papers/231.pdf.* 2004.
SURFER 8 USER'S MANUAL
ArcGIS 9.3 USER'S MANUAL

SURVEY AND 3D MODELING FOR SMALL SIZED OBJECTS

F. Girardi

DICAM – Department of Civil, Environmental and Materials Engineering – University of Bologna
Viale Risorgimento 2, 40136, Bologna, Italy
fabrizio.girardi@unibo.it

KEY WORDS: Photogrammetry, Macro-photography, Calibration, Laser Scanner, 3D Modelling

ABSTRACT:

Nowadays, requests for three-dimensional objects reconstructions and high-quality 3D representations are even more frequent. These requests increase over the years in many disciplines and areas, and they are expected to rise up according to nature and number of applications. The research, mostly based on selected case studies, aims to investigate the area from medium to small-sized objects, which, according to the author's opinion, has not yet been deeply investigated, as confirmed by the limited number of examples in the scientific literature (Yanagi, 2010). Although the applied methodology is not conceptually different from that commonly adopted within close range applications, the problems are different, and they need specific technical solutions and methodologies, in order to fulfil the accuracy requirements that small objects require. For this reason, here two specific geomatic techniques were taken into account: digital photogrammetry with Macro lenses, and laser scanners (in particular the triangulating type). These techniques lend themselves to fulfil, as best as possible, the requirements for metric and radiometric high accuracy surveys. They have been also tested in order to assess their potential, not only considering the final results, but also keeping into account the problems associated with their use. Some of the case studies encountered during the PhD research are here presented, they have been chosen to highlight what were the major problems faced during the research and how they have been solved.

1. INTRODUCTION

Working with small objects involves many disciplines such as civil and mechanical engineering, for test or studies on the shape of prototypes or further more analysis with FEM (finite elements methods) on their strength behaviour. Another important field is the Cultural Heritage, where different techniques can be applied for generating 3D models useful for virtual representation, virtual restoration or furthermore for objects duplication, digital archives and dimensional control. 3D models of small objects can find their utility also on forensic investigations, medical application (prosthesis production, dentistry, etc.) and many other disciplines.

The three-dimensional representation of real objects has ancient roots but a scientific approach to the problem has begun only in the early nineteenth century with the invention of the photography, and after with the technique called photo-sculpture. Only with the advent of computer science and the spreading of personal computers among the people, today we can talk to someone about "three-dimensional modelling" without the other person totally be unaware of what it means. We can say that today three-dimensional modelling has become part of a basic technological background which, thanks also to the web, has produced some practical implications in daily activities that are certainly of great interest. These activities allow the user to create, manage, simulate or test a wide variety of products, or scenarios, with a significant saving of money compared to the real counterpart.

Geomatics is, in this context, the discipline that identify the most appropriate techniques and tools to deal with 3D spatial data. Among all of them, a first classification can be operated by dividing the techniques in 2 classes, commonly defined as passive and active techniques (Beraldin et al., 2000; Guidi et al., 2010). The difference between them refers to the role that light, or more generally an electromagnetic radiation, has in the measurement process. The work will focus on a restricted part of these techniques, those that best lend themselves to applications from medium to small sized objects, and among these, photogrammetry by using Macro lenses and optical triangulation systems, particularly laser scanners. With these techniques is possible to create three-dimensional models with a high level of details, with accuracies in the order of a tenth of a millimetre, or even sub-millimetre, so able to describe in the best way the geometric information in relation to the dimensions of the object itself.

Nowadays, systems for distance measurement, such as the range-based laser scanner, due to their high productivity and the density which with these instruments are able to characterize a surface, are definitely proven as a mature technology. On the other hand, their flexibility, costs, and sometimes logistical problems in the use, have limited their widespread adoption, although important steps have been taken in this direction. From this point of view, the images are still a valid alternative with much lower costs, even if the automatic generation of accurate and detailed 3D models of objects is a complex process not yet completely resolved. The images, although they contain all the information needed for the generation of a 3D model, still need a massive user intervention; the operator has a primary role in the process of extraction and refinement of the model to achieve the desired accuracy (Remondino et al., 2004) .

Regarding the state of the art, however, there are other techniques used successfully in 3D surveys and three-dimensional modelling of small objects, such as X-Ray Tomography, TOF Phase-Shift laser scanners, TOF cameras, etc., but they are not presented here.

The objects presented hereafter as case of studies represent examples, involving different disciplines, to prove how the digital Macro-photogrammetry or the laser scanning technique can be widely applied. The objects are coming from different fields: a bronze statue from the Renaissance, ancient seals from

the Bronze Age in Turkey, coins, bas-reliefs or road pavements samples.

2. THE PHOTOGRAMMETRIC APPROACH

In the last years, thanks to software innovations and mainly to advances in electronics, that led to its progressive and rapid reduction of costs, the digital photography market has grown so quickly, day after day, that today analogic photography survives thanks to a minority of fans. This rapid expansion has been reflected also in photogrammetry, especially in close-range applications, where the expensive semimetric cameras have been replaced by digital consumer devices. The reasons are more than one: firstly a better cost/performance ratio, greater flexibility and ease of digital cameras, and secondly, nowadays, the digital image resolution has reached the analogic one; the sensors, today, cover a range between 12-20 Megapixels, which is sufficient for all the majority of the photogrammetric applications that require high accuracy.
In photography there is a particular field called macro-photography (sometimes close-up) characterized by high level of details at a very close distance. The magnification index is the ratio between the size of the image on physical support (film or digital sensor) and the physical dimensions of the photographed object. This kind of lenses has a different behaviour than the normal ones used in photography; in fact, even if they are sold as fixed focal length lenses, they show, after a first calibration test, an abnormal behaviour of the focal length. The lenses have a "focusing distance", a distance that you have to stand from the subject in order to properly focus on it. With the Macro lenses, the more the magnification index rise up, the more the distance object-camera decrease, and that is the opposite of how the majority of focal lenses work. In figure 1 it is possible to see how small are the areas captured for each magnification index, starting from the 1:4 and decreasing till the ratio 1:1, where the image area is equal to the size of the sensor.
Macro lenses are optically designed to obtain a more accurate results on small and flat surfaces, for this reason they are, among the all the types of lenses, the most optically correct.
As for all the type of lenses, the first problem to be solved in order to use the Macro lenses in photogrammetry is retrieving the calibration parameters.
The calibration procedure is commonly referred to as a self-calibration bundle adjustment, where the interior orientation and distortion parameters are recovered as part of the bundle-adjustment for photogrammetric triangulation (Fraser, 1997).
The behaviour of this kind of lenses has been investigated at each magnification index, which may correspond to a wide range of possible applications according to the object size and the required accuracy.

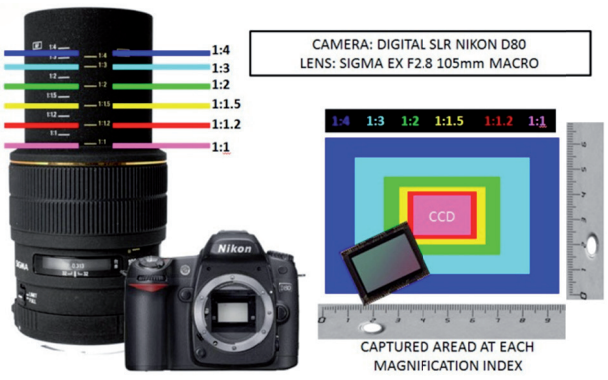

Figure 1. Sample of Macro Indexes for a 105 mm Macro lens mounted on a Nikon D80, and their captured area.

2.1 Long focal length lenses

To define the interior configuration of the optical rays at the shot time, we should know some parameters, like the principal distance and the position of the principal point; with them it's possible to define the spatial position of the perspective centre referred to the frame image. A series of additional parameters (APs) are added to keep into account the small perturbations from the ideal perspective behaviour that happen with the real use. The terms Δx and Δy in the next equation represent the departures from the collinearity model, they depend from the simultaneous presence of different error components, and their size can be seen as the sum of several contributions. Combining the error sources leads to the standard Brown eight-parameter model (Δx_p, Δx_p, Δc, K_1, K_2, K_3, P_1, P_2).

$$\Delta x = -\Delta x_p - \frac{\Delta c}{c}\bar{x} + \bar{x}\left(r^2K_1 + r^4K2 + r^6K_3\right) + \left(2\bar{x}^2 + r^2\right)P_1 + 2P_2\bar{x}\bar{y}$$

$$\Delta y = -\Delta y_p - \frac{\Delta c}{c}\bar{y} + \bar{y}\left(r^2K_1 + r^4K2 + r^6K_3\right) + \left(2\bar{y}^2 + r^2\right)P_2 + 2P_1\bar{x}\bar{y}$$

where:

$$\bar{x} = x - x_p \quad ; \quad \bar{y} = y - y_p$$
$$r^2 = \left(x - x_p\right)^2 + \left(y - y_p\right)^2$$

Upon linearization, the observation equations for the least-squares bundle adjustment are formed. The solution of this model is to estimate the additional parameters (APs) as well as internal and external orientation parameters:

$$A_1x_1 + A_2x_2 + A_3x_3 + w = 0$$

where x_1 represent the sensor exterior orientation parameters, x_2 the object point coordinates, and x_3 the camera calibration parameters. The matrices A_1, A_2, A_3 are the partial derivatives with respect to the parameters and w is the image coordinate discrepancy vector.

In photogrammetry the use of long focal length lenses can be useful in different types of applications, such as deformation monitoring, construction engineering, and traffic accident reconstruction. As mentioned, this work refers mainly to small objects, so we have used Macro lenses instead of the telephoto lenses, but we can assume that they have a similar behaviour. The problems involving this type of equipment mainly concern the analytical aspects of network orientation, to be more precise the retrieving of IO and EO parameters; problems can arise through over-parameterization, ill-conditioning and subsequent numerical instability in the normal equations of the bundle adjustment. While the focal length increase, the field of view (FOV) gets smaller, making the projective rays scheme to be more similar to an orthogonal projection (with rays parallel to each other) instead of an perspective one (with highly convergent rays). It has been shown (Stamatopoulos, 2010) that the problem is relevant when the FOV angle drop below 10°, which is equivalent to a 200 mm lens on digital SLR cameras in a 35 mm format.
Despite the eight-parameters model of Brown, discussed above, works in almost all the applications involving close-range photogrammetry, it presents some anomalies when using long focal length lenses. In such cases, we must pay particular attention to the parameters' behaviour; a careful selection of

them has to be performed, especially as the correlation between camera parameters, and interior and exterior orientation parameters increases with increasing focal length. A four-parameters subset of Brown's model can characterize the physical behaviour of a long focal lens avoiding the above mentioned problems. The parameters that are taken into account are the principal point position, the focal length and the radial distortion parameters. Even if the radial distortion is modelled by the well-known odd-order polynomial expression, for long focal length lenses it is known in literature that the third-order coefficient K_1 is sufficient to describe the radial distortion profile.

For over 40 years the photogrammetric community has assumed the value "-1" for the coefficients related to the parameters x_p, y_p.

However, given the instability of the equation system due to the use of long focal length lens, it is useful to step back and review the determination of the partial derivatives of the image correction model, especially terms for the principal point coordinates. The commonly employed terms:

$$\begin{array}{c} \\ \partial x \\ \partial y \end{array}\begin{array}{c} \begin{array}{cc} x_p & y_p \end{array} \\ \begin{pmatrix} -1 & 0 \\ \cdots & 0 \quad -1 \cdots \end{pmatrix} \end{array}$$

are replaced with:

$$\begin{array}{c} \\ \partial x \\ \partial y \end{array}\begin{array}{c} \begin{array}{cc} x_p & \qquad\qquad y_p \end{array} \\ \begin{pmatrix} -1-K_1r^2-2(x-x_p)^2K_1 & (x-x_p)r^2 \\ \cdots \quad (y-y_p)r^2 & -1-K_1r^2-2(y-y_p)^2K_1 \quad \cdots \end{pmatrix} \end{array}$$

This correction of the matrix coefficient A greatly improves the estimation of the interior orientation parameters in the case of lenses with long focal lengths, even if the magnitude of K_1 might be very small, in the order of 10^{-5} (Stamatopoulos, 2010).

During the research, calibration test were performed on different Macro lenses (Canon 100mm, Canon 60mm, Sigma 105mm) and on different SLR cameras (Nikon D80, Canon Eos 350D, Canon Eos 5D Mark II); an example is reported in figure 2. The results have shown how the self-calibration bundle adjustment with the modified model leads to parameter values with physical meaning. For example, with the classical model when cameras with very long focal lengths are involved, working closely to the maximum magnification indexes, the principal point coordinates were often recovered with a big shift in respect to the sensor central point, and sometimes even out of the CCD/CMOS area.

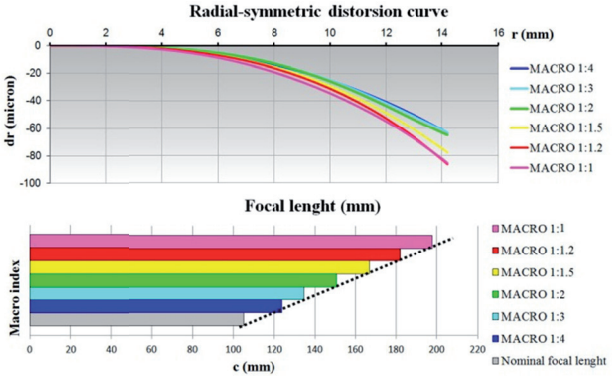

Figure 2. Sigma 105mm Macro lens on a Nikon D80. The radial distortion plot shows lower values (60-80 µm) compared to the lens commonly used in close range photogrammetry (up to 10 times this values). Even if the lens has a fixed nominal focal length, the test figured out that *c* increases linearly with the indexes till to double the initial value.

2.2 Some problems working with Macro-Photogrammetry

Considering the Macro lenses features so far presented, such as the very high level of detail, so far superior to any other common type of lens, or the very short focus distance, it would seem to make them ideal for photogrammetric applications (Bitelli et al., 2010). There are, however, some problems that make this type of lenses not so easily suitable for photogrammetric purposes, and they are essentially related to photographic problems. The biggest limitation is represented by the very small depth of field (DOF).

The depth of field of Macro lenses appears to be to the order of a millimetre or so and then, especially when strongly convergent images are taken, only a small part of the image is focused and useful to the operator. This situation is highly problematic during the self-calibration process where, in order to recover the network orientation and the interior parameters, it is necessary to see clearly all the coded targets in each part of the image (Cronk et al., 2006; Cronk 2007). The depth of field can also affect the successive phases concerning the DSM extraction. A very small DOF affects the image matching algorithms, as they cannot work on high blurred areas.

There is a way to increase the depth of field, and it is done of course by closing the diaphragm (increasing the *f*-number); in this way, however, the time exposure increases.

A great *f*-number, while is enhancing the depth of field, furthermore drops down the optical resolution due to diffraction problems caused by the small entrance pupil, as showed in figure 3.

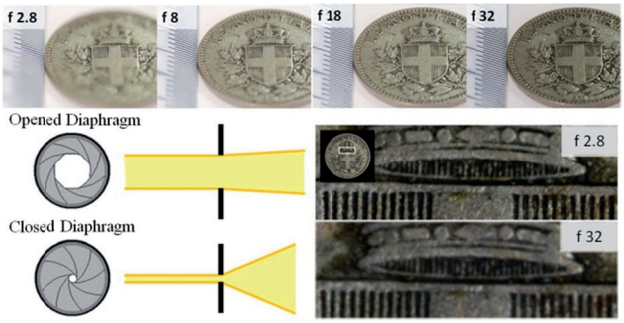

Figure 3. Different depth of field, and diffraction effects on the image by changing the diaphragm aperture. At lower *f*-numbers the image looks more sharply on the focused area.

Another problem closely connected to the resolving power of Macro lenses raised up during the calibration. Usually, for close-range applications the coded target are printed on a physical support; at this scale the type of support, mainly paper, doesn't have any influence to the final result. With Macro lenses, the targets are miniaturized so much (few mm) that the cellulose's microstructure that compose the paper cause an "bleeding effect" to the ink, resulting in loss of their circular shape.

The pseudo-circular shape is often not symmetrical, and leads to some problems especially during the recognizing phase, where the targets are accepted or refused by the algorithm according to some geometric criteria; even when they are classified as targets, the wrong shape leads to an incorrect determination of its centroid and its coordinates (fig.4).

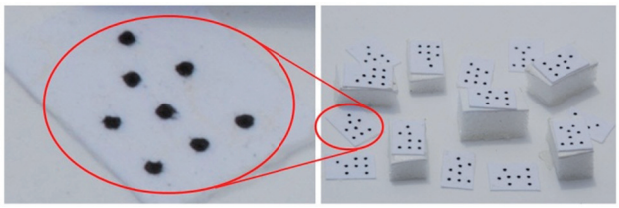

Figure 4. Ink bleeding on printed target cause errors in centroid coordinates determination.

In order to satisfy the criteria to recognize, classify and measure the targets even at this level of magnification, a specific solution was followed, realizing a photographic contact print by using a photographic negative generated from a digital file (fig. 5).
This solution leads to an high quality representation of each target, keeping their shape with a very high accuracy.

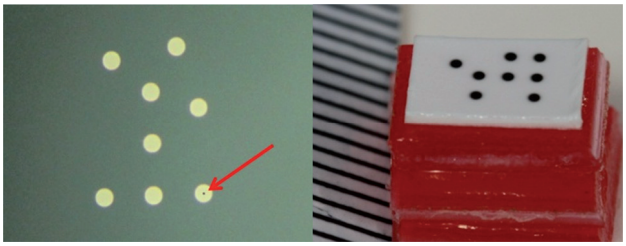

Figure 5. Digital slides used to print small targets (2-3 mm size)

A test was realized on small archaeological finds. An archaeological expedition of the University of Bologna has allowed the discovery of many important finds relating to an ancient commercial network in the Gaziantep region in Turkey; among these finds there are a lot of mould seals coming from the Bronze Age and they were the subject of a photogrammetric survey using these high resolution targets (Bitelli et al., 2011). An example is hereafter presented in figure 6. For such small objects, given the impossibility to perform a "topographic" survey with an accuracy sufficient for the purposes of the work, a different solution has been adopted. Some dots of the targets have been chosen as "control points", and their coordinates have been derived by using some gauge blocks to scale the network on distances measured by high precision. With this solution it has been possible to retrieve the object coordinates of any point with a high level of accuracy. The precision for the measurement of these distances is in the order of the pixel size (6µm), and they have been performed in X,Y,Z direction to don't privilege any of them (fig. 6).

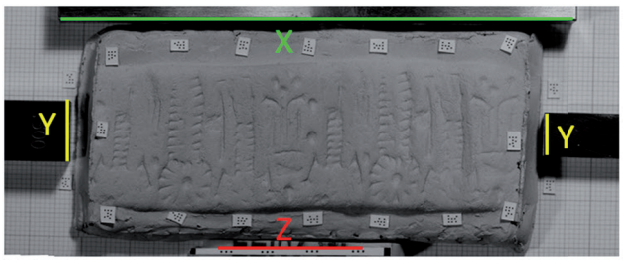

Figure 6. Gauge blocks are used to scale the model in X,Y,Z direction.

The entire network orientation has led to high accuracy values in determining the control points coordinates, with sigmas on X,Y,Z coordinates of the order of some microns. Using these points, a subset of different images has been oriented and then a digital surface model has been generated. The subset is made by pictures acquired in a normal position (fig. 7, the red cameras) , with a lower *f*-number, to improve the level of detail and the sharpness and to extend the depth of field. The resin used for the molds of the seals affected the image matching algorithm used to generated the DSM: the area-based matching approach suffered the colour uniformity, and provided a bit noisy result that needed to be filtered and smoothed.

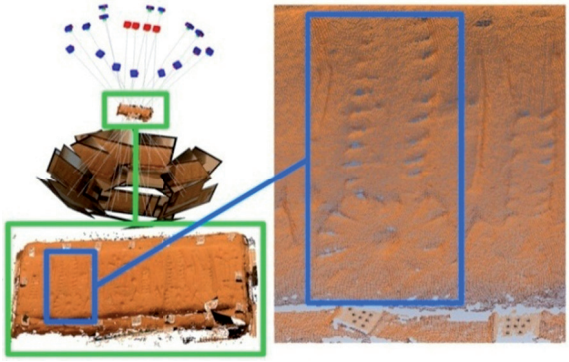

Figure 7. DSM generated by a subset of pictures

Unfortunately, as it is possible to see in the well-known formula: $\sigma_Z = \frac{Z}{B}\frac{Z}{c}\sigma_{pixel}$ the geometric constrains imposed by the Z/B and Z/c ratio strongly influence the accuracy in Z.
To improve the obtainable σ_Z accuracy should be able to drastically reduce the minimum focusing distance (Z distance), which as seen in the formula, goes with the square of its value. With the actual state of the art it is not possible to further reduce the minimum focusing distance for the consumer lenses, and it leads to precisions of the order of 0.15-0.3 mm, far away from the expected results with the Macro lenses. However, this range of precision is comparable with some of the instruments commonly used in the field of Archaeology and Cultural Heritage, like some triangulating laser scanners, and is suitable for a lot of applications.

2.3 Some aspects in image pre-processing

The goal of digital image pre-processing is to increase both the accuracy and the interpretability of the digital data during the image processing, as well as the quality of the final result.
The network orientation phase, when performed manually by the operator, usually requires no intervention on the images, a slight contrast or brightness adjustments are applied to help the operator's image interpretation, any other substantial change with this aim is preferably not applied. This because a change in radiometry can worsen the DSM extraction results, when performed by image matching algorithms. However, if even the orientation phase could be handled automatically and then a DSM is extracted by using algorithms for image matching, the image pre-processing phase can significantly improve the results. Below are presented some aspects taken into account to try to improve the final results.

2.3.1 JPEG vs RAW accuracy comparison

With the advent of modern DSLR cameras, the output data can be supplied with the common JPEG file format, or with the raw file, or both at the same time. A camera RAW image file contains minimally processed data from the image sensor. Raw image files are also called "digital negatives", as they fulfil the same role as negatives in film photography: the negative is not directly usable as an image, but has all of the information needed to create an image. Normally, the image is processed by

a raw converter in a wide-gamut internal colour space where precise adjustments can be made before conversion to a "positive" file format such as TIFF or JPEG for storage, printing, or further manipulation. Considering this possibility, a test was performed to check if it was possible to have a gain in accuracy by a manually controlled compression by the operator. A comparison has been performed between the JPEG dataset obtained directly from the camera and the one converted using Photoshop Camera Raw from the RAW files. Different dataset coming from three different SLR cameras has been checked and the results shows a decrease in the global self-calibration accuracy to the order of 10-20% when the JPEG(RAW) are used, that let the author to think reasonably that internal camera JPEG generation process results better in a loss of data that the one obtained through post-processing software. Considering these results, the data generated directly from the cameras can be considered the best starting point for self-calibration procedures.

2.3.2 Wallis Filter application

Developed in 1976, Wallis filter is often used to optimize images when a further application involving interest operators is needed. In literature there are many experiences and numerous experiments showing that interest operators are able to find a significantly greater number of points in the image where the Wallis Filter was previously applied. The Wallis Filter process applies a locally-adaptive contrast enhancement to a grey-scale raster: it operates locally, by adjusting the brightness values so that in these areas the local mean and standard deviation are consistent with those defined by designed parameters. During this research the Wallis filter has been used in a preliminary step for the subsequent use of the FAST operator.

2.3.3 FAST interest operator

There are different types of interest operators: their function is to identify some specific elements of an image such as points, angles, lines, or areas. Developed in the early 70's within the community of computer vision for tracking and object recognition, now they are used with good results also in photogrammetry. The FAST (Features from Accelerated Segment Test) interest operator, recently developed by Rosten and Drummond (2006) has been found to generally outperform other interest operators in speed, being faster than the Harris, SUSAN and SIFT interest operators commonly used in imaging applications (Rosten and Drummond, 2006). Beyond its speed, the FAST operator is also invariant to rotation and changes in scale, a critical element for image-based modelling from convergent images.
Its effectiveness can be improved by a combined use of the Wallis Filter; as shown in Figure 8 it has been applied to some coins and the number of interest points increases in this case significantly.

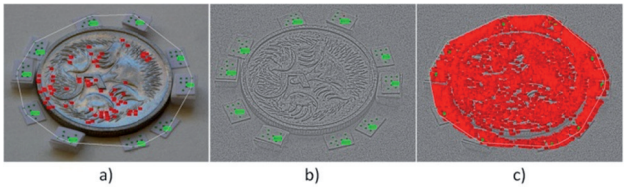

Figure 8. Appling the FAST operator without the Wallis filter the number of interest point are significant less. a) FAST operator on the original image; b) Image pre-processed with the Wallis filter; c) FAST operator on the image pre-processed with the Wallis filter

A surface reconstruction process has been subsequently performed using the interest points in a bundle-adjustment procedure in order to recover their spatial position (figure 9). These points can also be used as control points where is not possible to put any target on the object, for example when very small objects are used. Among the various modelling algorithms available, for this work has been used the one implemented for research purposes into the iWitness Pro software; it uses the Poisson Surface Reconstruction technique, proved to be an optimal approach for reconstructing surfaces from the point clouds generated from the interest points identified via the FAST operator (Jazayeri et al., 2008, Jazayeri, 2010).

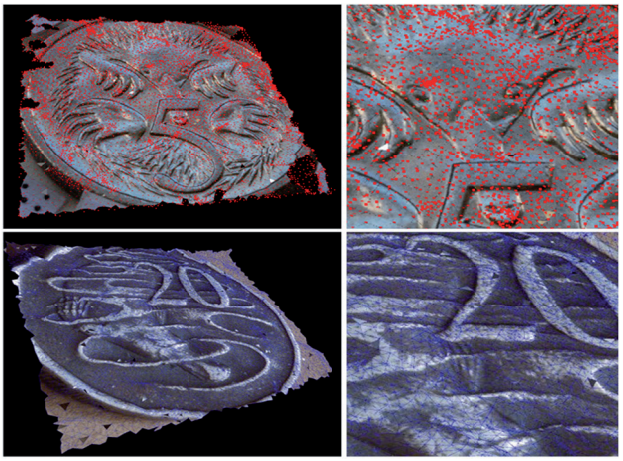

Figure 9. Object reconstruction by using the points generated by the FAST operator with the Poisson Surface Reconstruction.

2.3.4 Radiometric colour calibration

The phenomenology of colour perception is very complex topic that should be taken into account when quality and fidelity in colour reproduction have a primary role in the final product. It happens widely for applications regarding the Cultural Heritage field, for examples for paintings, mosaics or frescoes. The problem of randomness opinion between two people about the colour, especially when the object is illuminated by different light sources, posed the problem to find a method that can identify a colour in a unique way. The colour calibration is sometimes an underestimated aspect of the workflow that could be addressed by applying appropriate colour calibration procedures. As well known, the colour temperature of a light source is the temperature of an ideal black-body radiator that radiates light of comparable hue to that of the light source. Colour temperature is conventionally stated in the unit of absolute temperature, the Kelvin (K). In 1931, the CIE (Commission Internationale de l'Eclairage) has set numerical values, quantifying the responses of the average human eye to different wavelengths of light, and has also defined the normalized spectral composition of illuminants. During the calibration phase we will refer to the illuminant D65, which corresponds to the average daytime light (T = 6500 K); an example is shown on fig 10.
Through the use of the ColorChecker, cards on which different colours are reproduced with special inks, it is possible to calculate an ICC (International Colour Consortium) profile. This profile could be applied to any image taken under the same environmental conditions, avoiding the presence of the ColorChecker on the picture.

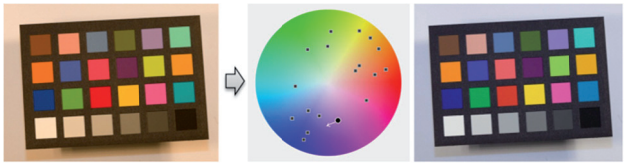

Figure 10. Colour calibration by using the ColorChecker. Before (Incandescent light bulb) and After (Illuminant D65 conditions).

3. 3D SENSORS

In the last 10 years we have seen a spreading use together coupled with a drastic reduction in costs for three-dimensional acquisition systems devices; the technological progress in terms of hardware and software solutions has been furthermore significant. Nowadays we are able to manage a huge amount of data that just few years ago were unthinkable. These facts can permit today a large number of applications for different categories of users, not only limited to advanced research structures. This research, as mentioned at the beginning, was focused on the laser scanning systems, especially on the triangulating type, most suitable for small sized objects.

3.1 Operating principles

According to the outline in figure 11, in a triangulating laser system the laser emitter produces a beam of energy that, due to a prior calibration of the rotating mirror, comes from the instrument at an known angle α, and goes to hit the surface of the object at the point A that has to be measured. The laser beam undergoes a reflection whose magnitude depends on the type of surface; a part of the reflected signal is received from the receiving sensor (usually a CCD or CMOS) positioned at a known distance, called baseline (b), from the emitter.

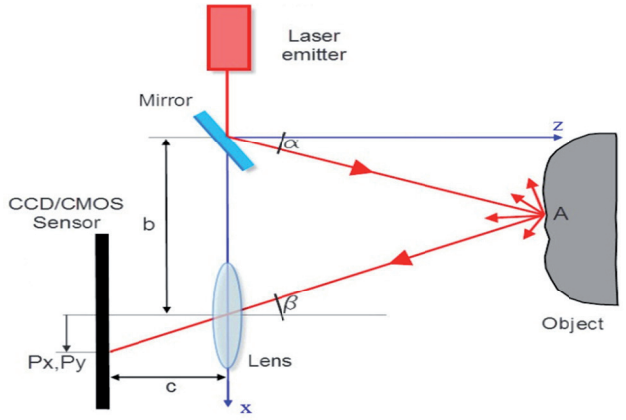

Figure 11. Triangulating laser scanner outline.

The angle β of the incoming ray is unknown, but it is possible to calculate it through the knowledge of the focal length (c) and position of the laser spot (P_x, P_y) recorded by the sensor array. The incoming horizontal and vertical angles are calculated as:

$$\tan\beta = \frac{P_x}{c} \quad ; \quad \tan\gamma = \frac{P_y}{c}$$

Knowing these angles it is possible to recover the three coordinates of the point A:

$$z_A = \frac{b}{\tan\alpha + \tan\beta}$$

$$x_A = \frac{b}{1 + \frac{\tan\beta}{\tan\alpha}}$$

$$y_A = \frac{b}{\frac{\tan\alpha}{\tan\gamma} + \frac{\tan\beta}{\tan\gamma}}$$

The workflow of the laser scanner survey (fig 12), and the subsequent 3D model generation, is usually performed by a succession of operations, starting from a planning phase, where some key decisions are taken such as the type of instrumentation that should be used in relation with the purposes for which the model is generated, passing through the data acquisition and finally ending with the post-processing operations.

The planning phase is a very delicate part of the survey, on which depend strongly the results of all the work.

The number of scans and their positions can be estimated in advance with a good level of approximation based on some simple rules, such as keeping an overlapping area between two adjacent scans of 30-40% (fig. 13), or using some convergent scan positions to avoid lack of data due to occlusions.

Depending on the geometrical and material characteristics of the object to be scanned it is then possible to further narrow the field to those instruments which ensure the precision and accuracy desired. Small objects, which can vary from a few centimetres to meter size, are usually scanned with instruments based on the principle of triangulation. For bigger sizes, it can be useful to move to other scanners, based on different principles, for example a TOF Shift-Phase.

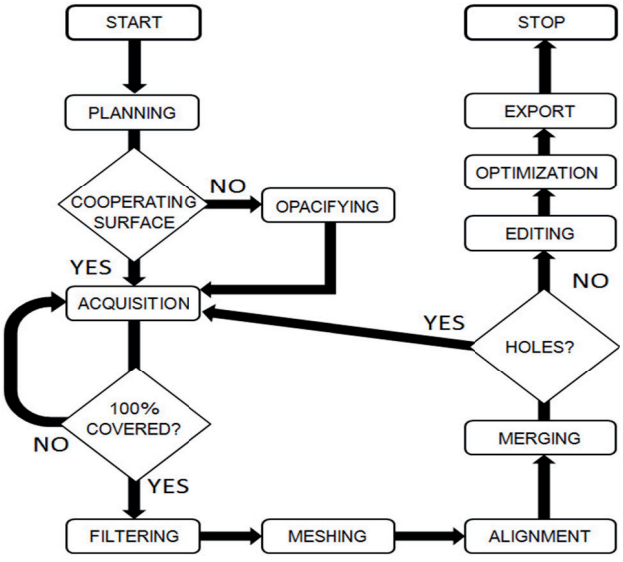

Figure 12. Flowchart of a 3D laser scanner survey.

Figure 13. Acquisition scheme of several (37) point clouds of a bass relief on S. Agricola's sarcophagus in Bologna. Each point cloud has an overlapping region of about 30-40% in both directions, horizontal and vertical.

Once the acquisition phase is ended, having taken care to have covered all the object's surface, the next step regards a preliminary filtering of the data. It is useful at this stage to reduce the following computational time, to eliminate all those parts that not belong to the object. The filtering of a raw unfiltered dataset is a task that must always be done. Omitting this step could lead to topological errors when creating the *mesh* or during the alignment between them.

The operation that transform a point clouds into a polygonal surface is called meshing. At the end of this process, the surface is organized as a network of triangles connected to each other, whose vertices coincide with the measured points.

The following step, one of the most delicate of the entire process, is represented by the alignment between the meshes. In this phase, errors can arise, which leads to geometric discrepancies between the real object and its digital copy. The causes of these errors must be sought in the size of the overlapping area between two adjacent meshes, and their morphological characterization. Usually, after a preliminary phase necessary to calculate the approximate 3D roto-translation matrix, where at least 3 tie-points in 2 scans are selected manually, a second step with ICP (Iterative Closest Point) procedures is involved. ICP algorithms perform a fine alignment by minimizing the difference between two clouds of points according to some criteria (Besl & McKay, 1992; Chen & Medioni, 1992; Johnson e Kang, 1997). In figure 14 is shown how 28 scans have been aligned in the survey of the small bronze statue representing Marsia, from A. Briosco, belonging to a bronze collection of the Medieval Museum of Bologna.

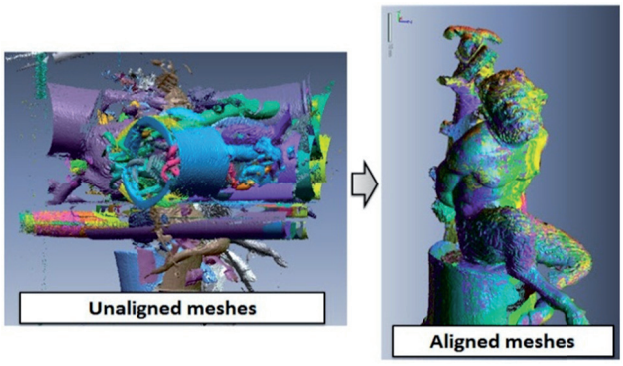

Figure 14. Alignment of 28 point clouds of an ancient bronze statue made by Andrea Briosco (aka Riccio) one of the most famous bronze sculptor of the Renaissance.

Once all the meshes are aligned in the same reference system, they have to be merged together, in order to create an unique surface. An additional level of data filtering has to be performed after the merging phase, useful to eliminate topological errors (discrepancies between the meshes), the presence of gaps and noise of the final surface. Editing the model means to correct all these kind of imperfections, keeping as much as possible the original geometry.

The last step of the workflow concerns the optimization of the data so far processed. The optimization can involve three aspects, the number of vertices composing the mesh, their spatial organization and texture. Not always a high definition model is needed, so not always all the data collected so far are necessary to characterize the 3D model. By applying some reducing or optimizing criteria (by curvature, by percentage, by distance,..) the surface can be completed, by filling the holes, or reorganized spatially and reduced in number of triangles, without losing in accuracy. Once the model is ready it can be exported in different file formats according to the expected use.

3.2 Limits

Laser scanners are instruments where the limitations are not related only to the technology used in their production (for example it is impossible to totally eliminate the divergence of a laser beam), but they are also related to physics aspects: a very limiting factor concerns the diffraction of laser light. The highest resolution reachable in the *xy* plane is defined as the minimum inter-distance between two distinct points that can be appreciated. Conventionally it is defined, for a given laser spot, with the Rayleigh criterion which states that two spots can be considered as distinct when the centre of one overlaps the first airy disk of the pattern of refraction of the second (fig. 15).

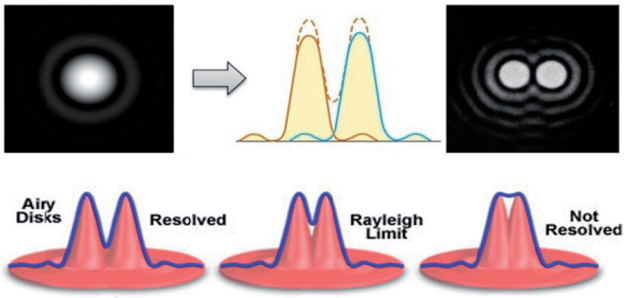

Figure 15. Rayleigh criterion that defines the maximum *xy* resolution for a given laser spot.

As for the resolution in *z*, the limiting factor is due to the speckle's effect. For a coherent optical imaging system, speckle is frequently considered as noise deteriorating image quality. A speckle pattern is a random intensity pattern produced by the mutual interference of a set of wave-fronts. When a coherent wave, characterized by a single phase, hits a real physical surface, characterized by a certain level of roughness, instead of an ideal one, there is a "disorder" in the beam caused by a series of reflections. These reflections are arising from each different microscopic element of the surface. Each of these waves since is characterized by values of phase and intensity, can contribute positively or negatively in the sum, when the contributions of coherent waves from many independent surface are added together. For this reason the intensity in the laser spot changes randomly, as shown in fig. 16. It physically implies an error in the exact determination of the laser spot position, since a deviation from the symmetry of energy distribution causes a shift (Δp) on its barycentre, with a consequently error in estimation of the *z* (fig. 17).

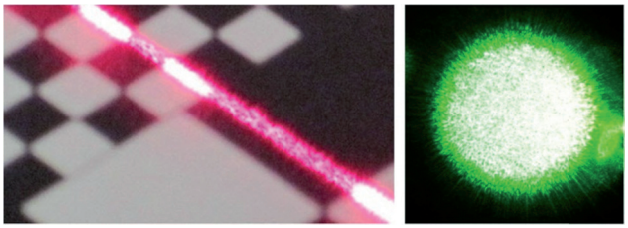

Figure 16. Speckle effect on laser spots.

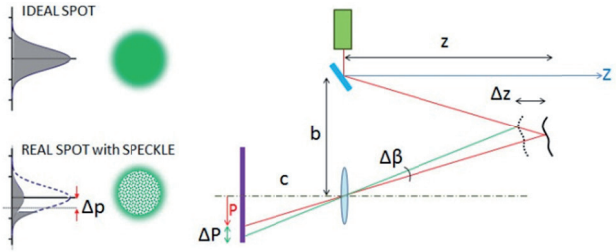

Figure 17. A small shift (Δp) on the sensor cause a Δz variation on the object shape.

Combining these two components, is it possible to know in advance, for a given type of laser wavelength (λ) and according to the object's size that is measured, what are the limits on the resolution on the plane *xy*, and along the *z* direction.

3.3 Error sources

Laser scanner behaviour often deviates from the ideal conditions; this is caused by several factors, such as the environmental conditions or the shape and material of the object. The errors introduced tend to provide a three-dimensional dataset that is a wrong estimate of the surface.

3.3.1 Range artefacts

Applying a laser scanner system on flat surfaces, the result is sometimes a 3D representation of the same scene, with some parts in relief or in depression. As shown in figure 18, due to high contrasted colour transition, a deviation from the symmetry of energy distribution causes a shift (Δp) on its barycentre. Depending on whether you are in the transition white/black or black/white, the direction of the shift (left or right respect the theoretical position of the spot), cause a ΔZ variation with the raising or lowering of the edge compared to the theoretical level as is shown before on the figure 17.
The same problem can arise when the laser beam hits an edge, and a part of it continue towards a background surface. The real sharp shape of the edges appears smoothed on the 3D model.

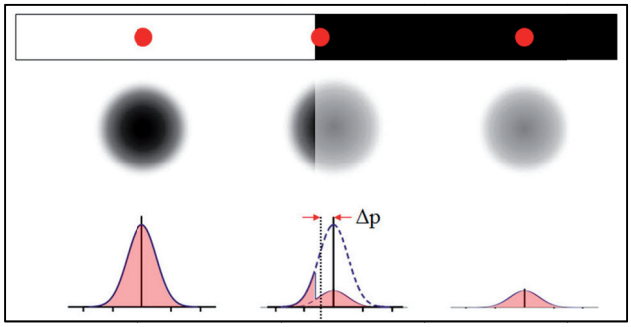

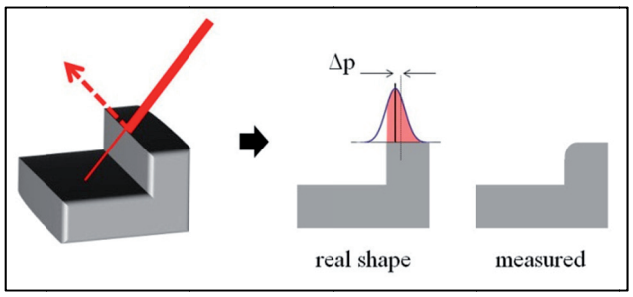

Figure 18. Range artefacts: the 3D data is affected by colour discontinuities (on top) and depth discontinuities (on the bottom).

3.3.2 Materials

The best possible response in terms of performance is when a return laser beam hits a surface material that do not cause any deviation from ideal behaviour.
Some materials such marble or bronze can instead present shift due to their physical properties. Translucent materials are very often used on the field of Cultural Heritage, let's think to some kind of stones, or glasses. As an example, a study on the marble has been performed (Godin et al., 2001) to investigate the laser penetration and how it causes the reflection of part of the signal at a different depth, due to material's proprieties. Even high reflective materials like metals causes errors: an example is shown in figure 19, where the small bronze statue of the XVI century described in 3.1 being scanned presented several range artefacts. The surface looks very rugged, even if it isn't like so. Not always it is possible to coat the object with a fine layer of talc or any other material that makes the surface cooperating. On the other hand, dealing with very delicate objects such the artworks exposed on museums, it is mandatory to work without interacting with the material of the object. The example on figure 19 shows the basement of the small bronze statue, each scan is affected by a range artefact in the area where the laser were perpendicular to the surface, beside this area the problem is not present; an accurate selection on the data belonging to the parts not affected by the range artefact can avoid a bad final result.

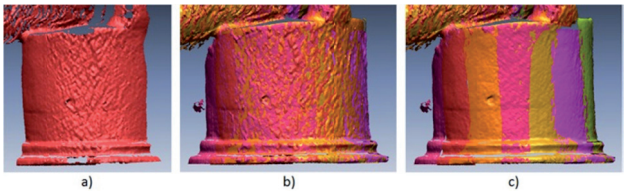

Figure 19. In *a*) are highlighted artefacts due to the nature of the bronze material, *b*) the redundant scans cause the spread of this artefact all over the object and *c*) a selection of the data produces a more accurate starting point for the further operations.

3.3.3 Adverse illumination

This type of problem occurs when the surface to be measured is strongly illuminated; this effect is accentuated for surfaces with a very clear texture. The result is a strong decrease in image contrast, which causes difficulty in the separation of the footprint of the laser beam and the background colour, hence making detection difficult. When the laser spot position is not obtained, the result consist in a lack of 3D data; an example is shown in figure 20, where an outdoor pavement (grass and stones) was scanned with a strong sunlight. Outside surveys with desktop laser scanner are for example an interesting

opportunity in transportation engineering to introduce the 3D data, in order to extend to new studies such as the analysis of surface morphology or the rain flow behaviour beside the traditional empiric road tests (Bitelli et al., 2010). For this reason an environment with a controlled illumination can improve the final results.

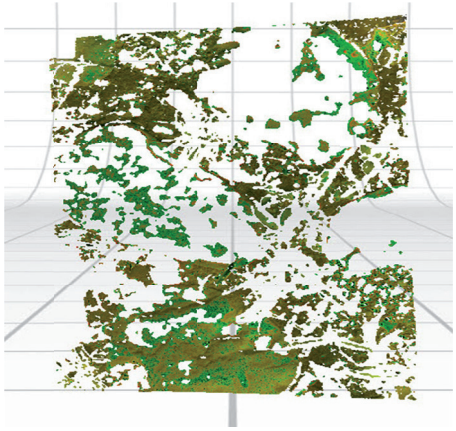

Figure 20. Outdoor pavement scanned under a strong sunlight illumination. The result consist in a lack of data where it was not possible to detect the laser profile on the object, and an alteration to the RGB colours.

3.3.4 Reflections

When working with highly reflective surfaces such as metals, it is possible that the laser beam is reflected and goes to illuminate other parts of the object which at that particular moment does not belong to the plane of the laser light (Bradshaw, 1999).
In some cases it may be possible to remove the problems of reflection, by coating the object with a temporary paint like talc.

4. CONCLUSION

Two thematic areas and instruments have been investigated, the image-based systems, using digital Macro photogrammetry, and the range-based systems, especially triangulation-based laser scanners.
The aim of the work was to analyse the theoretical and practical implications of these techniques when small objects are involved, highlighting the main problems and proposing appropriate operational methods.
As far as the digital photogrammetric approach, the network geometry and the optical behaviour of lenses used in this work, (Macro photography) cannot always borrow directly the classical mathematical models of close range photogrammetry, but instead some changes are needed in order to maintain stability during the bundle adjustment process. Classical models work in most of aerial or close-range photogrammetric applications, through the use of "wide" or "normal" lenses (focal lengths between 20 and 80 mm for small image formats), characterized by high divergence of the projection optical rays; the same cannot be done with long focal lengths lenses, where the very small divergence (FOV<10°) means that the classic model of perspective is closer to an orthogonal projection, with rays that tend to arrange themselves almost in parallel with each other. Considering the size of objects analysed, the main problem was to set a calibration field and then to define, with sufficient precision, a set of control points. The solution adopted led to a few microns sigma on the control point coordinates, which has been used in a second step to orient the network.
As for laser scanner workflow process, it has proven that different configurations in the parameter choice lead to different results. Considering that the final 3D model should be the best possible approximation of the real surface of the object, according to the instrument specifications, the three-dimensional modelling production should not just be the result of operations carried out automatically, but rather the result of an analysis of the actual situation and adoption of adequate choices.
Different case studies has been investigated during the research, like road pavements texture, ancient seals, small bronze statues, bas-reliefs, coins, etc. For each case, although the requirements in terms of accuracy, timing and costs of 3D modelling are significantly different, the survey and 3D modelling procedures do not greatly differ from those commonly used for larger objects. What is different is that for small sized objects we must shift the focus on problems related to the objects scale. For example a slight gap between the point clouds can badly affect the final mesh during the merging phase, for this reason every step has to be done with an high accuracy check-up. Other problems can arise when the artefacts, caused by the type of material, reach values to the order of the instrument accuracy, in this case the "geometric noise" can hide the real shape, and it's very hard to separate the two components. Besides the type of materials or the 3D modelling steps, there are other aspects that must be taken into account as an error sources: texture, lighting condition or the range and colour artefacts can increase greatly the incidence on the final product when dealing with small objects.
As frequently happens, it is not possible to determine if a technique is better than another, but is proven that speed of acquisition and the possibility of serialization process, makes the laser scanners a good solution for expeditious archaeological surveys in the Cultural Heritage field (but not only) with a high level of detail. On the other hand, digital Macro-photogrammetry is a low cost alternative to expensive instruments that not always can easily to take to site; however, it is subject to some physical constraints related to the lenses construction, such as the minimum focusing distance and the depth of field, and others related to photogrammetry principles like the Z/b ratio, as easily seen from the relationships that express the inaccuracies (σ_Z) in the normal case. Despite the fact that Macro lenses are able to reach a level of detail greater than any other type of lens, their features cannot be exploited completely in 3D modelling because of some limits represented by the very small depth of field that affect the exterior orientation of convergent images and also because on the market there isn't a commercial software for DSM generation from images strongly convergent. For this reason, the digital models don't have in general an accuracy comparable with those that the resolutions of the pair lens-sensor are able to produce. Despite this limit, digital models obtained with Macro lenses can be compared with those generated by laser scanning on the range of 0.1-0.3 mm. However, digital Macro photogrammetry can be very useful for diagnostic and morphological analysis of a variety of subjects involving different fields of application, even it present a disadvantages in terms of competitiveness with the laser scanners with regard to the applicability to large data sets, due also to the high manual intervention required for this type of technique.

5. ACKNOWLEDGEMENTS

A special thank goes to the Department of Geomatics of The University of Melbourne, to Prof. Clive Fraser for his support during my visiting period during PhD study, and to his staff, especially Simon Cronk, Ida Jazayeri and Christos

Stamatopoulos. I'm also grateful for the collaboration with Medieval Museum in Bologna, Basilica di Santo Stefano in Bologna, Turco-Italian Archaeological Expedition in the region of Gaziantep (Turkey), and the colleagues of DICAM Dept. – University of Bologna.

6. BIBLIOGRAPHY

Beraldin J.A., Blais F., Cournoyer L., Godin G., Rioux M., (2000) – Active 3D sensing, Modelli e Metodi per lo studio e la conservazione dell'architettura storica – Scuola Normale Superiore, Pisa 10: pp. 22-46.

Bitelli G., Girardi F. (2010) – Problematiche nel rilievo e modellazione tridimensionale di oggetti di piccoli dimensioni nel campo dei beni culturali – Atti XIV conferenza nazionale ASITA – Brescia 9-12 Novembre 2010, pp. 285-290.

Bitelli G., Simone A., Girardi F., Lantieri C. (2010): "Caratterizzazione di superficie e tessitura del manto stradale mediante tecniche a scansione laser", Bollettino della SIFET, 3,pp. 55-68, ISSN 1721971X.

Bitelli G., Girardi F. (2011) - Il rilevamento tridimensionale delle impronte dei sigilli di Tilmen Höyük – in "Kinku. Sigilli dell'età del Bronzo dalla regione di Gaziantep in Turchia", N. Marchetti ed., Ante Quem, pp. 58-66.

Bradshaw G. (1999) – Non-Contact Surface Geometry Measurement Techniques – Dublin, Trinity College Dublin, Department of Computer Science, TCD- CS- 46, pp. 26.

Cronk S., (2007) – Automated methods in digital close range photogrammetry – Thesis PhD.

Cronk S., Fraser C., Hanley H., (2006) – Automated metric calibration of colour digital cameras – The Photogrammetric Record, 21: pp. 355-372.

Fraser C. (1997) – Digital camera self–calibration – ISPRS Journal of Photogrammetry and Remote Sensing, vol. 52, issue 4, pp. 149-159.

Godin G., Beraldin J. A., Rioux M., Levoy M., Cournoyer L., (2001) – An assessment of laser range measurement on marble surfaces – Proceedings of the 5th Conference on Optical 3D Measurement Techniques, pp. 49- 56.

Guidi G., Russo M., Beraldin J. A. (2010) – Acquisizione 3D e modellazione poligonale – McGraw Hill, ISBN: 9788838665318.

Jazayeri I., (2010) – Image- Based modelling for object reconstruction – Thesis PhD, 2010.

Jazayeri I., Fraser C. S., (2008) – Interest operators in close-range object reconstruction – Vol. XXXVII. Part B5. Beijing.

Remondino F., Guarnieri A., Vettore A., (2004) – 3D Modelling of close-range objects: photogrammetry or laser scanning? – Proceedings of the SPIE, Volume 5665, pp. 216-225.

Rosten E., (2006) – High performance rigid body tracking – Thesis PhD.

Stamatopoulos C., Fraser. C., Cronk S., (2010) – On the self-calibration of long focal length lenses – ISPRS, Vol. XXXVIII, Part 5 Commission V Symposium, Newcastle upon Tyne, UK.

Yanagi H., Chikatsu H., (2010) – 3D Modeling of small objects using macro lens in digital very close range photogrammetry – ISPRS, Vol. XXXVIII, Part 5 Commission V Symposium, Newcastle upon Tyne, UK.

Yanagi H., Chikatsu H., (2010) – Performance evaluations of macro lenses for digital documentation of small objects – SPIE Videometrics, Range Imaging, and Applications X Proceedings Paper, San Diego, CA, USA

THE CONTRIBUTION OF MULTI- AND HYPERSPECTRAL REMOTE SENSING TO LANDSCAPE MONITORING AND ENVIRONMENTAL SUSTAINABILITY

Emanuele Mandanici

DICAM - Dept. Civil, Environmental and Material Engineering
Alma Mater Studiorum - University of Bologna
v. del Risorgimento, 2 Bologna
emanuele.mandanici@unibo.it

KEY WORDS: Radiometric correction, Lithologic classification, Reclamation monitoring, Water quality, Fayyum Oasis (Egypt)

ABSTRACT:

The development of multispectral sensors and the growing perspectives of hyperspectral sensors provide new tools for the investigation of the landscape and renew the need to redefine potential and accuracy limitations of traditional methodologies. This paper aims to examine, for some environmental applications, the critical points of the remote sensing problem as a whole. Specifically, the case study of the Fayyum Oasis (Egypt) has been chosen to assess the information content of satellite images under three different profiles, only in appearance distinct: the classification of surface lithology, the evaluation of the water quality and the land reclamation monitoring. To validate the results, some ground truth data acquired during a preliminary survey conducted in October 2010 have been used.

1 INTRODUCTION

The Fayyum, an Upper Egypt administrative and geographical entity, is a topographically depressed area, located on the hydrographic left of the river Nile (figure 1), about 90 km south-west of Cairo city, and it is bounded by cliffs that reach the highest elevation (about 300 meters) on the northern side. To the east is separated from the Nile valley by a modest arid relief (no more than 100 m high) and it is surrounded by the Libyan Desert on the remaining three sides. The northern and deepest part of the depression is occupied by Lake *Qarun*, whose surface lies at an altitude of approximately 45 meters below sea level and whose depth currently does not exceed eight meters. To the south and east side, the lake is surrounded by the agricultural land, intensively cultivated since ancient times and today in further expansion as a result of land reclamation. The thorough bibliographical research conducted on this site highlights that, although numerous studies were conducted in recent years, the uncertainties that still remain on the characterization of this environment make it a case study of great scientific interest and a privileged place to evaluate the information content of satellite images under *three* different profiles: the classification of *superficial lithology*, the monitoring of *land reclamation* and the assessment of *water quality*.

Although they are three distinct informative levels in terms of methodology, conceptually they are closely related, at least in the case study under consideration, and they are to be regarded as a whole to understand the specific relationship between environmental issues and human responses. Clearly, being an oasis surrounded by arid soils in the Libyan Desert, the vital element for Fayyum life is the availability of water, whose quality be suitable for agricultural purpose. Water supply is guaranteed by Nile River. Its waters are distributed to the oasis through a canal network, which discharges residual water in the final receptor, the Lake Qarun. Obviously the quality of lake water depends firstly on natural factors, related to geology and climate of the basin in which it resides. They determine the 'initial state' and the inherent frailty, which human activities impact on, especially the discharges of both agricultural and industrial activities. As a result, this lake, which has no outflow, has been suffering enormous problems of salinisation and pollution from agricultural fertilizers, not to mention the increasing concentration of heavy metals. Historical data, in fact, demonstrate that lake salinity passed

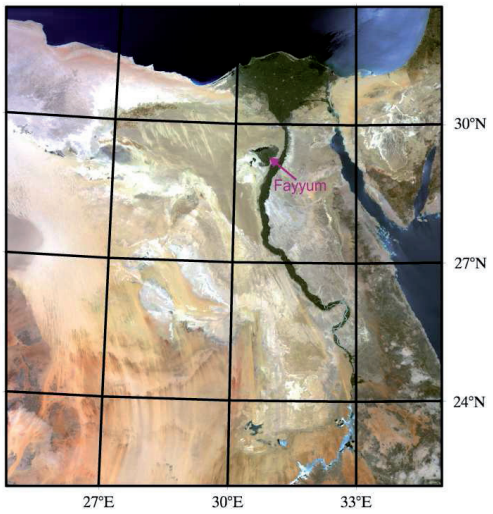

Figure 1: The Fayyum oasis is located in the Upper Egypt, west of the Nile River, and it is completely surrounded by the Libyan Desert.

from 15‰ (corresponding to slightly brackish water) at the beginning of the XX century to over 35‰ (hyper-saline water) in the last decade (El-Shabrawy and Dumont, 2009). Similarly nitrites and nitrates rose during last fifty years up to 12 μg/l. Not only fishing depends on the health state of the lake ecosystem, but also, indirectly, agricultural activity, since the salinity of the lake causes salinisation of groundwater and, ultimately, of farmland, resulting in productivity losses. Since 1989 the Fayyum oasis (especially Lake Qarun) has been designated as *conservation area*, because of its unique environmental, economic and cultural relevance. In fact there are numerous international scientific campaigns in the Fayyum, among which the twenty-year-long excavation mission at Bakchias by the Archaeology Dept. of the Bologna University. Recently, the expansion of cultivated land has become a threat also to the preservation of cultural heritage sites.

The issue of environmental sustainability of intensive agricultural use of the oasis is essentially a problem of deterioration of water and soil quality. This problem requires an adequate knowledge of

Figure 2: Location of the water sampling (red circles) and rock sampling (green triangles).

the geological context in which these lands are set and a capacity for monitoring the effects of adopted remediation; both aspects are necessary to develop a strategic plan for a sustainable economic development, taking care also of the preservation needs of the cultural heritage sites. This issue can not be addressed except by an interdisciplinary approach, in which remote sensing can play a key-role, by providing a synoptic view of the landscape from a regional to a local scale.

2 MATERIALS

2.1 Remote Sensing data

Several multispectral and hyperspectral images were acquired by different sensors at medium geometrical resolution. In particular multispectral ASTER images were selected for the study of surface lithology in the desert areas adjacent to Lake Qarun. Some Hyperion hyperspectral image together with ALI multispectral images were acquired on-demand, for the qualitative and quantitative assessment of water quality parameters. Finally, to evaluate the hypothesis that the deterioration of water quality can be related to the processes of extending the cultivated lands in recent decades, many Landsat archive images were used for change detection analyses.

2.2 Ground data

Generally speaking, the most sensitive aspects of the models adopted to extract information from Remote Sensing imagery are the calibration and the validation of the results. Both stages require ground truth and ancillary data. For the lithological classification and the water quality analyses, some ground truth data were acquired in October 2010, during an expedition in Fayyum, to support the twentieth excavation campaign at Bakchias by the Department of Archaeology of the University of Bologna, directed by Prof. Sergio Pernigotti. During a preliminary survey, some rock and loose sand samples were collected, furthermore several in situ measures of the *electrical conductivity* of the lake have been taken to infer water salinity. Location of all the sampling sites is shown in figure 2. As described in the next paragraph, all the samples underwent laboratory analyses to determine their mineralogical composition.

3 LITHOLOGY

To make a classification of the main outcropping lithologies, the imagery of the ASTER sensor was chosen. As known, it consists of fourteen bands: two in the visible part of the spectrum, one in the near infrared, six in the short-wave infrared and finally five in the thermal infrared. Because the classification process uses mineralogical indexes, calculated as the ratio between two or more bands, the values of ground reflectance and emissivity are to be used. The atmospheric correction in this case is advisable, but a high accuracy is not necessary. Thus, the standard products ASTER 07 XT (surface reflectance) and ASTER 05 (surface emissivity) were chosen. For the calculation of the indices needed for classification, all the fourteen bands were resampled to the resolution of thirty meters and the orthorectification was performed using the SRTM model (version 4).

From a geological point of view, the Fayyum depression is set up on a structural basin, called Gindi, in which up to 2,000 m of Eocene rocks were deposited over the faulted and folded Cretaceous-Paleocene strata (Dolson et al., 2002). At the beginning of the Eocene period the major part of the lands corresponding to the modern Egypt (as far as the 24° parallel) was flooded by a shallow tropical sea, as a consequence of a main transgressive episode started at the close of Mesozoic (Tawadros, 2001). In that context the Gindi was a structural low in which a deep water facies deposition took place. The Eocene rocks outcrop in the south-eastern part of the depression and in the north bank of the Lake Qarun and they are composed mainly of carbonates (Swedan, 1992, Abdel-Fattah et al., 2010). The middle and upper Eocene witnessed a gradual, but not continuous, regression of the sea over Egypt. During Oligocene period the coast line reached the latitude of Fayyum. Over the north escarpment the Eocene strata are overlaid by the Oligocene continental deposits of the Jabel Qatrani formation. It consists of a lower sequence dominated by coarse to gravelly friable sandstones, a middle marker bed of medium to coarse-grained gypsiferous sandstone and an upper sequence of variegated sandstone and sandy mudstone (Bown et al., 1986).

The problem of classification is therefore to distinguish, as far as possible, a wide shade of sedimentary rocks, consisting of varying fractions of carbonates and silico-clastic materials of different particle size. There are also evaporite deposits, largely composed of gypsum, and basalt extrusion outcrops. The main indexes on which the classification is based are as follows (Kalinowski and Oliver, 2004):

- *Silica Index*: $\frac{\rho_{10,65}}{\rho_{8,29}}$
- *Carbonate / Chloride Index*: $\frac{\rho_{2,26}+\rho_{2,40}}{\rho_{2,33}}$
- *Ferrous Iron Index*: $\frac{\rho_{2,16}}{\rho_{0,80}} + \frac{\rho_{0,55}}{\rho_{0,66}}$
- *Alteration Index*: $\frac{\rho_{1,65}}{\rho_{2,16}}$

The classification process was therefore organized by a decision tree implemented in ENVI (Bitelli et al., 2009). The first two nodes that make up the tree are used to exclude from the classification the surfaces corresponding to lakes and arable land, on which the vegetation prevents lithologic mapping. After this early stage, a fundamental distinction based on the index of silicates is implemented, which tends to separate the mainly silico-castic rocks from carbonate-dominated ones. A key feature of this decision tree is the presence of an "Unclassified" output at the end of *each* of the main branches: if the pixel does not satisfy any condition placed in different nodes, it is not classified. This structure prevents, as far as possible, incorrect attribution of pixels belonging to missing classes.

The results of the classification process are illustrated in Figure 3. A narrow and elongated strip to the south-west and some areas

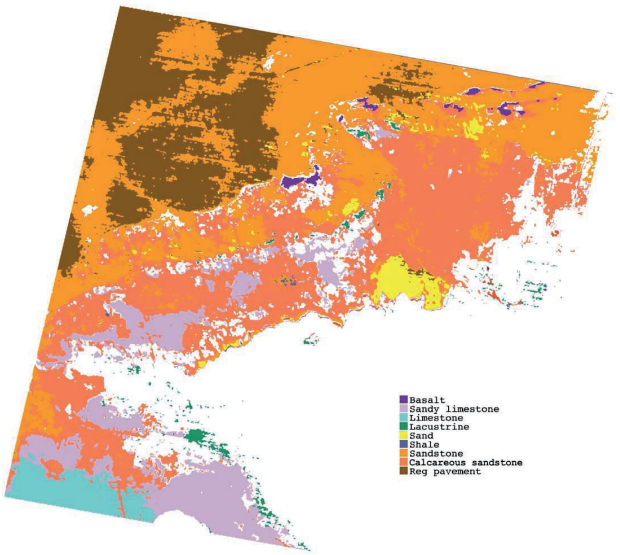

Figure 3: Lithological classification performed on the ASTER image acquired on June 24th 2007, by a decision tree.

north of the oasis of Fayyum remain unclassified. These areas often occur close to some deposits, clearly distinguishable because of particularly high values of carbonate index, which were labelled as "lacustrine", on the base of information available in literature (Kusky et al., 2011). Also the quarries located to the north-east of the lake remain unclassified, where the accumulation of mixed and remoulded materials makes the signal very confused. A defect consists also in the non-designation of loose sand longitudinal dunes in the Wadi Rayan area; the cause may be found in the possibly higher fraction of calcareous sands that compose these dunes.

Currently a rigorous validation of the obtained classification is not possible. It would require a large number of ground truth data or an independent map, with a comparable detail level, both not available. However, some preliminary evaluations, based on the results of laboratory tests carried out on samples collected during the 2010 field campaign, are possible.

For a large part of the collected samples, the reflectance profile was measured, in the wavelength interval ranging from 350 to 2500 nm. All measurements were performed at the Remote Sensing laboratory of the Atmospheric Pollution Institute of CNR in Rome, by means of a FieldSpec3 spectroradiometer by Analytical Spectral Devices Inc. The instrument is composed by three sensors, the first for visible light, with a spectral resolution by 3 nm, and the other two for the infrared, with a spectral resolution by 10 nm.

All samples, both rocks and loose materials, underwent XRF test (*X-ray fluorescence*), in order to determine the percentage composition of the major mineral kinds. The tests were performed at the XRF laboratory of the Earth Science and Environment department of Bologna University. XRF technique consists in exposing a sample to high energy radiation at controlled frequency. As a consequence of this bombardment, exposed atoms may eject an electron from the inner orbital. In such a case, the originated electronic hole causes a "fall" of electrons from the outer shells which fills the vacant one. This fall from the outer to the inner orbitals takes place with the emission of energy in form of X-rays, at a frequency governed by the atomic species. The obtained emission spectrum is therefore diagnostic of the tested material composition: frequencies provide information about the species,

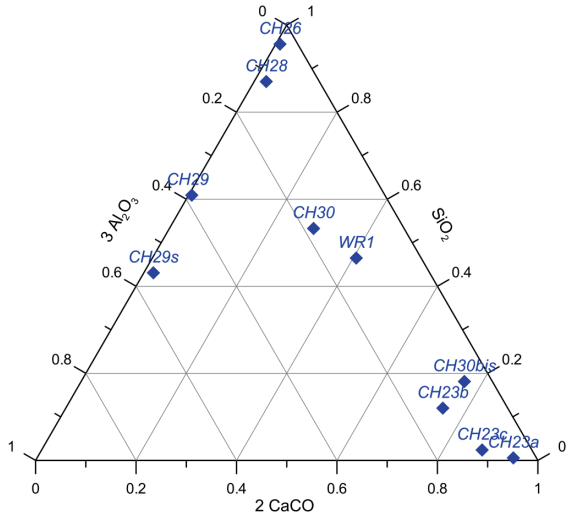

Figure 4: Ternary diagram of silicate, carbonate (exaggeration 2x) and aluminium oxides (exaggeration 3x) content. those samples which are mainly silico-clastic, such as quartz sand samples CH26 and CH28, are located close to the upper vertex; carbonate materials usually appear close to the lower right vertex; finally clay samples tend to occupy an equidistant position between upper and lower left vertexes of the diagram.

while intensities about concentrations. To properly compute the percentage of each constituent, an additional test is required, the "*Loss on ignition*" (LOI). This index represent the weight loss which the sample undergoes when it is heated to a temperature by 960°C for several hours. This procedure causes the dissolution and volatilization of the organic and carbonate fractions, allowing their quantification by weighting the sample before and after the heating. The results of these geochemical analyses are summarized in figure 4.

The samples collected are insufficient for a rigorous validation of the lithological classification, however, they provide encouraging information. In fact they show that the main materials are properly identified and those materials which are not included in the classification (such as gypsum) correctly remain unclassified.

4 LAND RECLAMATION MONITORING

The analysis of time series of satellite images is a powerful tool for monitoring the changes taking place in a certain territory. In particular, the availability of Landsat time series allows to cover a period of almost thirty years, although not continuously. In the case of Fayyum oasis, the analysis of change detection can be used to quantify the expansion of cultivated land occurred over the last decades, as a result of land reclamation and upgrading of the irrigation network. Given that these cultivations are surrounded only by desert soils, the classification can be carried out by calculating appropriate ratios and defining a threshold. The change detection can be performed in post-classification, according to the conceptual scheme shown in figure 5.

To ensure a correct evaluation of the results, the image time series which is going to be analysed must meet the following requirements:

1. geometric correction: the images must be perfectly co-registered, to avoid the detection of spurious changes;

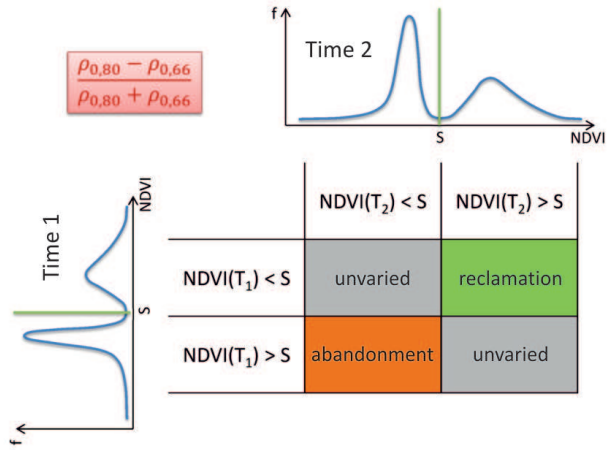

Figure 5: Conceptual framework for the analysis of change detection in post-classification. On the basis of a threshold value, to apply on the vegetation index, each pixel is tried for being classified as vegetated in a certain time, then a comparison is made with the next time step.

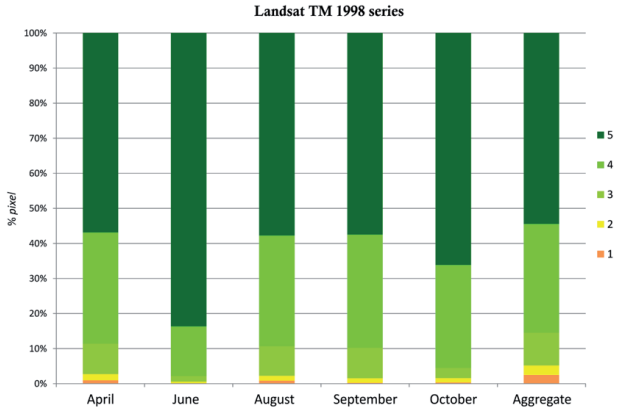

Figure 6: Statistics of the pixels classified as vegetation in each of the five images (taken in different seasons) and in the 1998 series considered as a whole. The colour refers to the number of images in which the same pixel results vegetated. The overall statistics on the right indicates that only 54% of pixels are classified as vegetated in all five images, and an additional 31% in four of the five images.

2. radiometric correction: if a unique threshold for all the images is adopted, each one must be calibrated and corrected for the atmospheric effects, at least in a relative way;

3. "temporal" correction: to avoid altered results, several seasonal effects, connected with ploughing cycles, must be addressed;

Maybe these corrections do not require a very high absolute accuracy, but the image time series should be as much *homogeneous* and *coherent* as possible.

From the radiometric point of view, this homogeneity can be obtained empirically with the following procedure. Firstly one image is chosen as reference and it is corrected by a radiative transfer model, parametrized with approximated values. In this case the 6SV model has been chosen because of its implementation of the "background desert" aerosol model, which appears particularly appropriate in this context. The 6SV model has been

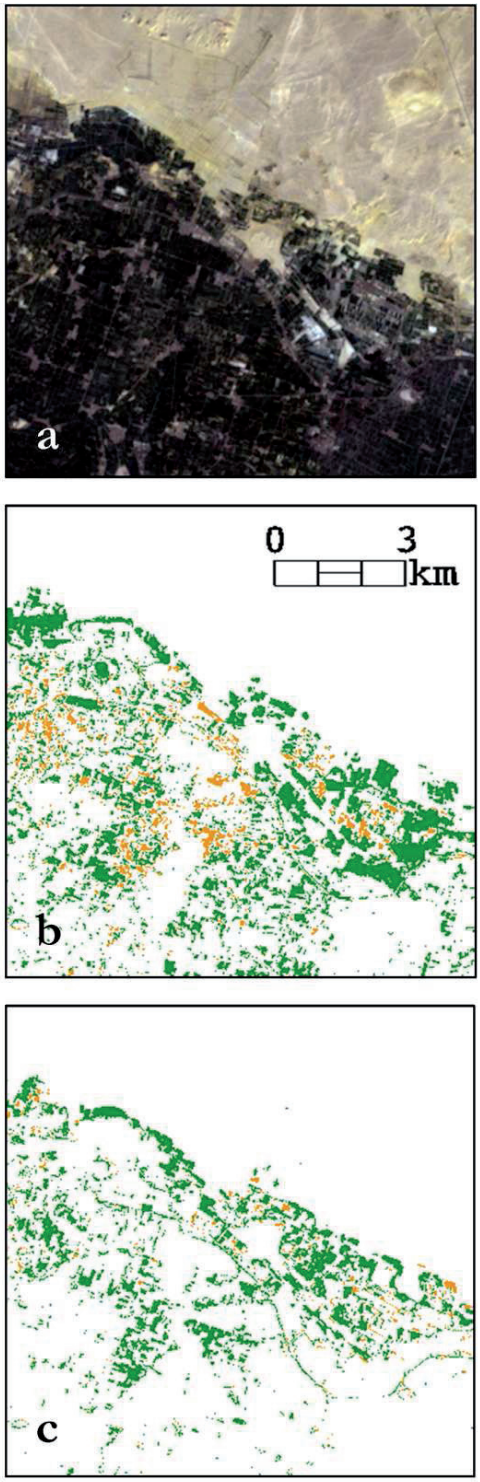

Figure 7: Example of identification of areas of farming expansion in the Fayyum oasis, precisely in the area surrounding the archaeological site of Bakchias. At the top, the true colour Landsat image of 2002 (a); in the middle, the land reclamation (green) occurred between 1984 and 1998 (b); at the bottom, between 1998 and 2002 (c). In ochre those areas which appear abandoned.

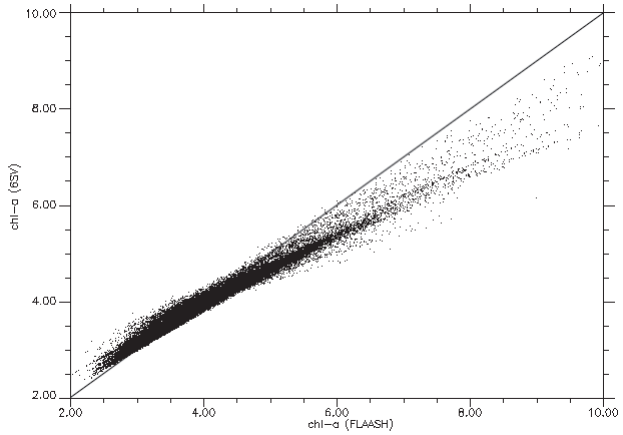

Figure 8: Scatter plot showing the differences between the chlorophyll concentration values computed by OC2 model, adopting the reflectance values obtained by FLAASH or 6SV models.

applied to the satellite images through the '*Visual SixS*', a software package developed by the author, which provides an user friendly graphical interface to the original 6SV and which adds specific routines to extend the support to Hyperion and World View 2 sensors (Mandanici, 2010). The second step consists in locating few pixels in correspondence of surfaces whose spectral characteristics can be assumed stable over time (for example the basalt outcrops in the north escarpment). Finally all the scenes of the time series are empirically calibrated on the reference one, performing an 'empirical line' on the invariable pixels.

The analysis of annual time series demonstrates also the strong influence of seasonal effects, due to the ploughing cycles and the variety of cultivated species. Figures 6 and 7 show the randomness of the results retrieved from a single scene and they highlight the opportunities to build the classification representative of a certain time by combining multiple images acquired in a relatively short lapse of time but in different seasons. Notwithstanding that the higher the redundancy the higher is the accuracy, the use of at least two images appears unavoidable, in order to achieve results which are not exclusively qualitative.

5 WATER QUALITY

Water quality is affected by both environmental and anthropic forces, thus the monitoring of its status is a vital task for the sustainable development of the entire area. The experimentation makes use of hyperspectral and multispectral images of Earth Observing 1 platform and Landsat ETM imagery. More precisely, two Hyperion and two ALI archive scenes acquired in August and September 2002, plus as many images acquired on demand in December 2009 and in October 2010 have been used for Lake Qarun. Since the signal reflected from water surfaces is very low, the main concern in the pre-processing chain is the radiometric calibration, especially the atmospheric correction. Several tests was conducted with different models (see figure 8), such as FLAASH and QUACK, both implemented in the ENVI software package, and Visual SixS (Bitelli and Mandanici, 2010a). The latter has been preferred, because it comes with a more appropriate aerosol model (the 'background desert') for the context of the study area. The aerosol model is in fact crucial for the chlorophyll concentration estimation, affecting mostly the visible wavelengths.

5.1 Chlorophyll concentration

The calculation of the concentration of chlorophyll-a was performed by using the OC4 model (Reilly, 2000). The Hyperion hyperspectral data has been spectrally resampled, using ENVI software, in order to simulate the SeaWiFS sensor acquisition bands, for which the OC4 model was originally developed. Before applying this procedure to Lake Qarun, some preliminary tests were carried out on Lake Garda (Bitelli and Mandanici, 2010b). They allowed to verify the effectiveness of the method by comparing the retrieved results with data published in literature and in particular with the results of a study by (Giardino et al., 2007), conducted on the same Hyperion image, by applying a rigorous bio-optical model.

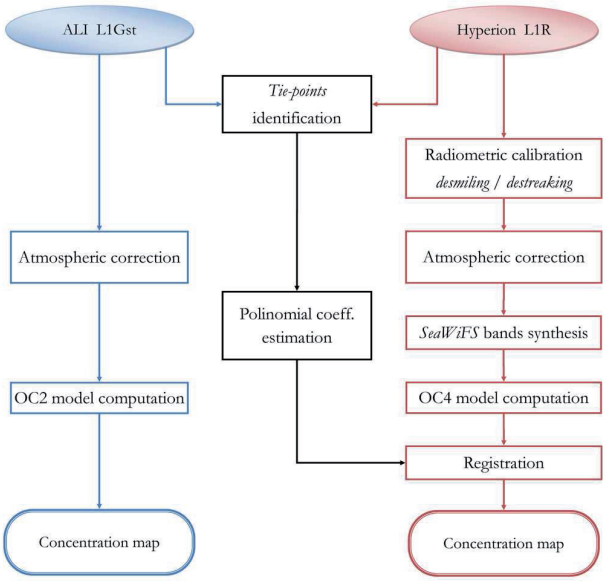

Figure 9: Outline of the processing work-flow to extract chlorophyll-a concentration from ALI and Hyperion satellite imagery.

Since the Hyperion scenes cover only a small extension of Lake Qarun (which is mainly elongated in East-West direction), the ALI sensor has been also used for a complete mapping. The ALI multispectral data consists of three bands in the visible and six ones in the infrared. The OC2 algorithm (Reilly, 2000) has been applied on these images, by virtue of the correspondence between the SeaWiFS bands used by this algorithm and those of ALI sensor (Bitelli and Mandanici, 2010b). The overall work-flow is shown in figure 9.

Detailed data about chlorophyll-a concentration in Lake Qarun are not available, but only average values for the entire lake or sporadic local information, often not fully documented (e.g. exact location or time of sampling missing). It is not possible therefore to perform a complete validation. Anyway the spatial distribution provided by the ALI multispectral images (figure 10) is consistent with the information available, resulting in a higher chlorophyll concentration in the eastern sector, near the main tributary inflows that carry nutrients. It should be noted, however, a strong underestimation of the absolute values of concentration, compared with average data in literature (Hussein et al., 2008). The difference, noticeable both in summer and in winter images, can be partly attributed to seasonal fluctuations, but further investigations are needed to establish the causes of this bias.

The comparison between the results provided by the OC4 model applied to Hyperion images (resampled to simulate SeaWiFS) and those obtained by OC2 model applied to ALI scenes is not straightforward (Bitelli and Mandanici, 2010a). In order to perform this comparison, the coefficient set required for a proper co-registration has been computed by identifying an adequate number of tie-points. The geometric transformation itself has not

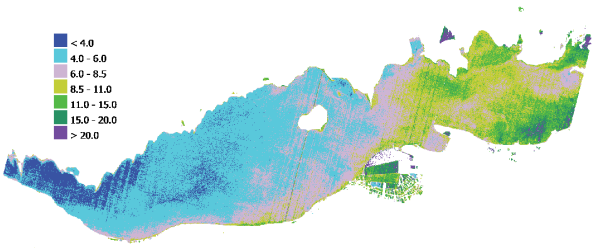

Figure 10: Chlorophyll-a concentration map, obtained by the ALI image acquired on 20th December 2009. The highest values occur in the eastern portion of the lake, in correspondence of the El-Batt canal mouth.

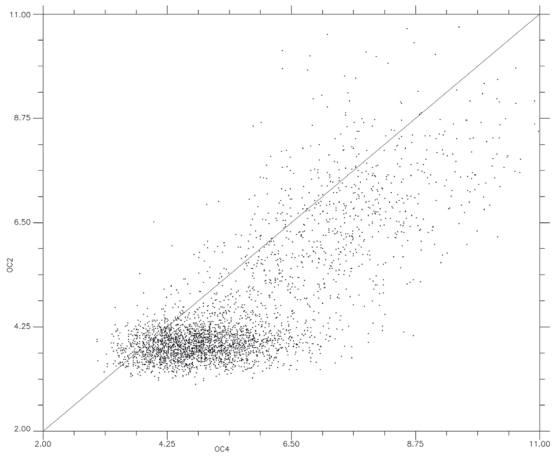

Figure 11: Scatter plot of the chlorophyll-a concentration values derived by the ALI-OC2 versus Hyperion-OC4 models. Even if the area is too limited for an exhaustive statistic, the values show a strong dispersion.

been applied to the original image but to the final chlorophyll concentration map, in order to avoid the influence of the resampling method on the retrieved values. Unfortunately, the overlap area is too small and the range of concentration values observed in this area is too limited to produce an exhaustive statistic. However a strong dispersion has been observed between ALI-OC2 and Hyperion-OC4 derived concentrations, as can be seen in figure 11.

5.2 Salinity

The adopted approach is empirical and it relies on in situ electrical conductivity measurements, by means of a conductivity meter. The approach is based on the conclusions of the work by (Lin and Brown, 1992), which highlight how the presence of sodium chloride in solution results in a decrease in intensity and a reduction in amplitude of the water absorption bands at the wavelengths of 1.5 μm and 2.1 μm. Assuming therefore that the multispectral sensor bands whose bandpass is close to those wavelengths can be sensitive to changes in salt content, while those far-off should not be affected, the following Water Absorption Salinity Index (WASI) is proposed:

$$WASI = \frac{\rho_{1.6} + \rho_{2.2}}{\rho_{0.8}} \quad (1)$$

in which the reflectance values ρ_λ in the involved bands appear. An increase in the numeric value of the index is expected to reflect an increase in the salinity of water, supposing that the reduced absorption causes an increase in reflectance only in those

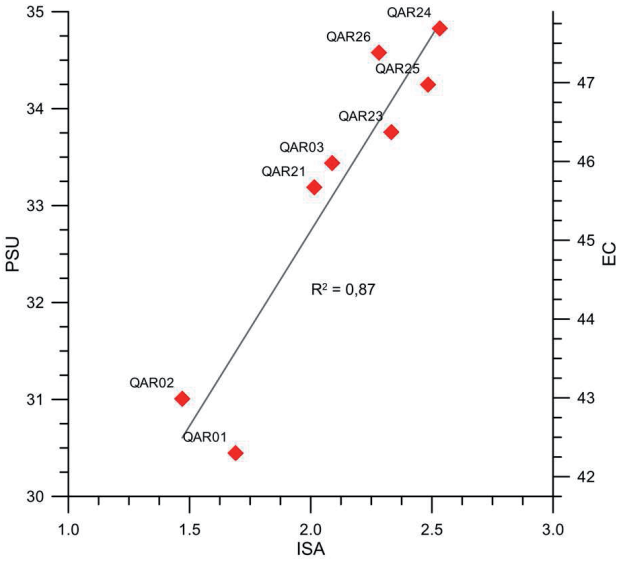

Figure 12: Correlation between WASI and practical salinity unit (PSU) values, obtained by in situ measurements carried out on Lake Qarun. On the right vertical axis the electrical conductivity (EC) values, expressed in μS/cm, are shown.

bands which appear at numerator. Of course the sodium chloride is not the only dissolved salt, but it can be assumed as the indicator, given its abundance and its spectral behaviour. In the case of the Fayyum oasis, the WASI has been computed adopting band 5, 7 and 4P of ALI sensor. The calculated values have been compared with the values of electrical conductivity measured in situ. As can be seen in the graph in figure 12, a good correlation has been found between the WASI values and the practical salinity units derived from conductivity measurements. However, the following aspects must be considered. The conversion from conductivity to practical salinity units, although not strictly appropriate for lake water (Williams and Sherwood, 1994), was performed to allow comparison with data from existing literature, but it does not alter the goodness of the correlation. In addition the point labelled QAR22 was discarded, because the conductivity value was found affected by a blunder.

Applying the coefficients computed by regression to the WASI values, the surface salinity map reported in figure 13 has been obtained. The retrieved values shows a good overall agreement with the seasonal averages reported in literature (Abd-Ellah, 2009). However, examining the results some problems arise. First, the reliability of the map is strongly influenced by the effect of the heavy stripe in the central portion of the lake. This effect makes less defined the salinity spot located south-west of the only island. The presence of this spot is not fictitious, as it is also visible to the left of striping lines. Obviously, only additional ground data will allow a proper validation.

5.3 Coastal water analysis

Given the problematic nature of the study of surface water salinity by remote sensing, it was decided to test the methodologies developed for the case of Lake Qarun on a second case study, the Adriatic coastal stretch between the Salinello and Tronto River mouths. Being the case of marine waters and not of a closed lake basin, the differences are profound. However, the two sites share a similar degree of salinity and marked eutrophication, therefore the comparison may be interesting. On 16th February 2011 some measurement operations were carried out on the coast of the Adriatic Sea between river Tronto and river Salinello mouths,

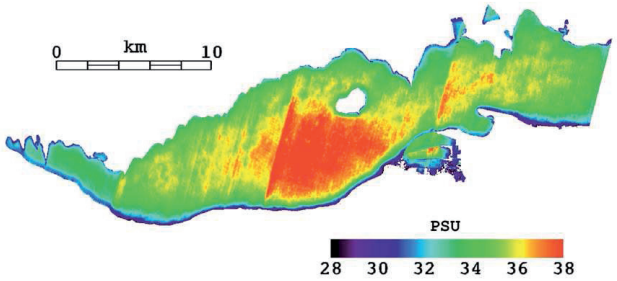

Figure 13: Surface salinity map of the Lake Qarun, obtained by the computation of WASI index on the ALI image acquired on 5th October 2010.

on board of a ship, belonging to the Professional Institute for Industry and Crafts of San Benedetto del Tronto. During five hours of navigation, eight samples of seawater were collected at the surface level; at the same time measurements of electrical conductivity were made.

Even for this case study, a good correlation has been found between the values of the WASI and PSU obtained from conductivity measurements. In this case the calculations have been made on a Landsat 7 ETM image acquired on January 12th 2011, being not available images of the EO1 platform. Unfortunately, the temporal distance between the image acquisition and the ground measurements is excessive, but inevitable because of the particularly unfavourable cloud cover during the period. The main limitation of Landsat imagery for this application is the radiometric resolution of eight bits only, which results in more noisy patterns of the WASI values. Furthermore it makes particularly difficult to perform the atmospheric correction on water surfaces, which are characterized, as known, by low values of radiance. The different sensor characteristics and the unfavourable atmospheric conditions may explain the differences in the coefficients of the empirical relationship between WASI and practical salinity.

6 CONCLUSIONS

The experiments carried out on the case studies of the Fayyum oasis in Egypt have allowed to track the entire information extraction process from multispectral and hyperspectral satellite imagery for environmental applications. The results obtained in the lithological classification, the reclamation monitoring and the water quality analyses, although partial because not yet fully validated on the ground, allow to highlight the potential of remote sensing as a key tool for the landscape monitoring at regional scale. What is most interesting is the possibility offered by remote sensing to link the contents and methods of different disciplines, such as chemistry, geology and biology, into a unified methodological approach. Just the cooperation between different research facilities has resulted in a significant amount of data from a few samples on the ground.

The highly interdisciplinary approach, pursued for the entire research, has also allowed to underline many critical issues that must be addressed in the processing of remote sensing data itself and particularly in comparing the information provided by the distinct analysis techniques of each discipline. The requirements of even the slightest amount of ground data, specially acquired or indirectly derived from other products, is a common factor in any remote sensing application, at least for validation purpose. Also here lies the need for an interdisciplinary approach, which should not be perceived as a limitation on remote sensing, but rather as a strength, thanks to which bringing the methodologies of different disciplines into a spatially and temporally integrated description of the landscape and the environmental dynamics.

ACKNOWLEDGEMENTS

The list of the people whose helpfulness makes this work possible is quite long. Firstly, the author is grateful to Prof. Gabriele Bitelli and Prof. Pietro V. Curzi for their confidence during the entire PhD programme. Secondly, a special thank must be addressed to the Archaeology Department team of the University of Bologna, directed by Prof. Sergio Pernigotti, for their help during the survey in Egypt. Finally, for the analyses of the ground samples, the author would like to thank Prof. Enrico Dinelli of the Earth Science Dept. of Bologna University and Prof. Rosamaria Salvatori of the Institute of Atmospheric Pollution Research of the National Research Council (CNR IIA) in Rome.

REFERENCES

Abd-Ellah, R. G., 2009. Outlook on past, present and future status of water salinity in lake qarun, egypt. World Journal of Fish and Marine Sciences 1(1), pp. 51–55.

Abdel-Fattah, Z. A., Gingras, M. K., Caldwell, M. W. and Pemberton, S. G., 2010. Sedimentary environments and depositional characteristics of the middle to upper eocene whale-bearing succession in the fayum depression, egypt. Sedimentology 57(2), pp. 446–476.

Bitelli, G. and Mandanici, E., 2010a. Atmospheric correction issues for water quality assessment from remote sensing: the case of lake qarun (egypt). In: U. Michel and D. L. Civco (eds), Earth Resources and Environmental Remote Sensing/GIS Applications Conference (Proceedings Volume), Vol. 7831, SPIE, p. 78311Z.

Bitelli, G. and Mandanici, E., 2010b. Utilizzo del modello oc-4 con dati iperspettrali per la caratterizzazione di acque lacustri. In: Atti XIV Conferenza ASITA, Brescia.

Bitelli, G., Curzi, P. V. and Mandanici, E., 2009. Morphological and lithological aspects in the northeastern libyan desert by remote sensing. In: U. Michel and D. L. Civco (eds), Remote Sensing for Environmental Monitoring, GIS Applications, and Geology IX (Proceedings Volume), Vol. 7478, SPIE, p. 74781W.

Bown, T. M., Kraus, M. J., Wing, S. L., Fleagle, A. J. G., Tiffney, B. H., Simons, E. L. and Vondra, C. F., 1986. The fayum primate forest revisited. Journal of Human Evolution 11, pp. 503–560.

Dolson, J., El-Barkooky, A., Wehr, F., Gingerich, P. D., Prochazka, N. and Shann, M., 2002. The eocene and oligocene paleo-ecology and paleo-geography of whale valley and the fayoum basin: implications for hydrocarbon exploration in the nile delta and eco-tourism in the greater fayoum basin. Technical report, American Association of Petroleum Geologists, Egypt Petroleum Exploration Society, Society of Exploration Geophysicists, Egyptian Geophysical Society, European Association of Geologists & Engineers.

El-Shabrawy, G. M. and Dumont, H. J., 2009. The fayum depression and its lakes. In: H. J. Dumont (ed.), The Nile. Origin, environments, limnology and human use., Monographiae Biologicae, Vol. 89, Springer, chapter 6, pp. 95–124.

Giardino, C., Brando, V. E., Dekker, A. G., Strömbeck, N. and Candiani, G., 2007. Assessment of water quality in lake garda (italy) using hyperion. Remote Sensing of Environment 109(2), pp. 183–195.

Hussein, H., Amer, R., Gaballah, A., Refaat, Y. and Abdel-Wahab, A., 2008. Polluton monitoring for lake qarun. Advances in Environmental Biology 2(2), pp. 70–80.

Kalinowski, A. and Oliver, S., 2004. ASTER Mineral Index Processing Manual. Remote Sensing Applications, Geoscience Australia.

Kusky, T. M., Ramadan, T. M., Hassaan, M. M. and Gabr, S., 2011. Structural and tectonic evolution of el-faiyum depression, north western desert, egypt based on analysis of landsat etm+, and srtm data. Journal of Earth Science 22(1), pp. 75–100.

Lin, J. and Brown, C. W., 1992. Near-ir spectroscopic determination of nacl in aqueous solution. Applied Spectroscopy 46(12), pp. 1809–1815.

Mandanici, E., 2010. Implementation of hyperion sensor routine in 6sv radiative transfer code. In: H. Lacoste-Francis (ed.), Proc. Hyperspectral Workshop, Vol. SP-683, ESA, Frascati.

Reilly, J. E., 2000. Seawifs postlaunch calibration and validation analyses, part 3. Technical Report 2000-206892(2), NASA Technical memorandum.

Swedan, A. H., 1992. Stratigraphy of the eocene sediments in the fayum area. Annals of the Geological Survey of Egypt V(XVIII), pp. 157–166.

Tawadros, E., 2001. Geology of Egypt and Lybia. A. A. Balkema.

Williams, W. and Sherwood, J., 1994. Definition and measurement of salinity in salt lakes. International Journal of Salt Lake Research 3, pp. 53–63.

TIME-OF-FLIGHT CAMERAS: TESTS, CALIBRATION AND MULTI-FRAME REGISTRATION FOR AUTOMATIC 3D OBJECT RECONSTRUCTION

D. Piatti [a]

[a]DITAG, Politecnico di Torino, Corso Duca Degli Abruzzi 24, 10129 Torino, Italy - dario.piatti@polito.it

KEY WORDS: Time-of-Flight, RIM camera, distance calibration, multi-frame, automatic registration, 3D reconstruction

ABSTRACT:

Time-of-Flight (ToF) cameras are new devices based on CCD/CMOS sensors which measure distances instead of radiometry at high speed (video frame rates). Since their first realizations, ToF cameras have shown a lot of interest in the scientific community, especially related to computer vision, computer graphics and robotics fields. Several improvements in both sensor resolution and data reliability have been carried on by the ToF camera manufacturers in ten years and, also thanks to these improvements, the fields of application have surprisingly enlarged. Current ToF cameras allow to acquire point clouds which show the same properties (both in terms of accuracy and resolution) of the point clouds acquired by means of traditional LiDAR devices; moreover, their cost is usually lower than ten thousands euros and their weight and dimensions allow a reduction of some practical problems such as transportation and on-site management. Nevertheless, the distance measurement performed by ToF cameras are usually characterized by some systematic errors, which have to be reduced in order to allow their usage for metric survey purposes.
The thesis is centred on two main topics: first, the development of procedures for measurement accuracy and precision evaluation and calibration of commercial ToF cameras; second, the use of ToF cameras in the Geomatics field, with the final aim of 3D object reconstruction. In particular, an innovative algorithm which allows to automatically perform the registration of point clouds acquired by ToF cameras without any reference target and an original filter for outlier elimination from the acquired data are proposed.

1. INTRODUCTION

In the last few years a new generation of active sensors (called Time-of-Flight (ToF) cameras or Range IMaging (RIM) cameras) has been developed, which allows to acquire 3D point clouds without any scanning mechanism and from just one point of view at video frame rates. The working principle is the measurement of the ToF of an emitted signal by the device towards the object to be observed, with the advantage of simultaneously measuring the distance information for each pixel of the camera sensor.
Such a technology is possible because of the miniaturization of the semiconductor technology and the evolvement of the CCD/CMOS processes that can be implemented independently for each pixel. The result is the possibility to acquire distance measurements for each pixel at high speed and with accuracies up to about one centimeter. While ToF cameras based on the phase-shift measurement usually have a working range limited to 10-30 m, RIM cameras based on the direct ToF measurement can measure distances up to 1500 m. Moreover, ToF cameras are usually characterized by low resolution (no more than a few thousands of tens of pixels), small dimensions, costs that are an order of magnitude lower with respect to LiDAR instruments and a lower power consumption with respect to classical laser scanners. In contrast to stereo, the depth accuracy is practically independent of textural appearance, but limited to about one centimeter in the best case (actual phase-shift commercial ToF cameras).

1.1 Motivation

At present the ability to capture the surrounding area at high speed in three dimensions is one of the most challenging tasks in many fields, such as industrial automation and production, mobile mapping, monitoring, automotive safety, autonomous mobile robotics and gaming.
For both dynamic and static scenes there is no low-price off-the-self system that provides full range, high-resolution distance information in real time such as in the case of ToF cameras.
Nevertheless, RIM cameras are usually characterized by some systematic measurement errors, which can strongly worsen the achievable distance measurement accuracy up to tens of centimeters in some cases. Therefore, suitable calibration procedures have to be developed.
One of the main topic of the thesis is to propose systematic procedures for the distance calibration of commercial ToF cameras, in order to estimate and increase their measurement accuracy. The calibration procedure presented in this work belongs to the direct calibration methods, since the distance measurement accuracy of RIM cameras is directly estimated and the resulting systematic errors are modeled. The main idea is to propose a procedure which does not require additional digital cameras or cost-effective high precision measurement racks or robot-arms to calibrate ToF cameras and which can be applied to any kind of RIM camera.
Suitable experimental tests are proposed in order to analyze the influence of several factors on the distance measurements, such as the camera warm-up during working time, the angle of incidence between the camera axis and the object surface, the presence of foreground objects close to the camera and the object reflectivity.
The second main topic of this work is the use of ToF cameras in the Geomatics field, with the final aim of 3D object reconstruction. Since ToF cameras acquire 3D point clouds at video frame rates, this potentiality can surely be exploited for this purpose. The main problem to be faced is the registration of the point clouds acquired from different view-points with ToF cameras. For this purpose, an algorithm for ToF point cloud

registration has been developed, which is called multi-frame registration algorithm. Exploiting both the amplitude images and the 3D information delivered by ToF cameras, the proposed algorithm allows to automatically perform the point cloud registration with a final accuracy which is very close to the measurement accuracy of the employed device. Another challenging topic proposed in the thesis (but not reported in this work) is the integration between ToF data and a multi-image matching approach for automatic 3D object breakline extraction, which can be very useful to speed-up the drawing production of the surveyed objects. In both cases, some improvements are proposed and discussed for future developments.

2. TOF CAMERAS

There are two main approaches currently employed in ToF camera technology: one measures distance by means of direct measurement of the runtime of a travelled light pulse, using for instance arrays of single-photon avalanche diodes (SPADs) (Albota et al., 2002; Rochas et al., 2003) or an optical shutter technology (Gvili et al., 2003); the other method uses amplitude modulated light and obtains distance information by measuring the phase difference between a reference signal and the reflected signal (Lange, 2000). While RIM cameras based on the phase-shift measurement usually have a working range limited to 10-30 m, ToF cameras based on the direct ToF measurement can measure distances up to 1500 m.
ToF cameras based on the phase-shift method usually deliver a range image and an amplitude image at video frame rates: the range image (or depth image) contains for each pixel the radial measured distance between the considered pixel and its projection on the observed object, while the amplitude image contains for each pixel the strength of the reflected signal by the object. In some cases an intensity image is also delivered, which represents the mean of the total light incident on the sensor (reflected modulated signal and background light of the observed scene). In some case, a sort of confidence map or flag matrix is also delivered, which contains information about the goodness of the acquired data (i.e. saturated pixels, low signal amplitudes,…). Usually, a 3D point cloud (with X, Y and Z coordinates referred to a coordinate system internal to the camera) is also delivered, with coordinates which have already been corrected form lens distortion by the camera manufacturer.

2.1 Typical distance measurement errors

As in all distance measurement devices, ToF cameras are typically characterized by both random and systematic distance measurement errors. In some cases, the influence of systematic errors has been strongly reduced by the manufactures, while other camera models still suffer from these error sources, thus limiting their actual applicability without suitable distance calibrations.
According to (Lange, 2000), typical sources of noise in solid state sensors can be subdivided in three different classes: photocharge conversion noise, quantization noise and electronic shot noise, also called quantum noise. Electronic shot noise is the most dominating noise source and cannot be suppressed.
Typical non-systematic errors in ToF distance measurements are caused by pixel saturation, “internal scattering”, “multipath effect”, “mixed pixels” and “motion artifacts”.
A pixel saturates when it gets too much signal: the resulting measurement is usually null or affected by gross errors. The saturation is often reached due to surfaces with high reflectivity to the camera signal or due to the presence of high levels of background light (i.e. sunlight).
Some models of ToF cameras suffer from the so called “internal scattering” artifacts: their depth measurements are degraded by multiple internal reflections of the received signal occurring between the camera lens and the image sensor. A common problem to all ToF cameras based on phase shift measurement is the “multipath effect” (or “external superimposition”), especially in the case of concave surfaces: small parts of diffusely reflected light from different surfaces of the object may superimpose the directly reflected signals on their way back to the camera. A common problem in data acquired with ToF cameras is represented by the so called “mixed pixels” or “flying pixels” or “jumping edges”: they are errant 3D data resulting from the way ToF cameras process multiple returns of the emitted signal. These multiple returns occur when a light beam hits the edge of an object and the beam is split: part of the beam is reflected by the object, while the other part continues and may be reflected by another object beyond. The measured reflected signal therefore contains multiple range returns and usually the reported range measurement for that particular ray vector is an average of those multiple returns. Finally, when dealing with real time applications or moving objects, the so called “motion artifacts” could affect the acquired data.
The result is that ToF data are often noisy and characterized by several systematic and random errors, which have to be reduced in order to allow the use of RIM cameras for metric survey purposes.

2.2 Measurement parameters

The most important measurement parameters using ToF camera based on the phase shift principle are the modulation frequency (f_{mod}) of the emitted signal and the Integration Time (IT) of the measurement.
The modulation frequency is in inverse proportion with respect to the signal wavelength and therefore to the “non-ambiguous range”[1]: higher is the modulation frequency, smaller the “non-ambiguous range” and lower the standard deviation of the distance measurements (σ_R). This statement originates from the following formulation of the standard deviation of the distance measurements (Büttgen et al., 2007):

$$\sigma_R = \frac{c}{4\pi \cdot f_{\mathrm{mod}} \cdot \sqrt{2}} \cdot \frac{\sqrt{B}}{c_{de\,\mathrm{mod}} \cdot A} \qquad (1)$$

where c is the speed of light, A is the amplitude of the reflected signal, B is the mean intensity of the reflected signal and c_{demod} is called demodulation contrast of the system: it represents the accuracy of the phase measurements and mainly depends on the pixel structure. More in detail, it describes the overall demodulation performance of the system: it is defined as the ratio between a value of measured amplitude electrons and the total number of electrons generated by the signal (Lange, 2000). Most of the recent cameras allow to use more than one modulation frequency, in order to allow multiple cameras working together.
According to (Anderson et al., 2005), the standard deviation of the distance measurements in the case of devices based on the phase shift method (Amplitude Modulated Continuous Wavelength – AMCW) is directly proportional to the signal wavelength λ and to the square of the measured distance R,

[1] The “non-ambiguous range” is equal to half of the wavelength of the employed signal.

while it is inversely proportional to the object reflectivity ρ and the cosine of the angle of incidence α:

$$\sigma_R \propto \frac{\lambda \cdot R^2}{\rho \cdot \cos\alpha} \quad (2)$$

Therefore, if the energy of the emitted signal is maintained constant (i.e. constant IT), the standard deviation of the distance measurements is strongly influenced by the distance between camera and object, the object reflectivity and the camera orientation with respect to the object surfaces. Specific tests have been performed about influence of both angle of incidence and object reflectivity on ToF distance measurements in the thesis.

The other fundamental measurement parameter is the integration time, which represents the length of time that the pixels are allowed to collect light. This parameter has several influences on the distance measurements. In particular, an increasing of the integration time (maintaining all other factors constant, such as distance to the object, object reflectivity, room temperature, modulation frequency, angle of incidence…) leads to several effects, such as: a better Signal to Noise Ratio (SNR) and, consequently, more precise data; since more time is requested to acquire a single frame, the data acquisition speed (frame rate) decreases; the discrepancy between real distance and measured distance may show little variations changing the integration time: an increasing integration time usually leads to slightly measured distances; since the illumination unit (e.g. LEDs) has to be on for longer periods, more heat is created in the system, which may influence the distance measurements stability.

3. DISTANCE CALIBRATION

In this work, the direct determination of systematic errors in the distance measurements of ToF cameras is performed. Even if this method requires more efforts in terms of accurate reference data acquisition, in this way the systematic errors are observed as directly as possible. The guiding principle of the performed tests is the "separation of variables": once the parameters which influence the distance measurements have been individuated thanks to experimental results and/or information from literature, the influence of each parameter on acquired data is analysed keeping all other parameters constant. Then, an attempt to model the systematic errors is performed, in order to increase the measurement accuracy of the device. Adopting the separation of variables should be a correct way to perform a systematic investigation of possible systematic error sources.

This chapter faces with the most significant experimental tests performed using the SR-4000 camera (Mesa Imaging) in order to analyse the main parameters which influence the distance measurements of the camera. Some of these tests have already been performed with the PMDCamCube3.0 camera (PMDTechnologies GmbH) too and reported in the following. Both the theoretical and experimental aspects are proposed in order to provide some procedures and methodologies which can be adopted for the distance calibration of any ToF camera model.

3.1 Warm up time period evaluation

Since semiconductor materials are highly responsive to temperature changes, temperature variations within a ToF camera can affect its distance measurements. In order to determine the warm up time period necessary to achieve distance measurement stability of the tested ToF cameras, the procedure described in the following was carried out. The influence of external temperature was not analysed in this work since no climate chamber was available.

The test consisted in positioning both the SR-4000 and the PMDCamCube3.0 cameras in front of a wall and acquiring data at several distances and integration times. The room temperature was maintained constant (20°C) for all the tests and the distance measurements were analysed for two hours of camera working in each test.

For each case five frames (range images) were acquired every five minutes of camera working and then averaged pixel by pixel in order to reduce the measurement noise. Since both cameras were not moved from their position in each test, variations during the working time of the mean and standard deviation of the averaged range images were considered.

In the case of the SR-4000 camera both the mean value and the standard deviation of the distance measurements vary during working time: a maximum variation of about -6 mm was detected for the mean value, while a maximum variation of about 3 mm was measured for the standard deviation. In the case of the PMDCamCube3.0 camera a maximum variation of about 120 mm was detected for the mean value, while a maximum variation of about 4 mm was measured for the standard deviation. Since the calculated variations are nearly constant after forty minutes of camera working, one can stand that a warm up period of forty minutes is sufficient to achieve a good measurement stability and therefore to exploit the best measurement performances in both cases.

Moreover, the camera warm up period is highly recommended in the PMDCamCube3.0 case, in order to avoid distance errors of several centimeters. Therefore, all the following tests were performed after this warm up period of about forty minutes.

3.2 Integration time and distance measurement precision

In order to estimate the precision (standard deviation) of the distance measurements acquired by the sensor pixels (n pixels), the following test was performed. Both cameras were positioned on a photographic tripod, parallel to a white wall. Then, 100 frames were acquired for several integration times. The test was then repeated at several distances between camera and wall.

For each pixel i, the mean value ($d_{i,m}$) and the standard deviation (σ_i) of the acquired distance measurements (number of frames $f = 100$) were estimated.

Besides other quantities, the mean value of the estimated standard deviations (m_σ) for all the pixels (n), which represents the mean precision of the sensor, was estimated for each test (i. e. for each integration time and each camera position of the two devices):

$$m_\sigma = \frac{\sum_{i=1}^{n} \sigma_i}{n} \quad (3)$$

As a term of example, in Figure 1 and Figure 2 a 3D representation of the σ_i term for each pixel of the whole sensor for both cameras is reported. The results of the test demonstrate that the measurement precision is higher in the central part of the sensor, since the signal amplitude is higher, as it was expected.

While for the SR-4000 camera only small variations of the mean value of the measured distances are detected considering different integration times, for the PMDCamCube3.0 camera

these variations are bigger (variations up to 0.040-0.050 m are observed).

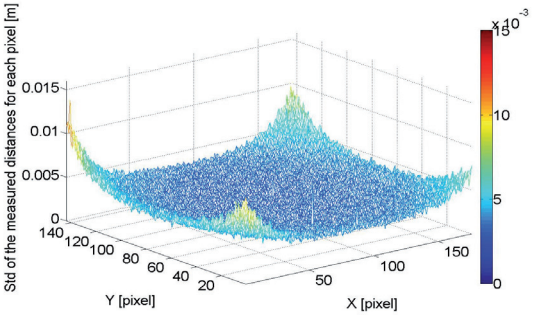

Figure 1. 3D representation of the σ_i over the whole sensor (SR-4000) (distance camera-wall: 1.30 m, IT 11 ms) (the color-bar is in meters)

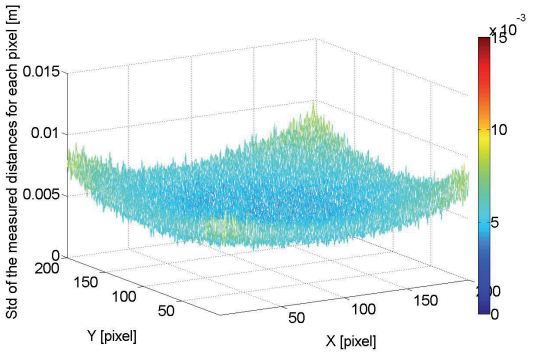

Figure 2. 3D representation of the σ_i term over the whole sensor (PMDCamCube3.0) (distance camera-wall: 1.30 m, IT 7 ms) (the color-bar is in meters)

These variations, which are related to the integration time changing, have to be taken into account when calibrating this sensor. Future works will deal with this aspect.

Finally, this test shows how important is the relation between the strength of the reflected signal and the distance measurement precision, which directly derives from equation (1). For this reason, it is important to properly adjust the integration time in order to have the highest amplitude values without reaching pixel saturation.

3.3 Distance measurement accuracy evaluation

The distance calibration procedure presented in this work belongs to the direct calibration methods, since the distance measurement accuracy of the ToF camera is directly estimated and the resulting systematic errors are modeled.

The proposed procedure does not require additional digital cameras or cost-effective high precision measurement racks or robot-arms. The following calibration method can be applied to any kind of ToF camera. Anyway, in this work only the results relative to the SR-4000 camera are reported, since only some preliminary tests have been performed on the PMDCamCube3.0 camera up to the publication of this work.

The proposed calibration procedure represents a way to obtain with a low-cost custom-made system a distance error model of the ToF camera distance measurements, that would be unique for all the camera pixels and which could be applied to data acquired with the standard software supplied with the tested camera.

Despite to many previous works in which only the central sensor pixel was considered, in this case the distance measurement errors are determined and modeled for a big central area of the camera sensor. The whole sensor was not considered because of the unmanageable geometric dimensions of the reference panel which would be necessary to fulfill the entire sensor also at the upper bound of the camera working range.

Suitable check measurements are acquired and comparisons with respect to LiDAR data on real objects are also reported in the thesis, in order to validate the proposed distance error model.

3.3.1 Data acquisition

The camera was positioned parallel to a vertical plywood panel (1.85 m × 2.52 m) supported by two adjustable tripods. The distance between the camera front and the panel was accurately measured using two parallel metal tape-measures. This solution was designed in order to obtain an economic way to directly estimate the camera distance measurement accuracy. Unfortunately, since the purchased panel wasn't perfectly flat, LiDAR and total station surveys of the plywood were performed in order to create a detailed model of the panel. A Mensi S10 laser scanner, which acquired about 780000 points with sub-millimetric precision, was employed.

After the camera warm up, the panel was positioned each five centimetres in the 0.50 ÷ 4.50 m distance range between the camera front and the plywood. Thirty consecutive frames were acquired for each panel position, using an acquisition time equal to the "auto acquisition time" suggested by the SR_3D_View software (Mesa Imaging).

The acquired data were processed using a custom-made Matlab® application in order to evaluate the distance measurement errors and estimate the distance error model. Since the panel did not fill the entire images delivered by the camera in almost half of the test distance gap, the analysis was limited to 7921 pixels which are contained in a sub-image of 89 × 89 pixels centered with respect to the central pixel of the camera sensor. For pixel in row i and column j position, the following terms were defined:

$$h_{i,j} = r_{i,j} - \frac{\sum_{f=1}^{n} m_{i,j,f}}{n} \tag{4}$$

$$g = \frac{\sum_{i=1}^{89}\sum_{j=1}^{89} h_{i,j}}{7921} \tag{5}$$

$$s = \frac{\sum_{i=1}^{89}\sum_{j=1}^{89}\sum_{f=1}^{n} r_{i,j,f}}{7921} \tag{6}$$

where, for each camera position: $h_{i,j}$ is the discrepancy between real distance and mean distance measured by pixel i,j; $r_{i,j}$ is the real distance between pixel i,j and its orthogonal projection on the panel; f represents a generic frame; n = 30 is the number of acquired frames for each position; $m_{i,j,f}$ is the measured distance for pixel i,j at the f-th frame.

The term $r_{i,j}$ is obtained combining the accurate metal tape measurements with the panel model in order to take into account the panel curvatures.

In equation (5), term g represents the mean value of the discrepancies $h_{i,j}$ for all the considered pixels in the area of analysis for a certain camera position. Term s in equation (6) represents the mean value of the measured distances for all the

considered pixels in the area of analysis for a certain camera position.
The variation of the mean values of the discrepancies (g) of all the considered pixels according to the mean measured distance (s) is reported in Figure 3: the discrepancies between measured distance and real distance show a maximum value of 0.011 m and a minimum value of –0.008 mm. These measurement errors are smaller than those of other Swiss Ranger cameras tested in previous works (e.g. Kahlmann et al., 2006; Weyer et al., 2008), since in the SR-4000 model many improvements have been made on this aspect. The obtained results reflect the declared absolute measurement accuracy of ±0.01 m for the SR-4000 camera (Mesa Imaging).
However, from Figure 3 one can observe that a systematic trend of the measurement errors still remains which needs to be corrected. These measurement errors (discrepancies) have been modeled with the following distance error model (e):

$$e = \lambda_0 + \lambda_1 \cdot m \cdot \sin(\lambda_2 \cdot m + \lambda_3) \quad (7)$$

where m is the pixel measured distance, λ_0 is a constant error and λ_1 represents a scale factor which multiplies a "wiggling error" modeled by a sinusoidal function (λ_2 = angular frequency, λ_3 = phase shift).

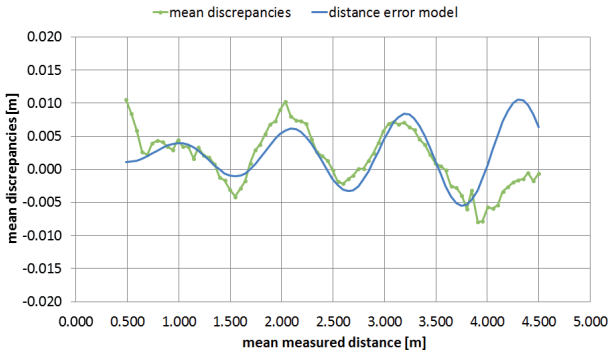

Figure 3. Variation of the mean values of the discrepancies (g) of all the considered pixels according to the mean measured distance (s) and distance error model.

As shown in Figure 3, the proposed distance error model well fits the distance measurement errors, apart from distances smaller than 0.7 m and larger than 3.7 m. The parameter values have been estimated by minimization of the square root of the squared differences between the experimental data and the distance error model function.
Also other models have been tested, in order to better fit the experimental data; nevertheless, in order to avoid over-parameterization and too complex models, the one proposed in equation (7) has been chosen.

3.3.2 Control measurements

In order to have a first check of the proposed distance error model, a procedure similar to the one adopted for the distance measurement accuracy estimation was adopted. After the camera warm up, the panel was randomly positioned at several distances from the camera, acquiring data with the "auto acquisition time". After averaging the thirty frames acquired for each position, each pixel distance measurement was corrected with the distance error model of equation (7). The mean values of the residual discrepancies for 7921 pixels are represented in Figure 4.
Figure 4 shows that, after applying the proposed distance error model of equation (7), the absolute values of residual discrepancies are smaller than the discrepancies without correction in the 1.5–4.0 m distance measurement range.

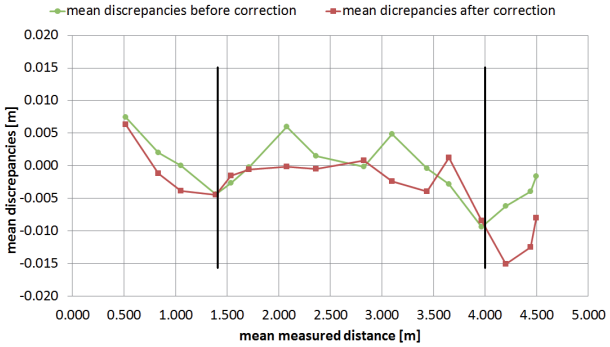

Figure 4. Mean values of the discrepancies (g) of all the considered pixels before and after distance error model correction.

For measurement distances up to about 1.5 m and longer than 4.0 m, the proposed distance error model generates greater absolute residual discrepancy values; in fact, as can be observed from Figure 3, this model badly fits distance deviations especially for longer distances than 4.0 m.
Since the 1.5–4.0 m distance measurement range is the most useful measurement range for the applications of the author's research group (architectural and archaeological surveys, object modeling and 3D indoor scene reconstruction), the proposed model is suitable for the aforementioned applications. Nevertheless, some attempts will be made in the future to improve this aspect. For instance, the measurement errors for distances shorter than 1.5 m and longer than 4.0 m could be modelled by polynomial functions.
Further confirmations of the validity of the proposed distance error model are presented in other tests reported in the thesis, related to quantitative comparisons with LiDAR data on real objects and study of influence of object reflectivity on distance measurements.

4. TOF POINT CLOUD REGISTRATION

One of the most commonly used algorithms for point cloud registration is the ICP approach. Nevertheless, registration of point clouds with only partial overlap is often trapped in local minima, especially when the sensor field of view is small, such as in the case of ToF cameras. As a consequence, the registration usually lacks in precision (Wang et al., 2009). Since ToF cameras deliver 2D images (amplitude and/or intensity images) and 3D point clouds, both kind of data can be exploited in order to perform the 3D point cloud registration. This is why, in the proposed method, the registration is performed by using both matched features on consecutive amplitude images and the 3D data acquired with a ToF camera.
A wide variety of scale and rotation invariant feature extraction methods have already been proposed for finding correspondences between images. The SIFT (Lowe, 2004) and SURF (Bay et al., 2008) methods are the most popular ones. The main strength of them is to produce a feature descriptor that allows quick and highly discriminatory comparisons with other features. As reported in the thesis, some works have already used one of these two feature detection algorithms in order to extract homologous points from adjacent amplitude/intensity images acquired with ToF cameras.

4.1 ToF data acquisition setup

In the proposed method, the SURF detection and matching algorithm is employed, since previous works, i.e. (Wang et al., 2009), demonstrated that it detects more features in small sensor configuration (as in the case of ToF cameras) and it is much faster with respect to the SIFT algorithm.
In this first realization, the proposed approach is related to the following scene acquisition conditions: the ToF camera acquisitions are performed from a stable position (i.e. photographic tripod) in order to acquire several frames (e.g. 10÷30) of a static scene; in this way, it is possible to average the acquired frames in order to reduce the measurement noise. Moreover, several camera positions are adopted, in order to survey the entire object, remembering to maintain an overlap of at least 50% between consecutive camera viewpoints. The choice of acquiring data from few static camera positions is justified by two main reasons: measurement noise reduction thanks to multi-frame acquisition, since the frames acquired from the same position are averaged pixel by pixel; limitation of the accumulated registration error: if the number of consecutive 3D point clouds to be registered increases, the accumulated registration error inevitably increases. The integration time is adjusted for each camera position, in order to avoid saturated pixels while maintaining high amplitude values and, therefore, precise distance measurements.

4.2 Algorithm description

Since ToF cameras deliver 2D images (amplitude and/or intensity images) and 3D point clouds, both kind of data are exploited in order to better perform the 3D point cloud registration. The proposed registration algorithm can be summarized in several processing phases (Figure 5), which are related to the registration of only two successive camera positions for simplicity.
Referring to two camera positions, let data acquired from the first camera position be in the local coordinate system *1*, while data acquired from the second camera position be in the local coordinate system *2*. First, a distance calibration model (if available) is applied to the acquired distance measurements, in order to reduce the systematic distance measurement errors. Then, the saturated pixels are automatically removed from the amplitude images, which have been averaged over *f* frames in order to reduce the measurement noise, and replaced by bilinear interpolation weighted on confidence values of the eight neighborhood pixels; this is necessary in order to avoid low contrast amplitude images, which can decrease the SURF performance. After that, the SURF algorithm is applied, in order to find matches between amplitude image *1* and amplitude image *2* (both averaged over *f* frames). The amplitude images do not need to be corrected from lens distortion since all their pixels exactly match the ones in corresponding *x*,*y*,*z* point cloud delivered by the ToF camera, which is already corrected from lens distortion[2]. A confidence threshold is applied to the matched features, in order to avoid unreliable pixel measurements. Moreover, a control is made in order to exclude the matches which are related to mixed pixels, thanks to the Mixed Pixel Removal (MPR) filter (see 4.3 Mixed Pixel Removal filter).
In this way, *m* homologous points/matches are obtained. Since the *m* points can still contain outliers and the least square solution is efficient by not robust with respect to them, it is necessary to exclude the outliers before estimating the parameters of the spatial similarity transformation between the two local coordinate systems. For this purpose, a robust estimator, the Least Median Squares (LMS) estimator (Rousseeuw and Leroy, 1987), has been implemented.
This estimator has a high breakdown point, which means that it can discriminate outliers and leverage points up to a percentage of 50% of the considered data. The parameter which has more influence on the LMS results is the threshold value of rejection *L*, that represents a preliminary hypothesis on the percentage of outlier contamination. After testing this estimator on several amplitude images acquired on real objects (i.e. indoor and outdoor scenes), a suitable threshold value of rejection has been adopted. Using the LMS estimator, four points are consecutively used for estimating the transformation parameters up to all combinations (or a predefined number of them) are performed using the considered *m* points; the final result is a set of *l* statistically reliable points, named correct matches in the following, which can be therefore used for the least square estimation of the transformation parameters.

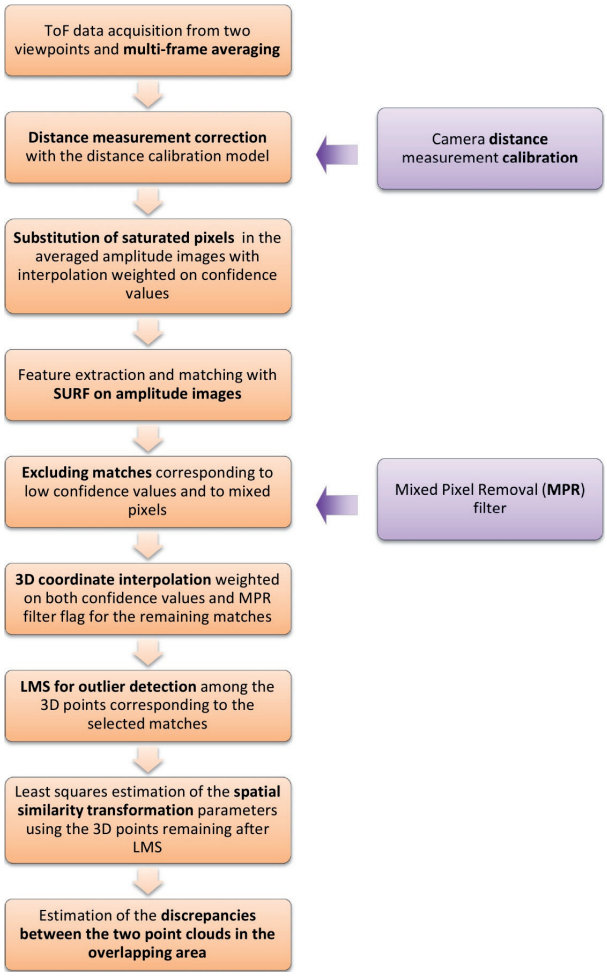

Figure 5. Main processing phases of the multi-frame registration algorithm for two camera positions.

In order to guarantee both a minimum number of matched features and to avoid a huge number of them to be processed by the LMS estimator, a check on the number of matches is performed before performing the LMS estimation.
The *x*,*y*,*z* coordinates of each correct match are interpolated among the four pixels around the considered point: a linear interpolation weighted on the pixel confidence values is

[2] This is the case of both the SR-4000 camera and the PMDCamCube3.0 camera.

performed in order to give more importance to 3D points which are more reliable and therefore to obtain more reliable results. Moreover, if a pixel has been chosen by the MPR filter as a mixed pixel, it is discarded from the interpolation since it contains unreliable 3D coordinates.
Using the obtained coordinates, the spatial similarity transformation is estimated with a least square fitting. In order to check the results, both the discrepancies on the points used for the spatial similarity transformation and the discrepancies (depth direction) between the two point clouds in the overlapping area are checked.
The multi-frame registration algorithm (Figure 5) is applied on each couple of successive camera positions and repeated until all 3D point clouds have been registered with respect to the first camera position. The described approach can be applied to each couple of overlapping amplitude images and 3D point clouds, in order to obtain a unique 3D point cloud.
The equations which allow to obtain the coordinates of the *i*-th point of the *n*-th camera position in the coordinate system *1* (which is the local coordinate system of the first camera position) are expressed in the following compact formula:

$$R_{2\to1}\cdot\left(\ldots\left(R_{n-1\to n-2}\cdot\left(R_{n\to n-1}\cdot F_i^{(n)}+T_{n\to n-1}\right)+T_{n-1\to n-2}\right)\right)\ldots T_{2\to1}=F_i^{(1)} \qquad (8)$$

where $R_{n\to n-1}$ and $T_{n\to n-1}$ represent the rotation matrix and the translation vector between the *n*-th camera position and the (*n-1*)-th camera position respectively.
Obviously, the registration errors sum up for each transformation, as in the typical case of free traverses. Nevertheless, if a loop closure is performed, or in the first and last camera positions some reference points of another coordinate system are present, an error relaxation can be performed on all registered point clouds. Future works will deal on this aspect, with the aim of reduce the registration error thanks to a global adjustment performed on all point clouds when homologous points from multiple camera positions are available and/or some reference points are available in the acquired scene.
In this first implementation, the multi-frame registration algorithm performs the spatial similarity transformation for both the original 3D point clouds (corrected with a distance calibration model if available, as in the case of the SR-4000 camera) and the 3D point cloud filtered by a suitable filter for mixed pixel removal, which is described in the following section.

4.3 Mixed Pixel Removal filter

A common problem in data acquired with ToF cameras is represented by the so called "mixed pixels" which are errant 3D data resulting from the way ToF cameras process multiple returns of the emitted signal.
In this work a filter for mixed pixel removal has been realized, which is called Mixed Pixel Removal (MPR) filter. The MPR filter can be applied directly on the acquired data (after averaging at least few frames), without any pre-filtering.
The MPR filter is based on both geometrical relations between neighborhood pixels and the approximate Ground Sample Distance (GSD) of the ToF camera pixels. The main idea is that a 3D point is a mixed pixel if its 3D coordinates differ from the 3D coordinates of at least one of its eight neighborhoods from a certain quantity *dist_thresold*, which is related to the estimated GSD for the median value of the distances (depths) measured by the nine considered pixels. The term *dist_threshold* is defined in the following way:

$$dist\_threshold = k\cdot GSD = k\cdot\frac{median(D_i)\cdot ps}{f} \qquad (9)$$

where k is determined empirically, taking into account the distance measurement accuracy of the ToF camera; $median(D_i)$ is the median value of the distance values D_i of the considered pixel and its eight neighborhood pixels; ps is the pixel size (hypothesis of square pixels) and f is the camera focal length.
The MPR filter has been applied on several indoor and outdoor scenes. In order to verify its effectiveness, a quantitative comparison has been performed estimating the percentage of points removed by the MPR filter and the percentage of points removed manually, using the Geomagic Studio 10 software for 3D visualization.
In Figure 6 an example of range and amplitude images (obtained after averaging 10 frames) acquired with the SR-4000 camera of an architectural frieze in front of a flat wall is reported. A lateral view of the original 3D point cloud (after averaging 10 frames) is reported in Figure 7 (left). As one can observe from Figure 7 (centre), the MPR filter removed all mixed pixels, with a percentage of removed points of 15%, which is a little bit higher than the percentage of manually removed points (12%).

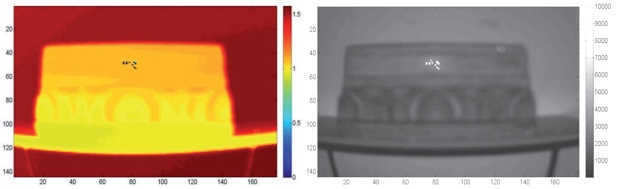

Figure 6. Range image (left, color scale in meters) and amplitude image (right, color scale in arbitrary units) acquired with the SR-4000 camera on an architectural frieze positioned in front of a wall (IT 7 ms).

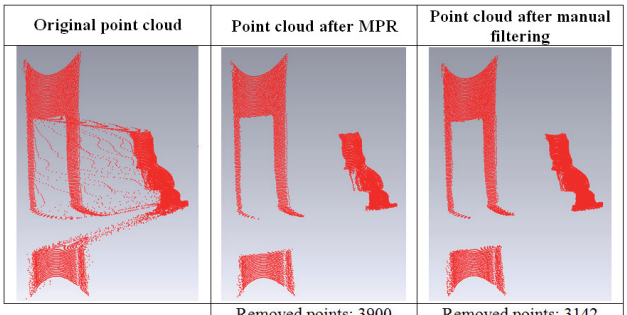

Figure 7. Lateral view of the 3D point cloud acquired with the SR-4000 camera on an architectural frieze: original point cloud (obtained after averaging 10 frames) (left) and the same point cloud after applying the MPR filter (centre) and after manual filtering (right).

The obtained results demonstrate the high performance of the proposed filter, which removed all mixed pixels in less than one second[3] in all tested cases, while manual filtering usually requires several minutes. One main drawback of the proposed

[3] With Matlab® version 2009b and Intel® Core™ i7 CPU (2.67 GHz) with 8 GB of RAM.

filter could be the higher percentage of removed points with respect to the case of manual filtering. Some attempts to increase the *k* term in equation (9) in order to save more points yielded several mixed pixels to be unfiltered. Nevertheless, it is worth nothing that, since at least two camera viewpoints are usually employed in order to better reconstruct an object, there is a redundancy of acquired data, which should remedy the small loss of valid points due to the MPR filter application. This aspect is confirmed by the performed tests, such as the one reported in the following section.

4.4 Test on real objects

In order to test the performance of the multi-frame registration algorithm, data were acquired of an indoor scene using the SR-4000 camera.
Since after the registration process all the 3D point clouds are referred to the local coordinate system of the first camera position and the transformation parameters are stored for each case, it is possible to estimate the positions occupied by the camera. In order to verify the quality of the registration process, an indirect way is to estimate the camera positions and comparing them with the reference positions thanks to the a suitable set up.
The SR-4000 camera was fixed to a calibrated bar, which allows several camera positions to be occupied along a straight line (Figure 8). Data were acquired from each position of the calibrated bar of the scene. Then, the multi-frame registration algorithm was applied to the acquired data. Since the camera moved in only one direction, after the 3D point cloud registration each translational component for the positions occupied by the camera was known. Actually, since the *x* camera axis could be not perfectly parallel to the calibrated bar, only the whole camera translation was accurately known (0.20 m).

Figure 8. SR-4000 camera positioned on the calibrated bar.

Some of the registration results which are automatically estimated by the multi-frame registration algorithm are reported in Table 1 for all the performed spatial similarity transformations. The mean values (m_x = -6.69E-12 m; m_y = -3.68E-10 m; m_z = -7.34E-11 m) and standard deviation values (σ_x = 0.007 m; σ_y = 0.005 m; σ_z = 0.005 m) of the discrepancies on the corresponding points used for each spatial similarity transformation and the mean value of the discrepancies in the *z* direction between each couple of point clouds of about 0.001 m demonstrate the goodness of the registration process.
Moreover, another check of the quality of the registration process has been performed. Since all camera positions were known thanks to the calibrated bar, using the estimated translation parameters (T_x, T_y, T_z), the 3D translational error (ΔT_{xyz}) between successive camera positions was calculated with respect to the reference displacement ($T_{reference}$) of 0.20 m performed thanks to the calibrated bar (Table 2).

Spatial similarity transformation [-]	**Mean value of the discrepancies in the overlapping area (*z* direction) [m]**
2→1	-2.29E-04
3→2	-0.002
4→3	0.001
5→4	-1.96E-05
6→5	0.003
7→6	0.003
Mean values	**0.001**

Table 1. Registration results for all performed spatial similarity transformations.

Since the *x* axis of the local coordinate system fixed to the camera could be not perfectly parallel to the calibrated bar, only the total translation in the three directions ($T_{reference}$) was accurately known, therefore only the 3D translational error was estimated:

$$\Delta T_{xyz} = T_{reference} - T_{xyz} = T_{reference} - \sqrt{T_x^2 + T_y^2 + T_z^2} \qquad (10)$$

In Table 2 the 3D translational error has been reported for each estimated spatial similarity transformation. The mean value of the translational error for all the six performed spatial similarity transformations is 0.013 m, which is very close to the absolute measurement accuracy of the SR-4000 camera and, therefore, acceptable.

Spatial similarity transformation [-]	**$T_{reference}$ [m]**	**T_{xyz} [m]**	**ΔT_{xyz} [m]**
2→1	0.200	0.192	0.008
3→2	0.200	0.183	0.017
4→3	0.200	0.185	0.015
5→4	0.200	0.198	0.002
6→5	0.200	0.183	0.017
7→6	0.200	0.184	0.016
	ΔT_{xyz} mean [m]		**0.013**

Table 2. Translational error between successive camera positions on the calibrated bar.

Since also the rotation parameters (ω, ϕ, κ) have been estimated, the real rotations (which are all null in the considered cases) have been compared with the estimated rotations. In Table 3 the discrepancies ($\Delta\omega$, $\Delta\phi$, $\Delta\kappa$) between actual rotations and estimated rotation parameters have been reported: the highest mean value of the discrepancies is about 0.6°. The mean value of the measured distances by the camera in the considered cases is about 1.6 m: an error of the estimated rotation of 0.6° will result in a displacement of about 0.015 m at that distance, which is close to the SR-4000 distance measurement accuracy (±0.01 m) and, therefore, still acceptable.
After registering each consecutive 3D point cloud, an attempt to apply successive spatial similarity transformations following

equation (8) was also performed, with the knowledge of the unavoidable propagation of the registration errors.

Spatial similarity transformation [-]	**Δω [°]**	**Δϕ [°]**	**Δκ [°]**
2→1	-2.14	1.71	0.71
3→2	-0.32	-0.50	0.01
4→3	-0.33	-0.60	0.57
5→4	-0.35	-0.02	0.35
6→5	-0.01	-0.69	0.80
7→6	-0.04	-0.67	1.05
Mean values [°]	**-0.53**	**-0.13**	**0.58**

Table 3. Reference rotations and estimated rotations for each spatial similarity transformation between successive camera positions.

The whole point cloud after the registration process of both the seven original point clouds and the seven point clouds after the MPR filter is reported in Figure 9.

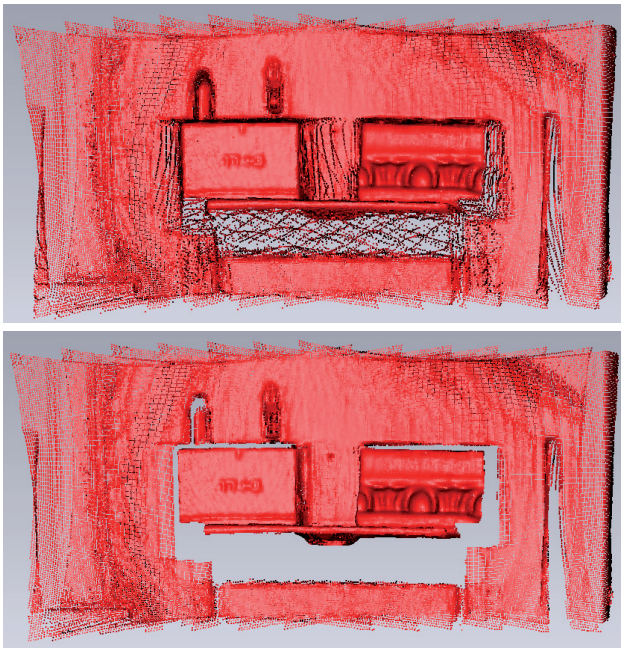

Figure 9. Front view of the final 3D point cloud after the registration of the original point clouds (without filtering) (up) and of the filtered point clouds (MPR filter).

Figure 9 shows the high quality of the final 3D point cloud of the observed scene after applying the multi-frame registration algorithm even without error relaxation thanks to loop closure or external reference points. The achieved results demonstrate the high performance of the MPR filter, which removed almost all mixed pixels from the acquired point clouds. Moreover, in the overlapping areas between the point clouds the point density is very high, overcoming in this way the poor lateral resolution typical of ToF cameras.
The obtained results demonstrate the good performance of the multi-frame registration algorithm, which allows to obtain a small registration error, that is close to the SR-4000 distance measurement accuracy.

5. CONCLUSIONS

Two main topics have been faced in the thesis, the distance calibration of ToF cameras and the implementation of automatic procedures for 3D object reconstruction using data acquired with commercial ToF cameras.
After a complete description of the working principle, state of the art and typical measurement errors of commercial ToF cameras, the problem of accuracy estimation of data acquired with RIM sensors has been faced. The adopted distance calibration procedure belongs to the direct calibration methods, since the distance measurement accuracy of ToF cameras is directly estimated using a custom-built system; the resulting systematic errors are modeled in order to increase the distance measurement accuracy. A procedure which does not require additional digital cameras or cost-effective high precision measurement racks or robot-arms to calibrate ToF cameras and which can be applied to any kind of RIM camera has been proposed. This procedure has been successfully applied to the SR-4000 camera: the obtained results confirmed the absolute measurement accuracy of about one centimeter declared by the camera manufacturer. A distance calibration model for all the camera pixels has been proposed, which increases the camera distance measurement accuracy up to five millimeters in the 1.5÷4.0 m interval of the whole working range of the SR-4000 camera, which is from 0.3 m to 5 m. In the next future, the same procedure for the evaluation of the distance accuracy of the PMDCamCube3.0 camera will be applied, in order to estimate and model the systematic distance measurement errors. The effectiveness of the distance calibration model proposed for the SR-4000 camera has been verified using suitable check measurements and comparisons with respect to LiDAR data acquired on real objects.
Suitable experimental tests have been designed and performed in order to analyze the influence of several factors on the distance measurements of ToF cameras. The warm-up time period evaluation highlighted that about forty minutes of device working are necessary in order to obtain a complete stabilization of the distance measurements acquired by both the SR-4000 and the PMDCamCube3.0 cameras. While for the first one the distance variations are limited to some millimeters, in the second case the camera warm up period is highly recommended in order to avoid distance errors of several centimeters. After testing the influence of integration time on the distance measurement precision for both cameras, some further tests have been performed on the SR-4000 camera, which will be performed on the PMDCamCube3.0 camera too in the next future. In particular, an experimental test showed that there is no appreciable variation of the distance measurement precision for camera orientations of about ± 45° with respect to the object surface normal. Then, it has been showed that the SR-4000 distance measurements are not affected by the "scattering artifacts" caused by the presence of foreground objects positioned at different distances in the scene, which drastically reduced the measurement accuracy of the previous camera model (SR-3000 camera). Finally, a systematic analysis on the influence of object reflectivity on the SR-4000 distance measurements demonstrated that this camera is quite insensitive to different object reflectivities. Nevertheless, some problems of pixel saturation and high noise have been observed for some materials, which are probably related to highly different reflectivities of the grains which constitute the tested materials.
As mentioned before, the second main topic of this work was the implementation of automatic procedures for 3D object reconstruction using data acquired with commercial ToF cameras. In particular, two procedures have been proposed.

The first one (not described in this work) is related to an innovative integration between ToF camera and multi-image matching approach for the automatic extraction of 3D object breaklines useful to speed-up the drawing production of architectural elements. Using the proposed approach, which exploits the ToF point cloud to strengthen the object breakline extraction, it is possible to drastically reduce both the data acquisition and processing times for 2D and/or 3D rough drawing generation. Future works will try to improve the performances of the integration algorithm and to increase the completeness of the achievable results. Moreover, further investigations will be performed to assess the geometric accuracy of the final drawings, in order to verify the maximum representation scale that can be achieved in order to have a correct metric representation and to limit the editing time for the final drawing production.

The second procedure relates to the automatic registration of 3D point clouds acquired with ToF cameras. The proposed algorithm, called multi-frame registration algorithm, exploits both amplitude data and 3D information acquired by ToF cameras. Homologous points are extracted and matched (SURF algorithm) from amplitude images acquired from different view-points and obtained after averaging multiple frames in order to reduce the measurement noise (so why the method is called "multi-frame registration"). After a robust estimation (LMS estimator) of the correct homologous points, the spatial similarity transformation parameters between two adjacent point clouds are estimated and the registration is performed, with estimation of the discrepancies between corresponding points. The robustness of the algorithm is improved by using a custom-built filter (called Mixed Pixel Removal filter), which practically removes all the "mixed pixels". These measurement errors are very frequent in complex indoor scenes and can drastically worsen the quality of the final 3D point cloud. The results of some tests about ToF data registration acquired on real objects in both indoor and outdoor conditions have been reported in the thesis, which show that the proposed algorithm allows to obtain registration errors which are close to the SR-4000 distance measurement accuracy and, therefore, very useful in the Geomatics fields. In the proposed approach, several frames are acquired from different static positions of the object to be surveyed; then, the multi-frame registration algorithm automatically performs the point cloud registration, without the need of any reference target such as in the case of LiDAR surveys. In the next future, the registration algorithm will also be applied to data acquired with the PMDCamCube3.0 camera and suitable comparisons will be performed with respect to the SR-4000 camera.

Some improvements and future works have been proposed in the thesis about the ToF data registration. In particular, even if in this work quantitative results have already been reported about the performance of the multi-frame registration algorithm, future works will deal with quantitative comparisons between data acquired with LiDAR instruments and ToF camera data after the registration process, using suitable reference points. In the case of outdoor scenes, a test will be performed with and without sunlight presence, in order to analyse the influence of sunlight on ToF camera performance. Moreover, some procedures will be developed in order to decrease the global registration error. In this way, the SURF algorithm could be applied to more than two consecutive images: for instance, if an overlap exists between not only the first and the second image, but also between the first and the third, homologous points which are common to all three images could be individuated and used to perform the registration process of the whole block of images. This approach should further decrease the registration error of the final 3D point cloud.

REFERENCES

Albota, M.A.; Heinrichs, R.M.; Kocher, D.G.; Fouche, D.G.; Player, B.E.; Obrien, M.E.; Aull, G.F.; Zayhowski, J.J.; Mooney, J.; Willard, B.C.; Carlson, R.R. Three-dimensional imaging laser radar with a photon-counting avalanche photodiode array and microchip laser. Appl. Opt. 2002, 41, 7671-7678.

Anderson, D.; Herman, H.; Kelly, A. Experimental characterization of commercial flash ladar devices. In Proceedings of International Conference on Sensing Technologies, Palmerston North, New Zealand, November, 2005.

Bay, H.; Ess, A.; Tuytelaars, T.; Gool, L.V. SURF: Speeded Up Robust Features, ComputerVision and Image Understanding (CVIU) – Vol. 110 (3), 2008; pp. 346-359.

Büttgen, B.; Seitz, P. Robust optical Time-of-Flight range imaging based on smart pixel structures. Trans. Circ. Sys. 2007, 1, 1512-1525.

Gvili, R.; Kaplan, A.; Ofek E.; Yahav, G. Depth keying, Proceedings of SPIE Electronic Imaging, vol. 5249, 2003; pp. 534-545.

Kahlmann, T.; Remondino F.; Ingensand, H. Calibration for increased accuracy of the range imaging camera SwissRanger. Int. Soc. Photogramm. Remote Sens. 2006, XXXVI, 136-141.

Lange, R. 3D Time-of-Flight distance measurement with custom solid state image sensors in CMOS/CCD-technology. Ph.D. Thesis, University of Siegen, Siegen, Germany, 2000.

Lowe, D. G. Distinctive image features from scaleinvariant keypoints, International Journal of Computer Vision, Vol. 60 (2), 2004; pp. 91–110.

Rochas, A.; Gösch, M.; Serov, A.; Besse, P.A.; Popovic, R.S. First Fully Integrated 2-D Array of Single-Photon Detectors in Standard CMOS Technology. IEEE Photonic. Technol. Lett. 2003, 15, 963-965.

Rousseeuw, P.J; Leroy, A.M. Robust Regression and Outlier Detection; Wiley Series in Probability and Mathematical Statistics; Wiley: New York, NY, USA, 1987.

Wang, J.J., Hu, G., Huang, S. and Dissanayake, G. 3d landmarks extraction from a range imager data for slam. In: Australasian Conference on Robotics and Automation, 2009.

Weyer, C.A.; Bae, K.; Lim, K.; Lichti, D. Extensive metric performance evaluation of a 3D range camera. *Int. Soc. Photogramm. Remote Sens.* 2008, *XXXVII*, 939-944.

Websites

Mesa Imaging. Available online: http://www.mesa-imaging.ch/ (accessed Dec. 2010).

PMDTechnologies GmbH. Available online:

http://www.pmdtec.com/ (accessed Dec. 2010).

A RADARGRAMMETRIC ORIENTATION MODEL FOR DIGITAL SURFACE MODELS GENERATION FROM SYNTHETIC APERTURE RADAR HIGH RESOLUTION IMAGERY: APPLICATIONS WITH COSMO-SKYMED AND TERRASAR-X

Francesca Pieralice

Area di Geodesia e Geomatica, Dipartimento di Ingegneria Civile, Edile e Ambientale
Università degli Studi di Roma "La Sapienza" Roma, Via Eudossiana, 18 00184 Roma
e-mail francesca.pieralice@uniroma1.it

KEY WORDS: Radargrammetry, stereo pair orientation, high resolution SAR imagery, RPCs, COSMO-SkyMed, TerraSAR-X

ABSTRACT:

Digital Surface and Terrain Models (DSMs/DTMs) have large relevance in some territorial applications, such as topographic mapping, spatial and temporal change detection, feature extraction and data visualization. DSMs/DTMs extraction from satellite stereo pair offers some advantages, among which low cost, speed of data acquisition and processing, surveys of critical areas, easy monitoring of wide areas, availability of several commercial software and algorithms for data processing. In particular, the DSMs generation from Synthetic Aperture Radar (SAR) imagery offers the significant advantage of possible data acquisition during the night and in presence of clouds.
The availability of new high resolution SAR spaceborne sensors as COSMO-SkyMed (Italian), TerraSAR-X (German) and RADARSAT-2 (Canadian) offers new interesting potentialities for the acquisition of data useful for the generation of DSMs following the radargrammetric approach, based at least on a couple of images of the same area acquired from two different points of view as for the standard photogrammetry applied to optical imagery.
The aim of this work was the development and the implementation of an original rigorous radargrammetric model for the orientation of SAR imagery, suited for the subsequent DSM generation. The model performs a 3D orientation based on two range and two zero-Doppler equations starting from SAR stereo pairs in slant range and zero-Doppler projection, acquired in SpotLight mode, that is at the highest resolution presently available (1 m ground resolution).
The model has been implemented in SISAR (Software per Immagini Satellitari ad Alta Risoluzione), a scientific software developed at Geodesy and Geomatic Institute of the University of Rome "La Sapienza". This software was at first devoted to the orientation of high resolution optical imagery, and in the last year it has been extended also to SAR imagery.
Moreover a tool for the SAR Rational Polynomial Coefficients (RPCs) generation has been implemented in SISAR software, similarly to the one already developed for the optical sensors.
The possibility to generate RPCs starting from a rigorous model sounds of particular interest since, at present, the most part of SAR imagery is not supplied with RPCs, although the Rational Polynomial Functions (RPFs) model is available in several commercial software. The RPCs can be an useful tool in place of the rigorous model in processes as the image orthorectification/geocoding or the DSMs generation, since the RPFs model is very simple and fast to be applied.
The model implemented has been tested on COSMO-SkyMed and on TerraSAR-X SpotLight imagery, showing that a vertical accuracy at level of better than 3 m is achievable even with quite few Ground Control Points.

1. INTRODUCTION

Today, imagery of our planet from spaceborne sensors are acquired continuously; a large number of satellite devoted to the Earth observation are available and also various kinds of sensors are on orbit.
As regards the Synthetic Aperture Radar (SAR) satellites for Earth observation, a possible geomatics application can be the generation of Digital Surface and Terrain Models (DSMs/DTMs).
DSMs and DTMs have large relevance in some territorial applications, such as topographic mapping, spatial and temporal change detection, feature extraction and data visualization.
DSMs extraction from satellite stereo pair offers some advantages, among which low cost, speed of data acquisition and processing, surveys of critical areas, easy monitoring of wide areas, availability of several commercial software and algorithms for data processing. In particular, the DSMs generation from SAR data offers the significant advantage of possible data acquisition during the night and in presence of clouds.
The availability of new high resolution SAR spaceborne sensors as COSMO-SkyMed (Italian), TerraSAR-X (German) and RADARSAT-2 (Canadian) offers new interesting potentialities for the acquisition of data useful for the generation of DSMs.
Two different approaches may be used to generate DSMs from SAR data: the interferometric and the radargrammetric one, both using at least a couple of images of the same area acquired from two different points of view.
The interferometry uses the phase differences information between the SAR images to lead the terrain elevation, unlike radargrammetric technique analyzes the signal amplitude and exploits the stereoscopy similarly to optical photogrammetric methods. Actually, due to the low resolution amplitude supplied by the spaceborne radar sensors available until now (at the level of tens of meters), usually the first approach has been used, being aware that the radar interferometry may suffer for lack of coherence, especially over areas with vegetation/forest.

At present, the importance of the radargrammetric approach is rapidly growing due to the new high resolution imagery (up to 1 m of ground resolution) which can be acquired by COSMO-SkyMed, TerraSAR-X and RADARSAT-2 sensors in SpotLight mode. In this sense, it seems useful to underline that the two approaches should be considered complementary, in order to obtain the best (accurate and complete) product.
The radargrammetric approach was first used in the 1950s; then, as mentioned, it was less and less used, due to the quite low resolution in amplitude of radar images, if compared to their high resolution in phase.
In the past radagrammetric applications was related both to aerial and to satellite sensors; as regards satellite sensors, in the last twenty years, some researchers have investigated the DSMs generation from SAR data acquired by the various sensors presently available. Some of results published in scientific literature are presented in this section.
Toutin has published numerous works in the field of remote sensing and DSMs generation from optical and SAR data (to this aim see (Toutin and Gray, 2000)). His investigations concerned at first radargrammetric applications with low resolution satellite, as ERS-1 and RADARSAT-1.
As regards ERS-1, its SAR instrument has a spatial resolution of 30 m; the DSM accuracy achievable from it in Toutin's works is about 24 m in (Toutin, 1995) and in (Toutin, 1996), and about 20 m in (Toutin, 2000a).
Moreover Toutin was involved in investigations related to the Canadian satellite RADARSAT-1, that have a spatial resolution up to 10 m in Fine mode; he studied about the possibilities to use same side or opposite side stereo pair, and about the relation between the DSM accuracy and the slope and aspect of the terrain relief (Toutin, 2000b).
By comparing the results for low and moderate relief, Toutin found that the relief is an important parameter that has an impact on the DEM accuracy. However, large radiometric disparities in the stereo pair depending on different factors related to SAR and surface interaction (moisture, roughness, vegetation, foreshortening, etc.) should affect the DEM accuracy; in fact, high radiometric disparities could invalidate results also in case of good geometric configuration of stereo images (Toutin, 1998).
DSM errors for RADARSAT-1 are at level of tens of meters, however, as mentioned; results are depending from stereo configuration, radiometric disparities or soil coverage and topography; for instance, DSM accuracy is almost linearly correlated with the terrain slopes (Toutin, 2000b).
Meric, Fayard and Pottier carried on some investigations about radargrammetric applications with SIR-C/X-SAR mission. In the Austran Alps, with a pixel size of 25 m, they achieved a percentage error of: 45% from 0 to 70 m, 40% from 70 to 130 m, and 15% from 130 to 200 m (Fayard et al., 2007).
Crosetto studied radargrammetric applications with RADARSAT-1 and the potentialities of integration and fusion of radargrammetric and interferometric results, in order to obtain the best (accurate and complete) product (Crosetto and Pérez Aragues, 1999).
Overall, the global accuracy achievable with old generation SAR sensors was around tens of meters.
At present, the goal is to improve the radargrammteric DSMs accuracy using the new generation sensors. To this end we recall the investigation of the research group of “Joanneum Research Institute” about TerraSAR-X satellite.
Some results was been published in (Raggam et al., 2010), where, for flat areas, the mean height differences are close to zero, while the standard deviation is about 3 m, while for forested terrain, mean values are between about 12 and 20 m, as well as standard deviations around 4 m. They investigated also the possibility to use a block of three SAR images.
Again, Toutin has published results about the application of his radargrammetric model to RADARSAT-2 imagery (Toutin and Chenier, 2009); results of preliminary geometric calibration are at level of 2 meters in height component for images in Ultrafine mode (1.56 m × 1.56 m pixel spacing).
In this context it is worth recalling that, at present, no results are publicly available as regards the radargrammetric potentiality of the Italian constellation COSMO-SkyMed.
It has to be underlined that DSMs generation following the radargrammetric approach consists of two basic steps, as for the standard photogrammetry applied to optical imagery: the stereo pair orientation and the image matching for the automatic detection of homologous points. In this thesis the topics related to image orientation of SAR stereo pairs in zero-Doppler geometry acquired in SpotLight mode have been investigated.
As regards the radargrammetric orientation model, it has to be underlined that, starting from the model proposed in the classical book of (Leberl, 1990), a refinement of the orbital model have to be taken into account to comply with and to exploit the potentialities of the novel high resolution (both in azimuth and in range). Then, the defined and implemented model performs a 3D orientation based on two range and two zero-Doppler equations, allowing for the least squares estimation of some calibration parameters, related to satellite position and velocity.
The model has been implemented in SISAR (Software per Immagini Satellitari ad Alta Risoluzione), a scientific software developed at Geodesy and Geomatic Institute of the University of Rome ``La Sapienza''. This software was at first devoted to the orientation of high resolution optical imagery (Crespi et al., 2009), and in the last year it has been extended also to SAR imagery.
Moreover, a tool for the SAR Rational Polynomial Coefficients (RPCs) generation has been implemented in SISAR software, similarly to the one already developed for the optical sensors.
The Rational Polynomial Functions (RPFs) model with the employment of RPCs is a well known method to orientate optical satellite imagery. In fact, some satellite imagery vendors have considered the use of RPFs models as a standard to supply a re-parametrized form of the rigorous sensor model in terms of the RPCs, that implicitly provide the interior and external sensor orientation. This generalized method is very simple, since its implementation is standard and unique for all the sensors; moreover the performances of the RPFs model using the RPCs can reach the level of the ones from rigorous models.
The possibility to generate RPCs starting from a rigorous model sounds of particular interest since, at present, the most part of SAR imagery is not supplied with RPCs, although the RPFs model is available in several commercial software. The RPCs can be an useful tool in place of the rigorous model in processes as the image orthorectification/geocoding or as the DSMs generation, since the RPFs model is very simple and fast to be applied. Deeper investigations in the least squares RPCs estimation underlined that many RPCs are correlated; so, in our approach the Singular Value Decomposition (SVD) and QR decomposition are employed to evaluate the actual rank of the design matrix and to select the actual estimable coefficients, avoiding an overparametrization of the model.
Finally, a particular care has to be put into the choice of the geometric configuration of the radargrammetric stereopairs; in fact, it is well known that the optimum one is when the target is observed in opposite-side view; however it causes large geometric and radiometric disparities, hindering the image matching, which is the second fundamental step for DSMs

generation after the imagery orientation. A good compromise is to use a same-side configuration stereo pair with a base to height ratio ranging from 0.25 to 2.0 (Meric et al., 2009) in order to increase the efficiency in the correlation image process.
In this thesis the results of some tests performed on COSMO-SkyMed and TerraSAR-X SpotLight stereo pairs are presented; the data available are a COSMO-SkyMed same-side stereo pair, acquired over the areas of Merano (Northern Italy), and three TerraSAR-X images, acquired over the area of Hannover (Northern Germany), from which a same-side and an opposite-side stereo pairs have been derived.
The results concern the stereo orientation using both the radargrammetric and the RPCs model. The results are compared to those stemming from commercial software PCI Geomatica v. 10.3, where the well known Toutin's model is implemented.

2. THE RADARGRAMMETRIC MODEL IMPLEMENTED IN SISAR

The radargrammetric approach performs a 3D reconstruction based on the determination of the sensor-object stereo model, in which the object position is computed by the intersection of two radar rays with two different look angles. The SISAR model is based on the assumption of zero-Doppler projection, that usually is the common projection in which the SAR imagery are distributed, since they are subjected to a focusing process.
The fundamental equations of the orientation model in zero-Doppler projection, Equations (1), define a Doppler circle, corresponding to the intersection of a range sphere, defined by the slant range R_S (see first equation of (1)), with a plane perpendicular to the flight (see second equation of (1)).

$$\begin{cases} \left|\vec{P}-\vec{S}\right| = R_S \\ \vec{v}\cdot(\vec{P}-\vec{S}) = 0 \end{cases} \quad (1)$$

Thus, in a stereo configuration, using at least a couple of images, the object position of a generic point is determined by the intersection of two Doppler circles (see Figure 1); in this way we have four equations and three ground coordinates unknowns.
The equations (1), in explicit form, read:

$$\begin{cases} \sqrt{(X_P-X_S)^2+(Y_P-Y_S)^2+(Z_P-Z_S)^2} - (D_S + CS\cdot I) = 0 \\ v_{SX}\cdot(X_P-X_S)+v_{SY}\cdot(Y_P-Y_S)+v_{SZ}\cdot(Z_P-Z_S) = 0 \end{cases} \quad (2)$$

where X_P, Y_P, Z_P are the coordinates of the generic ground point P in the local coordinate system (time independent)
X_S, Y_S, Z_S are the coordinates of the satellite in the local coordinate system (time dependent)
v_{SX}, v_{SX}, v_{SX} are the cartesian components of the satellite velocity in the local coordinate system (time dependent)
D_S is the so-called "near range"
CS is the slant range resolution or column spacing
I is the column position of point P on the image

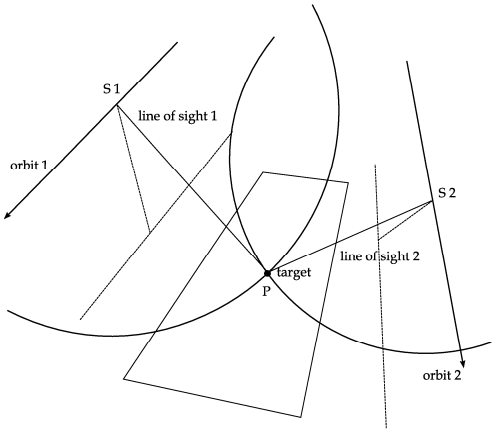

Figure 1. Intersection of Doppler circles in stereo configuration

As regards the satellite position computation, the basic assumption is that the orbital arc related to the image acquisition in SpotLight mode is quite short (about 10 Km), so that it could be conveniently modelled with a circular arc.
Circumference parameters are estimated by least squares adjustment using few orbital state vectors available in the ancillary data; the state vectors contain the satellite coordinates, expressed in ECI or ECEF system, generally sampled at regular interval times (for example 10 seconds) before and after the image acquisition. Using this information it is possible to reconstruct the orbital segment related to the SAR image.
Starting from each GCP coordinates on the ground, we find the corresponding position, and consequently the velocity, that satisfies the zero-Doppler constrain (first equation of (1)) along the satellite orbit, that means velocity perpendicular to the line-of-sight. In this way we can obtain a time of acquisition, a satellite position and velocity, for each GCP.
These times of acquisition are employed to estimate the parameters of the model.
The image coordinates I, J are related to the slant range R_S and to the time of acquisition t respectively. The parameters that establish the relation between image coordinates and "physical" parameters R_S and t can be considered as self-calibration parameters, since they provide a physical meaning to the image space.
The significance of the slant range R_S is clear from its definition: it represents the distance between the satellite and the target on the ground during the image acquisition. Its relation with the image coordinate I is:

$$R_S = D_S + CS\cdot I \quad (3)$$

where the near range D_S is a calibration parameter related to the range measure, and the slant range resolution CS is known from metadata; approximate value of these parameters may be found in the metadata file, then a refinement is least squares estimated.
As regards the image coordinate J and the time t, their relationship can be expressed by a linear relation, Equation (4), in which the start time of the acquisition (*start_time*) and the Pulse Repetition Frequency (*PRF*), the sampling frequency in azimuth direction, are involved.

$$t = start\_time + \frac{1}{PRF}J \quad (4)$$

Also in this case their approximate values are in the metadata file, then a refinement is provided in the least squares estimation.

3. RPC APPLICATION AND GENERATION FOR SAR IMAGERY

The Rational Polynomial Functions (RPFs) model with the employment of Rational Polynomial Coefficients (RPCs) is a well known method to orientate optical satellite imagery. In fact, some satellite imagery vendors have considered the use of RPFs models as a standard to supply a re-parametrized form of the sensor model in terms of the RPCs, secretly generated from their own physical sensor models.

Even if the rigorous models should theoretically provide the highest accuracy, they are only available for some satellites and can be managed by a few of commercially available software. Moreover, in order to estimate the unknown parameters of rigorous models, users are still faced with the challenging task of recovering the external orientation of the sensor using a set of GCPs usually no small than 10, for optical sensors. When no or few GCPs are available, users cannot recover the external orientation of the sensor and therefore they are unable to perform various mapping and data collection operations.

With the introduction of generalized sensor models, this situation has changed considerably. Generalized sensor models, such as the RPFs (Tao and Hu, 2001), have smoothed the requirement to manage a physical sensor model. Furthermore, as the RPCs implicitly provide the interior and (approximate) external sensor orientation, the availability of several GCPs is no longer a mandatory requirement.

Consequently, the use of the RPCs for photogrammetric mapping became a new standard in high-resolution satellite imagery, that is adopted for all the most important high and very high resolution sensors, such as Ikonos, QuickBird, WorldView-1 and GeoEye-1.

High resolution satellite imagery are now available in different formats and processing levels at an affordable price. These kinds of imagery and their growing availability are revolutionizing the role of satellite imagery in a number of applications ranging from intelligence to security, media, marketing, agriculture, utilities, urban planning, forestry, environmental monitoring, transportation etc.; in this sense, the users are not necessarily remote sensing experts, and they need a simple way to manage the data and the RPFs model represents a fundamental tool for exploiting the full geometrical potentiality of the imagery in a quite simple way.

Overall, the simplicity of the RPFs model is due to three important reasons: the implementation of the RPFs model is standard, unique for all the sensors and much more simple that the one of a rigorous model, which have to be customized for each sensor; the performances of the RPFs model, using a refinement transformation, if it is needed, can reach the level of the ones from rigorous models; the usage requires zero or, at maximum, quite few GCPs if refinement transformations are used, so that the cost for ancillary information is remarkably reduced with respect to rigorous models, which often require at least 10-12 GCPs for optical images or 5-6 for SAR images to supply a stable orientation.

Therefore, the use of RPCs could be conveniently extended also to SAR imagery. Therefore, considering that only RADARSAT-2 imagery are supplied with RPCs file, the RPCs generation tool already implemented in SISAR for optical imagery has been extended to comply with COSMO-SkyMed and TerraSAR-X imagery.

The RPFs relate object point coordinates (latitude φ, longitude λ and height h) to pixel coordinates (I, J), in the form of ratios of polynomial expressions.

Up to now, it is clear that the availability of all the coefficients directly enables the external orientation and GCPs are not necessary in theory. Nevertheless, since the residual bias may be present into the RPCs provided by the companies, the orientation can be refined on the basis of eventually known GPs, acting as GCPs. A possible refinement of the model, allowing for bias compensation, is accomplished in a quite common way with the introduction of a simple first order polynomial in the RPFs (equations (5)) whose parameters are estimated, provided a suitable number of GCPs (Fraser and Hanley, 2003).

$$I = A_0 + A_1 I + A_2 J + \frac{P_1(\varphi,\lambda,h)}{P_2(\varphi,\lambda,h)}$$
$$J = \mathrm{B}_0 + B_1 I + B_2 J + \frac{P_3(\varphi,\lambda,h)}{P_4(\varphi,\lambda,h)} \qquad (5)$$

The RPCs can be generated according to a so called terrain independent scenario, using a rigorous orientation model. A tool based on this approach is implemented in SISAR. A 2D image grid covering the full extent of the image is established and its corresponding 3D object grid with several layers slicing the entire elevation range is generated. The horizontal coordinates (φ; λ) of a point of the 3D object grid are calculated from a point (I; J) of the image grid using the already established and mentioned rigorous orientation model with an a priori selected elevation h. Then the RPCs are estimated in a least squares solution using as input of 3D object grid points and the image grid points (Crespi et al., 2009).

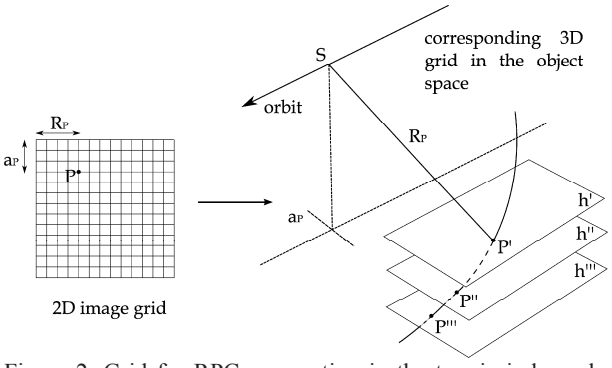

Figure 2. Grid for RPCs generation in the terrain-independent approach

In order to avoid instability due to high RPCs correlations, in our approach the Singular Value Decomposition (SVD) and QR decomposition are employed to evaluate the actual rank of the design matrix and to select the actual estimable coefficients. Moreover, the statistical significance of each estimable coefficient is checked by a Student T-test, so to avoid overparametrization; in case of not statistically significant coefficients, they are removed and the estimation process is repeated until all the estimated coefficients are significant ("parsimony principle").

It has to be underlined that the affine RPCs refinement is not always necessary in order to achieve the best accuracy. In fact, very often the RPCs provided together the optical imagery are affected by a systematic error that could be easily removed estimating the RPCs affine adjustment, whereas in some cases,

specially for the imagery projected on to ellipsoid (as IKONOS or QuickBird/WorldView Standard Orthoready imagery), only the simple shift refinement is significant and has to be applied. The significance of the refinement parameters has always to be evaluated by a significance test, as Student T-test.
As regards the RPCs generated by SISAR using a terrain-independent approach, they are calibrated on accurate GCPs, and they are not affected by biases, therefore refinement transformation is not needed in this case.

4. NEW GENERATION SAR SATELLITES

4.1 COSMO-SkyMed

COSMO-SkyMed (COnstellation of small Satellites for Mediterranean basin Observation) is the largest Italian investment in Space Systems for Earth Observation, commissioned and funded by Italian Space Agency (ASI) and Italian Ministry of Defense (MoD).
It has been created for a Dual-Use (Civilian and Defence), and it is actually a cutting edge system in the world in the Earth Observation field.
The system consists of a constellation of four Low Earth Orbit mid-sized satellites, each equipped with a multi-mode high-resolution Synthetic Aperture Radar (SAR) operating at X-band.
The fourth satellite has been launched on November 6, 2010; it is the last component of the mission, that is now finally fully operational.
The main goals of COSMO-SkyMed are related to a space mission having a dual nature (i.e. capable to satisfy civilian and defence customers) able to provide information and services to a number of activities and applications (such as risk management applications, cartography and planning applications, agriculture, forest, hydrology, geology, marine domain, archaeology, etc...).
The capability of acquisition in every weather and illumination condition, and of acquisition at regular short time intervals, makes COSMO-SkyMed suited to territory monitoring, to environmental planning and to emergency managing.
The Tandem interferometric configurations is supported, in which the two satellites fly in close proximity achieving the acquisitions with a temporal gap of 24 hours.
COSMO-SkyMed is able to operate in three different acquisition mode:
Enhanced SpotLight Mode: the antenna is steered during the acquisition time in order to illuminate the required scene for a time period longer than the one of the standard strip side view. The extension in azimuth direction is achieved by an antenna electronic steering scheme requiring the center of the beam steering to be located beyond the center of the imaged spot, thus increasing the observed Doppler bandwidth for each target.
The extension of the frame is about 11 Km × 11 Km, in azimuth and range direction respectively, the ground resolution is about 1 m × 1 m.
Stripmap Mode: it is the most common imaging mode, obtained by pointing the antenna along a fixed direction orthogonal to the orbit. The antenna footprint covers a strip on the illuminated surfaces as the platform moves and the system operates. The swath is about 30-40 km and the ground resolution is about 3 m × 3 m.
ScanSAR Mode: it allows larger swath in range with respect to the Stripmap one, but with a less spatial resolution, obtained by periodically stepping the antenna beam to neighbouring sub-swaths. The two different implementation allowed for this acquisition mode are WideRegion and HugeRegion, with a spatial resolution selectable from 30 m × 30 m to 100 m × 100 m.

4.2 TerraSAR-X

TerraSAR-X is a German mission, it is a Public Private Partnership (PPP) between the German Ministry of Education and Science (BMBF) represented through the German Aerospace Centre (DLR) and Europe's leading space company, EADS Astrium GmbH.
In the first stage a unique satellite was launched in June 2007, with a scheduled lifetime of 5 years; its design is based on well-founded technology and knowledge achieved during the successful Synthetic Aperture Radar SIR-C/X-SAR and SRTM missions.
It carries a high frequency X-band SAR sensor which can be operated in flexible imaging modes in order to meet the requirements of versatile applications.
It can acquire imagery in several operational mode, similar to the previously ones described for COSMO-SkyMed:
SpotLight: two kinds of scene size are available, 10 km × 10 km for the SpotLight mode with 2 m × 2 m ground resolution and 10 km × 5 km (width × length) in the HighResolution SpotLight (HS) mode with 1 m × 1 m resolution.
StripMap: in StripMap mode, a spatial resolution up to 3 m can be achieved. The standard scene size is 30 km × 50 km in order to obtain manageable image files; however, acquisition length is extendable up to 1,650 km.
ScanSAR: in the ScanSAR mode a spatial resolution of up to 18 m is achieved. The standard scene size is 100 km × 150 km (width × length) for easily manageable image files, but again, the acquisition length is extendable up to 1,650 km.
In June 2010 a "twin" of TerraSAR-x was launched, the satellite TanDEM-X (TerraSAR-X Add-On for Digital Elevation Measurement). It is a radar satellite almost identical to TerraSAR-X, that circles the Earth together with TerraSAR-X as a unique satellite formation.
They are at only a few hundred meters and they record data synchronously in the so-called StripMap Mode (3 m ground resolution) and thus acquire the data basis for an intereferometric global Digital Elevation Model (DEM) of an unprecedented quality, accuracy, and coverage, since coherence problems are totally solved by the almost contemporary acquisition of the two images used to form the interferogram.

5. RADARGRAMMETRIC MODEL AND RPCS GENERATION RESULTS

5.1 Data set

The available data for the experimentation are COSMO-SkyMed and TerraSAR-X SpotLight imagery.
As regards COSMO-SkyMed (CSK), we have two images forming a stereo pair over the area of Merano (Northern Italy). All images belong to the Level 1A (SCS) category products, that is focused data in complex format, in slant range and zero-Doppler projection.
The two scenes were acquired by two different COSMO-SkyMed satellites (CSK1 and CSK2), with incidence angles of 25.9 and 42.3 degrees respectively along a descending orbit, forming a same-side configuration stereo pair, with a base-to-height ratio equal to 0.3.
The area covered by the stereo pair is approximately 10 Km×10 Km (see Figure 3).
The stereo pair orientation is based on 20 Ground Points (GPs), used both as GCPs and CPs too (see Figure 4); horizontal

coordinates are derived from cartography (scale 1:5000) whereas the heights come from a LIDAR Digital Terrain Model (mean elevation accuracy of 0.25 m); both these data are free available on the website of the ``Provincia Autonoma di Bolzano'' (http://www.provincia.bz.it/urbanistica/cartografia/cartografia.asp).

As regards TerraSAR-X, we have three images acquired over the town of Hannover (Northern Germany); all images are HighResolution SpotLight (HS) products with extension of 10 Km×5 Km (see Figure 5).

Two images were acquired along an ascending orbit, one of these along a descending orbit. It is possible to choose various combination of images in order to form different stereo pairs; we selected a same-side stereo pair (composed by the first and the second images) with a base-to-height ratio equal to 0.15 and an opposite-side stereo pair (composed by the first and the third images) with a base-to-height ratio equal to 1.

Features of all images are in Table 1.

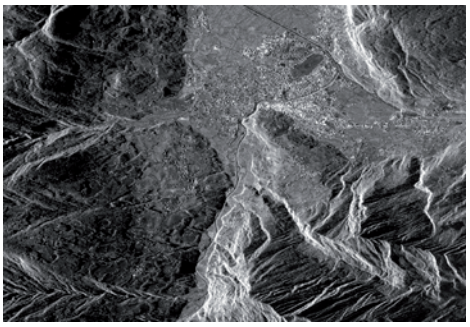

Figure 3. CSK scene of Merano

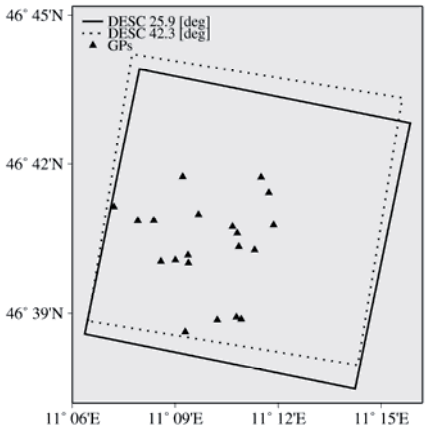

Figure 4. GPs distribution on Merano CKS images

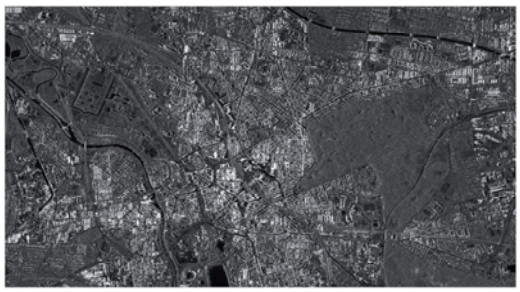

Figure 5. TSX scene of Hannover

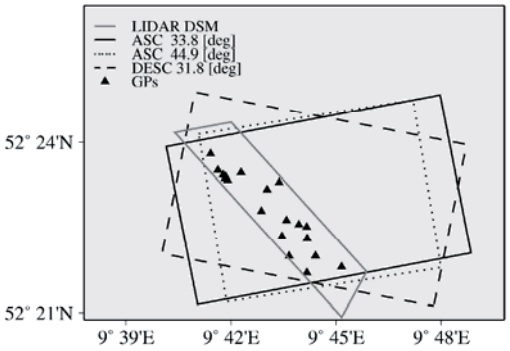

Figure 6. GPs distribution on Hannover TSX images

Sensor	Area	Acquisition date	Incid. Angle [deg]	Orbit	Look Side
CSK	Merano	30/11/2009	25.9	Desc	Right
	Merano	02/02/2009	42.3	Desc	Right
TSX	Hannover	05/12/2007	33.8	Asc	Right
	Hannover	10/12/2007	44.9	Asc	Right
	Hannover	29/12/2007	31.8	Desc	Right

Table 1. CSK and TSX images features

On the Hannover images 20 GPs were been selected, whose coordinates were been derived from a LIDAR DSM, available only on a limited area of the images. In this sense the GPs distribution is not optimal in respect to the orientation of the whole images, and the accuracy results have to be considered reliable only in the GPs area.

These data have been provided in the framework of the international project ``Evaluation of DEM derived from TerraSAR-X data'', organized by the current ISPRS (International Society for Photogrammetry and Remote Sensing) Working Group VII/2 ``SAR Interferometry''.

Here it has to be pointed out that the identification of GPs on the SAR imagery is usually much more difficult than in the case of optical imagery, so that an average error of 2-3 pixels (if not larger) have to be considered. In the Figure 7 the difference between a SAR image and an aerial optical image is shown. The interpretation of a SAR image needs of experience and understanding of radar phenomena, as the typical deformations as foreshortening, layover (see Figure 8) or shadowing.

Further additional problems came out for the GPs identification on the opposite-side stereo pair. In fact, only 13 GPs are visible on both images, since the areas illuminated on the first image are in the shadow on the second one. As shown in Figure 9, the two images, acquired on opposite-side looking, are significantly different. The GPs useful in this case are in open area, non occluded, visible and well illuminated by the satellite on both look sides.

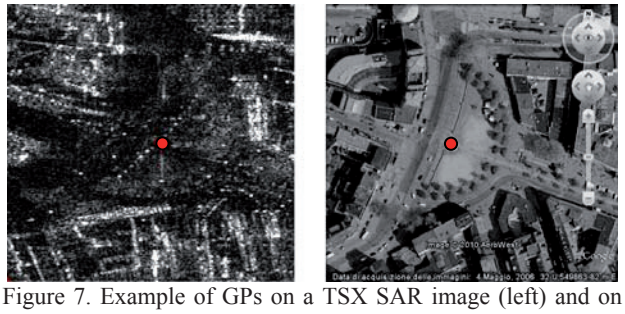

Figure 7. Example of GPs on a TSX SAR image (left) and on an aerial image (right)

Figure 8. Example of layover of an high building on Hannover TSX image (left) and the same building in an aerial image (right)

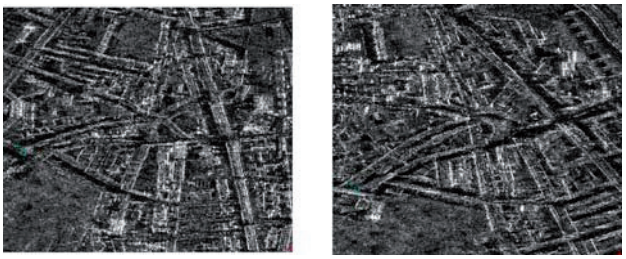

Figure 9. Same area on the ascending TSX image (left) and on the descending one (right)

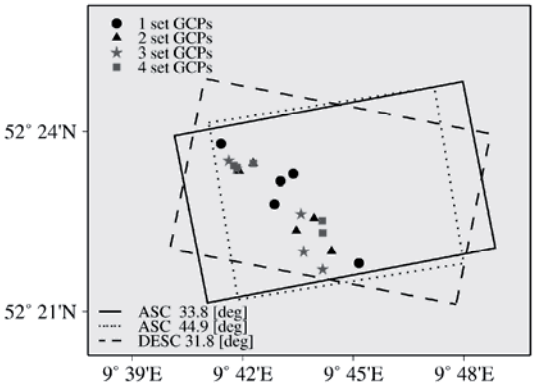

Figure 10. Example of 4 independent sets of 4 GCPs

5.2 Accuracy results of radargrammetric model and RPCs generation

To test the effectiveness of the new rigorous model implemented in the software SISAR, the stereo pairs have been orientated varying the number of GCPs and the model accuracy is analyzed, evaluating the RMSE computed over CPs residuals (RMSE CPs), following the standard Hold-Out Validation procedure for accuracy assessment.
In order to obtain significant results from the statistical point of view, for a given number of GCPs different tests were carried out, using independent sets of GCPs selected under the condition of a homogeneous distribution over the areas covered by the stereo pairs. In the Figure 10 an example of 4 different independent sets of 5 GCPs on Hannover test site is shown.
Moreover, SISAR results are compared with those achieved by the rigorous model implemented in the well known commercial software OrthoEngine v.10.3 (PCI Geomatica).
For Merano stereo pair, the horizontal accuracy is at level of 3.0 - 4.0 m, and the vertical one is better than 3.0 m (Table 2); no more than 9 GCPs were considered, to avoid to lower too much the number of the CPs.

In tables results, the accuracy is evaluated in terms of RMSE on CPs residuals, and the average, the median and the standard deviation of the RMSE obtained in the several tests carried out using independent sets of GCPs are shown.
As regards the model performance varying the independent sets of GCPs, the software shows a stable behaviour and the increase of GCPs number does not improve the results remarkably. In this respect, no more than 9 GCPs were considered, also because the number of the CPs would have been too small resulting in a meaningless RMSE CPs.
As regards the TerraSAR-X data, we have a same-side and an opposite-side stereo pair. In Table 3 the accuracy level achieved in the orientation tests with Hannover same-side stereo pair is presented. The horizontal and vertical accuracy are both at level of 2.5 - 3.5 m. As regards the model performance achievable varying the independent sets of GCPs, again the software shows a stable behaviour and the increase of GCPs number does not improve the results remarkably.

RMSE CPs CSK Merano				
Average [m]				
# GCPs	# Ind. Sets	North	East	Up
3	6	2.78	4.14	2.54
6	3	2.55	3.59	2.91
9	2	2.78	3.78	2.70
Median [m]				
# GCPs	# Ind. Sets	North	East	Up
3	6	2.81	4.22	2.41
6	3	2.36	3.76	2.67
9	2	2.78	3.78	2.70
Standard Deviation [m]				
# GCPs	# Ind. Sets	North	East	Up
3	6	0.41	0.3	0.23
6	3	0.27	0.24	0.38
9	2	0.17	0.01	0.19

Table 2. Results of the scientific software SISAR for Merano stereo pair

RMSE CPs TSX Hannover same-side				
Average [m]				
# GCPs	# Ind. Sets	North	East	Up
3	6	2.71	2.84	3.49
5	4	2.38	2.86	3.11
9	2	2.17	2.52	2.98
Median [m]				
# GCPs	# Ind. Sets	North	East	Up
3	6	2.70	2.76	3.44
5	4	2.49	2.85	3.18
9	2	2.17	2.52	2.98
Standard Deviation [m]				
# GCPs	# Ind. Sets	North	East	Up
3	6	0.55	0.35	0.42
5	4	0.34	0.25	0.19
9	2	0.00	0.20	0.24

Table 3. Results of the scientific software SISAR for Hannover same-side stereo pair

RMSE CPs TSX Hannover opposite-side				
Average [m]				
# GCPs	# Ind. Sets	North	East	Up
3	3	1.97	2.59	3.08
6	2	2.04	2.88	3.06
Median [m]				
# GCPs	# Ind. Sets	North	East	Up
3	3	1.94	2.63	2.84
6	2	2.04	2.88	3.06
Standard Deviation [m]				
# GCPs	# Ind. Sets	North	East	Up
3	3	0.11	0.32	0.38
6	2	0.17	0.29	0.31

Table 4. Results of the scientific software SISAR for Hannover opposite-side stereo pair

# GCPs	RMSE CPs CSK Merano		
	North [m]	East [m]	Up [m]
9	2.21	3.40	3.23
# GCPs	RMSE CPs TSX Hannover same-side		
	North [m]	East [m]	Up [m]
9	2.48	2.71	6.39

Table 5. Results of OrthoEngine v. 10.3 for Merano and Hannover stereo pairs

The results of the orientation of the opposite-side stereo pair with SISAR software are presented in Table 4. With this configuration the accuracy is at the same level as a same-side configuration.

Finally, just the best results obtained using the commercial software OrthoEngine v. 10.3 (PCI Geomatica), in which the model developed by T. Toutin is embedded, are presented in the Table 5. Only tests with 9 GCPs are displayed, since the OrthoEngine v. 10.3 is able to orientate the SAR image with radargrammetric model using 8 GCPs at minimum (PCI Geomatics, 2009), and the results obtained increasing the GCPs number are not significant due to the low number of CPs.

As regards the Hannover opposite-side stereo pair, GPs available (only 13) are not sufficient to orientate the images with OrthoEngine and to make a reliable accuracy assessment.

For all stereo pair previously considered, RPCs have been generated using the tool available in the SISAR software. Instead of 78 coefficients generally employed in a third order rational polynomial function, a much lower number of coefficients (about 20) are estimated, avoiding the overparametrization and selecting only the estimable and significant parameters as mentioned before.

Overall, the RPCs related to both the denominators of the RPFs are estimated up to the first order at maximum or they are not estimated at all, whereas those related to both the numerators are estimated up to the first or the second order.

The generated RPCs were used in order to orientate the stereo pairs; results of RPCs applications are presented in Table 6, Table 7, Table 8 (compare with Table 2, Table 3, Table 4, respectively) for all the available stereo pairs.

The RPCs generation, and the corresponding application, has been made using the GCPs independent sets as previously explained for the rigorous model.

The accuracy level is just close to the radargrammetric rigorous model one, what proves the effectiveness of the RPCs generation tool implemented in SISAR.

The RPCs refinement, as previously mentioned, is not necessary in order to achieve the best accuracy. In fact the SISAR RPCs are calibrated on GCPs and are not affected by biases.

In the Table 9 the application of the estimated adjustment parameters are presented for the Hannover same-side stereo pair; RPCs have been applied without any refinement and using 5 GCPs to estimate a shift and an affine adjustment. The adjustment does not improve the results, rather they get slightly worse; this behaviour is due to the lack of significance of the adjustment parameters and it worth to be clarified.

RMSE CPs CSK Merano - RPCs model				
Average [m]				
# GCPs	# Ind. Sets	North	East	Up
3	6	2.79	4.23	2.63
6	3	2.58	3.62	2.67
9	2	2.79	3.77	2.71
Median [m]				
# GCPs	# Ind. Sets	North	East	Up
3	6	2.72	4.09	2.61
6	3	2.33	3.79	2.42
9	2	2.79	3.77	2.71
Standard Deviation [m]				
# GCPs	# Ind. Sets	North	East	Up
3	6	0.37	0.49	0.21
6	3	0.46	0.40	0.37
9	2	0.23	0.02	0.02

Table 6. Results of RPC generation and application for Merano stereo pair

RMSE CPs TSX Hannover same-side – RPCs model				
Average [m]				
# GCPs	# Ind. Sets	North	East	Up
3	6	2.41	2.69	3.26
5	4	2.28	2.85	3.07
9	2	2.19	2.46	2.99
Median [m]				
# GCPs	# Ind. Sets	North	East	Up
3	6	2.28	2.61	3.12
5	4	2.37	2.72	3.06
9	2	2.19	2.46	2.99
Standard Deviation [m]				
# GCPs	# Ind. Sets	North	East	Up
3	6	0.39	0.29	0.50
5	4	0.26	0.35	0.13
9	2	0.02	0.04	0.21

Table 7. Results of RPC generation and application for Hannover same-side stereo pair

RMSE CPs TSX Hannover opposite-side – RPCs model				
Average [m]				
# GCPs	# Ind. Sets	North	East	Up
3	3	1.99	2.76	3.21
6	2	2.09	3.13	2.99
Median [m]				
# GCPs	# Ind. Sets	North	East	Up
3	3	1.98	2.45	2.82
6	2	2.09	3.13	2.99
Standard Deviation [m]				
# GCPs	# Ind. Sets	North	East	Up
3	3	0.12	0.48	0.58
6	2	0.21	0.42	0.36

Table 8. Results of RPC generation and application for Hannover opposite-side stereo pair

TSX Hannover same-side - RPCs adjustment results				
		RMSE CPs [m]		
Transf.	# GCPs	North	East	Up
none	-	1.84	2.58	3.14
shift	5	1.87	2.6	3.15
affine	5	2.1	2.95	3.83

Table 9. Results of the RPCs adjustment for Hannover same-side stereo pair

Hannover TSX same-side stereo pair		
Degrees of freedom		8
T_α with α=5		2.306
Parameter	T0	Result
$A_0^{(1)}$	0.960	non-significant
$A_1^{(1)}$	0.913	non-significant
$A_2^{(1)}$	0.973	non-significant
$B_0^{(1)}$	1.509	non-significant
$B_1^{(1)}$	1.036	non-significant
$B_2^{(1)}$	1.813	non-significant
$A_0^{(2)}$	1.025	non-significant
$A_1^{(2)}$	0.956	non-significant
$A_2^{(2)}$	1.104	non-significant
$B_0^{(2)}$	1.164	non-significant
$B_1^{(2)}$	0.741	non-significant
$B_2^{(2)}$	1.652	non-significant

Table 10. Significance Student T-test for the RPCs adjustment parameters in the case of the Hannover same-side stereo pair

In order to check the significance level of the refinement parameters a Student T-test at 5% level has been performed. In Table 10 an example of Student T-test is shown for the Hannover same-side stereo pair. All parameters of the affine adjustment are non significant; similar results have been obtained also for the others available stereo pairs. This test confirms the convenience of the SISAR RPCs application without any adjustment.

6. CONCLUSIONS

The aim of the work was the development and the implementation of a rigorous radargrammetric model for the orientation of SAR imagery, suited to the Digital Surface Model generation. The model performs a 3D orientation based on two range and two zero-Doppler equations.

The model was defined and implemented in the scientific software SISAR, developed at Geodesy and Geomatic Institute of the University of Rome "La Sapienza"'.

Moreover a tool for the RPCs generation suited to SAR imagery has been included in SISAR software. RPCs model is a well-known and validated method to orientate optical satellite imagery, representing a standard re-parametrized form of the rigorous sensor model. Its implementation is standard and generalized, it is available in several commercial software, and the performances of the RPCs model can be at the level of the ones from rigorous models.

The model implemented has been tested on COSMO-SkyMed and on TerraSAR-X images; both satellites are able to acquire imagery in SpotLight mode, representing the most advanced SAR technology actually available.

As regards COSMO-SkyMed, we have two images forming a stereo pair over the area of Merano (Northern Italy). The images belongs to the Level 1A (SCS) category products, that are focused data in complex format, in slant range and zero-Doppler projection. The area covered by both stereo pairs is approximately 10 Km × 10 Km.

As regards TerraSAR-X, we have three images acquired over the town of Hannover (Northern Germany), all images are HighResolution SpotLight (HS) products with extension of 10 Km × 5 Km. Two images were acquired along an ascending orbit, one of these along a descending orbit. It is possible to choose various combination of images in order to form different stereo pairs; we selected a same-side stereo pair and an opposite-side stereo pair.

To test the effectiveness of the new rigorous model implemented in the software SISAR, the stereo pairs have been orientated varying the number of GCPs and the model accuracy is analyzed, evaluating the RMSE computed over CPs residuals (RMSE CPs), following the standard Hold-Out Validation procedure for accuracy assessment. In order to obtain significant results from the statistical point of view, for a given number of GCPs different tests were carried out, using independent sets of GCPs selected under the condition of a homogeneous distribution over the areas covered by the stereo pairs.

Moreover, SISAR results are compared with those stemming from commercial software OrthoEngine v.10.3 (PCI Geomatica).

The accuracy evaluation shows that the vertical accuracy is at level of 3.0 m in the case of Merano; this preliminary results are satisfying, considering the mean accuracy of the available GPs.

As regards the model performance varying the independent sets of GCPs, the software shows a stable behaviour and the increase of GCPs number does not improve the results remarkably.

As for TerraSAR-X data, we have a same-side and an opposite-side stereo pairs over the town of Hannover. The accuracy level achieved in the orientation tests with both stereo configuration is about 2.5 - 3.5 m. Again, the software shows a stable behaviour.

The commercial software OrthoEngine provides basically the same level of accuracy of SISAR in the case of Merano stereo pair, whereas in the Hannover stereo pair the height accuracy with SISAR software is better than OrthoEngine one; a

significant difference between the two software is that OrthoEngine needs 8 GCPs at least for the orientation of SAR images, whereas SISAR gets good results also using few points (3 or 5 GCPs).
The application of RPCs model to SAR stereo pairs gives good results, absolutely comparable with those derived through the radargrammetric rigorous model, what proves the effectiveness of the RPCs generation tool implemented in SISAR.
The results obtained are representative of the geometric potentialities of SpotLight stereo pairs as regards 3D surface reconstruction.
Anyway, it has to be recalled that the accuracy of the DSMs generated by the radargrammetric approach is strictly affected by the quality of the subsequent matching procedure, which is presently a hot topic and will be addressed in the future investigations.

7. APPENDIX - FURTHER INVESTIGATION ABOUT THE ORBIT REFINEMENT

In the last months further investigation about the orbit refinement have been addressed. In particular the simple model of circular orbit could be not sufficiently accurate in order to obtain the best accuracy from SAR imagery. A second model, that has been preliminary tested, is an orbit modelled on the interpolation of the state vector position through the Lagrange polynomial. Using this kind of orbit we noted that good accuracy has been achieved using only the metadata information, without the employment of GCPs. For example in the case of Merano CSK imagery accuracies are about of 2.8 m, 3.5 m and 2.7 m in East, North and vertical components respectively. This fact prove the high intrinsic geolocation accuracy of SAR imagery, but more test and analysis should be performed in order to verify the possibility of geolocation improvement using also few GCPs.

Acknowledgements
The COSMO-SkyMed stereo pairs was made available by e-Geos S.p.A., Rome (Italy), in the frame of a collaboration agreement.
The TerraSAR-X stereo pairs have been provided in the framework of the international project “Evaluation of DEM derived from TerraSAR-X data” organized by the ISPRS (International Society for Photogrammetry and Remote Sensing) Working Group VII/2 “SAR Interferometry”, chaired by Prof. Uwe Soergel – Leibniz University Hannover.
Moreover the author thanks very much Sysdeco Italia S.r.l., who supplied a temporary license of the OrthoEngine v. 10.3 software.
Finally, I am very grateful to my Ph.D. supervisor, Prof. Mattia Giovanni Crespi, and to the research team of the “Area di Geodesia e Geomatica”, especially to Ing. Paola Capaldo, Ing. Francesca Fratarcangeli and Ing. Andrea Nascetti.

References

Crespi, M., Fratarcangeli, F., Giannone, F., Pieralice, F., 2009. Chapter 4 - Overview on models for high resolution satellites imagery orientation, In: Li D., Geospatial Technology for Earth Observation data, Springer, Heidelberg: Shan J., Gong J. (Eds.)

Crosetto, M., Pérez Aragues, F., 1999. Radargrammetry and SAR interferometry for DEM generation: validation and data fusion, Proceedings of CEOS SAR Workshop, ESA-CNES, Toulouse, France

Fayard, F., Meric, S., Pottier, E., 2007, Matching stereoscopic SAR images for radargrammetric applications, International Geoscience and Remote Sensing Symposium, Barcelona

Fraser, C. S., Hanley, H. B., 2003. Bias compensation in rational functions for Ikonos satellite imagery, Photogrammetric Engineering and Remote Sensing, 69(1), pp. 53-57

La Prade, G., 1963. An Analytical and Experimental Study of Stereo for Radar, Photogrammetric Engineering, 29(2), pp. 294-300

Leberl, F.W., 1990. Radargrammetric image processing, Artech House, Norwood, USA

Meric, S., Fayard, F., Pottier, E., 2009. Chapter 20 - Radargrammetric SAR image processing, In: Pei-Gee Peter Ho (Eds.), Geoscience and Remote Sensing, Intech

PCI Geomatics, 2009. PCI Geomatica 10.3 User Guide

Raggam, H., Gutjahr, K., Perko, R., Schardt, M., 2010. Assessment of the Stereo-Radargrammetric Mapping Potential of TerraSAR-X Multibeam Spotlight Data, IEEE Transactions on Geoscience and Remote Sensing, 48(2)

Tao, C.V., Hu, Y., 2001. The rational function model. A tool for processing high resolution imagery, Earth Observation Magazine, 10(1), pp. 13-16

Toutin, T., 1995. Generating DEM from Stereo Images with a Photogrammetric Approach: Examples with VIR and SAR Data, EARSeL Advances in Remote Sensing, 4(2)

Toutin, T., 1996. Opposite Side ERS-I SAR Stereo Mapping over Rolling Topography, IEEE Transactions On Geoscience And Remote Sensing, 34(2)

Toutin, T., 1998. Stereo RADARSAT for Mapping Applications, 2nd International ADRO Symposium, Montreal, Canada

Toutin, T., 2000a. Stereomapping with SPOT-P and ERS-1 SAR} images, International Journal of Remote Sensing, 21(8)

Toutin, T., 2000b. Evaluation of Radargrammetric DEM From RADARSAT Images In High Relief Areas, IEEE Transactions

Toutin, T., Gray, 2000. L., State-of-the-art of elevation extraction from satellite SAR data, ISPRS Journal of Photogrammetry & Remote Sensing ", 55, pp 13-33

Toutin, T., Chenier, R., 2009. 3-D radargrammetric modeling of RADARSAT-2 Ultrafine Mode: preliminary results of the geometric calibration, IEEE Geoscience and Remote Sensing Letters, 6(2)

Questa raccolta di ricerche è stata pubblicata con il contributo della SIFET (Società Italiana di Fotogrammetria e Topografia).
L'AUTeC ringrazia la SIFET per l'attenzione e la sensibilità dimostrate per il lavoro dei Dottori di Ricerca che hanno conseguito il titolo nel 2011.

Associazione Universitari di Topografia e Cartografia

c/o DICA, Dipartimento di Ingegneria Civile, Ambientale e Aerospaziale dell'Università di Palermo
Viale delle Scienze, Edificio 8, 90128 Palermo
Prof. Benedetto Villa tel. 091/23896223, fax 091/588853, e-mail benedetto.villa@unipa.it

Finito di stampare nel dicembre 2011 presso Pixart s.r.l. Mestre (Ve)

Stampato con il contributo di

ISBN 978-88-905917-4-7

Dicembre 2011